



Ashraf, Khuram Umar (2014) Studies of the green sulphur bacterial reaction centre from *Chlorobaculum tepidum*. PhD thesis.

<http://theses.gla.ac.uk/6379/>

Copyright and moral rights for this thesis are retained by the author

A copy can be downloaded for personal non-commercial research or study, without prior permission or charge

This thesis cannot be reproduced or quoted extensively from without first obtaining permission in writing from the Author

The content must not be changed in any way or sold commercially in any format or medium without the formal permission of the Author

When referring to this work, full bibliographic details including the author, title, awarding institution and date of the thesis must be given

**Studies of the Green Sulphur Bacterial  
Reaction Centre from *Chlorobaculum  
tepidum***

**Khuram Umar Ashraf  
BSc.(Hons.), Mres**

Submitted in fulfilment of the requirements for the degree of Doctor  
of Philosophy

School of Molecular, Cellular and Systems Biology  
College of Medical, Veterinary and Life Sciences

University of Glasgow

2014

## Author's declaration

This thesis is an original composition which describes work performed entirely by myself unless otherwise cited or acknowledged. Its contents have not previously been submitted for any other degree. The research for this degree was performed between 2010 and 2014.

Signature.....

Printed Name .....

## Abstract

Photosynthetic organisms harvest sunlight through antenna light-harvesting complexes. Light absorbed by chromophores is transferred down an energy gradient to a reaction centre (RC) where photoinduced electron transfer occurs. A charge-separated state is generated that preserves some of the original light energy as electrochemical potential. By studying these RCs allows for us to deduce how they function through the elucidation of their structure, which ultimately allows for artificial mimics to be made.

*Chlorobaculum tepidum* (*C. tepidum*) is a green sulphur photosynthetic bacterium that contains a type I RC. Light energy is transferred to the RC from chlorosomes via a soluble Fenna-Mathews-Olson (FMO) protein. Although the structure of FMO has been solved on its own, little is known about the molecular organization of the reaction centre complex.

This thesis looks at two of the RC sub-units (PscB and PscD) that are water-soluble. To understand the contribution that these proteins make to RC function, they have been made in *E. coli* using an in-house expression vector. Using a 3C protease - iLOV - biotin acceptor domain - His10 (CLBH) tag, both PscB and PscD can be readily purified on a milligram-scale in four simple steps (Ni<sup>2+</sup>-affinity, subtractive IMAC (immobilized metal affinity chromatography) after cleavage with 3C protease, gel-filtration). PscD and PscB have been labelled with <sup>15</sup>N and <sup>13</sup>C for structural analysis by NMR, so far PscD has shown to be partially disordered implying that a potential binding partner may be required. PscB has shown to be well structured and is in the process of having its structure elucidated. The binding of PscD with FMO and ferredoxin from *Arabadopsis thaliana* has also been assessed by isothermal calorimetry to help identify the function of this protein.

Here it is also observed that when the RC is coupled to plasmons a near 5 fold increase is observed in fluorescence enhancement as compared to RC by itself. Plasmonic metallic nanoparticles are able to drastically alter the emission of vicinal fluorophores. Metallic nanoparticles can influence the fluorescence emission of nearby molecules by enhancing the absorbance of the molecule, and by modifying the radiative decay rate of that molecule. And this is what is

observed. This can further be increased when coupling the RC to the Plasmon by placing a silicon dioxide ( $\text{SiO}_2$ ) spacer in-between the RC and nanoparticle. This is the highest fluorescence enhancement observed to date.

As yet, no green sulphur bacterial RC has had its structure determined. Here, purification protocols have been developed that allow milligram quantities of a complex between the RC and FMO to be prepared. As well as identifying the best suitable detergents for solubilising and purifying the RC, two different populations of the RC have been discovered that can be separated by sucrose density gradients. Vapor diffusion, lipidic-cubic phase (LCP), bicelle, and co-crystallisation trials have been performed with pure RC-FMO. Thus far, promising crystals have been obtained when the RC has been co-crystallised with ferredoxin to 60 Å. These promising crystals are the first of its type, as this is the first type 1 RC crystal obtained.

## Acknowledgements

No matter how hard or difficult my path is, I will always walk it smiling 😊

I would firstly like to thank Professor Richard Cogdell for all of his guidance and supervision, he has provided me with wonderful opportunities and was never afraid to give me a clip behind the ear when I needed it. Thank you Richard for taking a chance on me. I would also like to thank Dr Alastair Gardiner, and Dr Heiko Lokstein for all of their help, support, guidance, and friendship throughout my PhD. I could always rely on them to put a smile on my face with a terrible joke.

I would like to thank the University of Glasgow for funding my 4 year PhD, as well as Solar fuels EU.

I have had the great honor to work with both past and present members of the Cogdell group, who I would like to thank: Dr Aleksander Roszak, Dr Sarah Henry, Dr Anne-Marie Carrie, Dr Rachel Mulvaney, June Southall, Kirsty Hacking, Laura Cranston, Dr Tatas Brotosudarmo, Claire Osborne and Yvonne Mitchell. I also want to thank two honorary Cogdell members and my good friends Dr Niall Fraser and Dr Alette Brinth. I always believed that it was the scientist that makes the project, but it is the people that make the lab. So thank you all for making my journey fun, it would have not been possible without any of you. I would like to say special thanks firstly to Dr Niall Fraser, for all the science chat, advice and his constant questioning of my data to make me a better scientist and for the CLBH tag. I would like to extend my thanks to my two really good friends who shared the journey with me Dr Alette Brinth and Dr Rachel Mulvaney for their great friendship and the long and helpful scientific discussions, they were always there when I needed them and never once said “no” to me, for even after they had left they did not leave me. Thank you for all your help guys.

I have been lucky enough to have had the opportunity to meet and collaborate with many great groups. I would like to thank Professor Oh-Oka and Dr Chihrosan (Univeristy of Osaka) for their His-tagged reaction centre. I would also like to thank the group of Dr Sebastian Mackowski (Nicolaus Copernacus University) and his group Lukasz, Dorota and Nikodem for all there help on the plasmonic

enhancement experiments. I would like to thank Prof. Martin Caffrey (Trinity College Dublin) and his group for allowing me to come over and learn the In-meso method. I want to say a special thanks to Dr Brian Smith who helped me with the NMR data and Dr Sharon Kelly for helping me with ITC and SPR, I am sure they got tired of me annoying them, but they never once showed it. I would also like to thank Dr Rhys Grinter for the ferredoxin construct, and the rest of the Walker group for the science chat.

Throughout my PhD people have come and gone from the Level 2 GBRC so I would like to say thanks to all the past and present members that have come and gone. I would like to give a special thanks to the Friday Curry crew, it always gave me something special to look forward to.

I would also like to say thanks to my good friends Yusuf Shabbir and Waseem Ahmed (Cinema buddy) for the great laughs and for reminding me that there was a life outside of the lab.

I would lastly like to say thanks my loving family, for all of their love and support and for putting up with me these past 4 years. They stayed with me every step of the way, through all my ups and downs, and never once complained, it never felt as though I was doing a PhD by myself. So I would like to dedicate my PhD to my mum; Farhat Ashraf, dad; Mohammed Ashraf, sister; Rabia Ashraf and my little brother; Bilal Ashraf.

*“He who issues forth in search of knowledge is busy in the cause of Allah till he returns from his quest.”* -Prophet Muhammad (s (PBUH)) as reported by Anas Ibn Malik in Al Tirmidhi, hadith #420.

# Table of contents

Author's declaration .....	ii
Abstract.....	iii
Acknowledgements.....	v
List of tables .....	xii
Chapter 1 - Introduction.....	1
1.1 Overview of Photosynthesis .....	1
1.1.1 Electron transport Chain .....	4
1.1.2 Oxygenic Photosynthesis .....	4
1.1.2.1 The Z-scheme .....	5
1.1.3 Anoxygenic photosynthesis .....	7
1.1.3.1 Purple photosynthetic bacteria.....	8
1.1.3.1.1 Purple photosynthetic antenna system .....	10
1.1.3.2 Green sulphur photosynthetic bacteria.....	11
1.2 Photosynthetic reaction Centres .....	12
1.2.1 Reaction centre Comparison.....	14
1.2.2 Photosystem II reaction centre.....	15
1.2.2.1 Archetecture of PSII .....	15
1.2.2.2 Electron tarnsfer pathway of PSII .....	17
1.2.2.3 Water oxidation.....	18
1.2.3 Photosystem I reaction centre .....	20
1.2.3.1 Archetecture of PSI.....	20
1.2.3.2 Electron pathway of PSI.....	24
1.2.4 Type II RC from purple photosynthetic bacteria.....	26
1.2.5 Type I RCs from the green sulphur bacteria <i>Chlorobaculum tepidum</i> .....	28
1.2.5.1 Absorption spectral properties of <i>Chlorobaculum tepidum</i> ...	30
1.2.5.2 Absorption spectral properties of Fenna-Mathews-Olson (FMO) . .....	32
1.3 Membrane proteins and the challenges faced with structural elucidation .....	32
1.3.1 Detergents.....	34

1.3.2	X-ray crystallography of membrane proteins .....	35
1.3.2.1	Vapor diffusion .....	36
1.3.2.2	In meso crystallisation .....	37
1.4	Artificial photosynthesis .....	39
1.4.1	Plasmon and fluorescence enhancement .....	39
1.5	Thesis Aims .....	42
Chapter 2 - Methods and Materials .....		43
2.1	Strains .....	43
2.2	Media .....	43
2.2.1	Culture Medium for Growth of <i>Chlorobium tepidum</i> .....	43
2.2.2	Luria Broth (LB) & Terrific Broth (TB) for <i>E. coli</i> growth.....	43
2.2.3	NMR Minimal media (1 x M9).....	43
2.3	Sodium dodecyl sulphate-polyacrylamide gel electrophoresis (SDS-Page) .....	44
2.4	<i>Chlorobium tepidum</i> .....	44
2.4.1	Growth room/conditions for <i>C. tepidum</i> .....	45
2.4.2	Harvesting of cells .....	45
2.4.3	Membrane preparation .....	45
2.4.4	Preparation of the <i>C. tepidum</i> His-tagged RC .....	46
2.4.4.1	Solubilisation: .....	46
2.4.4.2	Nickel purification: .....	46
2.4.4.3	Sucrose density Gradients .....	47
2.4.4.4	Size exclusion chromatography: .....	47
2.4.4.5	Amido black assay .....	47
2.4.4.6	Light induced Oxygen consumption .....	49
2.4.4.7	Thermostabilisation of the <i>C. tepidum</i> RC.....	49
2.5	Purification of FMO .....	50
2.6	Genomic extraction of <i>C. tepidum</i> .....	50
2.7	PCR amplification and sub-cloning strategies .....	51
2.8	Expression vector modification of the pET21a vector.....	52
2.9	CLBH incorporation into modified pET21a vector.....	53
2.10	Amplification of PscD and PscB.....	53
2.11	Insertion of PscD/PscB in the modified pET21a expression vector containing CLBH.....	53

2.12	Insertion of PscB in the novagen pET28a expression vector for NMR studies.....	53
2.13	Using iLOV to measure expression of PscD and PscB .....	54
2.13.1	Test expression .....	54
2.13.2	SDS page identification of expressed target proteins.....	55
2.13.3	Measuring iLOV fluorescence expression of PscB/PscD-CLBH in 96 well plates .....	55
2.14	Protein expression and purification of PscD-CLBH.....	55
2.14.1	Preparation of PscD-CLBH.....	55
2.14.2	Nickel affinity chromatography .....	55
2.14.3	Cleavage of the CLBH tag by 3C protease .....	56
2.14.4	Subtractive IMAC (Immobilised Metal Affinity Chromatography)...	56
2.14.5	Gel filtration .....	56
2.14.6	Wester Blot analysis of cleaved CLBH tag using an iLOV antibody .	56
2.15	Purification of 3C protease.....	57
2.16	Protein Expression and Purification of PscB .....	58
2.16.1	Preparation of PscB .....	58
2.16.2	Nickel Affinity chromatography .....	58
2.17	Expression and purification of ferredoxin from <i>Arabidopsis thaliana</i> ..	58
2.18	Circular Dichroism (CD) .....	59
2.19	Nuclear Magnetic resonance (NMR) .....	59
2.20	Isothermal titration calorimetry (ITC).....	59
2.21	Biocore .....	60
2.22	Crystallisation .....	60
2.23	Lipidic Cubic Phase (LCP)/in-meso crystallisation .....	60
2.23.1	In meso crystallization set up using the SIAS robot .....	61
2.24	Incorporation of <i>C. tepidum</i> RC in lipidic bicelles .....	63
2.25	Plasmon enhancement experiments of <i>Chlorobium tepidum</i> RC and FMO .....	63
Chapter 3 -Isolation, Purification & stabilisation of the <i>C. tepidum</i> RC and FMO protein .....		65
3.1	Introduction .....	65
3.2	Growth of <i>C. tepidum</i> Cells .....	66

3.3	Choosing the best detergent with which to solubilise the <i>C. tepidum</i> RC	67
3.3.1	Detergent selection for solubilisation and purification	69
3.4	Large scale purification of the His-tagged RC complex	72
3.5	SEC purification and detection of the RC by silver staining	75
3.6	Discovery of RC heterogeneity:	77
3.6.1	Determining RC protein concentration by Amido black assay	78
3.6.2	Discovery and separation of the two different populations of FMO-RC by SEC and Sucrose Gradients	79
3.7	The effect of light on <i>C. tepidum</i> RC	86
3.8	Assaying RC functionality and activity: Light induced oxygen consumption using a Clark-type electrode	88
3.9	FMO purification	90
Chapter 4 - Plasmonic fluorescence enhancement with photosynthetic pigment-protein complexes		92
4.1	Introduction	92
4.2	Coupling <i>C. tepidum</i> RCs to silver nanoparticles	93
4.3	Fluorescence Enhancements of <i>C. tepidum</i> RC	94
4.4	Fluorescence Decays of <i>C. tepidum</i> RCs on SIFs and glass substrates	98
4.5	Effect of Silicon dioxide (SiO <sub>2</sub> ) spacers	99
4.6	RCs on Silver Nanowires	101
4.7	Plasmonic enhancement of FMO fluorescence	102
Chapter 5 - Expression, purification and characterisation of PscD and PscB		106
5.1	Introduction	106
5.2	The CLBH tag	106
5.3	pET21a expression vector modification and insertion of CLBH	107
5.4	PscD and PscB amplification and insertion in to pET21a vector containing CLBH	111
5.5	Test expression of PscD-CLBH and PscB-CLBH	113
5.6	Using iLOV to measure expression of PscD and PscB	116
5.6.1	Absorption spectra of iLOV	117
5.6.2	Expression of PscD and PscB using iLOV	117
5.7	Expression and Purification of His tagged 3C protease for the removal of the CLBH tag	120

5.8	Identifying the disordered segments of the PscD and PscB.....	122
5.9	Purification of PscD and Cleavage of CLBH tag .....	123
5.10	Purification of PscB & challenges with the CLBH-tag .....	127
5.11	PscD CD (circular dichroism) .....	131
5.12	PscD and PscB homology modelling .....	133
5.12.1	PscD .....	133
5.12.2	PscB .....	138
5.13	Expression and purification of Ferredoxin from <i>Arabidopsis thaliana</i> for binding experiments.....	140
5.14	ITC of PscD with FMO and ferredoxin .....	142
Chapter 6 - Structural studies on the <i>C. tepidum</i> RC and the two peripheral proteins PscB and PscD .....		144
6.1	Introduction .....	144
6.2	NMR of PscD and PscB.....	144
6.2.1	1D NMR spectra of PscD and PscB.....	145
6.2.2	2D HSQC NMR spectra of PscD and PscB .....	147
6.2.3	PscB - NMR temperature studies to increase tumbling .....	149
6.2.4	PscB - T2 (Spin-spin relaxation) experiments .....	151
6.2.5	Triple resonance experiments.....	153
6.3	Crystallisation of the <i>C. tepidum</i> RC .....	156
6.3.1	In meso Crystallisation .....	156
6.3.2	In meso absorption spectrum.....	158
6.3.3	<i>C. tepidum</i> RC in 7.7 MAG .....	161
6.3.4	Lipid Bicelles for the crystallisation of <i>C. tepidum</i> RC .....	163
6.3.5	Interaction of RC with Ferredoxin using light induced oxygen consumption assay and SPR.....	165
6.3.6	Co-crystallisation with Ferredoxin.....	168
Chapter 7 - Conclusions and Future Outlook .....		171
Appendices .....		176
Bibliography .....		181

## List of tables

Table 1.1 Depiction of two types of RC complexes present in photosynthetic organisms. ....	3
Table 1.2 Genera of anoxygenic phototrophic purple bacteria [24] .....	9
Table 3 Measured Excitation power .....	64
Table 4 Concentration of purified <i>C. tepidum</i> RC obtained by the amido black assay and worked out based on the calibration curve obtained in figure 3.12...	79
Table 5 Calculated enhancement factors of RCs on SIFs compared to that of RCs on glass .....	97
Table 6 Information on the CLBH tag.....	107
Table 7 Sparse matrix crystal screens used to set up crystal trays of RC + ferredoxin .....	168

## List of figures

Figure 1.1 Equation of plant and algae photosynthesis.....	1
Figure 1.2 van Neil equation.....	2
Figure 1.3 Electron transport diagram for all types of RCs found in different organisms .....	4
Figure 1.4 Diagrammatic view of a Chloroplast.....	5
Figure 1.5 Depiction of oxygenic photosynthesis.....	7
Figure 1.6 Schematic picture of the purple bacterial photosynthetic membrane. ....	11
Figure 1.7 Comparison of the three types of reaction centre found in photosynthetic organisms. ....	14
Figure 1.8 Structure of the PSII complex .....	16
Figure 1.9 View of the PS II monomer from above facing the luminal side (Ferrira 2004) .....	17
Figure 1.10 Image depicting cofactors which are involved in electron transport	18
Figure 1.11 Proposed Mechanism of water oxidation in PSII. ....	19
Figure 1.12 PS I structure, shown as a trimer at 2.5 Å from <i>Synechococcus elongatus</i> . ....	21
Figure 1.13 The ferredoxin docking site. A side view image of the plant PS I monomer.....	22
Figure 1.14 depiction of The PsaC, PsaD and PsaE subunits from PS I. ....	23
Figure 1.15 A side view of the structure of plant photosystem I. ....	25
Figure 1.16 Structure of the <i>Blc. viridis</i> RC .....	26
Figure 1.17 The cofactors of the RC from <i>Blc. viridis</i> .....	28
Figure 1.18 The model of photosynthetic apparatus of <i>Chlorobium tepidum</i> ....	29
Figure 1.19 Absorption spectrum of the <i>Chlorobaculum tepidum</i> RC .....	31
Figure 1.20 Absorption spectrum of FMO from <i>C. tepidum</i> .....	32
Figure 1.21 Structures of Eukaruotic and prokaryotic membrane proteins over the years.....	33
Figure 1.22 Illustration of the phase diagram .....	37
Figure 1.23 Picture depicting the events of lipidic cubic phase.....	38
Figure 1.24 Illustration of surface Plasmon resonance on metal. ....	40
Figure 1.25 Jablonski digaram. Metal vs no metal.....	41

Figure 2.1 Diagram showing the “the pscA gene duplication” method to express the WT and His-tagged RC. ....	45
Figure 2.2 Dispensing of the RC in monoolein row by row (A - C), using the SIAS robot. ....	61
Figure 2.3 The robot selecting the precipitant from the deep well blocks (A) and dispensing it on the RC in meso (B). The LCP tray of the RC in meso with precipitant can clearly be observed (C).....	62
Figure 3.1 Absorption spectra <i>C. tepidum</i> RC, obtained by Ni <sup>2+</sup> -affinity purification. Image modified from Oh-Oka (2013) [160].....	65
Figure 3.2 Growth conditions of <i>C. tepidum</i> cells .....	66
Figure 3.3 Absorption spectra of RC membranes before and after solubilisation. ....	68
Figure 3.4 Absorption spectrum of RC membranes at each stage of the nickel purification. ....	70
Figure 3.5 Absorption Spectra comparing the RC before and after precipitation	71
Figure 3.6 observation of the RC band during nickel purification.....	73
Figure 3.7 Protein gel of <i>C. tepidum</i> RC at each stage of the solubilisation and Nickel purification.....	73
Figure 3.8 Absorption spectrum of RC after nickel purification. ....	74
Figure 3.9 SEC profile of <i>C. tepidum</i> RC on a Sepharose S-200 column .....	75
Figure 3.10 Absorbance spectrum of before and after purification of the RC. Were the distinct features of the RC are observed. ....	76
Figure 3.11 Silver stained gel of pure RC. ....	77
Figure 3.12 Amido Black calibration curve using BSA standards.....	79
Figure 3.13 UV absorbance of the <i>C. tepidum</i> RC grown from 75-120 litres of cells. ....	80
Figure 3.14 Absorption spectra of fractions taken from SEC profile. ....	81
Figure 3.15 Test sucrose gradients for the identification of the different populations of FMO-RC.....	82
Figure 3.16 Continuous (30-35%) Sucrose Density Gradients of the <i>C. tepidum</i> RC ran O/N. ....	83
Figure 3.17 Absorption spectra of the three bands obtained after sucrose density gradients were run. ....	84
Figure 3.18 SEC profiles of the upper and lower RC bands taken from sucrose gradients. ....	85

Figure 3.19 Effect of Light on the <i>C. tepidum</i> RC. ....	87
Figure 3.20 Clarke-type electrode trace of MV reduction of dissolved oxygen ..	89
Figure 3.21 Purification, identification and absorbance spectrum of FMO. ....	91
Figure 4.1 Absorption spectra of Silver Island Film (SIF) (black line) and RCs (red). ....	93
Figure 4.2 Emission spectra of reaction centre. ....	95
Figure 4.3 Histograms of emission intensities of RCs on glass and SIFs. ....	96
Figure 4.4 Enhancement factors for the different excitation wavelengths. ....	97
Figure 4.5 Fluorescence decays of <i>C. tepidum</i> RCs on SIFs and glass substrates.	99
Figure 4.6 Effects of a SiO <sub>2</sub> spacer thickness on fluorescence of RCs coupled to nanowires. ....	100
Figure 4.7 Wide field microscope view of RC on nanowires. ....	101
Figure 4.8 X-ray structure of the FMO trimer. ....	102
Figure 4.9 Spectral properties of FMO and SIFs. ....	103
Figure 4.10 Histograms of emission intensities of FMO on differently prepared substrates. ....	104
Figure 4.11 Fluorescence decay curves of FMO on glass and on SIF .....	105
Figure 5.1 Incorporation of PscD and PscB into the CLBH tag. ....	107
Figure 5.2 Restriction maps of the WT pET21a and the modified pET21a. ....	108
Figure 5.3 Restriction maps and DNA gel for successful construction of the CLBH encoding gene incorporated into the modified pET21a vector. ....	110
Figure 5.4 1% DNA agarose gels showing amplification of PscD and PscB. ....	111
Figure 5.5 Restriction analysis of modified pET21a plasmid containing CLBH with the DNA encoding for PscD and PscB. ....	112
Figure 5.6 4-12% SDS-page gel of PscD-CLBH time course test expression on LB and TB at 22°C and 37°C induction times. ....	114
Figure 5.7 4-12% SDS-page gel of PscB-CLBH time course test expression on LB and TB at 22°C and 37°C induction times. ....	115
Figure 5.8 Structure of the light oxygen volage 2 (LOV2 or iLOV) domain from <i>Arabidopsis thaliana</i> . ....	116
Figure 5.9 Absorption spectra of iLOV. ....	117
Figure 5.10 Absorbance measurement of iLOV of PscD-CLBH taken at different time intervals, in TB and LB, at 22°C and 37°C. ....	118
Figure 5.11 Absorbance measurement of iLOV of PscB-CLBH taken at different time intervals, in TB and LB, at 22°C and 37°C. ....	119

Figure 5.12 Purification of human rhinovirus 3C protease by size exclusion chromatography .....	121
Figure 5.13 4-12% SDS-page gel of the 3C SEC profile. ....	121
Figure 5.14 Disorder prediction order of PscB. ....	122
Figure 5.15 Disorder prediction order of PscD. ....	123
Figure 5.16 Fluorescence of iLOV from the CLBH tag during IMAC.....	124
Figure 5.17 4-12% SDS-page analysis of PscD Nickel purification and 3C cleavage .....	125
Figure 5.18 Western blot analysis using the polyclonal iLOV antibody CLBH ....	126
Figure 5.19 Absorption Spectra comparison of iLOV from the CLBH tag and PscB-CLBH.....	128
Figure 5.20 4-12% SDS-page analysis of PscB nickel purification and the PscB pigmented sample.....	130
Figure 5.21 Absorption spectra of PscB, PscB-CLBH and the iLOV from the CLBH tag. ....	131
Figure 5.22 Far UV CD spectrum of PscD.....	132
Figure 5.23 Near UV CD spectrum of PscD.....	133
Figure 5.24 Sequence alignment of the <i>C. tepidum</i> PscD amino acid sequences with PsaD from photosystem I from different organisms. ....	134
Figure 5.25 Phyre2 homology model of PscD with secondary structure prediction .....	135
Figure 5.26 structural homology modeling of PscD in comparison to PsaD. ....	137
Figure 5.27 Sequence alignments of the iron-sulphur proteins from different organisms. ....	138
Figure 5.28 Phyre2 homology model of PscB with secondary structure prediction .....	139
Figure 5.29 A. Ferredoxin bound to nickel and B. After elution of the Nickel column .....	140
Figure 5.30 SDS-page gel of ferredoxin after passing it over the Superdex S75 SEC column .....	141
Figure 5.31 Absorption spectra of ferredoxin .....	141
Figure 5.32 ITC experiments of PscD with FMO and Ferredoxin. ....	143
Figure 6.1 1D 1H-NMR spectrum of recombinant PscD. ....	146
Figure 6.2 1D 1H-NMR spectrum of recombinant PscB. ....	146
Figure 6.3 2D, 15N-HSQC, spectrum of recombinant PscD .....	148

Figure 6.4 2D, <sup>15</sup> N-HSQC, spectrum of recombinant PscB .....	148
Figure 6.5 2D-HSQC spectra of PscB. Temperature effects of PscB ranging from 298 K to 323 K.....	150
Figure 6.6 T <sub>2</sub> (Spin-Spin) relaxation delay of PscB.....	152
Figure 6.7 T <sub>2</sub> relaxation of PscB .....	153
Figure 6.8 Triple resonance experiments HNCO, HNCA and CBCA(CO)NH .....	154
Figure 6.9 HBHA(CO)NH triple resonance experiment of PscB.....	155
Figure 6.10 Absorption spectrum of the <i>C. tepidum</i> RC .....	157
Figure 6.11 In-meso set up using the lipid syringe to mix the monolein and the RC .....	158
Figure 6.12 Spectral changes on the breakdown of the <i>C. tepidum</i> RC .....	159
Figure 6.13 Spectral difference of RC in solution with RC in monolein .....	160
Figure 6.14 Absorption spectrum of the difference of <i>C. tepidum</i> RC in 9.9 MAG taken away from the RC in solution. ....	161
Figure 6.15 Absorption spectrum of <i>C. tepidum</i> RC In solution (black line) and RC in 9.9 (red line) and the RC in 7.7 MAG (Green line).....	162
Figure 6.16 Three possible outcomes of the in meso crystallisation of the <i>C. tepidum</i> RC.....	162
Figure 6.17 RC absorption comparison of RC in solution and RC in bicelles .....	164
Figure 6.18 Clarke-type electrode trace of ferredoxin reduction of dissolved oxygen.....	166
Figure 6.19 SPR of RC and ferredoxin .....	167
Figure 6.20 Examples of crystals of RC + ferredoxin in the Cryo 1 & 2 screens. ....	169
Figure 6.21 Examples of crystals of RC + ferredoxin in the JCSG screens .....	169
Figure 6.22 Grid loop and diffraction pattern of the <i>C. tep</i> RC + ferredoxin crystal.....	170

## List of Abbreviations

+	Oxidised state
-	reduced state
*	excited electronic state
2D	2-dimensional
3D	3-dimensional
$\alpha$	Alpha
$\beta$	beta
Å	Angstrom
A	Acceptor
Amp	Ampicillin
<i>A. thaliana</i>	<i>Arabidopsis thaliana</i>
ATP	Adenosine Triphosphate
Au	Arbitrary units
B800	Bulk Bchl with a maximal absorbance at 800 nm
B820	Bulk Bchl with a maximal absorbance at 820 nm
B850	Bulk Bchl with a maximal absorbance at 850 nm
BChl	Bacteriochlorophyll
CD	Circular Dichroism
Chls	Chlorophylls
CMC	Cell Micelle Concentration
CO <sub>2</sub>	Carbon Dioxide
CPMG	Carr-Purcell-Meiboom-Gill
cDNA	Complementary DNA
Cu	Copper
DE52	Diethylaminoethyl cellulose
DLS	Diamond light source
DNA	Deoxyribonucleic acid
DM	Decyl- $\beta$ -D-maltoside
DDM	Dodecyl- $\beta$ -D-maltoside
DTT	Dithiothreitol
<i>E. coli</i>	<i>Escherichia coli</i>
EDTA	Ethylenediaminetetraacetic acid

FAD	Flavin Adenine Dinucleotide
FD	Ferredoxin
FeS	Iron Sulphur
FMN	Flavin mononucleotide
FMO	Fenna-Mathew-Olson
FNR	Ferredoxin-NADP reductase
FID	Free Induction Decay
FU	Fluorescence units
GFP	Green Fluorescent Protein
GPCR	G-protein Coupled Receptors
H <sub>2</sub>	Hydrogen
H <sub>2</sub> O	Water
H <sub>2</sub> S	Hydrogen Sulphide
H	Heavy
HRV 3C	Human rhinovirus 3C protease
iLOV	Improved Light-Oxygen-Voltage domain
IPTG	Isopropyl-β-D-1-thiogalactopyranoside
ITC	Isothermal Titration Calorimetry
Kan	Kanamycin
L	Light
LB	Luria Brorth
LH1	Light Harvesting 1 Complex
LH2	Light Harvesting 2 Complex
LCP	Lipidic Cubic Phase
M	Medium
MAG	Monoacylglycerol
MW	Molecular Weight
MWCO	Molecular weight cut off
NADP	Nicotinamide Adenine diphosphate
NIR	Near infra red
NMR	Nuclear magnetic resonance
O <sub>2</sub>	Oxygen
OD	Optical density
OEC	Oxygen evolving centre
PCR	Polymerase chain reaction

PEG	Polyethylene glycol
Pi	Isoelectric point
PSI	Photosystem I
PSII	Photosystem II
PSU	Photosynthetic Unit
PQ	plastiquione
PQH <sub>2</sub>	Plastiquinol
Q/ QH <sub>2</sub>	Quinone/Quinol exchange
<i>Rba</i>	<i>Rhodobacter</i>
RC	Reaction centre
RPM	Rate per minute
SDS-page	Sodium dodecyl sulphate polyacrylamide gel Electrophoresis
SDG	Sucrose Density Gradient
SEC	Size exclusion chromatography
SIF	Silver Island Films
SPR	Surface Plasmon resonance
TB	Terrific Broth
TCA	Tricarboxylic acid

# Chapter 1 - Introduction

---

## 1.1 Overview of Photosynthesis

Photosynthesis is one of the most important biological processes on earth by converting solar energy in to chemical energy. Photosynthesis has mainly been known to be associated with oxygenic photosynthesis, even though scientific evidence suggests that the first photosynthetic organisms evolved from anoxygenic photosynthetic organisms. This is due to the early history of photosynthesis [1-3]. In 1640 Jean Baptist van Helmont showed that plants, over a 5 year long experiment, consumed water and not the surrounding soil, which is what was believed to be true then. This was confirmed by a Swiss chemist, Nicolas-Théodore de Saussure, in 1804. Nicolas-Théodore de Saussure showed that the increase of the mass of a plant as it grows was not due the uptake of water alone, but also due to the uptake of Carbon Dioxide (CO<sub>2</sub>) [4]. It was later in 1845 that a German physician, Julius Robert von Mayer, was first to state the law of the conversion of energy, that energy is neither created nor destroyed. He stated that the energy from the sunlight was stored, in part, as chemical energy in the organic matter, as a sugar (Figure 1.1). This gave rise to the basic reaction by which photosynthesis was used to produce food (such as glucose) in green plants and algae (Figure 1.1) [1, 5].

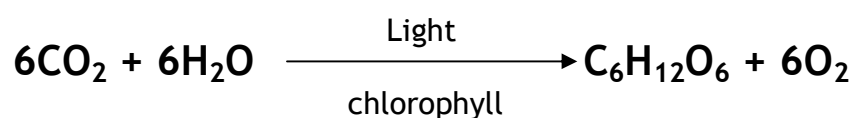


**Figure 1.1 Equation of plant and algae photosynthesis**

There are many types of photosynthetic organisms, their photosynthetic reaction centres can be classified into two groups based either on the type of terminal electron acceptor the RCs have, or their oxygen-evolving ability i.e. oxygenic or anoxygenic (Table 1.1) [1, 6]. The most flourishing and widely distributed photosynthetic organisms on the present earth are oxygenic phototrophs, such as plants, algae, and cyanobacteria, which utilise water as an electron source for their

growth and evolve oxygen as a by product of water cleavage reaction. All of prokaryotic phototrophs other than cyanobacteria, such as purple bacteria, green sulphur bacteria, heliobacteria, and filamentous anoxygenic photosynthetic bacteria (FAPs), are anoxygenic ones, which are most commonly called 'photosynthetic bacteria'.

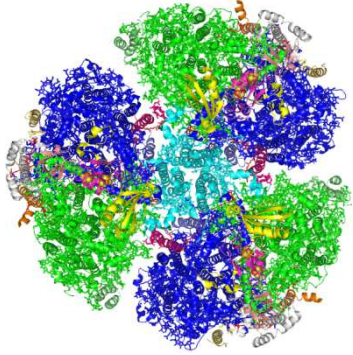
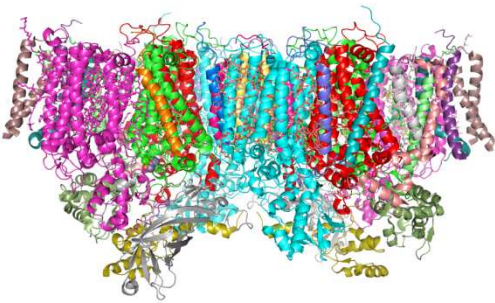
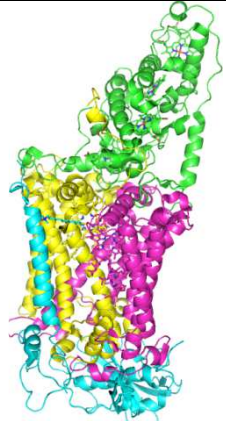
Anoxygenic bacterial photosynthetic organisms differ in several ways from green plants and algae, in that the essential pigments within photosynthetic bacteria are bacteriochlorophylls, which are analogues of chlorophylls [2, 5]. For bacterial systems to assimilate CO<sub>2</sub> they must be provided with a reducing substance, such as sulphide or reduced organic compounds [1-2, 4, 7]. By studying purple sulphur bacteria and green sulphur bacteria, Cornelius van Niel in the 1920s, was the first scientist to demonstrate that photosynthesis is a light-dependent redox reaction, in which hydrogen from an oxidisable compound reduces carbon dioxide to cellular materials. This gave rise to the van Neil equation (Figure 1.2), which shows the overall reaction of all photosynthetic organisms [1-2, 4, 7]. When water is the oxidisable substrate oxygen is produced and the van Neil equation can be applied to oxygenic photosynthesis [7].



**Figure 1.2 van Neil equation.**

General overall equation of photosynthesis, proposed by Van Neil. The (CH<sub>2</sub>O) represents stored organic matter. Generically the oxidisable substrate can be called 2H<sub>2</sub>A. Where A represents an electron acceptor.

Photosynthesis can be divided into two partial reactions that have been called the light and dark reactions. In the light reactions solar energy is used to power the synthesis of ATP and NADPH. In the dark reactions the free energy released through cleavage of the phosphoanhydride bonds of ATP and the reducing power of NADPH are used to fix and reduce CO<sub>2</sub> to form carbohydrate. The carbohydrate is a reduced molecule that can be oxidised to release energy [1]. This can be thought of as a fuel. Photosynthesis is able to make a reduced molecular fuel by using a constant supply of electrons, either from water (H<sub>2</sub>O) or reduced sulphur compounds, depending on the type of organism [8-9].

<u>Type</u>	<u>Type I</u> (Fe/S cluster as terminal electron acceptor)		<u>Type II</u> (Quinones as terminal acceptors)	
	<u>Name</u>	Homodimeric <b>Green Sulphur bacteria</b>	Heterodimeric <b>Photosystem I</b>	Heterodimeric <b>Photosystem II</b>
<u>Organism</u>	<i>Chlorobaculum</i>	Cyanobacteria, Plants, Algae	Cyanobacteria, Plants, Algae	<i>Rhodospseudomonas viridis</i>
<u>Oxygenic/Anoxygenic</u>	Anoxygenic	Oxygenic	Oxygenic	Anoxygenic
<u>Structure</u>	?			

**Table 1.1 Depiction of two types of RC complexes present in photosynthetic organisms.**

Oxygenic photosynthesis releases oxygen where as anoxygenic does not. Within Oxygenic systems you will always find Photosystem I and photosystem II together. Within anoxygenic systems you will only find one type of RC, depending if it is either purple bacteria or a green bacteria. Green bacteria can be further subdivided into either green 'sulphur' or green 'non-sulphur' bacteria.

### 1.1.1 Electron transport Chain

RCs are considered to be at the heart of photosynthesis, and this is where the primary photochemistry and several of the secondary electron transfer reactions take place. These are a complex of proteins, pigments and co-factors that carry out the energy conversion reactions of photosynthesis and depending on the type of RC and the organism containing the RC they have different electron transport chains (Figure 1.3) [10]. However, additional electron transfer processes are necessary before the reduction of NADP and the production of ATP. These include the cytochrome bc<sub>1</sub> and b<sub>6</sub>f complexes. These complexes oxidise quinols produced by photochemistry in type II RCs or via cyclic processes in type I RCs and pumps protons across the membrane, which makes ATP by utilising the proton motive force. All phototrophic organisms have a cytochrome bc<sub>1</sub> or b<sub>6</sub>f complex of generally similar architecture [11].

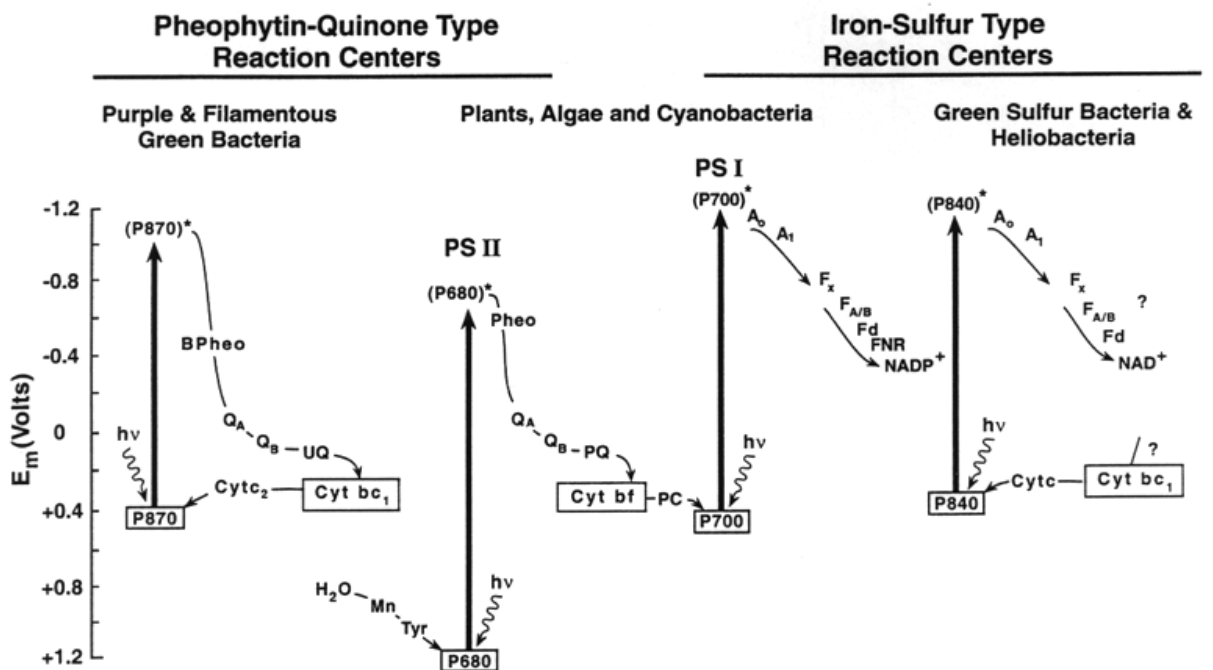


**Figure 1.3 Electron transport diagram for all types of RCs found in different organisms**

Electron transport pathways found in different organisms. Plants, algae and cyanobacteria contain both type I and type II RCs. Whereas Purple and green sulphur bacteria contain one of each [10].

### 1.1.2 Oxygenic Photosynthesis

Oxygenic phototrophs, such as plants, algae, and cyanobacteria are the most flourishing and widely distributed photosynthetic organisms on earth, which

utilise water as an electron source for their growth and evolve oxygen as a by-product of water. It is considered that oxygenic phototrophs had emerged in the ocean ca. 3.5 billion years ago [12], and the release of oxygen from the oxidation of water, over time, changed the anaerobic atmosphere into the present aerobic one [13].

The reactions of oxygenic photosynthesis in algae and plants take place within a special cell organelle, the chloroplast (Figure 1.4). The chloroplast has two outer membranes, which enclose the stroma. Inside the stroma is a closed membrane vesicle, the thylakoid [14]. Unlike plants, thylakoids within cyanobacteria are located in the cytoplasm. The thylakoids are flattened sacks bounded by membranes called lumen. CO<sub>2</sub> fixation occurs within the stroma. Whereas the conversion of light energy into chemical energy, where the photosynthetic pigments, fats, proteins and enzymes which are arranged in photosystems are found occurs in the thylakoid membrane [15-16].

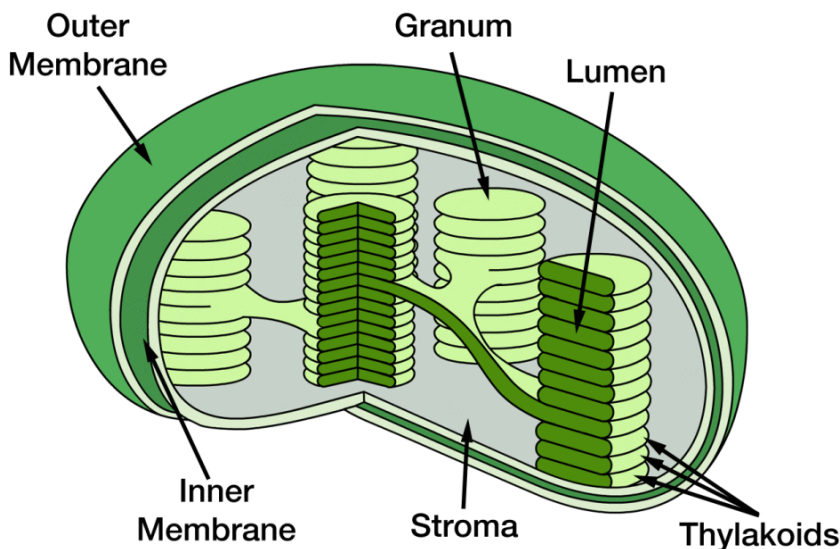


**Figure 1.4 Diagrammatic view of a Chloroplast.**

The chloroplast is composed of an outer and an inner membrane, which contains Granum that are stacks of thylakoids, this is where the light reaction takes place. The chloroplasts also contain the stroma, the site of CO<sub>2</sub> fixation [14].

#### 1.1.2.1 The Z-scheme

Reduction of CO<sub>2</sub> into biomass is carried out by using energy utilised for the light independent reaction. Both ATP and electrons in the form of NADPH or reduced ferredoxin are needed for biological CO<sub>2</sub> reduction. The source of electron is

ultimately dependant on the type of organism, it can either be  $\text{H}_2\text{O}$ ,  $\text{H}_2\text{S}$ ,  $\text{H}_2$  or any other type of reduced inorganic compound [17].

Light dependant water oxidation, NADP reduction and the formation of ATP were first shown to be carried out in the chloroplasts thylakoid membrane. These reactions were shown to be catalysed by two protein complexes or photosystems, photosystem I (PSI) and photosystem II (PSII). Where PSII would carry out oxidative chemistry and PSI would carry out reductive chemistry. The formation of ATP was due to the ATP synthase molecule, or better known as F-ATPase molecule, by utilising the proton motive force formed by the light reaction (Figure 1.5 B) [18].

The Z-scheme represents the steps in the light reactions, showing the pathway of electron transport from water to  $\text{NADP}^+$  (Figure 1.5 A). The primary redox reactions of photosynthesis start with the excitation of pairs of special reaction centre chlorophyll (a) molecules, labeled as P680 (in PSII) and P700 (in PSI). PSII absorbs a photon, which is excited to an electronic state (called P680\*). In the excited state it then quickly gives up an electron to pheophytin, becoming into oxidized P680 ( $\text{P680}^+$ ). The excitation energy comes either from directly absorbed light or by energy transfer from adjacent pigment molecules in protein complexes called antennas. The P680 is regenerated when  $\text{P680}^+$  extracts electrons from water, resulting in the production of  $\text{O}_2$ .  $\text{P680}^+$  is a very strong oxidizing agent (about 1.23 V at pH 7.0). Extracting electrons from water requires substantial energy. The electrons pulled from water by Photosystem II are used to reduce plastoquinone (PQ) to plastoquinol ( $\text{PQH}_2$ ). 4 protons from water are released into the lumen, lowering its pH, which in turn forms a pH gradient between the stroma & lumen. A second photo-oxidation reaction occurs at photosystem I [19]. Cytochrome  $b_6f$  accepts electrons and converts  $\text{PQH}_2$  to PQ; more protons are released into lumen. The next electron acceptor here is a protein called plastocyanin, with its bound copper atom. The copper atom can be reversibly oxidized or reduced as  $\text{Cu}^+$  and  $\text{Cu}^{2+}$ . So it can carry an electron. Photosystem I can absorb energy from sunlight, exciting an electron within a group called P700. The excited  $\text{P700}^*$  gives an electron to  $\text{A}_0$ , producing oxidized P700 ( $\text{P700}^+$ ) and reduced  $\text{A}_0$  ( $\text{A}_0^-$ ). In PSI the electron on  $\text{A}_0^-$  is passed ultimately to  $\text{NADP}^+$  via several other intermediates:  $\text{A}_1$ , a phylloquinone (vitamin K);  $\text{F}_x$ ,  $\text{F}_A$ ,

and  $F_B$  (which are immobile (bound) iron-sulphur proteins), ferredoxin (which is a mobile iron-sulphur protein molecule) and the enzyme ferredoxin-NADP reductase (FNR) (which is actually an oxido-reductase and whose active group is FAD (flavin adenine dinucleotide)) [6, 17, 20].

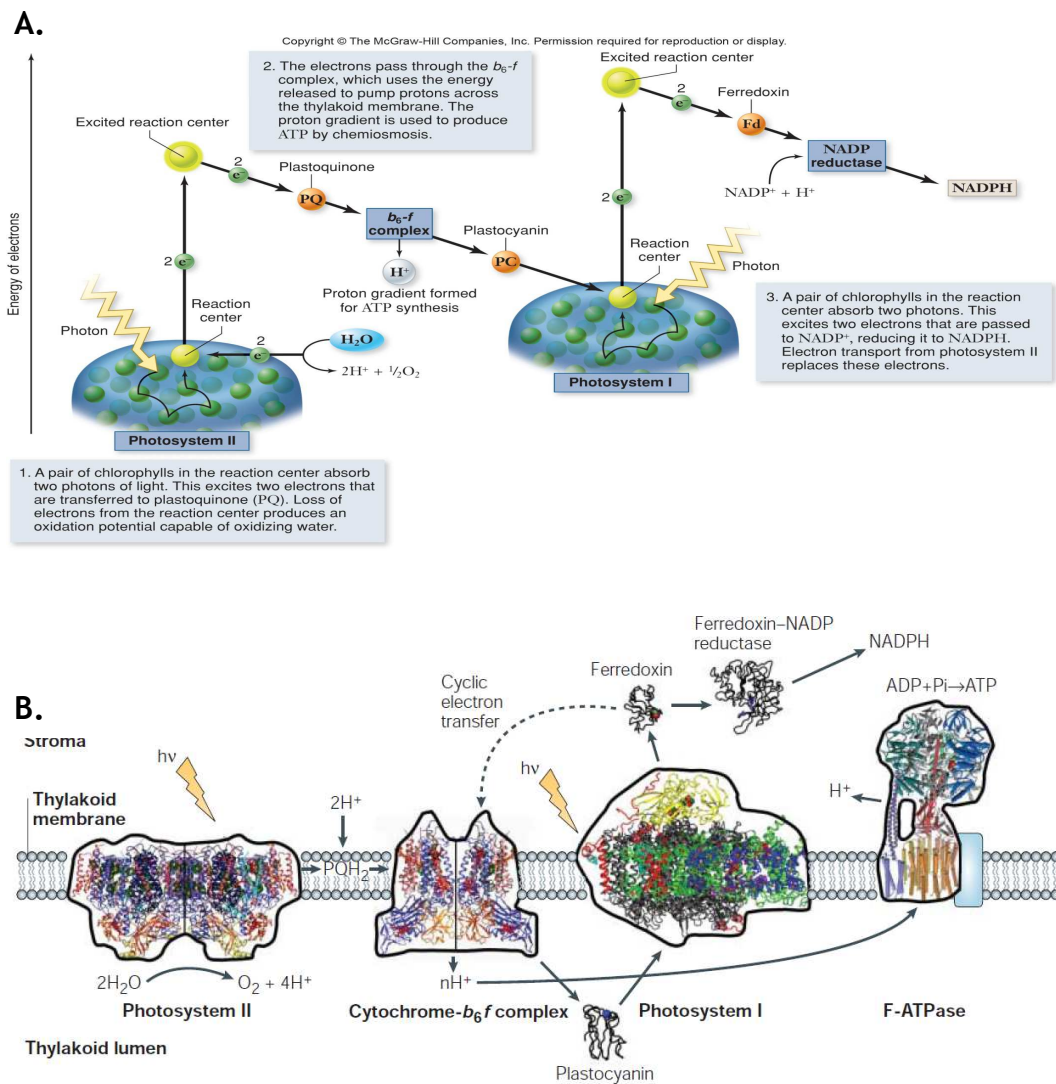


**Figure 1.5 Depiction of oxygenic photosynthesis**

**A.** The Z-scheme. The energy diagram of the light reactions in photosynthesis, showing the transfer pathway of water (PSII) to  $NADP^+$ . **B.** shows the four large membrane-protein complexes, including the F-ATPase, in thylakoid membranes that drive oxygenic photosynthesis.

### 1.1.3 Anoxygenic photosynthesis

One of the most interesting facts of purple or green phototropic bacteria is their ability to use bacteriochlorophyll mediate processes to carry out anoxygenic photosynthesis. The process of photosynthesis, in anoxygenic phototropic bacteria, is carried out in the absence of oxygen as syntheses of the

photosynthetic pigments are repressed by oxygen. Unlike oxygenic photosynthetic organisms, anoxygenic photosynthesis do not utilise water as an electron donor [1]. These bacterial phototrophs have just one type of reaction centre, either type I or II, and require electron donors of lower redox potential than water. Based on their morphological and physiological properties anoxygenic phototrophic bacteria are an extremely heterogeneous eubacteria. Based on their phenotype we are able to differentiate between purple bacteria, purple sulphur bacteria, green sulphur bacteria, green bacteria and heliobacteria [2, 9]. Five major eubacterial groups have been identified by 16S rRNA analyses. Among these, one is represented in oxygenic photosynthesis (as mentioned in section 1.1.2), cyanobacteria, one by green sulphur bacteria, one by *Chloroflexus*, one by phototrophic purple bacteria and one by *Heliobacterium* [9].

#### **1.1.3.1 Purple photosynthetic bacteria**

Purple bacteria are gram-negative prokaryotes containing photosynthetic pigments bacteriochlorophylls and carotenoids. Purple bacteria can be classified into two main groups, purple sulphur bacteria (Gammaproteobacteria) and purple non-sulphur bacteria (Alpha- or Betaproteobacteria), this is dependent on how they utilise sulphide as an electron donors. Anoxygenic phototrophic purple bacteria are a major group of photosynthetic organisms. They can grow autotrophically with CO<sub>2</sub> as sole carbon source [7, 21-23].

Nearly 5 genera of anoxygenic purple bacteria are known, Table 1.2 lists some of the genera of purple bacteria [1, 9, 21]. In nature purple bacteria can be found in lakes, lagoons or even sewage, environments containing high concentrations of sulphide. Densely stratified 'plates' of purple bacteria form only in the deep waters of lakes, where both oxygen and light are limited due to the presence of plants, cyanobacteria and algae closer to the surface .

Taxonomy/phylogeny	Genus (abb.)	Morphology	Species (Examples)
Purple non-sulphur bacteria	<i>Rhodobaca</i> ( <i>Rca.</i> )	Cocci to short rods	<i>bogoriensis</i>
Alphaproteobacteria	<i>Rhodobacter</i> ( <i>Rba.</i> )	Rods	<i>capsulatus</i> , <i>sphaeroides</i>
	<i>Rhodovulum</i> ( <i>Rdv.</i> )	RodsCocci	<i>sulfidophilum</i>
	<i>Rhodospseudomonas</i> ( <i>Rps.</i> )	Budding rods	<i>acidophila</i> , <i>palustris</i>
	<i>Rhodoblastus</i> ( <i>Rbl.</i> )	Budding rods	<i>globiformis</i>
	<i>Blastochloris</i> ( <i>Blc.</i> )	Budding rods	<i>sulfoviridis</i> , <i>viridis</i>
	<i>Rhodomicrobium</i> ( <i>Rmi.</i> )	Budding rods	<i>vanniellii</i>
	<i>Rhodobium</i> ( <i>Rbi.</i> )	Rods	<i>marinum</i>
	<i>Rhodoplanes</i> ( <i>Rpl.</i> )	Rods	<i>serenus</i>
	<i>Rhodocista</i> ( <i>Rcs.</i> )	Spirilla	<i>centenaria</i>
	<i>Rhodospirillum</i> ( <i>Rsp.</i> )	Spirilla	<i>rubrum</i> , <i>photometricum</i>
	<i>Phaeospirillum</i> ( <i>Phs.</i> )	Spirilla	<i>molischianum</i>
	<i>Rhodopila</i> ( <i>Rpi.</i> )	Cocci	<i>globiformis</i>
	<i>Rhodospira</i> ( <i>Rsa.</i> )	Spirilla	<i>trueperi</i>
	<i>Rhodovibrio</i> ( <i>Rhv.</i> )	Vibrio	<i>salinarum</i>
	<i>Rhodothallasium</i> ( <i>Rts.</i> )	Spirilla	<i>salexigens</i>
	<i>Roseospira</i> ( <i>Ros.</i> )	Spirilla	<i>mediosalina</i>
<i>Roseospirillum</i> ( <i>Rss.</i> )	Spirilla	<i>parvum</i>	
Betaproteobacteria	<i>Rhodocyclus</i> ( <i>Rcy.</i> )	Curled Vibrios	<i>tenuis</i>
	<i>Rhodoferax</i> ( <i>Rfx.</i> )	Rods, Vibrios	<i>antarticus</i>
	<i>Rubrivivax</i> ( <i>Rvi.</i> )	Rods, curved rods	<i>gelatinosus</i>
Purple Sulphur Bacteria			
Gammaproteobacteria			
Family <i>Chromatiaceae</i>	<i>Allochromatium</i> ( <i>Alc.</i> )	Rods	<i>vinosum</i>
	<i>Amoebobacter</i> ( <i>Amb.</i> )	Cocci in plates or clumps	<i>purpureus</i>
	<i>Chromatium</i> ( <i>Chr.</i> )	Rods	<i>okenii</i> , <i>weissei</i>
	<i>Halochromatium</i> ( <i>Hch.</i> )	Rods	<i>salexigens</i>
	<i>Isochromatium</i> ( <i>Isc.</i> )	Rods	<i>buderi</i>
	<i>Laprobacter</i> ( <i>Lpb.</i> )	Rods	<i>modestohapilophilus</i>
	<i>Laprocystis</i> ( <i>Lpc.</i> )	Cocci in clusters	<i>roseopersicina</i>
	<i>Marichromatium</i> ( <i>Mch.</i> )	Rods	<i>purpuratum</i>
	<i>Rhabdochromatium</i> ( <i>Rbc.</i> )	Rods	<i>marinum</i>
	<i>Thermochromatium</i> ( <i>Tch.</i> )	Rods	<i>tepidum</i>
	<i>Thioalkalicoccus</i> ( <i>Tac.</i> )	Cocci	
	<i>Thiobaca</i> ( <i>Tba.</i> )	Rods	
	<i>Thiocapsa</i> ( <i>Tca.</i> )	Cocci	<i>roseopersicina</i>
	<i>Thiococcus</i> ( <i>Tco.</i> )	Cocci	<i>pfennigii</i>
	<i>Thiocystis</i> ( <i>Tcs.</i> )	Cocci to short rods	<i>violacea</i>
	<i>Thiodictyon</i> ( <i>Tdc.</i> )	Rods in aggregates	<i>elegans</i>
	<i>Thioglavicoccus</i> ( <i>Tfc.</i> )	Cocci	
	<i>Thiohalocapsa</i> ( <i>Thc.</i> )	Cocci	<i>halophila</i>
	<i>Thiolamprovum</i> ( <i>Tlp.</i> )	Cocci	<i>pedioforme</i>
	<i>Thiopedia</i> ( <i>Tpd.</i> )	Cocci often in plates	<i>rosea</i>
	<i>Thiorhodococcus</i> ( <i>Trc.</i> )	Cocci	<i>minor</i>
	<i>Thiohodovibrio</i> ( <i>Trv.</i> )	Vibrios to spirilla	<i>winogradskyi</i>
	<i>Thiospirillum</i> ( <i>Tsp.</i> )	Spirilla	<i>jennese</i>
Family <i>Ectothiorhodospiraceae</i>	<i>Ectothiodhorospira</i> ( <i>Ect.</i> )	Vibrios to spirilla	<i>shaposhnikovii</i>
	<i>Halorhodospira</i> ( <i>Hlr.</i> )	Vibrios to spirilla	<i>neutrophilla</i>
	<i>Thiorhodospira</i> ( <i>Trs.</i> )	Vibrios to spirilla	<i>sibirica</i>
	<i>Ectothiorhodosinus</i> ( <i>Ets.</i> )	Rods	<i>mongolicus</i>

Table 1.2 Genera of anoxygenic phototrophic purple bacteria [24]

### 1.1.3.1.1 Purple photosynthetic antenna system

Bacteriochlorophyll is the main light harvesting (LH) pigment in purple photosynthetic bacteria, unlike oxygenic organisms i.e. cyanobacteria that contain chlorophyll. Bacteriochlorophyll is a closely related magnesium porphyrin that has a more saturated tetrapyrrole ring. This allows for BChl molecules to absorb at longer wave lengths compared with chlorophyll [1, 22, 25].

The purple photosynthetic light reactions begin with absorption of a photon by the LH or antenna system. There are generally two types of antenna complexes, that carry out the initial photon capture, and are known as light harvesting 2 (LH2) and light harvesting 1 (LH1) complexes [26]. The absorbed excitation is transferred energetically downhill to the reaction center (RC) in less than 100 ps. This then initiates an electron transport cycle between the RC, cytochrome bc<sub>1</sub>, and cytochrome c (Figure 1.6), this in turn generates the proton motive force that drives the production of ATP [21, 27-29].

The reaction centre, where charge separation takes place after the energy is funneled to, is surrounded by LH1 and LH2. The LH1 antenna forms a 1:1 stoichiometric complex with the RC, known as the core complex. Most purple photosynthetic bacteria contain LH2 and the core complex (LH1-RC). But there are purple bacterial organisms such as *Rhodospirillum (Rs.) rubrum* that only contain the core complex [30]. Both of these LH complexes are governed by the same principles. Hydrophobic apoproteins, called  $\alpha$  and  $\beta$ , each of which has a single membrane-spanning  $\alpha$ -helix are noncovalently bound to Bacteriochlorophyll *a* and the carotenoids. The LH complexes are oligomers of these  $\alpha\beta$  pairs, together with their associated pigments [31-32].

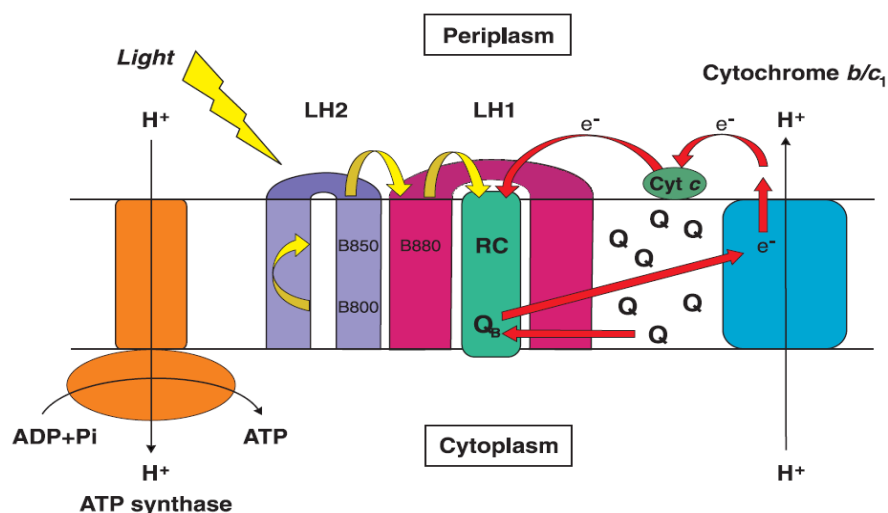


**Figure 1.6 Schematic picture of the purple bacterial photosynthetic membrane.**

LH complexes harvest the energy of a photon and funnel the energy down an energy gradient until it reaches the reaction centre (RC). At the RC electron transfer reactions are initiated at the Bchl special pair. The electron is passed to nearby cofactors down a redox gradient until it reaches a quinone molecule ( $Q_B$ ). When the quinone is reduced by the first electron, charge separation is generated across the membrane. The quinone is subsequently further reduced and doubly protonated. The resultant quinol molecule then diffuses through the membrane to the cytochrome  $b/c_1$  complex where it is oxidised and a proton motive force is generated which is used by ATP synthase to synthesise an ATP molecule.

There are different types of BChl a molecules that can be found in purple bacteria. There is the B800 and the B850 in LH2, and B875 in LH1 that absorbs at 800, 850, and 875 nm. However, these can differ from species to species, even more so it has been shown that the absorption can be different within the same species under different light conditions [25, 27-28, 33].

### 1.1.3.2 Green sulphur photosynthetic bacteria

Green sulphur bacteria are obligatory anaerobic photoautotrophic bacteria, and classified into a phylogenetically and physiologically distinct group, *Chlorobi*.

They are gram-negative eubacteria and have no developed membrane structure as thylakoids in chloroplasts and cyanobacteria or chromatophores in purple bacteria. Therefore, their light reactions occur in the cellular membrane. They are usually found in anoxic and sulfide-rich freshwater, either in the bottom sediment or deep layers of the water column, or within microbial mats.

Recently they have also been found in some extreme environments such as the anoxic layer 100 meters below the surface of the Black Sea [34], deep-sea hydrothermal vents in the Pacific Ocean [35], and the microbial mats of Octopus and Mushroom Springs in Yellow Stone National Park [36]. To be able to adapt to

such dim-light environments, all green sulphur bacteria so far characterised have developed unique light harvesting organelles attached to the membrane, called 'chlorosomes'. A Chlorosome is like a 'bag' that is made of a monolayer of lipid and contains self-aggregates of BChl *c*, *d*, or *e*, depending on species.

Chlorosomes can capture the light energy and transfer it to the RC with high efficiency; these allow the organisms to grow at remarkably low light intensities. All well characterised strains fix carbon dioxides by the reductive (also called 'reverse') tricarboxylic acid (TCA) cycle instead of the common Calvin cycle. Most species utilise the electrons derived from oxidation of inorganic sulphur compounds such as sulfide, thiosulfate, and/or elemental sulphur, while a few species can use ferrous iron [37-38].

## 1.2 Photosynthetic reaction Centres

Reaction centres (RC) are a complex of proteins and pigments along with cofactors, which carry out primary energy conversion reactions of photosynthesis. RC complexes can be classified into two types based on their terminal electron acceptors, Type I and II RCs. Type I RCs, also known as 'iron-sulphur (Fe-S) type' RC, contain three low potential Fe-S clusters as terminal electron acceptors [30, 39-40]. The Type I RC can generate a highly energized electron to reduce ferredoxin (Fd), which is a soluble electron carrier and used as the electron donor for NADP<sup>+</sup> reduction by ferredoxin-NADP<sup>+</sup> oxidoreductase (FNR) [37, 41-42]. Type II RCs, also known as 'pheophytin-quinone type' RCs, have two pheophytin *a* and two quinone molecules as primary and terminal electron acceptors. Unlike Type I RCs, Type II RCs can not reduce Fd, but instead carry out a double reduction of the terminal quinone acceptor, QB. These two types of RCs have obvious different biochemical and physiological functions, which are closely related to the overall photosynthetic electron transport pathways in photosynthetic organisms. Oxygenic phototrophs possess both types of RC complexes (PS I and PSII) [22]. PS I is a Type I RC which reduces Fd and oxidize soluble metal-containing carriers, cyt *c*<sub>6</sub> or plastocyanin [43-44].

PSI, PSII, and RC II (from purple bacteria) consist of two core polypeptides which are almost identical but partially different and are considered to have been diverged from the same polypeptide. Therefore, these RCs were referred to as

heterodimeric. RC II, from the purple bacterium *Blastochloris Viridis* [45], was the first crystal structure to be reported. The First membrane protein ever to be solved to atomic level (2.5 Å), by Deisenhofer *et al.* 1985 [45], through X-ray crystallography was this reaction centre. This led onto other heterodimeric crystal structures being solved such as the PSI from cyanobacterium *Thermosynechococcus elongatus* [46], and the higher plant *Arabidopsis thaliana* [47-48], PS II from *T. elongatus* [16, 49], and RC II from the purple bacterium *Rhodobacter Sphaeroides* [26, 50-51]. These structures of heterodimeric RCs have revealed structure relationships between RC complexes. Structural information about the reaction centre contributed greatly to the understanding of its complicated reaction mechanism. Electron transfer coupled with proton translocation across the membrane is a feature common to bioenergetic processes such as oxidative phosphorylation and photosynthesis. The resulting electrochemical gradient facilitates ATP synthesis. Key players in bioenergetics are integral membrane proteins and co-factors embedded in the membrane complexes. Hence, structural data about membrane protein complexes contribute greatly to obtaining a profound understanding of the reaction mechanism. A lot of effort has been made in research to elucidate membrane proteins involved in these bioenergetic processes in order to be able to carry out structure-function studies [14, 52].

## 1.2.1 Reaction centre Comparison

A Comparison of the three types of reaction centre found in photosynthetic organisms (Figure 1.7), Purple bacteria, photosystem II and photosystem I, show that in the purple bacterial reaction centre two of the polypeptide chains, L and M are arranged around an axis of 2-fold rotational symmetry within the photosynthetic membrane (shown in red Figure 1.7) [6, 53-54].

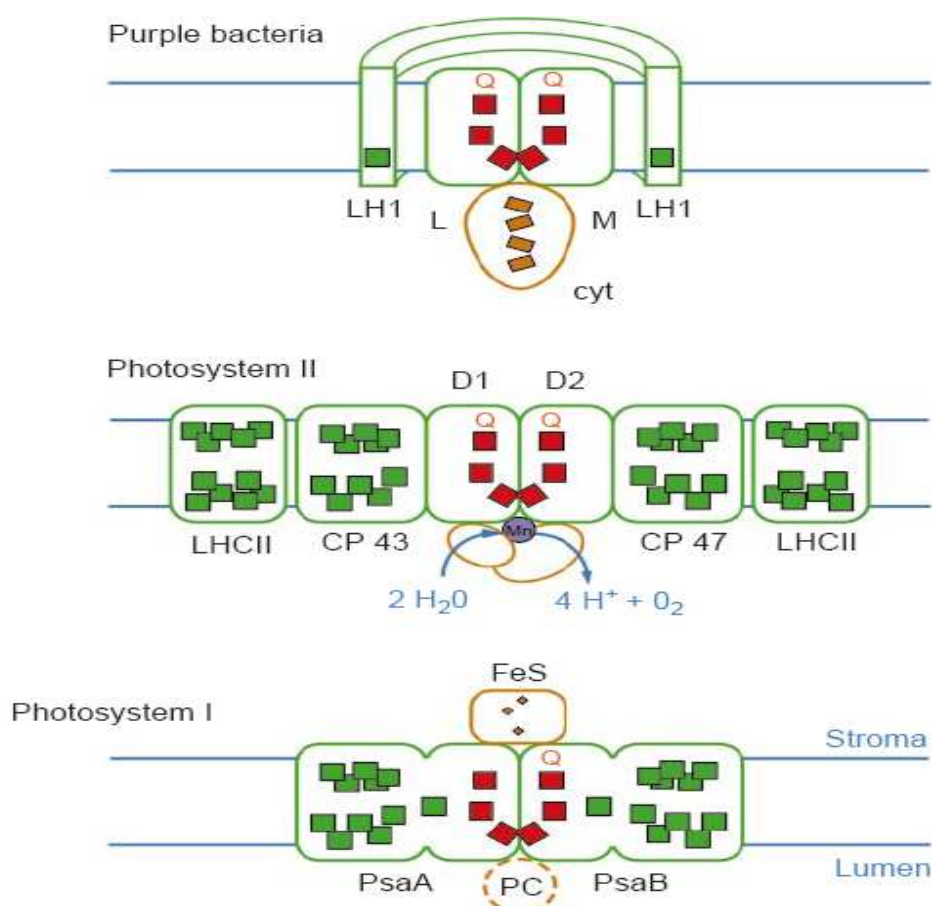


**Figure 1.7 Comparison of the three types of reaction centre found in photosynthetic organisms.**

Top, bacterial reaction centre. The L and M subunits, which bind the pigments active in charge separation (red), are related by local near two-fold symmetry. The reaction centre is surrounded by a ring of light-harvesting proteins (LH1). Electrons are fed into the reaction centre by a haem-binding cytochrome (cyt). Centre, photosystem II. The D1 and D2 proteins are structurally and functionally homologous to the L and M subunits of the bacterial reaction centre and hold the active pigments in a similar configuration. Light energy is collected by LHCII and channelled into the reaction centre by the core antenna proteins, CP43 and CP47, which are positioned at either side of the D1-D2 heterodimer. The resulting charge separation enables the manganese cluster on the luminal surface to withdraw electrons from water, releasing oxygen into the atmosphere. Bottom, photosystem I. The PsaA and PsaB proteins form a PSII-like heterodimer. PsaA and PsaB each consist of a reaction centre system equivalent to D1 or D2, and a core antenna equivalent to CP43 or CP47. Electrons are taken from reversibly bound plastocyanin (PC) on the luminal side, and delivered to the iron-sulphur clusters (FeS) on the stromal side, where they are used to reduce  $\text{NADP}^+$ .

The reaction centre is surrounded by a ring of light-harvesting proteins (LH1). Electrons are fed into the reaction centre by a haem-binding cytochrome (cyt). Photosystem II (Shown in the centre of Figure 1.7), contain proteins, known as D1 and D2, which are structurally and functionally homologous to the L and M subunits of the purple bacterial reaction centre and hold the active pigments in a similar configuration. Light energy is collected by LHCII and channelled into the reaction centre by the core antenna proteins, CP43 and CP47, which are positioned at either side of the D1-D2 heterodimer (Further discussed in section 1.2.2.1) [17]. The resulting charge separation enables the manganese cluster on the lumenal surface to withdraw electrons from water, releasing oxygen into the atmosphere. Photosystem I (at the bottom of Figure 4) [55]. The PsaA and PsaB proteins form a PSII-like heterodimer. In PSI, N-terminal domains of PsaA & PsaB are similar to CP43 & CP47. The C-terminal domains of PsaA & PsaB each consist of a reaction centre system equivalent to D1 & D2 subunits [56]. Distribution of peripheral antenna Chls of PSI bound to N-terminal domains of PsaA & PsaB, similar to that for CP43 & CP47. Electrons are taken from reversibly bound plastocyanin (PC) on the lumenal side, and delivered to the iron-sulphur clusters (FeS) on the stromal side, where they are used to reduce  $\text{NADP}^+$  [5, 57-58].

## 1.2.2 Photosystem II reaction centre

The light reactions begin at “photosystem II” (The “II” refers to the fact it was the second photosystem to be discovered even though the light reaction starts here). Photosystem II is a “light activated oxidation-reduction enzyme”. The oxygen we breathe is a product of the photosystem II reaction. The OEC (Oxygen evolving complex)/Mn cluster is found at the PSII complex. The overall structure of PSII was solved by Werner Kühlbrandt (1998) at 8 angstroms, from *Thermosynechococcus elongatus* (*T. elongatus*), and later by Ferreira *et al* (2004) revealing the OEC at 3.5 angstroms, and recently (2011) from *T. vulcanus* at 1.9 Å [56, 59-60].

### 1.2.2.1 Architecture of PSII

PSII is a dimer in both plants and cyanobacteria, consisting of 17 protein subunits to which 30-40 Chlorophylls and 8-12 carotenoids that are non-covalently bound. From the 17 protein subunits, 14 of these subunits are membrane

intrinsic, whereas PsbO, PsbU and PsbV do not contain membrane alpha helices and are located at the luminal side (Figure 1.8) [59, 61].

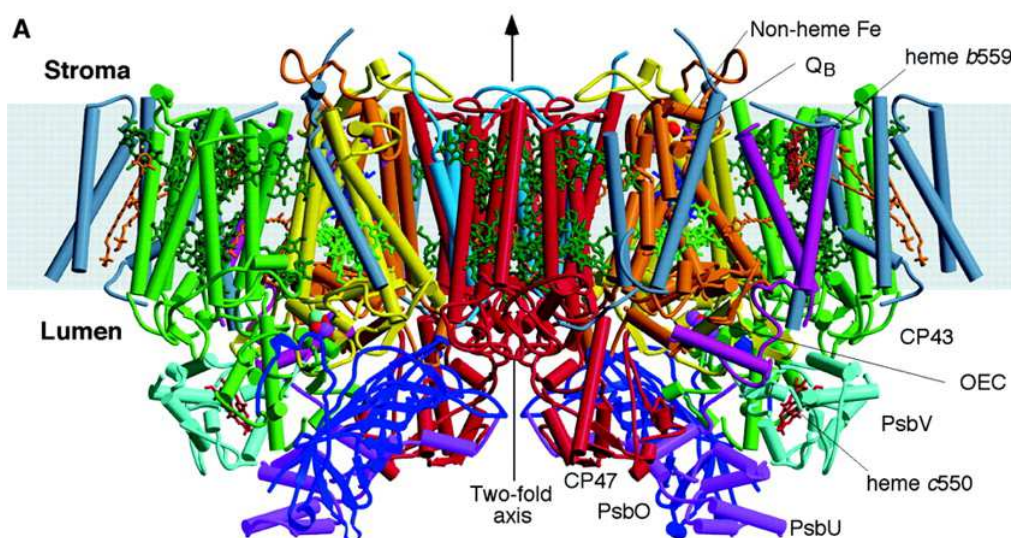


**Figure 1.8 Structure of the PSII complex**

Structure of PSII solved at 3.8-3.2 Å from *T. elongatus*. The D1 and D2 subunits are in Yellow and Orange. CP47 in red and CP43 in green [59].

The D1 and D2 subunits form the centre of the PSII monomer complex. Each of these subunits comprises 5 transmembrane helices (A to E) organised in a manner almost identical to that of the L and M subunits of the reaction centre of photosynthetic purple bacteria (bRC). Due to the high redox potential of P680, PSII experiences high photodamage. D1 which binds most co-factors of the electron transport chain including the Mn cluster [49]. This protein has to be replaced every half hour in bright sunlight. The central core of D1 and D2 are on either side of the antenna proteins CP47 and CP43, each of these subunits consisting of 6 transmembrane helices. Outside the CP43/D1-D2/CP47 core are 13 transmembrane helices. PsbE and PsbF are the alpha and beta subunits of Cyt b559. PsbL, M and T (Figure 1.9) are involved in dimer formation. And the proteins PsbX and PsbI stabilises chlorophylls of the D1 and D2 subunits. And the four small subunits may help facilitate carotenoid binding, as 4 of the seven beta-carotenoids are found in there vicinity [59, 62].

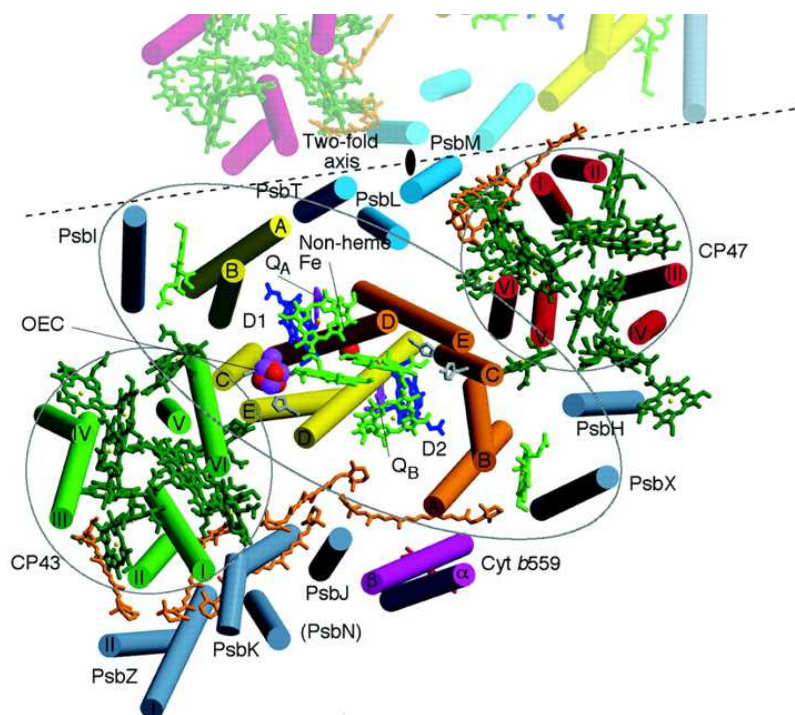
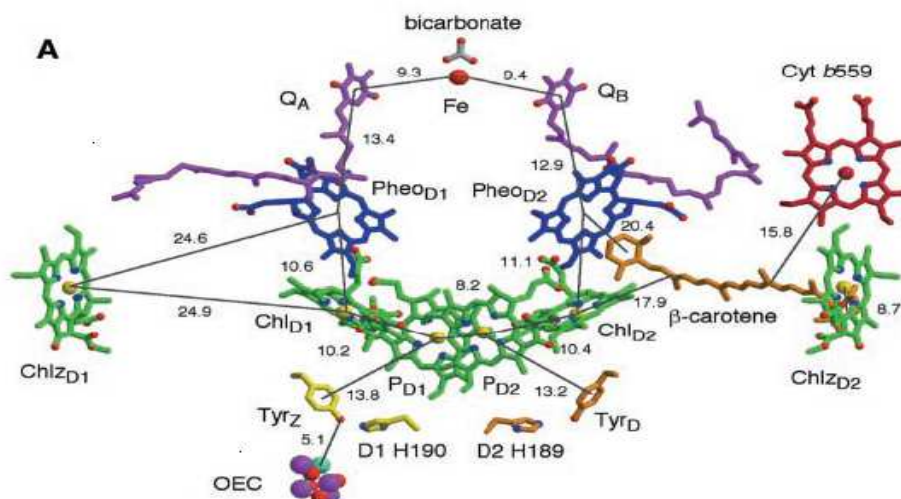


Figure 1.9 View of the PS II monomer from above facing the luminal side (Ferrira 2004)

### 1.2.2.2 Electron transfer pathway of PSII

PS II reactions are powered by light-driven electron transfer across the Reaction center (RC) composed of the D1 and D2 subunits. Upon illumination, the chlorophyll P680 (shown as PD1) (Figure 1.10) releases an electron by creating a resonance energy, making electrons go from a ground to an excited state [63]. The energy is passed through many chlorophyll molecules until reaching the P680 RC. The electron is then passed to pheophytin (mobile carrier, in the D1 subunit). Which passes its electron to plastoquinone (PQ)  $Q_A$  and then to plastoquinone  $Q_B$  (by Fe, which is the electron carrier), the plastoquinone molecules are embedded in the D2 and D1 proteins. It is passed to a “plastoquinone” molecule, or “PQ”. PQ can accept 2 electrons (along with two Hydrogens), to form fully reduced  $PQH_2$ . After accepting 2 electrons  $Q_B$  is protonated, then released into the membrane matrix. Except  $Q_B$  all redox active cofactors involved are located on the D1 side of the RC. After two subsequent electron transport the doubly reduced  $Q_B$  binds two photons and leaves the binding pocket as  $PQH_2$ , and the empty pocket is filled from a PQ pool [56, 64-65].



**Figure 1.10** Image depicting cofactors which are involved in electron transport

Release of an electron by P680 causes it to become a cationic radical, this is reduced by TyrZ which becomes a neutral tyrosine radical that acts as an oxidant for the water oxidation process at the OEC. In each photocycle, P680 is re-reduced by extracting one electron from the Mn cluster (OEC) with a redox active tyrosine functioning as an intermediate electron carrier between P680 and the Mn cluster [5, 66].

### 1.2.2.3 Water oxidation

Two water molecules are oxidised into molecular oxygen, “fuel” in the form of this reaction is in the form of reduced Quinone, Plastiquonone (PQ) which is reduced to plastoquinol (PQH<sub>2</sub>). The OEC - oxygen evolving center (cluster of 4 Mn and 1 calcium) is buried deep within the PSII complex, it is buried more than 20Å from the surface of the protein [16, 64]. This is extremely beneficial as water is a very difficult molecule to oxidise and there can not be any other molecules present in the solution to be oxidised instead. One challenges faced with the OEC being buried so far within PS II is that electrons and protons have to move out of the site, and also transport water in and oxygen out so there has to be present specific transport pathways to allow this [66]. Photosynthetic water splitting is one of the most important reactions on the planet, since it is the source of nearly all the oxygen in the atmosphere. Information has been obtained from a wide range of approaches regarding PS II, unfortunately, the mechanism of water oxidation is not yet fully understood, but what is known is that the oxidation of water to molecular oxygen requires four electrons and four

protons from two molecules of water [67-68]. Two X-ray studies at 3.8 and 3.7 Å had given direct hints from the structure of PSII, but none of these models revealed the complete details of the OEC and nor the surrounding protein residues, information vital for formulating a reaction mechanism for water oxidation. But structural studies done by Ferreira *et al.* [59], on the PS II, revealed that the OEC is a cubane like  $\text{Mn}_3\text{CaO}_4$  cluster (Figure 1.11).

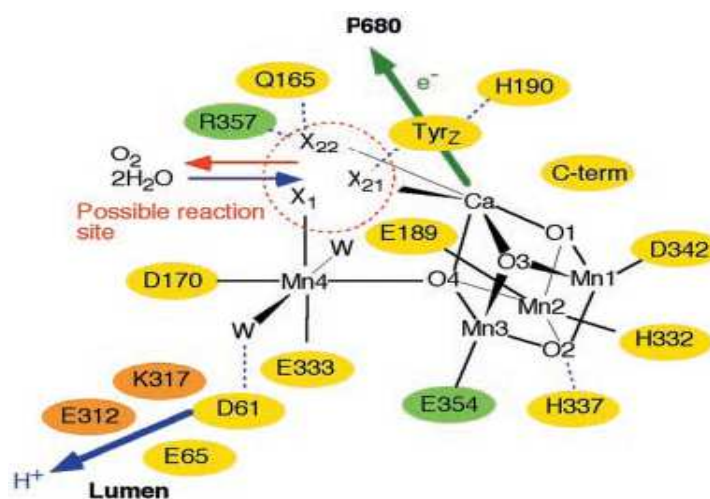


**Figure 1.11 Proposed Mechanism of water oxidation in PSII.**

Structure of the manganese centre. A cubane like cluster, with residues associated with the oxidation of water

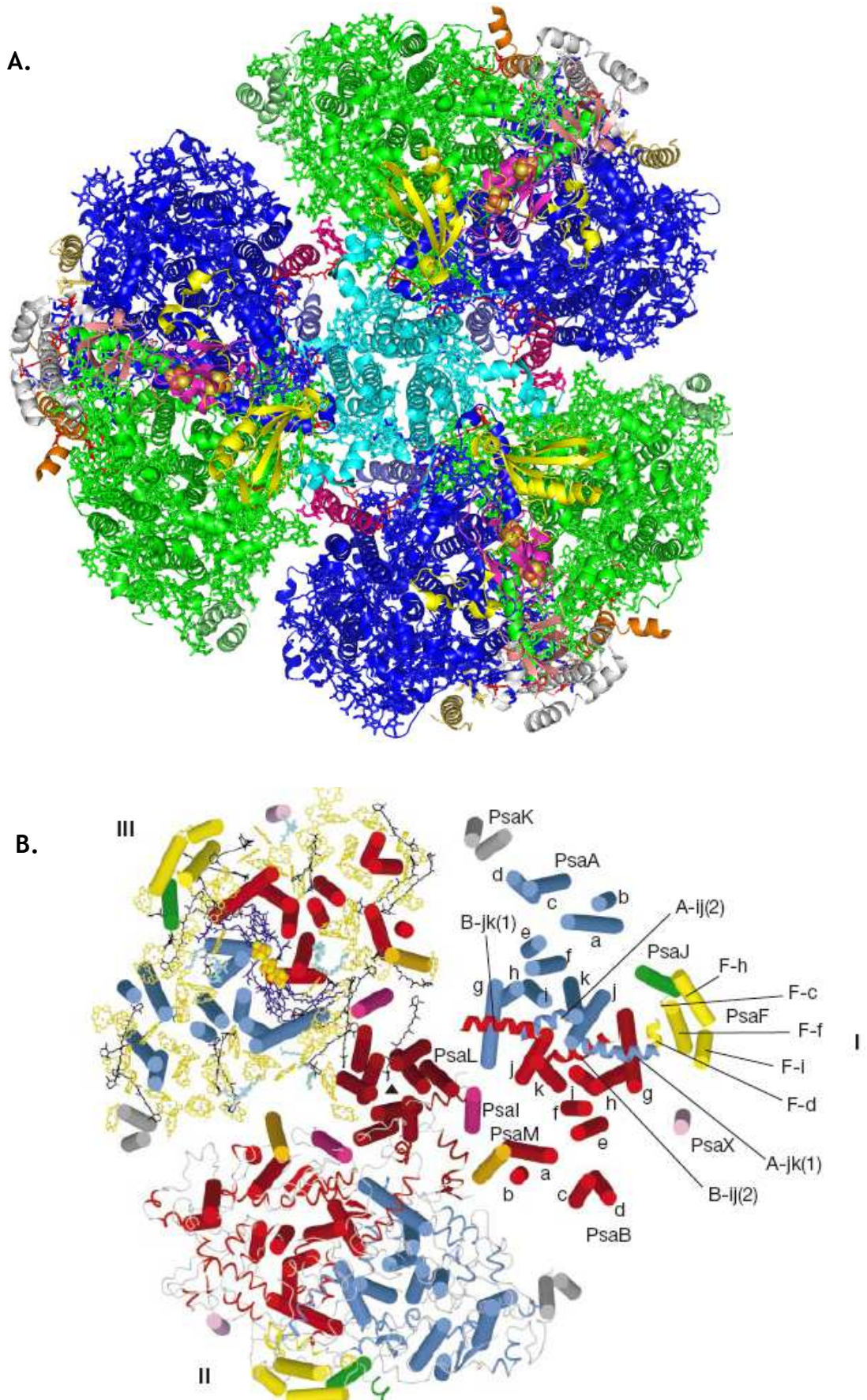
The OEC contains four manganese ions, one calcium ion and, almost certainly, a chloride ion. Experiments carried out by Kok and Joliot established that the OEC operates in a four step catalytic cycle, existing in a five oxidation states, known as S-states [69-70]. The OEC is oxidised in one electron step from  $S_0$  (the highest reduced state) to  $S_4$  (The most oxidised), by the repeatedly photo-oxidised chlorophyll centre P680. Ferreira *et al.* proposed Asp170, Glu189, His332, Glu333, Asp342 of D1 and E354 of CP43 as ligands for the Mn cluster. However, the structure of PS II at 3.2-Å resolution shows a similar but not identical arrangement for the Mn atoms and the ligands. Both structures agree on Asp 170, His 332 and Glu 333 being possible ligands to the Mn cluster. However, Biesiadka *et al.* see Glu 189 as more distant to the Mn cluster, in a position that may bridge the Mn cluster and TyrZ radical that acts as an oxidant for the water oxidation process at the OEC, as mentioned previously [16, 59, 71].

### 1.2.3 Photosystem I reaction centre

Photosystem I (PSI) catalyses the light driven electron transfer from the soluble Cu-containing protein plastocyanin on the luminal side (i.e. the inside of the thylakoids) to ferredoxin at the stromal side (outside) of the thylakoid membrane. Photosystem I is another large membrane-embedded complex [18, 20, 58].

#### 1.2.3.1 Architecture of PSI

In cyanobacteria PS I exist in both monomeric and trimeric forms. Each monomer of the cyanobacterial PS I consists of 12 protein subunits to which 127 cofactors (chlorophylls, carotenoids, FeS clusters and phylloquinones) are noncovalently bound [20, 43, 63, 72]. In cyanobacteria, it is a symmetric trimer, with 31 transmembrane helices, 96 chlorophyll and 22 carotenoid molecules. The photoreactive center in photosystem I is at the molecule called P700. PSI structure solved of cyanobacterial by Jordan *et al.* at 2.5Å [46], is shown to be a trimer (Figure 1.12) [14, 42, 73].



Cyanobacterial PSI consists of 12 different protein subunits, with names ranging from PsaA to PsaX. The large subunits PsaA and PsaB are the most important proteins they harbor most of the antenna system as well as most of the cofactors of the electron transport chain [48]. PsaA and PsaB are major subunits of photosystem I and seem to have homology to each other [74-76]. The six smaller membrane embedded proteins surround the core formed by PsaA and PsaB. Their main function is the stabilisation of the antenna complex. PsaL, also, is involved in the formation of the trimer. The three subunits PsaC, PsaD and PsaE, which are located at the stromal side of PS I form a “hump” providing an potential docking site for ferredoxin (Figure 1.13) [46-47, 77-78].

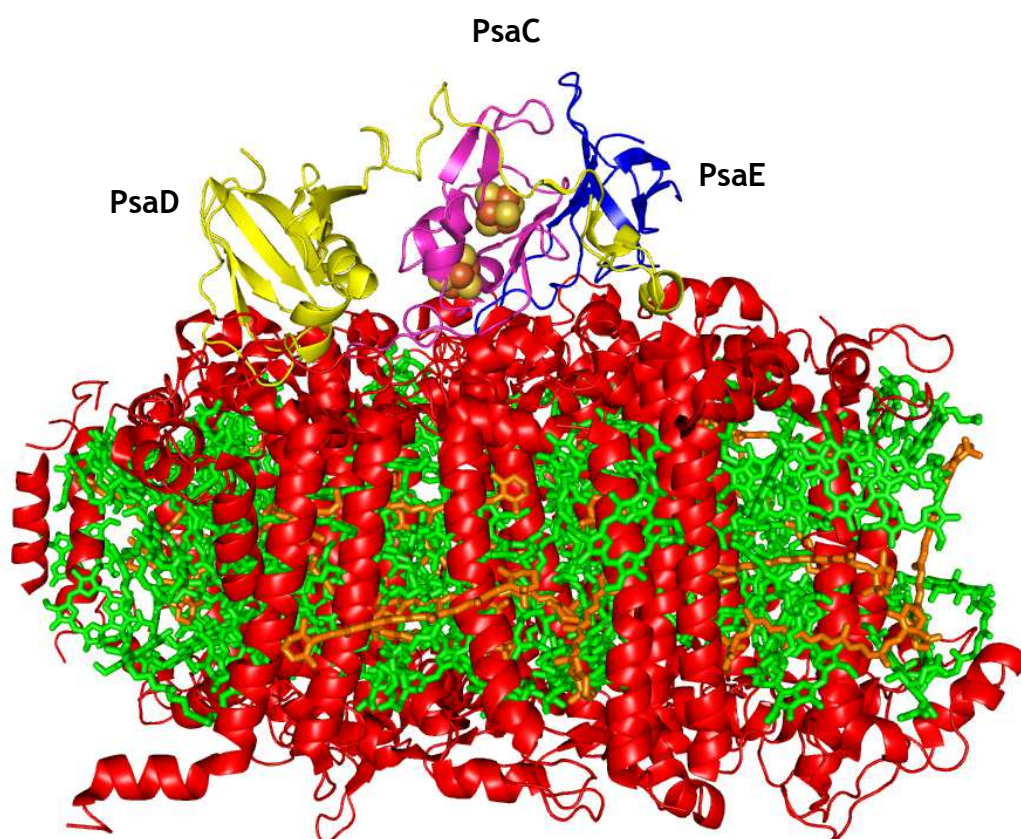


**Figure 1.13 The ferredoxin docking site. A side view image of the plant PS I monomer.** Image showing the "hump" that is involved in the docking of ferredoxin to PS I. The three subunits shown to be involved in the docking of ferredoxin are colored in yellow (PsaD), purple (PsaC), and blue (PsaE). The rest of the subunits are colored in red, with the head groups of the chlorophyll shown as green and the carotenoids as orange.

The subunit PsaC carries the two terminal Fe-S (Iron sulphur) clusters FA and FB (Figure 1.14 A), which consists of two short  $\alpha$ -helices connecting the two Fe-S clusters [40]. The PsaC subunit has two conserved regions, CXXCXXCXXXCP, within these sequence motifs the cysteines help provide the ligands to the Fe (Iron) atoms [79-80].

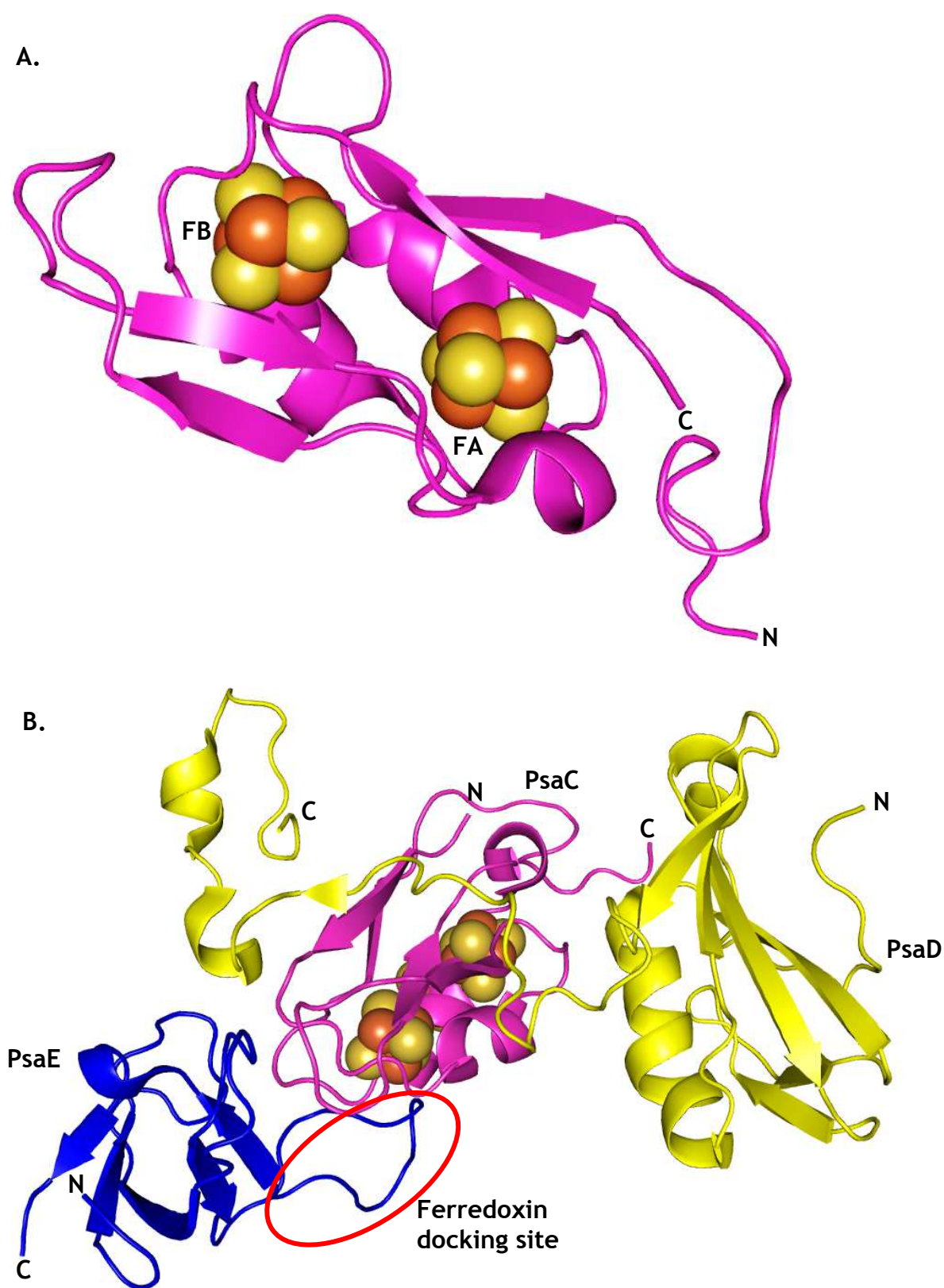


**Figure 1.14 depiction of The PsaC, PsaD and PsaE subunits from PS I.**

A & B. Shows The PsaC (in purple) subunit which harbors the two terminal Fe-S clusters (FA and FB). B. Shows how all three subunits come together to form the docking site for ferredoxin. The possible ferredoxin docking site is indicated. PsaC can be seen in purple, PsaD can be seen in yellow and PsaE is colored in blue.

The subunit PsaD plays a major role in the function and assembly of PSI [81]. This subunit consists of a large antiparallel four-stranded  $\beta$ -sheet. The fourth  $\alpha$ -strand is connected to the only  $\alpha$ -helix of PsaD by a short loop [82-83]. This helix forms interactions with both PsaC and PaA. Due to the N and C termini of this subunit being unstructured, the assembly of PsaD into PSI complex confers structural rigidity to the protein through extensive interprotein interactions with not only PsaC and PsaA, but also PsaB, PsaL and PsaM [84-85]. The C terminus of the subunit allows for PsaD to wrap around PsaC (Figure 1.14 B), this allows for the formation of several contacts between PsaC, PsaD and PsaE [83]. This wrapping around affect of PsaD to PsaC allows for the stabilisation of the electron acceptor sites in PS I, by keeping PsaC in its correct orientation. As well as the stabilising effect that PsaD plays, it has another crucial role [74]. PsaD has been shown to be involved in the docking of ferredoxin. Lelong *et al.* has shown through crosslinking experiments that electron transfer through photosystem I to ferredoxin is fully competent. As well as this over expressed ferredoxin has been shown to bind ferredoxin [86-87].

PsaE is involved in the docking of the soluble electron acceptors, ferredoxin. The structure of the PsaE subunit, solved by NMR showed it to consist of 5 antiparallel stranded  $\beta$ -sheets [77, 88]. However, this is in a conformationally different from that in solution, since the loop connecting the  $\beta$ -sheets  $\beta$ 3 and  $\beta$ 4 was not well resolved, and therefore was thought to be flexible [89]. It was hypothesised that, due to this flexibility PsaE most likely interacts with PsaC and the stromal sides of PsaA and PsaB, allowing for a different structural conformations [90-91].

### 1.2.3.2 Electron pathway of PSI

Light capturing is performed by the large antenna systems, which are associated with PSI, consisting of 90 antenna chlorophylls and 22 carotenoids. The energy is transferred to the centre of the complex, where the electron transport chain is located (Figure 1.15) [3, 92-93]. The P700 chlorophylls get excited from a ground state to the excited state. The electron is transferred from the P700 across the membrane by a chain of electron carriers. The electron is transferred from P700 to A (a chlorophyll A molecule) (through Hydrogen bonding), then on wards to A0

(also a chlorophyll A molecule), from there to A1 (a phylloquinone molecule) [94-95]. And from there to the three FeS clusters Fx, Fa and Fb, these are coordinated by 4 cysteines two of which are provided by PsaA and the other two provided by PsaB. The electron is then transferred to ferredoxin at the docking site, which transfers the electrons to ferredoxin NADP reductase, also known as FNR. After two electrons are transferred to FNR NADPH is made. And the gradient created by ETC (electron transport chain) is utilised by ATP synthase to create ATP [44, 96-97]. After this has been done P700 has to be reduced to complete the reaction cycle. There is a docking site at the luminal site for the soluble electron carrier protein plastocyanin [98-99].

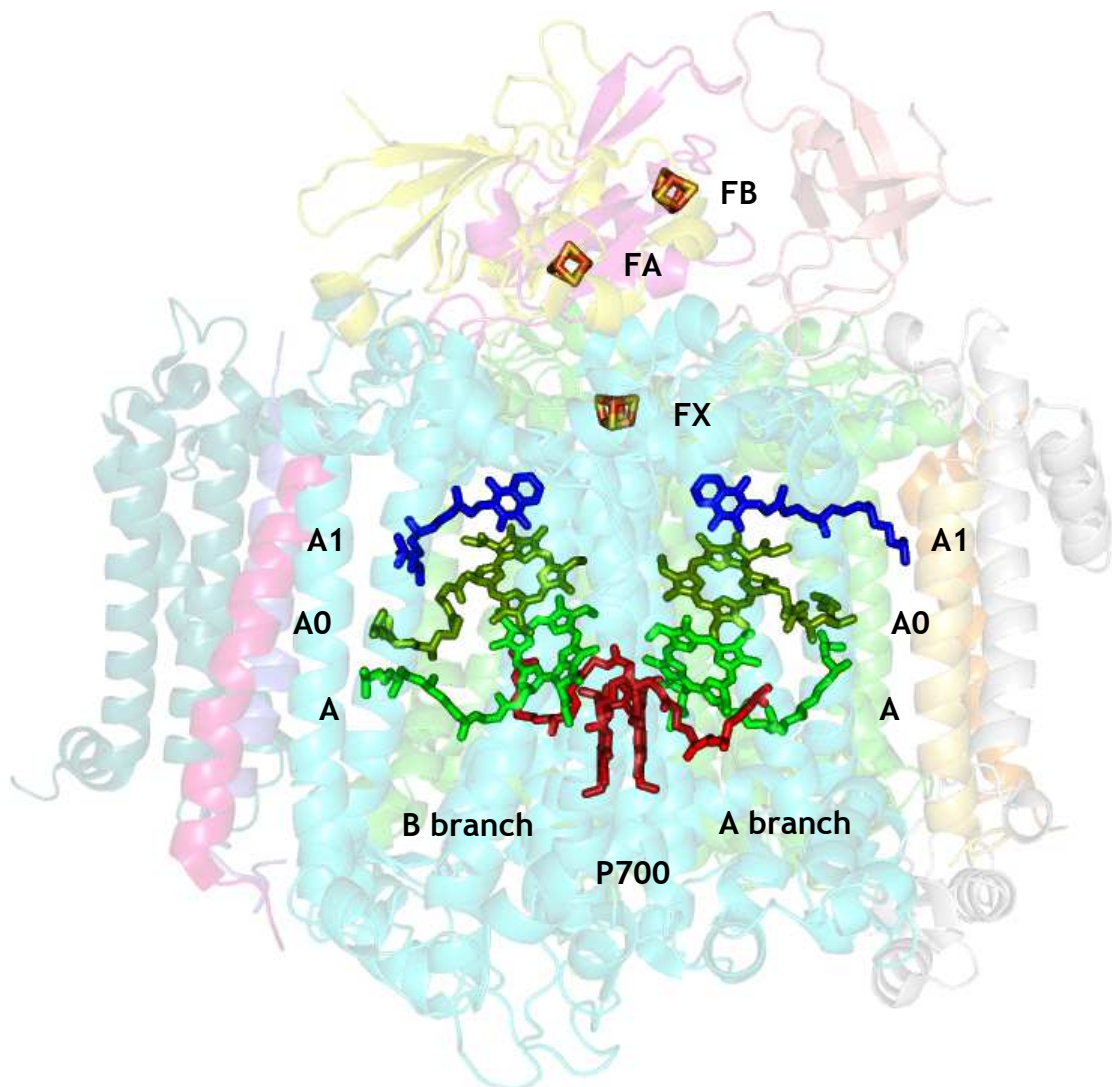


**Figure 1.15 A side view of the structure of plant photosystem I.**

PSI showing the cofactors involved in light-induced electron transport, i.e., P700, A0, A1, FX, FA, and FB, are shown along with the backbones of the 16 subunits. In the electron transport chain, the P700 Chl (red) and the other Chl (green) are indicated (A and A0). The quinones (blue) and, in the iron-sulphur clusters, the iron (orange) and the sulphur (yellow) are also indicated.

### 1.2.4 Type II RC from purple photosynthetic bacteria

The first membrane protein to have its structure solved by X-ray crystallography was purple RC from (*Blc.*) *viridis* (previously *Rhodospseudomonas viridis*) in 1985. This led to a Nobel prize given to H. Michel and colleagues in 1988 [45, 50, 100]. In contrast to higher plants, algae, and cyanobacteria of oxygenic photosynthesis, which contain the membrane bound PSI and PSII, the anoxygenic only has one type of RC [51, 54]. While the iron-sulphur types of RC of heliobacteria and anaerobic green sulphur bacteria have RCs similar to that of PSI, the pheophytin-quinone type RCs of purple bacteria resemble the RC of PSII (Figure 1.7) [25, 45, 100].

Most bacterial reaction centers contain four protein subunits referred to as H (heavy), M (medium), L (light) and the cytochrome-c subunit (Figure 1.16) [23, 27, 33].

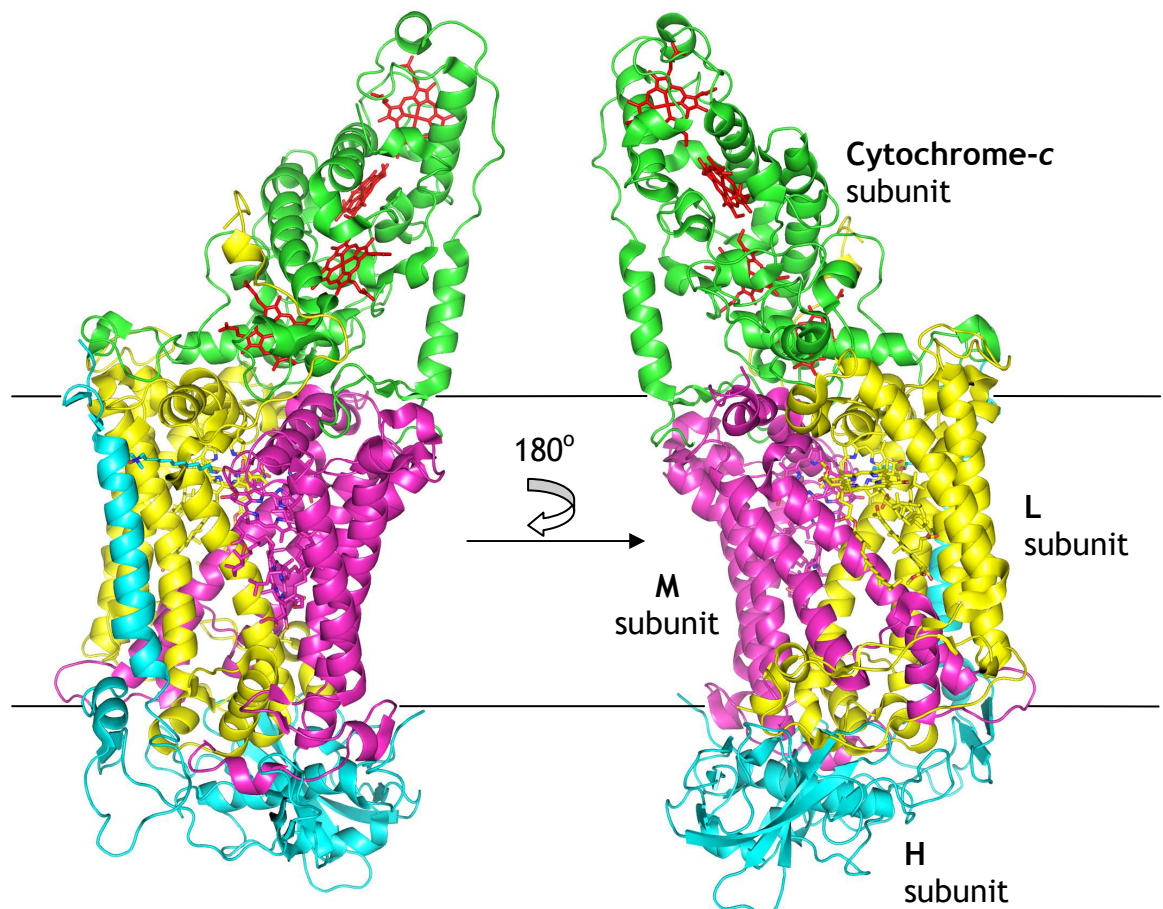


**Figure 1.16 Structure of the *Blc. viridis* RC**

Structure of the *Blc. viridis* RC modeled on pymol (PDB file 1PRC). The complex contains the four subunits cytochrome-c (green), H subunit (blue), L subunit (yellow), and the M subunit (magenta). The L and M subunits are both membrane bound and have 5 transmembrane helices. The cytochrome-c subunit is attached on the periplasmic side. The hemes are shown in red.

The main core of the *Blc. viridis* RC is formed by the L and M subunits. These subunits both possess 5-transmembrane spanning alpha helices (A-E) [24]. Both these subunits contain 10 cofactors, which are non-covalently bound. Perpendicular to the membrane both the L and M subunits are related by a two fold axis of symmetry [58, 63]. This two-fold axis of symmetry are also related by their cofactors, and these can be split in to two branches, A and B. The cofactors in branch A are associated with the L subunit, whereas the cofactors in branch B are associated with the M subunit (Figure 1.17). Both the L and M subunits bind 2 strongly coupled Bchl molecules ( $P_{A/B}$ ), 2 monomeric Bchl molecules ( $B_{A/B}$ ), 2 Bacteriopheophytin molecules (Bpheo) ( $H_{A/B}$ ), 2 quinone molecules ( $Q_{A/B}$ ) and an  $Fe^{2+}$  ion [28, 75]. The H subunit is bound to the L and M subunits on the cytoplasmic side of the membrane. One of the  $\alpha$ -helices, of the H subunit, is anchored to the membrane (Figure 1.16). The cytochrome-c subunit can be found to be electrostatically attached to the periplasmic side of the membrane. The four hemes and the two heme binding segments make up the core of the cytochrome subunit. For every heme binding site there is an  $\alpha$ -helix running parallel to the heme plane, a loop, and the sequence Cys-X-Y-Cys-His for the heme attachment site [101].

The arrival of excitation energy at a special pair at the periplasmic end of the RC triggers a membrane-spanning four-step electron transfer along the A-branch of cofactors, which results in the reduction of a quinone at the so-called  $Q_B$  site near the cytoplasmic side of the membrane (Figure 1.17) [102-103]. When the  $P_{A/B}$  BChl molecules are excited to a singlet state,  $P_{A/B}^*$ , an electron is transferred to the  $B_A$  molecule. The  $P^+B_A^-$  state is very short-lived so the electron is then transferred to  $H_A$ . From  $H_A^-$  the electron is transferred to  $Q_A$ . At this stage radical pairs can be accumulated due to the distance of the donor and acceptor. From  $Q_A$  the electrons are transferred to  $Q_B$  due to the presence of  $Fe^{2+}$  [104-105]. The charge separation takes place once the electron and proton have been accepted by the quinone bound in the  $Q_B$  binding site. For the quinone to be fully reduced it requires 2 electrons and 2 protons, so once one electron and one proton are bound by the quinone in the  $Q_B$  binding site, the process of electron transfer begins again by the cytochrome-c subunit re-reducing the  $P^+$  back to P. Once the quinone is fully reduced it is released from the  $Q_B$  binding pocket [9, 29, 106-107].

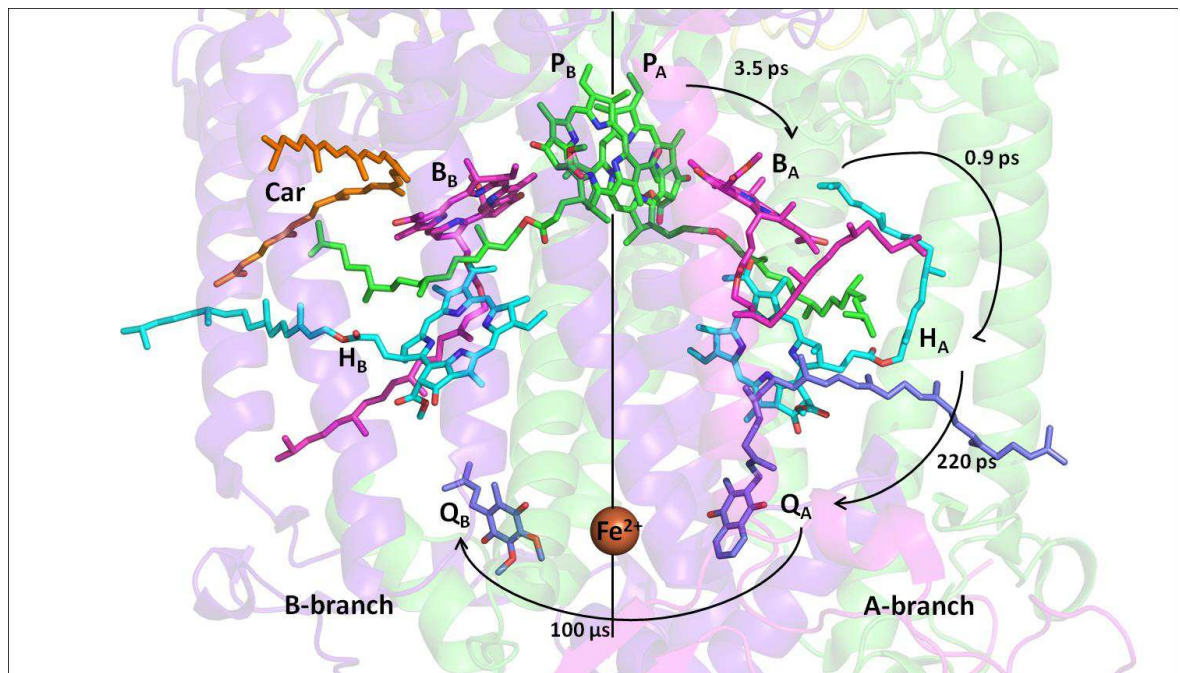


**Figure 1.17** The cofactors of the RC from *Blc. viridis*.

The cartoon of the protein scaffold is visible in the background. It is clear to see from this that the 2 branches of cofactors, B and A are more associated with M (purple) and L (green) subunits respectively. The A branch carries out the electron transfer [103].

### 1.2.5 Type I RCs from the green sulphur bacteria *Chlorobaculum tepidum*

*C. tepidum* (formerly *Chlorobium tepidum*), is one of the best characterised strains, which is commonly used as the model species of green sulphur bacteria. Its complete genome sequence has been available in green sulphur bacteria in 2002 by TIGR (The Institute for Genome Research, USA) [34, 108].

The green sulphur bacterial RC complex consists of only five subunits, from PscA-D and Fenna-Mathews-Olson (FMO) protein (Figure 1.18) [57, 109]. Therefore, it has a much simpler architecture compared to the heterodimeric PS I of oxygenic phototrophs, which are composed of 12 subunits [110-112].

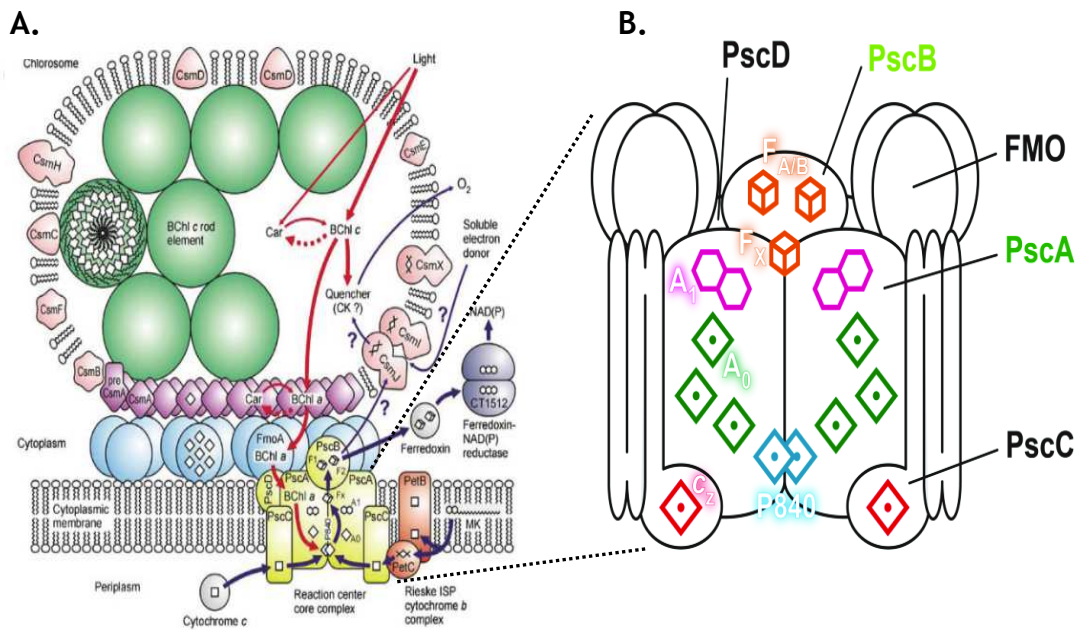


**Figure 1.18 The model of photosynthetic apparatus of *Chlorobium tepidum*.**

**A.** RC shown within its membrane, bound to FMO, which in turn is bound to the chlorosome. Red and blue arrows represent electron transfer and excitation energy transfer, respectively. **B.** The model of subunit organisation of the green sulphur bacterial RC complex. Electron acceptors identified spectroscopic studies are also shown at expected binding positions. BChl a, Chl a, and c-type hemes are shown as cyan, green, and red squares, respectively. Three Fe-S clusters are shown as orange cubes. The purple row of two hexagons represents naphthoquinone molecules.

Functions of the subunits of the green sulphur bacterial RC complex have been well characterised by biochemical and spectroscopic studies [113-117]. Green sulphur bacteria contain a type I RC with three iron-sulphur centers that are functionally very similar to those of PSI [118]. The main difference for the type I RC from green sulphur bacteria compared to that of PS I is that the RC from green sulphur bacteria is homodimeric whereas PS I is heterodimeric [57, 112, 119-120].

PscA is the core polypeptide, where two PscA subunits form the core protein. It is partially homologous to PsaA and PsaB of core polypeptides of PS I. Sequence alignment with PS I from *S. elongatus* shows conserved Histidine residues in positions that could provide axial ligands of the primary electron donor (P840) [118]. In addition to this Lysine and Glutamic acid residues occur in positions that could serve as axial ligands of both the first Chl (A) and the second Chl (A<sub>0</sub>) of the putative chains of the electron acceptors branching from the P840 [121-123].

PscB is the functional homologue of PsaC in PS I, which contains two 4Fe-4S clusters, F<sub>A</sub> and F<sub>B</sub>, as terminal electron acceptors [37, 39-40, 97, 124]. PscC is

the membrane-bound c-type cyt, which is also called 'cytochrome cz' It is unique subunit for the green sulphur bacterial RC complex serving as the physiological secondary electron donor [125-128]. The first step in the conversion of light energy into chemical free energy begins with the excitation of the special pair (P840 to P840<sup>+</sup>) of BChl a in the RC complex. To be able to achieve high efficient solar energy conversion it is important for the photo-oxidised P840<sup>+</sup> to be re-reduced rapidly [129]. In a thermophilic green sulphur bacterium, *Chlorobaculum (Cba.) tepidum*, P840<sup>+</sup> is re-reduced by the PscC subunit. It has been demonstrated that two molecules of cyt cz (c551 and c553) are contained in the RC complex. Cyt cz has three membrane-spanning  $\alpha$ -helices in its N-terminus and a heme containing moiety in its C-terminus. The C-terminal domain protrudes into the periplasmic space and carries electrons directly from menaquinol: cyt c oxidoreductase to P840 [130-132].

PscD is the small dispensable subunit responsible for the effective energy transfer from the chlorosome to the RC. Its amino acid sequence shows a significant similarity to PsaD in PS I; but, it is not a functional homologue [121].

FMO protein is the water-soluble light harvesting complex attached to the RC complex. Its crystal structure was determined as the first case of pigment-containing proteins [133-134]. It forms a trimeric structure binding seven or eight BChls *a* in each monomer, and mediates energy transfer from chlorosome to the RC. Although the crystal structure of the green sulphur bacterial RC complex is still lacking, subunit organization of the green sulphur bacterial RC complex has been constructed from the three-dimensional image of the purified RC complex by the single particle analysis using STEM (Scanning Transmission Electron Microscopy) [126, 135].

#### **1.2.5.1 Absorption spectral properties of *Chlorobaculum tepidum***

The RC core complex of green sulphur bacteria is embedded in the cytoplasmic membrane and contains the photosynthetic reaction centre and a number of antenna pigments. It is related to the antenna reaction centre complex of Photosystem I (PS I). In the tepidum RC there are four different genes encoding the RC proteins, *pscA*, *pscB*, *pscC*, and *pscD*, which have all been sequenced.

They encode the 82 kDa PscA reaction centre protein, the 24 kDa PscB iron-sulphur protein, the 23 kDa cytochrome PscC cytochrome *c* and a 17 kDa PscD protein with unknown function. The PscA protein is hypothesised to be homodimeric and it shows homology to PsaA and PsaB of PS I, but in green sulphur bacteria only a single gene of this type has been identified [108].

All green sulphur bacteria contain BChl *a* in their RC complex. Characteristic absorption bands of RC BChl *a* are the  $Q_y$  transition band at ca. 816 nm, the  $Q_x$  transition band ca 610 nm and the Soret band at ca. 370 nm (Figure 1.19). The PscA homodimer binds most components of the electron transport chain and the core antenna pigments. The primary electron of P840 is believed to be a dimer of BChl *a*. Photobleaching experiments indicate that its absorption maximum is around 837 nm (Figure 1.19). In addition to BChl *a*, the reaction centre of green sulphur bacteria contains a pigment absorbing near 670 nm (Figure 1.19), which is thought to act as a primary electron acceptor,  $A_0$ . This Chl *a* at 670 nm has been shown to be Chl *a* esterified with  $\Delta^2,6$ -phytyadienol, rather than phytol as in plants and cyanobacteria, but is otherwise identical to plant Chl *a* [136].

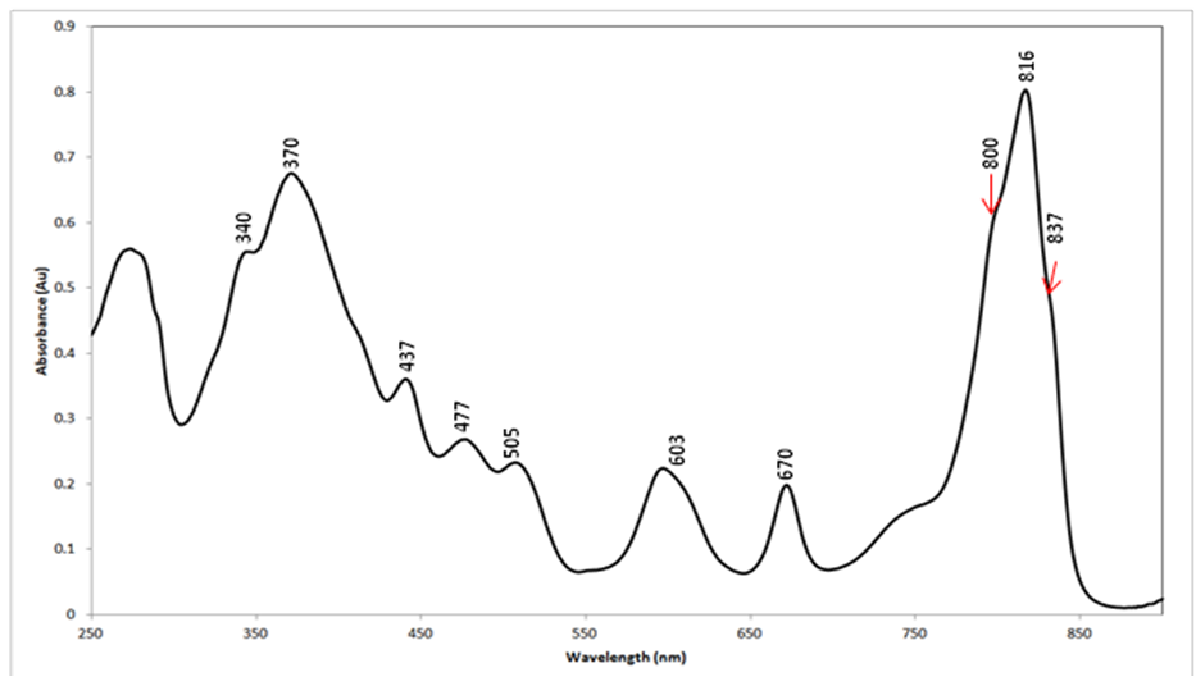


**Figure 1.19 Absorption spectrum of the *Chlorobaculum tepidum* RC**

*C. tepidum* RC measured in solution at room temperature. At 340, 370, 603 and 816 nm, the characteristic absorption bands of BChl *a*, and additionally, the shoulder at 837 nm indicating the primary donor, are seen. The peak at 670 nm contributes to the primary electron acceptor, which is the Chl *a*. Absorption bands in the wavelength range from 437 to 505 nm arise from the carotenoids, rhodopin and/or hydroxychlorobactene.

### 1.2.5.2 Absorption spectral properties of Fenna-Mathews-Olson (FMO)

The FMO is BChl *a* binding protein found in green sulphur bacteria. FMO is a water-soluble antenna protein which mediates energy transfer between the chlorosomes and the RC (Figure 1.20). Characteristic absorption bands of the FMO BChl *a* are the  $Q_y$  transition band at ca. 808 nm, the  $Q_x$  transition band ca 598 nm and the Soret band at ca. 370 nm (Figure 1.20) [137].

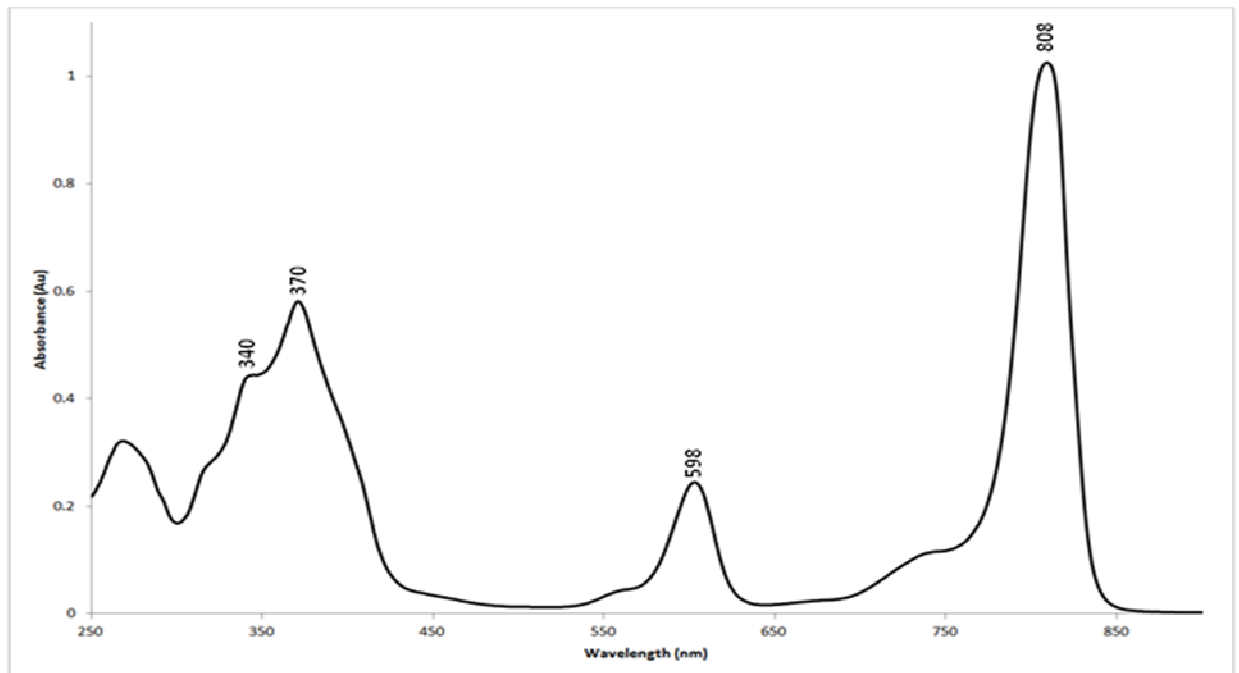


**Figure 1.20 Absorption spectrum of FMO from *C. tepidum***

FMO measured in solution at room temperature. At 340, 370, 598 and 808 nm, the characteristic absorption bands of BChl *a* from FMO. The  $Q_y$  transition band is at 808 nm, the  $Q_x$  transition band 598 nm.

## 1.3 Membrane proteins and the challenges faced with structural elucidation

Membrane proteins play critical roles in a wide-range of physiological and pathological processes. There are many different types of membrane protein, some bind to the membrane surface only whereas others have transmembrane domains, and can be classified into two broad categories (intrinsic and extrinsic) according to the nature of the interactions between the protein and the membrane. Membrane proteins, roughly, make up about 30% of the proteome, but the number of membrane proteins whose structures have been solved to date and deposited in the protein data bank (PDB) is relatively small compared to its soluble counterparts. Published reports of membrane protein structures in

the database comprise of 838 membrane proteins, as compared to soluble proteins which comprise of 91387 [138]. This is due to the challenges faced in expressing them in high enough quantities for structural studies, being able to solubilise them in appropriate detergents, and then being able to crystallise them.

The first membrane protein to have its structure solved to atomic resolution was in 1985 and was from the photosynthetic reaction centre from purple bacteria *Rhodospseudomonas viridis* [100]. Since then there has been a gradual rise in the number of membrane protein structures solved. In recent years we have seen a dramatic increase in the number of membrane protein structures that have been solved (figure 1.21). This is not only due to better expression, better purification protocols, and an increase in thermostability of membrane proteins, but also due to the technological advances that are being made within this field [139].

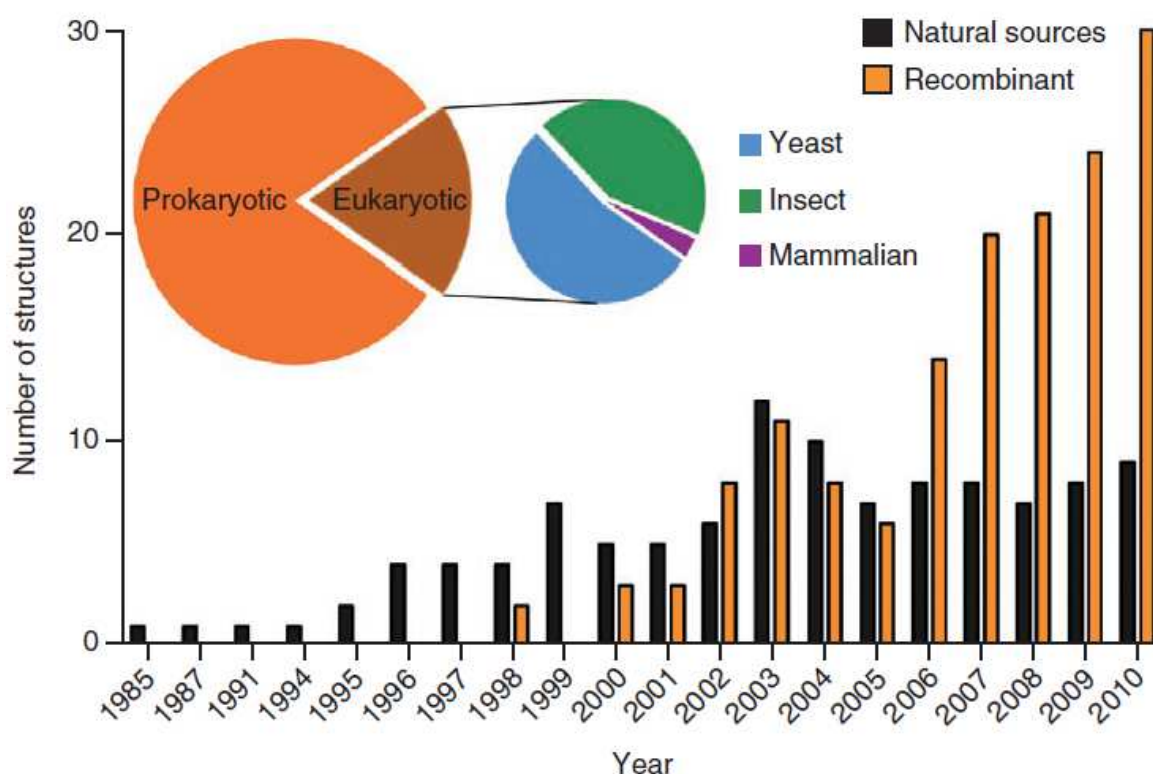


**Figure 1.21 Structures of Eukaryotic and prokaryotic membrane proteins over the years [139]**

Once sufficient expression has been achieved, the next challenge is being able to get stable protein after the purification steps. The native membrane envi-

ronment allows for stability to membrane proteins through its lipid composition and physicochemical properties. To be able to extract these membrane proteins from their native environment detergents have to be used. However, using detergents to solubilise the membrane proteins can be damaging, sometimes. All detergents are denaturing in some form, some are more “harsh” than others and due to this many membrane proteins cannot be purified, through solubilisation, as they rapidly denature or often aggregate and even cause the loss of function. This latter of the two is mainly associated with membrane proteins from higher eukaryotes, and most membrane proteins whose structures have been determined are from bacteria or archaea, with an emphasis on homologs of mammalian proteins. These structures have been solved mostly using X-ray diffraction in combination with detergent crystallisation protocols.

### 1.3.1 Detergents

Detergents solubilise membrane proteins by mimicking the natural membrane environment normally inhabited by the protein. Detergents themselves are amphipathic molecules, and within an aqueous solution they form micelles. All detergents consist of a polar head group and a hydrophobic tail. This allows for the tail to cover the hydrophobic regions of the membrane protein while the head group can face the aqueous environment allowing the protein to stay soluble.

On the basis of their structure detergents can be put in to four different categories: ionic, bile acid salts, non-ionic and zwitterionic detergents. Ionic detergents, such as sodium dodecyl sulfate (SDS), contain a head group with a net charge that can be either cationic or anionic. They also contain a hydrophobic hydrocarbon chain or steroidal backbone. Ionic detergents are considered to be extremely strong solubilisers, but these detergents can often have a negative effect on the protein. Due to the harsh properties of these detergents they can sometimes strip essential lipids required for functional activity from the surface of the target protein or even denature the protein. But it has been shown that a membrane protein, solubilised with such a detergent as SDS can be renatured by detergent exchanging into a more renaturing detergent such as non-ionic detergents, this however does not imply that it would take up

a 3D-conformation that it would in-vivo. Unlike its counterparts non-ionic detergents contain an uncharged hydrophilic head groups, these are much milder and tend to be non-denaturing. This allows for membrane proteins to be solubilised without changing the functionality of the protein. One of the issues with the tail of the detergent is the actual size, the carbon length. The bigger the micelle the more chance that the protein retains its functionality the smaller the micelle the smaller the chance the protein is able to retain its functionality. This is one of the reasons that alkylglucosides, such as n-dodecyl- $\beta$ -D-maltoside (DDM), are in membrane protein solubilisation as many proteins can be readily solubilised in a functional state in DDM. This however is not the most ideal detergent for structural studies. As one of the issues you face with a bigger micelle is the lack of protein-protein contact, as the hydrophilic regions are covered by the micelle.

The choice of detergent is very important for each membrane protein, and for each protein a different detergent may apply. However, there are properties that are common to all detergents that may help in deciding which the most suitable detergent to be used. The critical micelle concentration (CMC) can be defined as the concentration of detergent molecules to spontaneously form micelles. Therefore it is important that the detergent of choice has a concentration higher than the CMC. This can differ depending on if your protein is either membrane associated or an integral part of the membrane.

### **1.3.2 X-ray crystallography of membrane proteins**

An understanding of the function of proteins require detailed knowledge of their three dimensional structure. NMR and X-ray crystallography have been important tools in elucidating the structure of proteins. Crystallography, especially, has played an important role for the structure determination of many membrane proteins. Arguably NMR is still in its developing stages within the membrane protein world but has made great strides as this was made evident in the 2012 structure determined through NMR of the chemokine receptor, a GPCR (G protein coupled receptor) involved in the immune and inflammatory responses implicated in many disorders, including tumor growth [140].

### 1.3.2.1 Vapor diffusion

Proteins can be prompted to form crystals when placed in the appropriate conditions. In order to crystallise a protein, you would typically require pure and highly concentrated amounts of the protein. The purified protein undergoes slow precipitation from an aqueous solution. This is usually achieved by equilibration with precipitants, which influence the solubility of proteins, but at the same time cannot denature them such as ammonium sulphate or polyethylene glycol. The precipitant drives the formation of nucleation sites (Figure 1.22), which as the protein concentration within the drop increases due to water loss, forms the site of crystal growth and as a result individual protein molecules align themselves in a repeating series of "unit cells" by adopting a consistent orientation termed the "crystalline lattice", this can be observed in the phase diagram (Figure 1.22) [141].

The formation of well-ordered crystals requires slow, regulated crystal growth which is highly influenced by the protein's concentration and solubility. So by selecting the correct precipitant it can allow crystal growth. However, working with membrane proteins we face an additional challenge, membrane proteins require appropriate detergents in order for it to stay in solution [142]. Often, when trying to crystallise membrane proteins, we observe that the precipitant reacts with the detergent which can cause the detergent to phase separate. When this takes place the membrane protein will usually never crystallise as it would have precipitated in the oily detergent phase. This problem was overcome, first in 1980, when two scientists, independently of each other, discovered by adding small amphiphile molecules could shift the phase separation point to be above the critical precipitation point, allowing the formation of crystals [143-144].

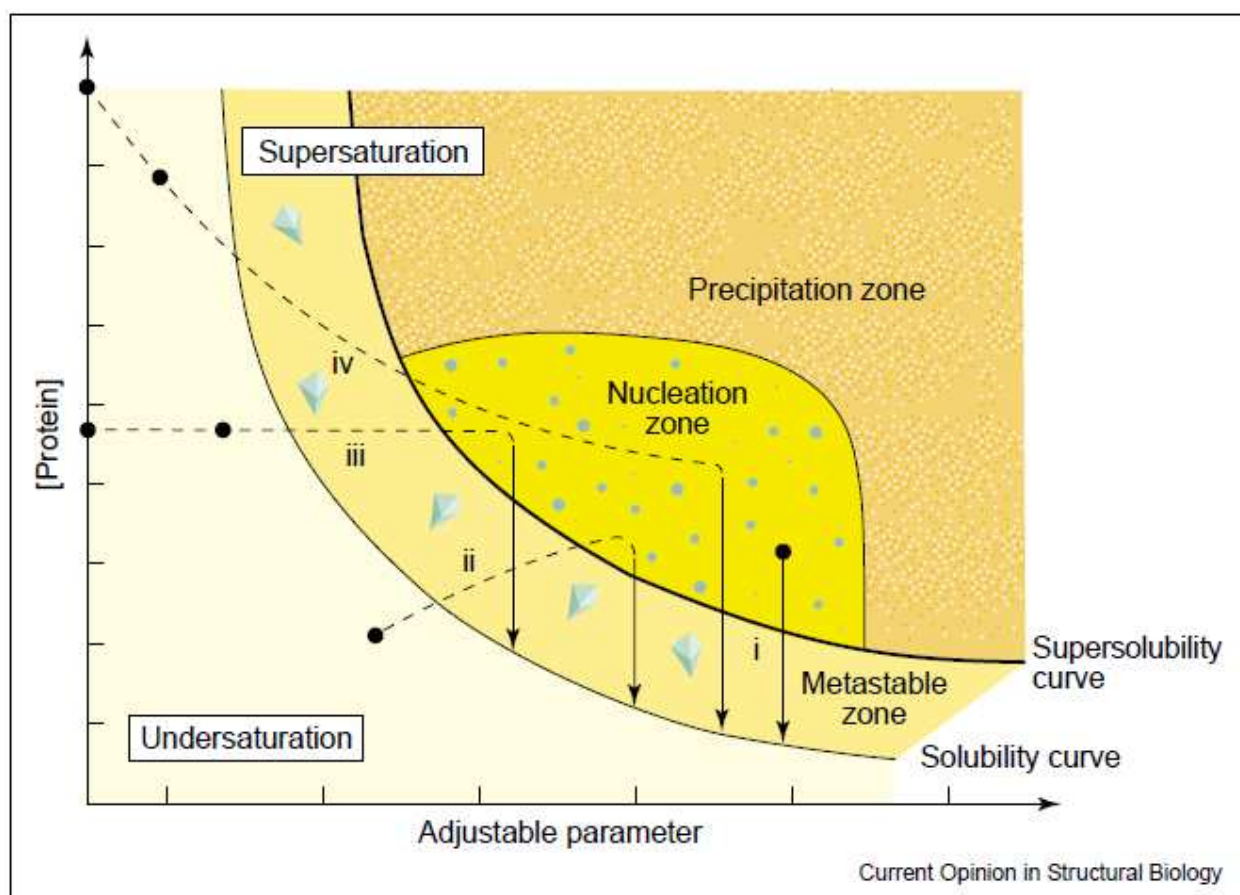


**Figure 1.22 Illustration of the phase diagram**

Black spots indicate the initial condition of the protein, the arrows indicate the final state and the dashed lines is the indicative of the progress of the protein crystallisation [141].

### 1.3.2.2 In meso crystallisation

The choice of detergent for a membrane protein is very important as not only does it keep the protein in solution but the detergent itself can often mask the hydrophilic regions of the protein, preventing the formation of crystal contacts [145]. By using large chained detergents, such as DDM (Dodecyl maltoside), can keep the protein intact but prevent the formation of crystals due to no protein-protein contact. Therefore, a protein that is “happy” in a large chained detergent that cannot form protein contacts faces an even bigger challenge for protein crystallisation. This dilemma was overcome in 2003 by a method known as in meso phase [146], where the protein is crystallised in a lipid environment. This is greatly advantageous as the target protein is taken out of the potentially harmful environment of a detergent micelle (in which the protein was solubilised), and is instead placed in a more “natural” environment.

The three types of in meso phases are the sponge, cubic and lamellar. The difference between them is the ratio of aqueous solution to lipid and hence the degree of organisation. Any of the in- meso phases might yield crystals. One in ten integral membrane protein structures in the PDB (Protein Data Bank) have been solved using this crystallisation technique [147].

The technique involves making an artificial lipid bilayer, linked through a network of interconnected aqueous pores, incorporating the protein of interest in which it can be crystallised. The bilayer is formed initially in a highly ordered cubic mesophase and is shifted by addition of the precipitant to a second mesophase from which the protein can crystallise (Figure 1.23). The difficulty lies in obtaining the initial cubic phase, which is difficult to work with as it is extremely viscous and sticky making it difficult to handle [148].

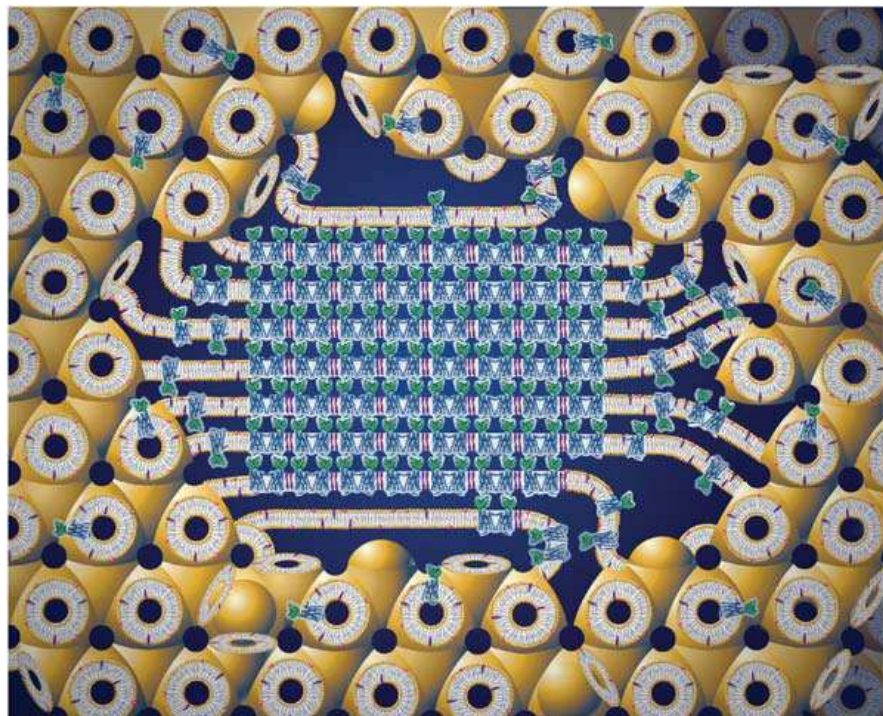


**Figure 1.23** Picture depicting the events of lipidic cubic phase.

The protein inserts itself into the curved bilayers of the cubic phase (tan). Stability of the cubic membrane is shifted by the addition of a precipitant causing the phase separation. Protein molecules diffuse from the bilayer of the cubic phase to lock into the lattice of allowing protein contact (midsection of figure).

## 1.4 Artificial photosynthesis

The sunlight is the most abundant form of energy available on earth. To utilise energy from sunlight to promote photochemical reactions to produce solar fuels, we must understand and improve both the capture and transfer of excitation energy and the effective capture of photons at a reactive site. This may allow the design of molecular devices which by employing the principles of natural photosynthesis can produce high value compounds e.g. solar biofuels.

One possible way to increase absorption of photoactive molecules is their interaction with plasmons. Plasmons are large local electromagnetic fields at metal surfaces, which can be very useful for certain kinds of spectroscopies and optical trapping [149].

There will always be limited amounts of absorbance from solar energy when trying to organise photosynthetic complexes as a monomolecular layer on to surfaces. Nature has found a way around this by stacking these complexes on top of each other to optimise absorbance, but another way which can be used in hybrid systems is employ the unique properties of plasmonic materials.

### 1.4.1 Plasmon and fluorescence enhancement

Electrically conductive materials, such as metals, have a large “pool” of electrons within them that are essentially free to move about the material. When an electric field is applied to the conductor, the electrons are pushed into new positions, leaving positive “holes” behind. The electrons tend to flow along the surface of the metal, and the net positive charge left behind is also on the surface. The induced charges on the surface create their own induced electric field that tends to cancel the applied electric field within the conductor. Electric fields tend not to penetrate very far into metals, and this observation forms the basis of the Faraday cage [150-151].

It was first suggested in 1946 that “Spontaneous emission could be modified by resonant coupling to the external electromagnetic environment”. There are many ways to do this. One important strategy to achieve fluorescence enhancement is to utilise metallic nanoparticles, which are known to drastically

alter the emission of vicinal fluorophores [152]. Metallic nanoparticles can influence the fluorescence emission of nearby molecules in several ways: by enhancing the optical intensity incident on the molecule through near field enhancement, by modifying the radiative decay rate of the molecule, and by increasing the coupling efficiency of the fluorescence emission to the far field through nanoparticle scattering [15]. All these processes can be controlled by molecule- nanoparticle separation, nanoparticle size, and geometry [149].

Surface plasmons (SP) are waves that propagate along the surface of a conductor. The conductor is usually a metal. plasmons are light waves that are trapped on the surface because of their interaction with the free electrons of the conductor. In this interaction, the free electrons respond collectively by oscillating in resonance with the light wave (Figure 1.24). The resonant interaction between the metal/dielectric surface charge oscillation and the electromagnetic field of the light constitutes the SP and gives rise to its unique properties [15, 153].

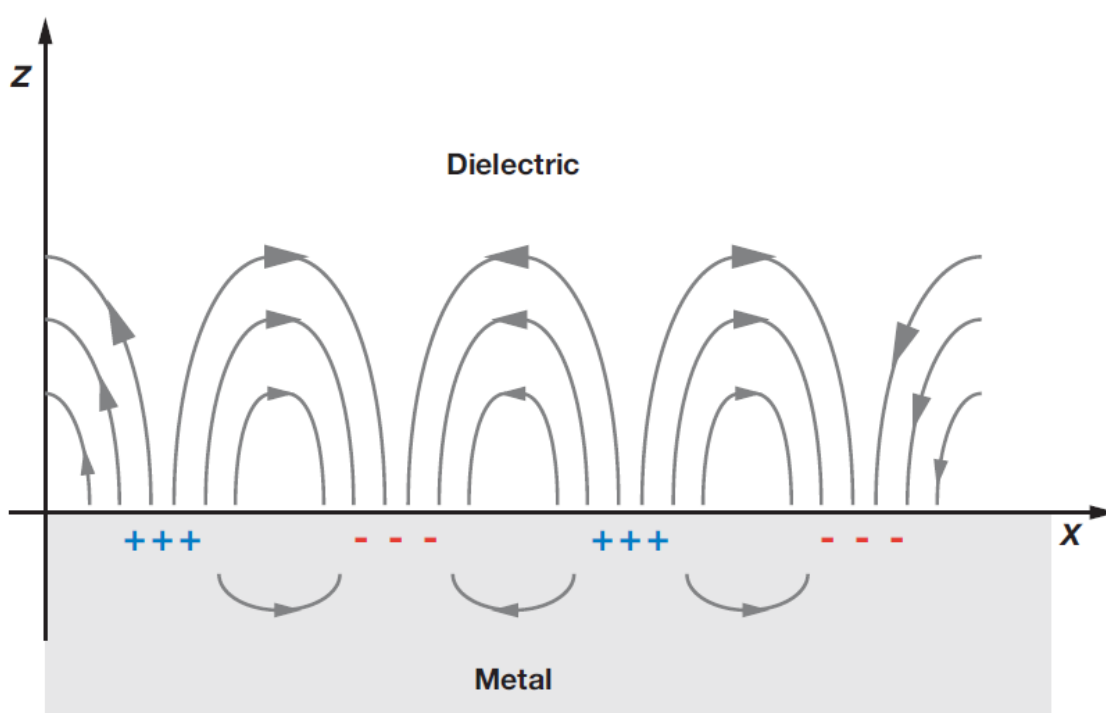


**Figure 1.24 Illustration of surface Plasmon resonance on metal.**

Picture depicting Surface plasmon on a metal surface. By applying an electromagnetic field to the metal the electrons within this metal will start to oscillate together with the applied electrical field.

The unique properties of metals to modify fluorescence are due to changes in the rates of excitation and emission. Several effects are possible. One effect is

the so called “lightning rod effect.” A metal particle can amplify the incident light field by interactions of the light with the freely mobile electrons in the metal. This effect is shown in the Jablonski diagram by an additional excitation field  $E_m$  (Figure 1.25). This effect can be dramatic [154-155].

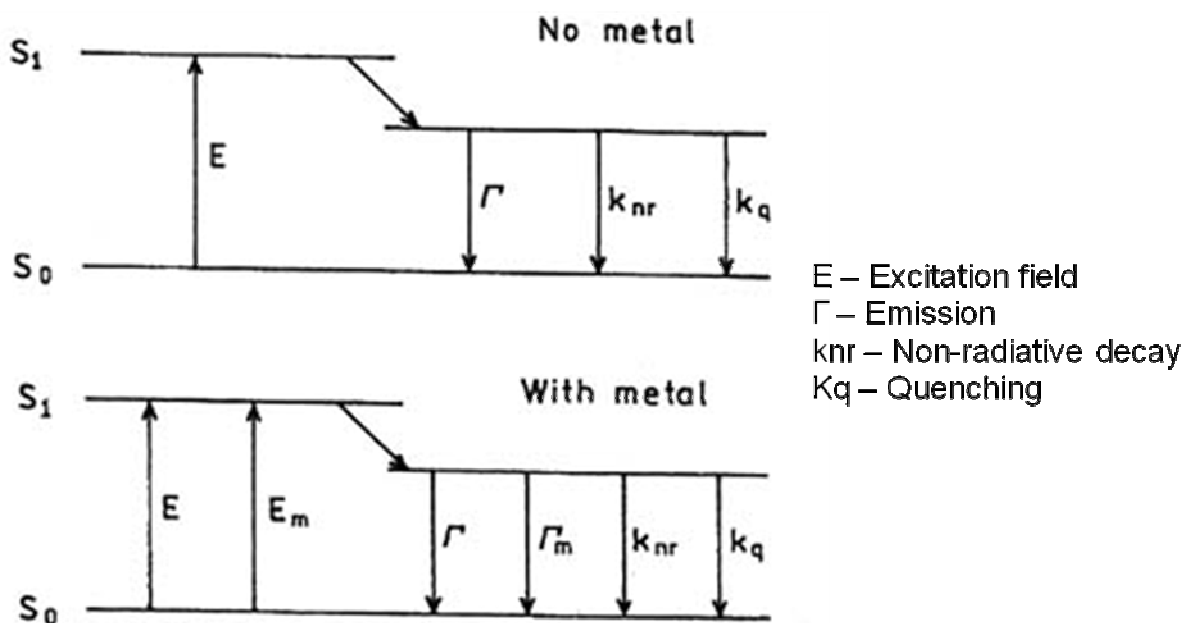


**Figure 1.25 Jablonski diagram. Metal vs no metal**

Jablonski diagram showing the excitation field in the presence and absence of a metal. With the addition of a metal an extra excitation field has been added, resulting in increased emission. Upon excitation, either on metal or no metal, the molecule can either fluoresce, or go through Non-radiative decay, and or be quenched. Quenching plays a huge factor in the presence of a metal, here the distance of the molecule to the metal has to be at an optimal distance for a decreased amount of quenching, or non at all.

## 1.5 Thesis Aims

There were 4 major aims in this thesis. Firstly, to develop a isolation and purification method for the *C. tepidum* RC. This was extremely important moving on to the next aims. The second aim was to obtain crystals for the of crystallisation of the RC. Yet, to date there are no crystals of any green sulphur type I RCs, this can seen as the missing link. This RC is the only one that is homodimeric and it is thought that the other RCs from different organisms have evolved from a similar homodimeric RC. The third aim was to couple a manmade system with something nature had provided. The aim here is to attempt to increase the fluorescence enhancement of a protein-pigment molecule when attached to plasmons, this would therefore give great insight on designing artificial mimics for the purposes of fuel production, by giving us insight on which systems can be used inconjunction with plasmons. Finally the last aim is to look at two of the peripheral proteins that associate themselves with the *C. tepidum* RC, PscD and PscB. As both of these proteins are soluble the aim is to design a construct where by both these proteins can be purified easily. By studying these proteins we are able to start to fit the function of the *C. tepidum* RC together. This would also greatly aid in answering questions such as if PscD associates itself with FMO or ferredoxin and PscB. By studying these pheripheral proteins by themselves we can start to elucidate its function and attempt to solve there structures.

## Chapter 2 – Methods and Materials

---

### 2.1 Strains

*Escherichia coli* strain DH5 $\alpha$  (Invitrogen) was routinely used for transforming and propagating both the cloning and recombinant expression plasmids. All protein production in *E. coli* was carried out in *E. coli* strain BL21 (DE3) (Novagen) or BL21 (DE3) containing a pGro7 plasmid encoding for protein folding chaperones.

Recombinant colonies were cultured in either Luria Broth (LB) or Terrific Broth (TB) containing appropriate antibiotics for selection.

### 2.2 Media

#### 2.2.1 Culture Medium for Growth of *Chlorobium tepidum*

The CL medium (N.U. Frigaard & D.A. Bryant, 2001 Appl. Environ. Microbiol) is suitable for routine culture of *C. tepidum* [156]. All the stock solutions are in appendix 1. All are stored at 4°C. The CS solution is made up fresh every time as the sulphide easily oxidises in the air.

#### 2.2.2 Luria Broth (LB) & Terrific Broth (TB) for *E. coli* growth

*E. coli* was grown either in Luria Broth (1% tryptone (w/v), 0.5% yeast extract (w/v) and 1% NaCl (w/v)) or Terrific Broth (1.2% tryptone (w/v), 2.4% yeast extract (w/v) and 4% glycerol (v/v) supplemented with 1x potassium salts (17 mM KH<sub>2</sub>PO<sub>4</sub> and 72 mM K<sub>2</sub>HPO<sub>4</sub>)) (Appendix 2).

#### 2.2.3 NMR Minimal media (1 x M9)

M9 minimal media was routinely used for the expression of the target proteins in *E. coli* for NMR studies. For isotopically labelled protein, the bacteria were grown in 500 ml of M9 minimal media (Appendix 3) rather than LB or TB.

For labelling of PscB additional trace elements were added for the growth and stabilisation of PscB, these trace elements did not interfere with the labelling of the target proteins and has been well established by Vishniac and Santer, 1957 [157].

### **2.3 Sodium dodecyl sulphate-polyacrylamide gel electrophoresis (SDS-Page)**

The purity of all proteins for the purposes of this thesis was assessed by SDS-PAGE. All samples were prepared by adding 1X sample buffer and 1 mM DTT. The samples were then heated at 80°C for 10 mins. The samples were loaded, along with the protein marker, and run on a Pre-cast NuPAGE4-12% Bis-Tris gels (Novex), which were used according to the manufacturer's instructions 4-12% SDS-PAGE at 200 V for 35-40 minutes with 1x SDS running buffer, using a BioRad power pack. The gels were then stained in either SimplyBluesafe stain (Life Technologies), or Silver stain (Invitrogen) as per the manufacturer's instructions.

### **2.4 *Chlorobium tepidum***

The His-tagged RC was obtained from the green sulphur bacterium *C. tepidum*, this was given from the group of Prof. Oh-Oka (Osaka University). The "pscA gene duplication" strategy to obtain tagged RC complexes. The mutated pscA gene encoding the tagged RC core protein with an affinity tag is incorporated into the recA locus. This causes the disruption of the recA gene and the duplication of the pscA gene (Figure 2.1). This strategy includes two different ideas. Firstly, since the recA gene is responsible for homologous DNA recombination and repair the tagged-RC gene is an ideal subject for homologous gene expression. Secondly, as the authentic pscA gene is supposed to express the wild-type RC core protein, the duplication mutant can grow despite containing a tagged RC gene.

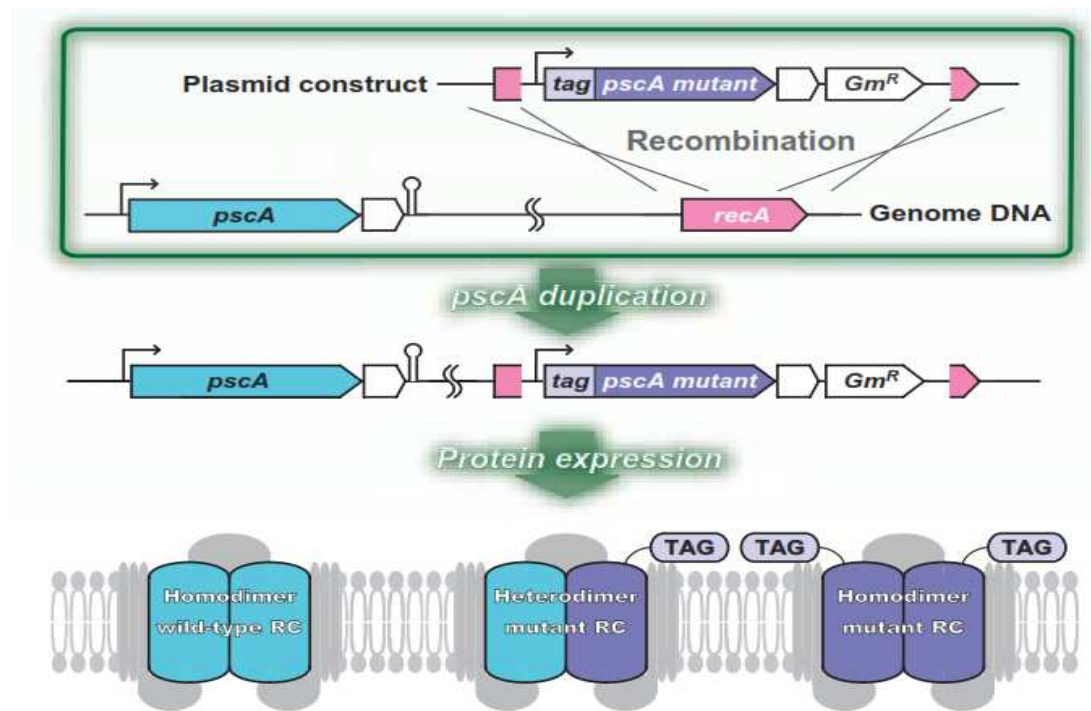


Figure 2.1 Diagram showing the “the pscA gene duplication” method to express the WT and His-tagged RC.

### 2.4.1 Growth room/conditions for *C. tepidum*

Since *Chlorobium tepidum* is a thermophilic anaerobic bacteria. The optimal growth temperature is 43-50°C, under anaerobic conditions (air tight bottles). To allow for the temperature to increase to 43°C a fish tank surrounded by foil and illuminated by 100W light bulbs from above was created. The 100W light bulbs were put above the tank to allow the temperature to increase, if temperature was too high the light bulbs were raised and vice versa. This allowed for about 10 x 1L bottles to be put in and grown at the one time.

### 2.4.2 Harvesting of cells

The *C. tepidum* cells expressing the His-tagged RC complex were grown in 1-liter medium bottles at 43°C. After 3-4 days of cultivation, cells were harvested by centrifugation at 12,000 x g for 30 min and stored at -80°C until use.

### 2.4.3 Membrane preparation

All buffers and resins used for preparation of the RC's were fully degassed and supplemented with 10 mM L-cysteine to give appropriately reducing conditions.

All green sulphur bacterial strains, so far found, have unique large vesicles attached to the cytoplasmic membranes called Chlorosome. It is difficult to obtain pure cytoplasmic membranes (chlorosome free membranes) in high yield. Thus, chlorosome containing membranes (crude membranes) are usually prepared for the RC purification.

The pelleted down cells are resuspended in cell resuspension buffer (50 mM Tris pH8, 1 mM EDTA, 2 mM DTT, 10mM L-cysteine, 0.2 mM PMSF ), and homogenised (to remove large clumps) before putting it through the cell disrupter (25psi) to break them open. The broken cells were centrifuged at 10,000 x g for 30mins at 4°C (low speed spin) to remove the cell debris. The supernatant was collected and put through a high speed spin, 110,000 x g for 1 hour at 4°C, obtaining the membrane pellets. The membrane pellets were resuspended in 50 mM Tris pH8, 2 mM DTT, 10mM L-cysteine, 0.2 mM PMSF. The cells were frozen until used.

#### **2.4.4 Preparation of the *C. tepidum* His-tagged RC complex**

##### **2.4.4.1 Solubilisation:**

Preparation of chlorosome-containing membranes and their subsequent solubilization were carried out as previously reported (Oh-oka 1993) with a modification as follows: the membranes at a concentration of 10 mg/ml BChl (a+c) were solubilised, for 2 hours with 30 mM n-octyl- $\beta$ -D-glucopyranoside ( $\beta$ -OG, Sigma) in 50 mM Tris-HCl (pH 8.0), 300 mM NaCl, 2 mM dithiothreitol, at room temperature.

##### **2.4.4.2 Nickel purification:**

After removing unsolubilized materials by centrifugation at 110,000 x g for 1 h, 200 ml of the resultant supernatant was mixed with 60 ml of a 50% suspension of the Ni<sup>2+</sup> immobilized sepharose resin, which had been pre-equilibrated with the same buffer as used in the solubilisation. The mixture was gently shaken in a conical flask with a tilt shaker for 1 h, and loaded into an empty column. The column was washed with 200ml of wash buffer (50 mM Tris-HCl pH 8.0, 300 mM NaCl, 20 mM imidazole, and 0.1% DDM to exchange the detergent). The His-

tagged RC complex was eluted with elution buffer (50 mM Tris-HCl pH 8.0, 300 mM NaCl, 300 mM imidazole, and 0.1% DDM).

#### **2.4.4.3 Sucrose density Gradients**

The eluted *C. tepidum* was then concentrated by ultrafiltration with a 50 kDa MWCO membrane (Minicon concentrator, Millipore) with the addition of 0.15% Cymal-5 to stop concentration dependant aggregation. The concentrated samples were run on a continuous sucrose density gradient. Initial sucrose density trials had shown that a continuous sucrose gradient (with 0.01% DDM and 0.15% Cymal-5) ranging from 30-35% allowed the sample to be devoid of any heterogeneity. This gave two bands and the most intense band at the top was taken further for purification.

#### **2.4.4.4 Size exclusion chromatography:**

The eluted fractions were desalted into buffer containing no imidazole. For purification by gel filtration, the eluted fraction was concentrated by ultrafiltration with a 100 kDa cutoff membrane (Minicon concentrator, Millipore). The concentrated sample was run on a Sepharose S-200 (GE healthcare) size exclusion column in the appropriate buffer (20 mM Tris pH 8, 75 mM NaCl, 0.01% DDM). Samples from fractions corresponding to the peak in the UV absorbance were measured by absorption spectroscopy. Fractions containing the RC were pooled and concentrated.

#### **2.4.4.5 Amido black assay**

Amido black assay was used to work out the concentration of the *C. tepidum* RC and correlate that back to an OD at 816 nm.

Samples for a for a standard curve were prepared by pipetting 0, 5, 10, 20, 40, and 80µl of bovine serum albumin (BSA), 0.2 mg/ml (0.2 mg/ml BSA) into centrifuge tubes and then adjusting the total volume to 225 µl. This allowed for known protein concentrations; 0, 1, 2, 4, 8, and 16µg.

*C. tepidum* RC samples, of unknown concentrations were aliquoted after measuring its absorption at 816 nm. Six samples were prepared of the RC with

the appropriate buffer (20 mM Tris pH 8, 150 mM NaCl, 0.01% DDM); undiluted, 1:2, 1:10, 1:25, 1:50, and 1:100 in a final volume of 225  $\mu$ l and was placed in to a 96 well plate. 30  $\mu$ l of Tris-HCl, pH 7.5, 1 M with sodium dodecyl sulfate (SDS) 2% (Tris-HCl) was carefully added to each sample, to avoid the presence of any bubbles. To each well 50  $\mu$ l of 90% trichloroacetic acid (90% TCA) was also added. The samples were then mixed by pipetting and left to incubate for 2 min at room temperature to allow for the protein to precipitate. The samples were then transferred in to wells of the Bio-Dot manifold (AfCS-Bio-Rad Bio-Dot) containing the nitrocellulose membrane. A gentle vacuum was applied to drain the wells. The 96 well plate containing the samples was then rinsed with 200  $\mu$ l of 6% trichloroacetic acid (6% TCA) and the transferred to the appropriate manifold well using the same tip used to load the protein sample in the first transfer of the manifold. Another gentle vacuum was applied to drain the wells, with also an addition of 100  $\mu$ l of 6% TCA to each well. The vacuum was left on for 5 mins to assure that all the solution in each well was drained. The membrane was then gently removed, and was cut around the section of the membrane containing filtrate from the wells. This membrane piece was then placed in a petri dish and Amido black stain solution (Amido black stain) was added to cover the filter. The membrane was stained for approximately 45 min on a shaker after which the amido black was gently poured off and was rinsed for 45 sec with water. The membrane was then destained with 3 x rinses of Amido black destain solution (Amido black destain), each destain step was incubated for 3 min gently shaking. The membrane was then washed with a final water wash for 3 min any excess water was drained of the blot using a paper towel. The stained spots on the membrane were carefully excised and placed in a centrifuge tube, with appropriate labels. To each tube 0.5 ml of Amido black elution solution (elution solution) was added and left for 10 mins after vortexing. The absorbance of each eluate was measured at 630 nm on the spectrophotometer. The concentration was measured using the standard curve generated by plotting the OD of the protein standards versus their content of protein (as  $\mu$ g, ranging from 0 to 16).

#### 2.4.4.6 Light induced Oxygen consumption

Functionality of the RC has been assessed by light driven electron transport from ascorbate-reduced 2,6-dichloroindophenol (DCPIP) to methyl viologen (1,1-dimethyl-4,4-bipyridinium,  $MV^{2+}$ ) with a Clarke-type electrode (Oxygraph, Hansatech, Kings Lynn, UK). The intensity of the light was  $1200 \mu E m^{-2}$ , this was controlled by using a KL 1500 LCD lamp (SCHOTT). The buffer within the Clarke type electrode was 20 mM Tricine pH 8 with the addition of 0.1% DDM. The program used to measure the  $O_2$  consumption was "O2 view". In the first instance 1000  $\mu l$  of air saturated water was added to the chamber stirring, to equilibrate the electrode the oxygen was saturated with the addition of a small spatula of sodium Dithionite ( $Na_2S_2O_4$ ), which is a strong reductant. The chamber was then cleaned with water, this process was repeated three times, before the addition of 20 mM Tricine pH 8 with the addition of 0.1% DDM. To this 10  $\mu l$  of MV (5 mg/ml) was added to reduce the  $O_2$ . 20  $\mu l$  of DCPIP (3 mg/ml) was added as an electron donor. Before adding the DCPIP to the chamber, the DCPIP was reduced by the addition of 200  $\mu l$  of Ascorbate (20 mg/ml) to the 1 ml of DCPIP (3 mg/ml). The colour change from dark blue to yellow was observed. And finally 10  $\mu l$  of RC (anywhere between 0.4-1 mg/ml) was added to the chamber before the addition of light.

#### 2.4.4.7 Thermostabilisation of the *C. tepidum* RC

All thermostabilisation experiments of the *C. tepidum* RC were carried out by purifying the RC (as described in section 2.4.4), once pure RC had been obtained they were aliquoted out in equal volumes and buffer exchanged in appropriate buffers with a range of pH values. All buffers contained 150 mM NaCl and 0.01% DDM. The concentration of all the buffers used were 20 mM; HEPES (pH 7.0 and 7.5), Tris (pH 7.5 and 8.0), CAPSO (pH 9.0 and 9.5) and CAPS (pH 10 and 10.5). All samples were then placed on a heat block at  $65^\circ C$  and after every 10 min the samples were taken out and put on ice to measure its absorption using a Shimadzu UV-1700 Pharmaspec spectrophotometer. This was carried out continuously for every 10 min until the RC had completely broken down.

## 2.5 Purification of FMO

15 g of DE52 resin was equilibrated in 50 column volumes of equilibration buffer (20 mM Tris pH 8) in a glass centered column. The wash fraction from the nickel affinity purification of *C. tepidum* was kept, as this contained the FMO protein. To completely dissociate all the FMO from the RC the wash buffer should contain a higher concentration of salt 500 mM or more (50 mM Tris-HCl pH 8.0, > 500 mM NaCl, and 0.1% DDM). The wash, from the nickel column was buffer exchanged in to 20 mM Tris pH 8 O/N. The wash was passed over the DE52 resin in the glass centered column and the FMO was eluted with increasing salt concentrations (NaCl 150 - 200 mM).

## 2.6 Genomic extraction of *C. tepidum*

Genomic DNA extraction was carried out as described by Sambrook & Russell [158]. *C. tepidum* was grown to log phase and 10-20 ml of culture was pelleted. The cell pellet was resuspended in 1 ml of the extraction buffer (10 mM Tris pH 8, 100 mM EDTA and 1% SDS), this was incubated for 1 Hour at 37°C. EDTA is a chelating agent, widely used for permeabilization. Its effectiveness is a result of its ability to bond the divalent cations of  $\text{Ca}^{2+}$ ,  $\text{Mg}^{2+}$ . The last ones stabilise the structure of membranes. The SDS is a molecule whose unique properties enable manipulation (disruption or formation) of hydrophobic-hydrophilic interactions among molecules in biological samples. SDS, here, is used to as a detergent to lyse cells. The extraction buffer allows for the genomic DNA to be extracted from the cells. Proteinase K (100 µg/ml) was added to break down cellular proteins. The solution was incubated with Proteinase K for 2 hours at 50°C. After the solution had become translucent a final concentration of 20 µg/ml of RNaseA was added and left to incubate at 37°C for 30 mins. A 1:1 ratio was added of Phenol:chloroform:isoamyl alcohol (25:24:1), and this was gently vortexed forming an emulsion without shearing the genomic DNA. The samples were then centrifuged for 10 minutes in a Jencons-PLS spectrafuge 24D at 16300 x g. The aqueous phase (upper aqueous phase) was carefully removed into a fresh tube without disturbing the lower phase. 10 M ammonium acetate was then added to the upper aqueous phase (2:1 Upper aqueous:Ammonium acetate) to precipitate the DNA. Two volumes of 100% chilled ethanol was added, this

allowed any contaminants to be left behind as the entire DNA precipitated. The samples were then centrifuged for 20 minutes in a Jencons-PLS spectrafuge 24D at 16300 x g. The supernatant was removed and washed with Ethanol (70%) twice and an additional spin for 5 mins at 16300 x g after each wash step. The pellet was then left to air dry on the bench for 15-20 mins. The DNA pellet was then resuspended in sterile water and heated at 50°C for 2 hours to dissolve the DNA. The quality and quantity of the genomic DNA was assessed by gel electrophoresis.

## 2.7 PCR amplification and sub-cloning strategies

All PCR reactions were performed using KOD HotStart DNA Polymerase (Merck Biosciences) using the appropriate template and primer combinations. Typically, PCR reactions consisted of an initial 2 min Polymerase activation step at 98°C. This was followed by 39 cycles each consisting of a DNA denaturation step (95°C for 10s), primer annealing (55°C for 10s) and DNA extension (70°C for 10s per kb of DNA being amplified). After the last cycling step, the PCR reaction was concluded with a further 5 min at 70°C to ensure all *de novo* DNA synthesis had occurred.

PCR products were run on 1% (w/v) agarose gels alongside a 1kb DNA ladder (Promega). DNA was visualised using SYBR Safe DNA gel stain (Invitrogen). DNA fragments were extracted from the agarose gel using QIAquick Gel Extraction kit (QIAGEN).

Extracted PCR products were ligated into the blunt ended Pjet1.2 vector using the thermo scientific CloneJET PCR cloning kit (Thermo Scientific) prior to ligation into the modified pET21a-CLBH (3C cleavage site, improved Light oxygen voltage domain, Biotinylation domain, and His 10 tag) expression vector.

The ligation mixture was transformed into DH5α cells by heat shock (15 min incubation on ice; 42°C heat shock for 25 sec; 5 min recovering time on ice; 1h shaking at 37°C in LB), plated-out on LB agar plates containing 100 µg/ml ampicillin (Invitrogen) and incubated overnight at 37°C.

Several colonies for each pJET1.2 construct were grown up in 5 ml of LB containing 100µg/ml ampicillin overnight at 37°C. Plasmid DNA was isolated from cell cultures using the QIAprep spin miniprep kit (QIAGEN). The identity of recombinants was confirmed first by restriction digest and then by sequencing (MWG eurofins, London). At a later stage, DNA fragments were sub-cloned from the pJET1.2 vectors into the modified pET21a-CLBH expression plasmid using the EcoRI and NotI sites of the expression plasmid. Ligation reactions were performed using T4 DNA ligase (New England Biolabs). Glycerol stocks were prepared for all *E. coli* transformants containing the desired plasmids and stored at -80°C. All restriction enzymes stated were used with appropriate buffer from Fermentas FastDigest.

## **2.8 Expression vector modification of the pET21a vector**

A modified version of the pET21a (Novagen) recombinant plasmid had been created in which clone inserts had to be ligated into the EcoRI and NotI sites immediately upstream of the CLBH tag located between the NotI and BamHI sites.

Towards this goal, cloning sites upstream of the EcoRI site had to be eliminated. To do this the plasmid pET21a (Novagen), was digested at its NdeI and BamHI sites. Digestion was left for 1 h at 37°C, and run on a 1% agarose gel for confirmation that the selected restriction sites had been removed, by using the Qiagen gel purification kit the plasmid was isolated.

20 µl of modified pET21a was blunt ended with the addition 3 µl DNA polymerase (NEB), 3 µl Taq and 4 µl dNTPs (10 mM). The blunt ended mixture was left for 70°C for 30 min. Blunt ends of the modified pET21a were circularised by ligating the blunt ends together with 8 µl of the modified blunt ended pET21a DNA, 1 µl of DNA ligase and 1 µl of the DNA ligase buffer (10 x ligase buffer), and was left at room temperature for 1 hour (or 4°C O/N). This was then transformed into DH5α cells. Recombinant colonies of the newly modified pET21a plasmid (transformed into DH5α) were selected and grown overnight. Recombinant plasmid was isolated (Qiagen miniprep kit) and sequenced in order to confirm correct modification of the recombinant pET21a plasmid.

## 2.9 CLBH incorporation into modified pET21a vector

The CLBH tag (a gift from Dr Niall Fraser), was ligated into the PvuI and NotI sites of the modified pET21a vector. Ligation was left at room temperature for 1 hour. Modified pET21a containing the CLBH tag was transformed into *E. coli* DH5 $\alpha$  cells and confirmation of successful ligation of the CLBH was established by sequencing.

## 2.10 Amplification of PscD and PscB

PscD and PscB DNAs were amplified by PCR using genomic DNA as template (as described in section 2.6). PscD was amplified using the primers CAAGAATTCATGCAACCTCAGCTCAGC (forward) and TTAGCGGCCGCTTTGAAAACTGGTTCG (reverse); PscB DNA was amplified using the primers CAAGAATTCATGGCCGAACCTGTTGAA (forward) and TTAGCGGCCGCTCTGGCTTCGCGATGGAAA (reverse). Both sets of primers contained the EcoRI and NotI restriction sites (restriction sites are coloured red and the bases matching the PscD and PscB genes are in green). The PCR fragments were sub cloned into the pJET1.2 vector (as described above in 2.7).

## 2.11 Insertion of PscD/PscB in the modified pET21a expression vector containing CLBH

Modified pET21a-CLBH was digested at the EcoRI and NotI sites. Digestion was run on a 1% agarose gel and isolated using a Qiagen gel purification kit. The plasmid pET21a-CLBH and PscD/PscB insert in pJET1.2 were digested with EcoRI and NotI and ligated using T4 ligase overnight at 4°C. The ligation was transformed into DH5 $\alpha$  cells. Recombinant PscD/PscB-CLBH in the modified pET21a plasmid was grown overnight and isolated using the Qiagen miniprep kit. Sequencing then confirmed the successful ligation of PscD/PscB into modified pET21a-CLBH.

## 2.12 Insertion of PscB in the novagen pET28a expression vector for NMR studies

For purposes of expression and purification of the target protein, PscB was also ligated in to the pET28a (Novagen) vector. This PscB construct was used for

structural characterisation purposes. As well as the pET28a (Novagen) vector, PscB was digested from the modified pET21a-CLBH construct, using the restriction enzymes EcoRI and NotI. Digestions was run on a 1% agarose gel and isolated using a Qiagen gel purification kit. Ligation of PscB into the pET28a vector was carried out by using T4 ligase overnight at 4°C. The ligation was transformed into DH5α cells. Recombinant PscB in the pET28a plasmid was grown overnight and isolated using the Qiagen miniprep kit. Sequencing then confirmed the successful ligation of PscB into the pET28a vector.

## **2.13 Using iLOV to measure expression of PscD and PscB**

iLOV was readily used to measure the expression of the target protein and as the protein fluoresces under UV (ultra violet) it allowed the target protein to be detected in every step of the purification method. iLOV was a gift from Prof. John Christie (University of Glasgow)

### **2.13.1 Test expression**

Transformation of the modified pET21a-CLBH construct containing PscD and PscB into BL21 (DE3) cells and BL21 (DE3) cells containing the plasmid pGro7, were plated on an LB agar plate containing the appropriate antibiotics. Single colonies were taken and inoculated into LB containing antibiotic and grown overnight for 16 hours. Overnight cultures were used to inoculate 50ml of LB and 45ml of TB supplemented with 5ml of 1x potassium salts. The cells were grown until the OD<sub>600</sub> reached 0.6, and expression of PscD was induced by addition of 1 mM IPTG (isopropyl β-Dthiogalactopyranoside). Expression of the GroEL/ES complex was induced by addition of Aribanose (2mg/ml). Following induction, cultures were further incubated at 22°C or 37°C. For analysis of expression, 1ml of sample was removed before and throughout a 16 hour time period. The 1ml cell samples were pelleted at 13,000 rpm and stored at -20°C until they were ready to analyse either on a 4-12% SDS-PAGE gel or by fluorescence using the iLOV.

### **2.13.2 SDS page identification of expressed target proteins**

Pellets were resuspended in 1ml water (H<sub>2</sub>O) containing 1 x bugbuster (Novagen) and incubated for 2 h at room temperature. Samples were then heated at 50°C for 5 mins and spun at 16300 x g on a table top centrifuge (Jencons-PLS spectrafuge 24D) for 1 minute before analysing on SDS-page (4-12% Bis-Tris).

### **2.13.3 Measuring iLOV fluorescence expression of PscB/PscD-CLBH in 96 well plates**

Samples prepared in section 2.13.1, for both PscD/PscB-CLBH, were measured on a FLUOstar OPTIMA plate-reader. The target proteins containing iLOV within the CLBH tag were excited at 450 nm and the emission was measured at 520 nm. The samples were prepared by adding 200 µl of each sample to a black 96 well plate (Corning).

## **2.14 Protein expression and purification of PscD-CLBH**

### **2.14.1 Preparation of PscD-CLBH**

Overnight cultures were subcultured in 8 x 500ml of TB medium containing 1 x Potassium Salts, ampicillin (100 µg/ml), and chloramphenicol (0.02 mg/ml). The cells were grown until the OD<sub>600</sub> was ~0.6 and induced with 1 mM IPTG (isopropyl β-D-thiogalactopyranoside) and Arabinose (2 mg/ml). Following induction, the culture was further incubated for 16 hours at 22°C shaking (180 rpm). For analysis of expression, sample was removed pre and post induction with IPTG to analyse on a 4-12% SDS-PAGE. Cells were harvested by centrifugation at 12,000 x g for 30 min at 4°C. The cell pellets were re-suspended in binding buffer (50 mM NaPi pH 7.5, 150 mM NaCl, 10% Glycerol 0.1 mM EDTA). Resuspended cells were lysed by three passages through a cell disrupter at 20 kPSi, and centrifuged in a Sorvall JLA 8.1000 rotor at 4000 x g for 30 minutes at 4°C. The supernatant was retained and the pellet discarded.

### **2.14.2 Nickel affinity chromatography**

The cell extract of the spun down supernatant from the lysed *E. coli* cells containing PscD-CLBH was loaded onto the 5ml nickel column. Following binding,

non-specifically bound proteins were washed off the column with 10 column volumes of wash buffer (50 mM NaPi pH 7.5, 300 mM NaCl, 0.1 mM EDTA, 10% Glycerol and 75 mM imidazole), and bound protein was eluted using 20 ml of the elution buffer (50 mM NaPi pH 7.5, 150 mM NaCl, 0.1 mM EDTA, 10% Glycerol and 500 mM imidazole).

### **2.14.3 Cleavage of the CLBH tag by 3C protease**

Cleavage of the PscD from the CLBH tag was carried out by buffer exchanging the PscD-CLBH in a no imidazole buffer (50 mM NaPi pH 7.5, 150 mM NaCl, and 10% Glycerol). PscD-CLBH was then subjected to 3C cleavage by the addition of the of 3C protease (1 mg/ml), 1 mM DTT and 1 mM EDTA, and left in the cold room (4°C) O/N to cleave.

### **2.14.4 Subtractive IMAC (Immobilised Metal Affinity Chromatography)**

After cleavage, the cleaved PscD-CLBH protein was buffer exchanged into 50 mM NaPi pH 7.5, 150 mM NaCl, 0.1 mM EDTA, and subjected to subtractive. Any PscD still bound to the Nickel column non-specifically was washed off with wash buffer 2 (50 mM NaPi pH 7.5, 150 mM NaCl, 0.1 mM EDTA, 20 mM imidazole). The PscD was dialysed into a buffer containing no imidazole and concentrated in a 10,000 MWCO concentrator.

### **2.14.5 Gel filtration**

PscD was passed applied to a superdex 75 gel filtration column (GE Healthcare) equilibrated in sodium phosphate buffer (50 mM NaPi, pH 7.5, 150 mM NaCl, 0.1 mM EDTA). Fractions containing protein were analysed by SDS-PAGE for purity, and pure fractions were pooled and retained for further work.

### **2.14.6 Wester Blot analysis of cleaved CLBH tag using an iLOV antibody**

The iLOV antibody was a gift from Prof John Christie (Univeristy of Glasgow). Preceding western blotting, protein samples were separated by mass by SDS-PAGE (4-12% Bis-Tris SDS, section 2.3). The protein bands from the unstained

gels were transferred to nitrocellulose membrane (Invitrogen) using a XCell II Blot Module (Invitrogen). Western transfer was carried out in transfer buffer (5.8g Tris pH 8.5, 2.9g Glycine, 0.4g SDS, 20% per litre) at a constant voltage of 100 V for 1 h. To block non-specific binding the membrane was immersed in 10% non-fat dried milk in TN buffer (2.4g Tris, 8.8g NaCl/Litre, pH 7.2) with 0.1% Tween20 for 1 hr at room temperature (2g marvell in 20ml TN buffer + 0.1% tween). The membrane was rinsed briefly with 3 changes of TN buffer + 0.1% Tween20, and a final wash step, 2 times 10 mins, in TN buffer + 0.1% Tween20. Immunoblotting of the nitrocellulose membrane was carried out using polyclonal iLOV antibody and left to incubate for 30 mins on orbital shaker. The membrane was then briefly rinsed with 3 changes of TN Buffer + 0.1% Tween20 and then washed with TN buffer + Tween20, 3 x 15min washes. The membrane was then incubated with secondary antibody (Anti-rabbit) for 15 minutes at room temperature. The membrane was washed again with the TN buffer three times. The membrane was then treated with Amersham<sup>TM</sup> ECL<sup>TM</sup> prime western blotting reagent (GE Healthcare life sciences) as per manufacturer's instructions.

## 2.15 Purification of 3C protease

The HRV 3C (Human rhinovirus 3C or 3C) protease construct was a gift from Dr Niall Fraser (University of Dundee). The 3C protease was expressed in *E. coli* using the same protocol as that for PscD-CLBH (Section 2.14) with the exception that LB was used for cell growth rather than TB, that there was no glycerol present in any of the buffers and the final step of the purification the buffer contained 1 mM DTT and 1 mM EDTA. 3C protease was concentrated using a 10 kDa MWCO centricon (Sartorius), and applied to a superdex 75 gel filtration column (GE Healthcare) equilibrated with 50 mM Tris pH 8.0, 150 mM NaCl, 1 mM EDTA and 1 mM DTT. Fractions containing pure HRV 3C protease were collected, snap-frozen with liquid nitrogen after the addition of 20% Glycerol, and stored at -20°C.

## 2.16 Protein Expression and Purification of PscB

### 2.16.1 Preparation of PscB

Overnight cultures were subcultured in 16 x 500ml bevelled edged flasks of TB medium containing 1 x Potassium Salts, Kanamycin (50 µg/ml). Cells were grown until the OD<sub>600</sub> was ~0.6 and induced with 1 mM IPTG (isopropyl β-D-thiogalactopyranoside). Following induction, the culture was further incubated for 16 hours at 37°C shaking (190 rpm). For analysis of expression, sample was removed pre and post induction with IPTG to analyse on a 4-12% SDS-PAGE. Cells were harvested by centrifugation in a Sorvall JLA 8.1000 rotor at 4000 x g for 30 minutes at 4°C. The pellet was re-suspended in binding buffer (50mM NaPi pH 7.5, 150 mM NaCl, 0.1 mM EDTA and 10% glycerol). Resuspended cells were lysed by three passages through a cell disrupter at 20 kPSi, and centrifuged in a Beckman JA-20 rotor at 10,000 rpm for 30 minutes at 4°C. The supernatant was retained and the pellet discarded.

### 2.16.2 Nickel Affinity chromatography

The cell extract of the spun down supernatant from the lysed *E. coli* cells containing PscB was loaded onto the 5ml nickel column. Following binding, non-specifically bound proteins were washed off the column with 10 column volumes of wash buffer (50 mM NaPi pH7.5, 300 mM NaCl, 0.1 mM EDTA, 75 mM imidazole and 10% glycerol), and bound protein was eluted using 20ml of the elution buffer (50 mM NaPi pH 7.5, 150 mM NaCl, 0.1 mM EDTA, 500 mM imidazole and 10% glycerol).

## 2.17 Expression and purification of ferredoxin from *Arabidopsis thaliana*

The ferredoxin construct was a gift from Dr Rhys Grinter (University of Glasgow). The ferredoxin was expressed in *E. coli* using the same protocol as that for PscD-CLBH (Section 2.14) with the exception that LB was used for cell growth rather than TB and when the cells were expressed they were induced at 28°C O/N. The wash buffer also contained a lower concentration of imidazole as the target

protein only contained a 6 x His tag (50 mM NaPi pH 7.5, 300 mM NaCl, 10% Glycerol and 25 mM imidazole).

## **2.18 Circular Dichroism (CD)**

CD experiments were carried out using a Jasco J-810 spectropolarimeter. Spectra were recorded in the far ultra violet (UV) region (wavelength 260 to 180 nm) using standard sensitivity, bandwidth 1.0nm, data pitch 0.2nm and scan speed of 50 nm/min. Protein samples were measured using 0.2mm or 0.5mm cuvettes (Hellma). Near UV CD spectra (wavelength 320 to 250 nm) were recorded using same settings as far UV except scan speed, 10nm/min. All spectra were recorded at room temperature.

## **2.19 Nuclear Magnetic resonance (NMR)**

NMR spectra were recorded using a Bruker AVANCE 600 spectrometer equipped with a TCI cryoprobe. All NMR samples were in 20 mM sodium phosphate buffer pH 7.7, 75 mM NaCl and placed in a 5mm NMR tube with 5% D<sub>2</sub>O. Experiments were performed at varying temperatures from 278K to 313K, for PscB the experiments were performed at 314K. Resonance assignments for PscD and PscB were obtained using isotopically enriched protein samples (<sup>15</sup>N and <sup>13</sup>C, Sigma).

## **2.20 Isothermal titration calorimetry (ITC)**

All ITC experiments were performed on a VP-ITC microcalorimeter (MicroCal LLC) in a 20mM NaP buffer pH7, 75 mM NaCl for ferredoxin and FMO with the target proteins (PscD in the same buffer) in the cell (cell volume = 1.4005 ml) and the FMO (0.06 mM) and ferredoxin (0.1 mM) proteins in the syringe. Both FMO and Ferredoxin were titrated in to PscD (0.01 mM) using an initial injection of 1 µl followed by 28 x 10 ul injections, stirring at 310 rpm. Any data obtained for these complex formations were fitted to a single site binding equation after correction for heat of dilution of using MicroCal ORIGIN software.

## 2.21 Biocore

SPR (Surface Plasmon resonance) was performed using a Biacore 2000 (GE Healthcare, London, UK). The target protein was covalently immobilised on to the flowcell of a CM5 biosensor chip by amine coupling according to the manufacturer's instructions. The immobilisation density was 900 response units. Sensorgrams were generated at a flow rate of 40  $\mu\text{l}/\text{min}$  using 20 mM NaP pH 7.4, 150 mM NaCl, and 0.01% DDM as running buffer and regeneration between injections with ethanolamine.

## 2.22 Crystallisation

All the sitting drop vapor diffusion method of crystallising proteins carried out at Glasgow University were set up using a Cartesian nanovolume crystallisation robot (Genomic Solutions Ltd.) in 96-well plates. The target protein and the precipitant had a final volume of 1  $\mu\text{l}$  in each well by mixing 500 nl of each. All trays were stored at room temperature unless stated otherwise. All Trays were monitored by using a MEIJI EMZ light microscope. Any possible crystal hits were tested using the in-house X-ray machine (Diffractometer, Rigaku MicroMax-007 and Mar345 dtb detector)

## 2.23 Lipidic Cubic Phase (LCP)/in-meso crystallisation

All in meso crystallisation were carried out in Trinity College Dublin in Prof. Martin Caffrey's Lab under the supervision of Dr Alette Brinth. Photosynthetic reaction centres from *C. tepidum* were prepared to a high purity as previously described and shipped to Dublin. To observe that no changes were made to the RC, due to the trip, the absorbance was measured using a Uvikon absorbance spectrophotometer. In-meso trays were set up using the lipidic cubic phase crystallisation method described by Caffrey et al. (2009) in which monoolein (NuChek Prep., Inc.) and 53 mg/ml of protein solution (in 20 mM Tris pH 8, 75 mM NaCl, and 0.01% DDM) were mixed 3:2 (Lipid:Protein, in a final volume of 85  $\mu\text{l}$ ) until transparent, non-birefringent and solid cubic phase was formed. The absorbance of the RC was also measured in meso using a Spectramax 96 well plate reader, the data was analysed using the SoftmaxPro software. The robot, used to set up the trays, was a SIAS robot (Caffrey et al. 2009).

### 2.23.1 In meso crystallization set up using the SIAS robot

The homemade screens (Appendix 1) were set up in forward and reverse. The sample was set up using the SIAS robot, in each row of the plate the sample was first dispensed (Fig 2.2) and then the robot, after each row would dispense the precipitant (Fig 2.3). Each 96-well screen required 2  $\mu$ l of protein. And was set up as according to Appendix 4.

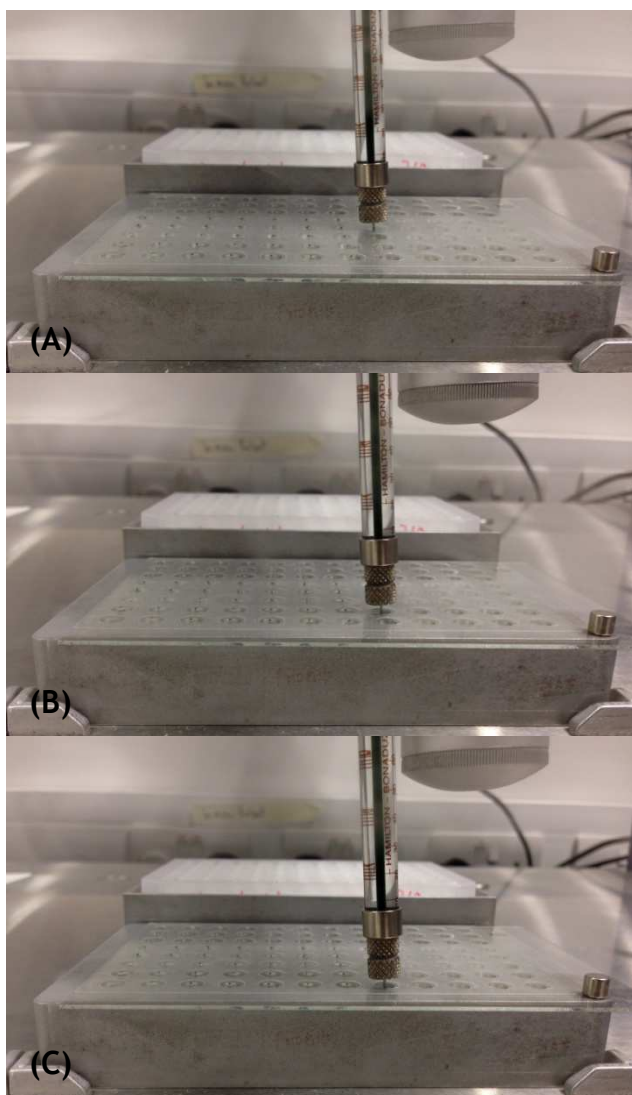
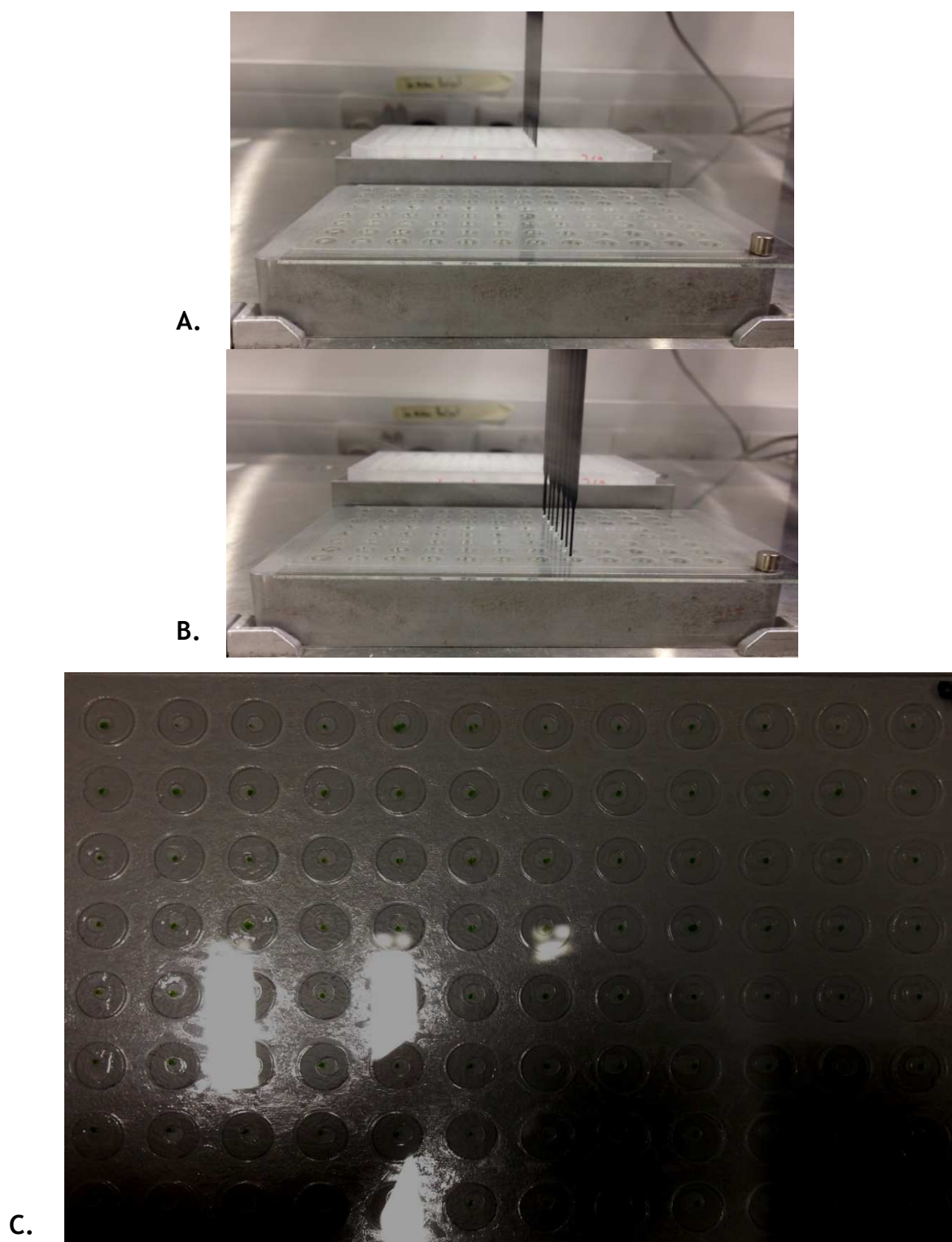


Figure 2.2 Dispensing of the RC in monoolein row by row (A - C), using the SIAS robot.



**Figure 2.3** The robot selecting the precipitant from the deep well blocks (A) and dispensing it on the RC in meso (B). The LCP tray of the RC in meso with precipitant can clearly be observed (C).

## 2.24 Incorporation of *C. tepidum* RC in lipidic bicelles

Lipidic bicelles were prepared and incorporated to with the *C. tepidum* RC according to Rachna Ujwal and James U. Bowie (2011) [159]. Bicelles were prepared using the lipid:amphiphile combinations DMPC (1,2-dimyristoyl-sn-glycero-3-phosphocholine):CHAPSO( 3-[(3-cholamidopropyl) dimethylammonio]-2-hydroxy-1-propanesulfonate). Both DMPC and CHAPSO were weighed out and dissolved in deionised water. The molar ratio of DMPC:CHAPSO was chosen to be 2.8:1 and the final bicelle concentration was 40%. To obtain homogeneous lipid in water it was subjected to repeated cycles of heating (40-50°C), cooling (on ice) and vortexing for the lipid to go in to solution. After completion the bicelles were stored at -20°C to stop hydrolysis of the phospholipd head group.

The bicelle was added to the purified RC (~20mg/ml) in a 1:4 (v/v) ratio, giving a final bicelle concentration of 8%. As the bicelle is temperature sensitive going from a viscous liquid at low temperatures to turning in to a gel at higher temperatures, the RC-bicelle mixture was done on ice at 4°C. The mixture of RC-bicelle was gently pipetted until the solution was clear and homogenous. The sample was incubated on ice for 30 min to allow for complete reconstitution of protein in to bicelle. Crystal trays were set up using the in house Cartesian robot. The trays used for the bicelles were made by the Cartesian by dispensing the percipetants in there allocated wells (500 nl) but the RC-bicelle solution was added to each well by hand with a pipette (500 nl) as the robot could not dispense the RC-bicelle due to the room temperature being too high causing the change in phase for the RC-Bicelle. All the plates were stored at 20°C.

## 2.25 Plasmon enhancement experiments of *Chlorobium tepidum* RC and FMO

All Plasmon enhancement experiments were carried out in Poland (Torun) at Copernicus University, in the lab of Prof. Sebastian Mackowski. All SIF and Ag nanowires were made by the group of Prof. Sebastian Mackowski, as according to Kadir Aslan *et al* [151]. Each nanowire is 100 nm by 100 µm. *C. tepidum* RC samples and FMO were prepared by diluting the RC with 5% water solution of PVA (polyvinyl alcohol) to obtain a solution with 2% PVA concentration. Such

concentration is used for its exquisite parameters for layer spin-coating. The RCs were spin-coated in PVA matrix over glass and over silver island film (SIF). The glass sample was used as a reference for the SIF sample. Spin coating of 50 $\mu$ L RC-FMO solution with 2% PVA on the SIF surface, and a spun quickly at 5000 rpm to allow a homogenous distribution of RC-FMO on the surface.

Measurements of enhancement of fluorescence of the RC on silver island film were carried out by measuring intensities of emission for various excitations. To measure the emission spectra filters consisting of 750nm and 780nm long pass filters were used, filtering out any emission not coming from the RC and reflected excitation. Emission spectra were measured for over 200 spots on the sample surface to estimate the intensity of emission. Lasers with wavelengths of 405nm, 485nm, 532nm, 589nm and 640nm were used. The laser power was adjusted to obtain good intensity and spectral resolution for the sample on glass and on SIF over 1s CCD exposition time. The power was measured after the objective that was used to focus the excitation beam and collect the emitted fluorescence. The measured power is shown in table 3.

Laser Wavelength	Laser Power
405 nm	120 $\mu$ W
485 nm	160 $\mu$ W
532 nm	136 $\mu$ W
589 nm	90 $\mu$ W
640 nm	166 $\mu$ W

**Table 3 Measured Excitation power**

For acquisition and analysis of spectra Andor Solis were used, as an Andor CCD camera was used for acquisition (an Andor iDus coupled to an Amici prism was used as a spectrometer -

[http://www.andor.com/scientific\\_cameras/idus\\_spectroscopy\\_ccd/](http://www.andor.com/scientific_cameras/idus_spectroscopy_ccd/)). For lifetime measurements a Becker & Hickl (B & H) Time Correlated Single Photon Counting setup was utilised, consisting of picosecond pulse lasers (405nm, 486nm and 640nm were used at 50MHz repetition rate) and a Single Photon Avalanche Photodiode. B & H software was used in order to measure the fluorescence decays.

## Chapter 3 –Isolation, Purification & stabilisation of the *C. tepidum* RC and FMO protein

### 3.1 Introduction

This chapter describes the purification and stabilization of the *C. tepidum* RC. The aim was to obtain pure monodisperse, stable RC protein for purposes of using the RC for plasmonic enhancement and to try to elucidate its structure by X-ray crystallography. The *C. tepidum* strain used was a gift from Prof. Oh-Oka (University of Osaka). This strain contained a His-tagged RC (*recA::(HisAB-aacC1)* strain) and was constructed in 2010 [122]. The His-tagged *C. tepidum* RC does not interfere photosynthetic growth and has been reported to have the same absorption spectrum as the wild type (WT) RC [160]. This is illustrated in figure 3.1 (modified from Oh-Oka 2013 [160]) showing a band around 810 nm, which contributes to the antenna BChls *a* associated with FMO proteins and the RC complex. The absorption shoulder observed at around 840 nm is specific to the special pair of BChls *a*, P840, within the RC complex.

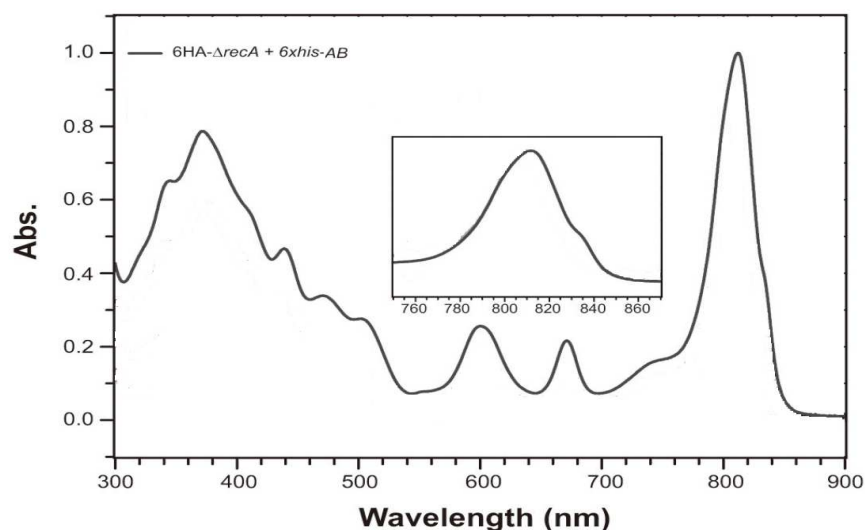


**Figure 3.1 Absorption spectra *C. tepidum* RC, obtained by Ni<sup>2+</sup>-affinity purification. Image modified from Oh-Oka (2013) [160].**

Absorption spectra of the *C. tepidum* RC obtained from *C. tepidum* strain pDSK5191-6xhis-pscAB with Ni<sup>2+</sup>-affinity chromatography purification procedure. The absorption band around 810 nm is contributed by antenna BChls *a* associated with FMO proteins and the RC complex as well, while the absorption shoulder around 840 nm is specific to a special pair of BChls *a*, P840, within the RC complex.

### 3.2 Growth of *C. tepidum* Cells

*C. tepidum* grows optimally at 43°C (T.M. Wahlund et al., 1991 Arch. Microbiol) [111]. All the *C. tepidum* cells were grown in a fish tank surrounded by tin foil, illuminated with light at 43°C, as observed in figure 3.2 A. Glycerol stock cultures in the -80°C freezer were inoculated in 100-250 mls of media in a durran bottle (fisher scientific), after 3-4 days of well grown culture the *C. tepidum* were inoculated in to larger cultures (10 x 1 l bottles) and placed overnight in the dark to remove oxygen before placing it in the fish tank for the cells to grow (Figure 3.2 B). The cells utilises reduced sulphur compounds (sulphide, thiosulphate) as an electron source for its growth. A typical culture solution shows a deep dark green colour due to the bacteriochlorophyll c aggregates in the chlorosome. Figure 3.2 B shows (going from left to right) the growth of the *C. tepidum* cells until a dense green colour is observed.

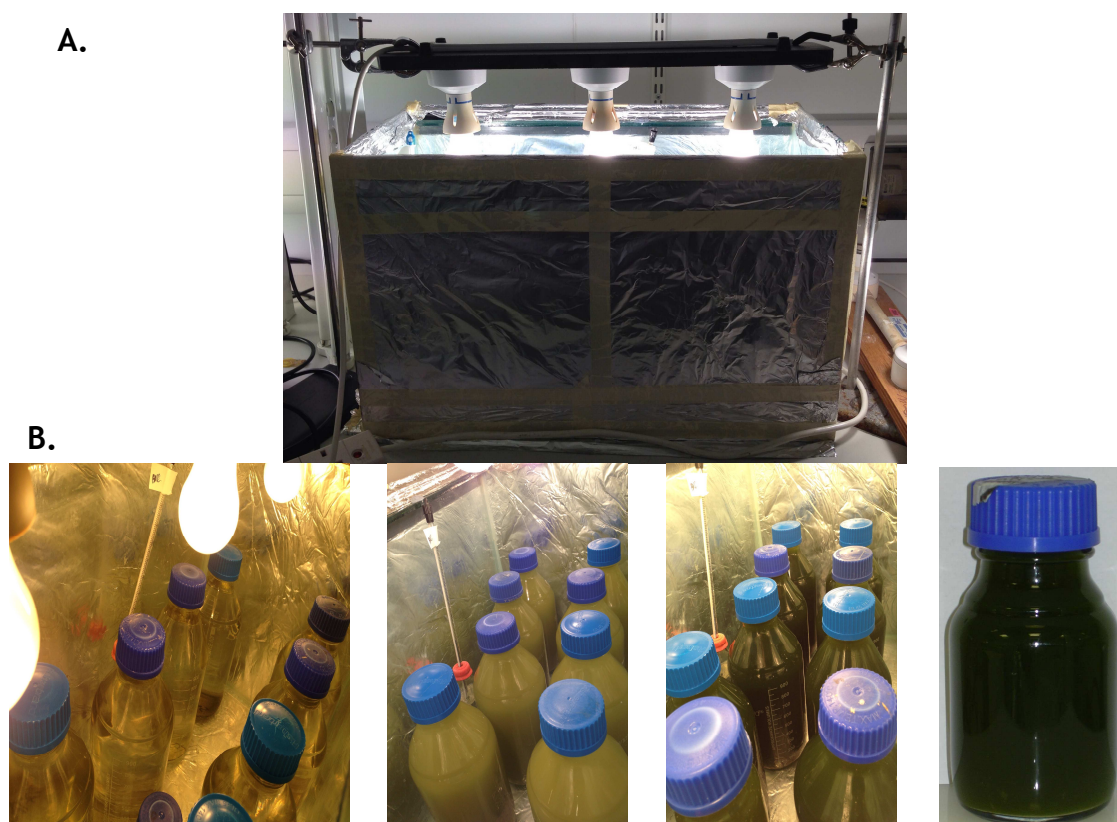


**Figure 3.2 Growth conditions of *C. tepidum* cells**

**A.** A fish tank covered with tin foil with illumination from above to allow for the temperature to increase to 43-50°C for optimal growth of cells, as well as providing sufficient light for bacteria to grow. **B.** Cells grown in 1l bottles under anaerobic conditions as cells are oxygen sensitive. Bottles were shaken once every 12 hours, until media went from clear (Far left) to a denser colour (Middle picture), until the cells reached the correct growth phase and was visualized by the intensity of the green colour (Far right).

### 3.3 Choosing the best detergent with which to solubilise the *C. tepidum* RC

Since there are no well defined rules for choosing the “best” detergent a range of detergents were tested for their ability to solubilise the *C. tepidum* RC. The typical protocol for testing the detergents for their ability to solubilise the *C. tepidum* RC was as follows; membranes were prepared as described in section 2.4.3 a solution of these membranes was made up in 50 mM Tris pH8, 1 mM EDTA, 2 mM DTT, 10mM L-cysteine, 0.2 mM PMSF and the standard concentration of the membranes was equivalent to 10 mg/ml of Bchl. This standard solution was divided in to 5 equal 10 ml aliquots. Each aliquot was then used with one of the following detergents.

Five detergents were tested;  $\beta$ -OG (Octyl-beta Glucoside), DDM (n-dodecyl beta-D-maltoside), DM (dodecyl maltoside), MNG-3 (maltose-neopentyl glycol), and LDAO (Lauryldimethylamine-oxide). The standard detergent solubilisation conditions were used the detergent at three times the CMC and an incubation time of 2 hours at room temperature in the dark. Subsequent to each incubation each aliquot was subjected to a high speed centrifugation at 110,000 x g for 1 hour at 4°C (as mentioned in the methods and materials section 2.4.3).

Absorption spectra were then recorded for each supernatant and the results of this are shown in figure 3.3 B. Figure 3.3 A shows the abs spectra of the un-solubilised membranes for comparison. In figure 3.3 A the main peak at 750 nm arises from the pigments associated with the chlorosome. The supernatant was then taken from each of the solubilised membranes and the absorption of the neat supernatant was measured to analyse the effects of each detergent by looking at the absorbance at 808 nm, which comes from the FMO protein as well as the RC (Figure 3.3 B). The absorption spectra, in figure 3.3 B, clearly showed that all the detergents except MNG-3 had solubilised the *C. tepidum* RC. A clear peak round 808 nm was observed after solubilisation of the RC membranes in each detergent, which is indicative of the FMO and the Bacteriochlorophyll *a* peak belonging to the special pair within the RC.  $\beta$ -OG (black line), DDM (red line), DM (green line) and LDAO (blue line) all had peaks at 808 nm, which can be seen in figure 3.3 B, indicating that it had retained the FMO and the RC. Whereas, MNG-3 (purple line in figure 3.3 B) had no peak at 808 nm but did have

a large peak at around 671 nm indicating that there was a higher proportion of chlorosomes retained. In figure 3.3 B both DDM (red) and DM (green) had a large peak about 671nm indicating that as well as the RC a large portion of chlorosomes were being solubilised, as this peak at 671nm was indicative of the bacteriochlorophyll c within the chlorosomes. This was not a huge issue as the RC is His-tagged and could easily be purified. MNG-3 and LDAO proved not to be the best at solubilising the membranes of *C. tepidum*. This was measured quantitatively by comparing the ratios of the 671 nm peak (Bchl c from Chlorosomes) with the 808 nm peak (Bchl a from RC), this showed that the 671:808 nm for LDAO was 120:1, for DM it was 2:1 and for DDM it was 1:1.  $\beta$ -OG, however was the best at solubilising, as observed in the absorbance values at 808 nm in figure 3.3 B (black line), not only had it retained more of the 808 nm peak but also had less chlorosomes (671 nm):FMO-RC (808 nm), which was 1:3.

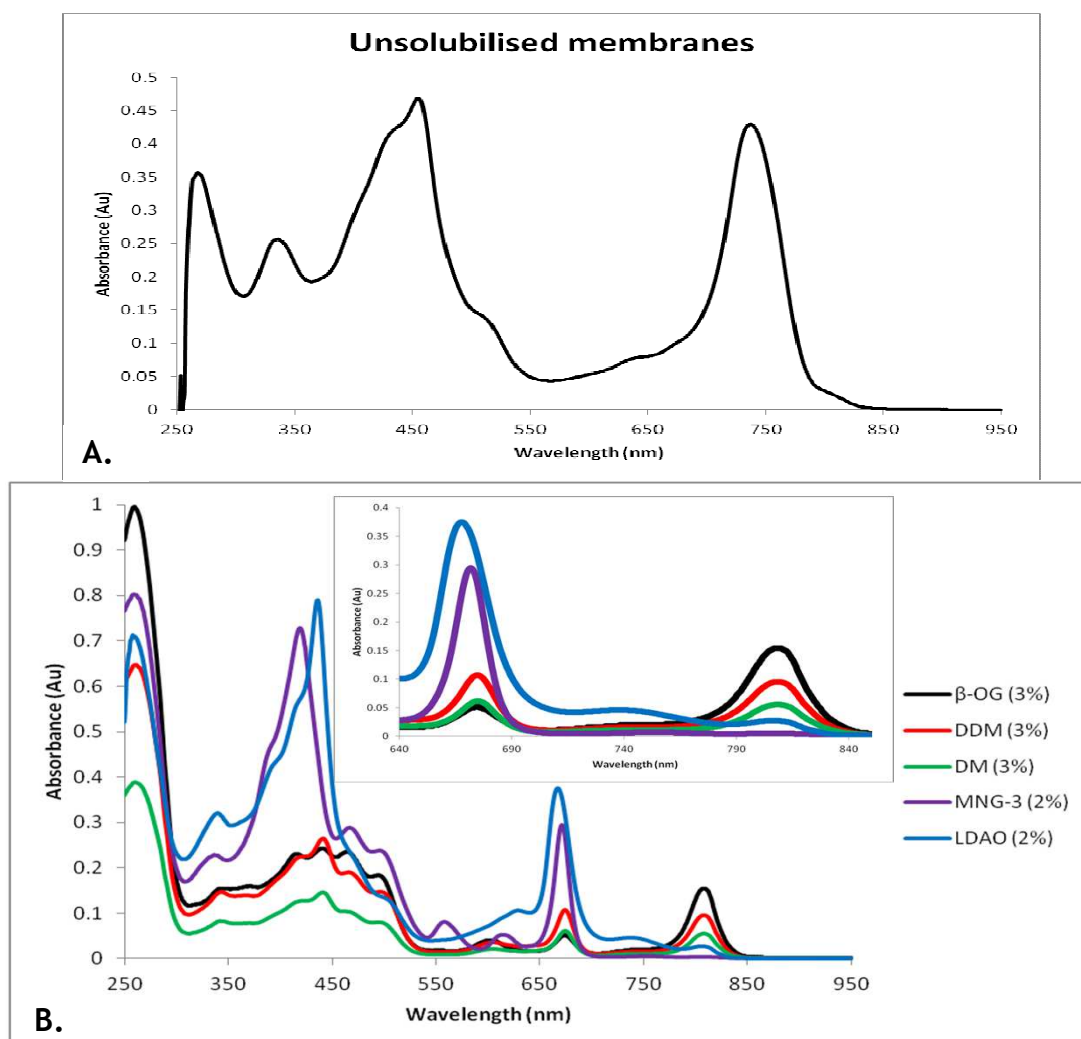


**Figure 3.3 Absorption spectra of RC membranes before and after solubilisation.**

**A.** Shows the spectrum of the unsolubilised membranes of the *C. tepidum*. **B.** Solubilisation with five different detergents;  $\beta$ -OG, DDM, DM, MNG-3 and LDAO.  $\beta$ -OG, DDM and DM successfully solubilised the membranes.  $\beta$ -OG was the best, which is indicative of the 808 nm peak observed in all three spectra showing the Bchl a.

### 3.3.1 Detergent selection for solubilisation and purification

$\beta$ -OG, DDM and DM successfully solubilised the RC out of its native membrane. These three detergents were used to carry out a test solubilisation and nickel purification of the *C. tepidum* RC. Three aliquots of 10 ml of membranes (5 mg/ml) were solubilised in with each one of the above detergents at room temperature for 2 hours in the dark. After subjecting each of the solubilised membranes to a high speed centrifugation at 110,000 x g for 1 hour the supernatant was taken and passed over a nickel column, as described in section 2.4.4.2. The RC had been passed over the nickel column three times to assure that the RC had bound to the nickel, on the final pass over the flow through was collected for all three samples and had its absorbance measured (Figure 3.4). The flow through samples, in figure 3.4 (blue lines), in all three of the solubilised samples show a small peak at around 808 nm, this is indicative of free FMO. It was also noted that in the flow through samples the peaks at 671 nm for DDM and DM were much bigger than the  $\beta$ -OG peak. This was, as stated earlier (section 3.1.1), when solubilising with DDM and DM there are more chlorosomes retained, so as the samples are passed over the nickel column the chlorosomes do not bind and are retained in the flow through. All three nickel columns were then subjected to a nickel wash with the appropriate detergents in 50 mM Tris-HCl pH 8.0, 300 mM NaCl, 20 mM imidazole. The samples were collected and its absorbance measured as indicated in figure 3.4 (red line), which showed a peak at 808 nm in all three samples indicative of FMO, either free or unspecifically bound to the column. All three nickel columns were then eluted with the appropriate detergents in 50 mM Tris-HCl pH 8.0, 300 mM NaCl, and 300 mM imidazole. After measuring the absorbance for all three of the eluted samples it was clearly observed that there was the presence of the 816 nm peak in all three peaks (Figure 3.4 green line), with a shoulder on the left hand side at 808 nm and a shoulder on the right hand side of the 816 nm peak measured at 837 nm, belonging to the special pair of the RC. It was also evident, based on the absorbance values, in figure 3.4 B (green lines), that DDM and DM had retained the same amount of RC when measuring the absorbance at 816 nm, which was 0.25. Whereas  $\beta$ -OG had retained more of the RC as it had two times as much at 816 nm in comparison to DDM and DM, which was 0.5, as observed in elution absorbance spectra in figure 3.4 B (green line) of  $\beta$ -OG.

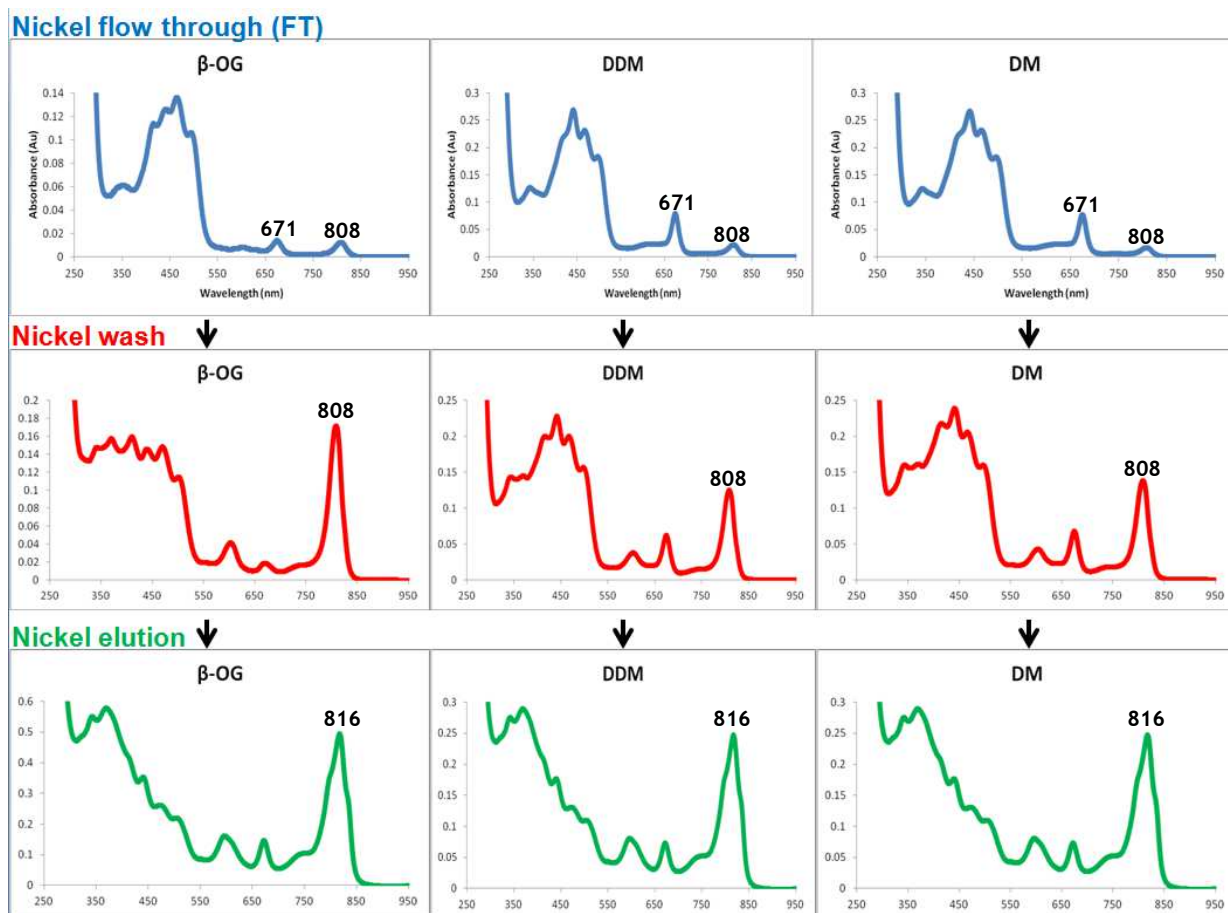


**Figure 3.4 Absorption spectrum of RC membranes at each stage of the nickel purification.** Solubilised and purified in three different detergents;  $\beta$ -OG, DDM and DM. The RC was successfully purified in all three detergents, this could be observed by the characteristic peak of the *C. tepidum* RC in the Nickel elution spectra above (green).  $\beta$ -OG proved to be the best at solubilising the RC out of its native membranes as it retained more RC, the was measured by the absorbance.

Deciding on which detergent to use was not only based on which solubilises the RC the best, but also to ensure that the RC is able to maintain its stability and monodispersity in which ever detergent it resides in. Even though there were three detergents identified that the protein could be solubilised and purified in, both  $\beta$ -OG and DM proved to be not compatible with the RC. After the nickel purification stage, within 8-12 hours the RC, in both  $\beta$ -OG and DM started to precipitate. It was observed that since the prep prepared in  $\beta$ -OG and DM was turbid that something had precipitated, this was confirmed when the absorption spectra was measured (Figure 3.5 green) of the RC purified in  $\beta$ -OG and DM after 12 hours. It was clearly seen by the absorption, in figure 3.5 green line, that there is an incline in absorption going from 950-250 nm, this is due to light not being able to pass through the sample when measuring the absorption. By taking each of the precipitated samples and centrifuging it, separating the pellet from

the supernatant, I was able to obtain the spectra of each of the clear supernatant and the pellet, which was re-suspended in buffer (Figure 3.5 black and red). It was evident that the precipitate was the RC as the pellet was green, and when the pellet were re-suspended in a 20 mM Tris pH 8, 150 mM NaCl and 0.01% DDM buffer, by measuring the absorption of the pellet it could be seen that the RC had precipitated as seen in figure 3.5 (black line). The absorption spectra contained the 816 nm peak with a shoulder on the left hand side at 808 nm, and a shoulder on the right at 837 nm indicative of the RC spectra. The supernatant, from the centrifuged samples, were also taken and had their absorption spectra measured (Figure 3.5 red line). The absorption spectra showed the RC peak that was left un-precipitated, there was also a decrease in absorbance of the RC, and there was no longer an incline in this sample from 950-250 nm. From this it was evident that a lot of sample had precipitated, as observed in the decrease in absorbance. And even though the RC in the supernatant was stable more of the sample began to precipitate within the next hour.

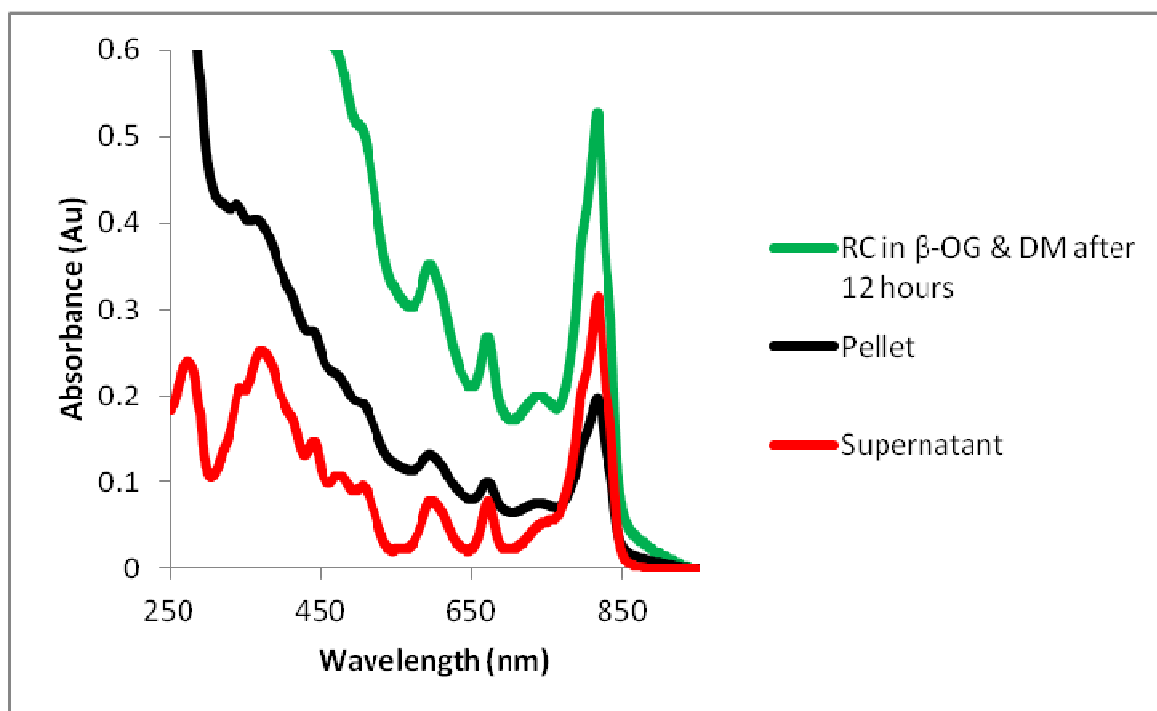


**Figure 3.5 Absorption Spectra comparing the RC before and after precipitation**

Absorption spectra showing the RC in both  $\beta$ -OG and DM after the nickel purification (green). 8-12 hours later the precipitate pellet (black) and supernatant (red) were separated, to show that the precipitate was in fact the RC.

The conclusions from the small scale solubilisation and nickel purifications of the RC revealed, by measuring the absorption, that  $\beta$ -OG solubilised the best (Figure

3.4). This was clearly shown as the *C. tepidum* membranes solubilised in  $\beta$ -OG retained more of the RC, as compared with DDM and DM. DM can also solubilise the RC but along with  $\beta$ -OG causes the RC to precipitate out in the later purification stages (Figure 3.5). DDM solubilises just as well as DM but has a longer alkyl chain (12 chained detergent) and does not precipitate. All three detergents showed that the RC could be purified successfully, but further optimisation was required.

It was concluded that two detergents would be optimal for the *C. tepidum* RC. The choice of detergent to solubilise was  $\beta$ -OG as it proved to be the most effective, but during the nickel purification stages the RC was detergent exchanged during the wash step in to DDM for stability purposes.

### **3.4 Large scale purification of the His-tagged RC complex**

A crude fraction containing the RC complex was obtained after extraction with  $\beta$ -OG from chlorosome-containing membranes of the *recA::HisAB-aacC1* strain, followed by its isolation using a  $\text{Ni}^{2+}$  affinity chromatography, as described in experimental procedures (Section 2.4.4.2). As expected, dark green material was adsorbed onto the  $\text{Ni}^{2+}$  immobilized resin (Figure 3.6). The column was then washed with 50 mM Tris-HCl pH 8.0, 300 mM NaCl, 20 mM imidazole, and 0.1% DDM, in order to remove any non-specifically weakly bound components. The RC was then eluted by increasing the concentration of imidazole to 300 mM keeping the rest of the buffer the same. The elute contained the major polypeptides of the green sulphur bacterial RC [57], that is, PscA (55 kDa), PscB (23 kDa), PscC (23 kDa), PscD (17 kDa), and the water soluble protein FMO (43 kDa). No band corresponding in the apparent molecular mass to the PscB appeared to be observed, when ran on a 4-12 % SDS-page gel stained with commasie blue (Figure 3.7, elution lane), this is due to the PscB (iron sulphur protein) readily being oxidised. PscB also runs as a diffuse band, therefore, not running at the correct molecular weight on the SDS-page gel. Further purification step by a gel filtration chromatography with Sepharose S-200 revealed that these polypeptides were co-eluted from the column and formed a stable complex as the His-tagged RC complex. The His-tagged RC complex was successfully expressed in the

*recA::(HisAB-aacC1)* strain and could be obtained in a single step as well as considerably high purity by a Nickel chromatography. Since the RC is coloured, at each stage of the purification it is easy to follow by eye (Figure 3.6).

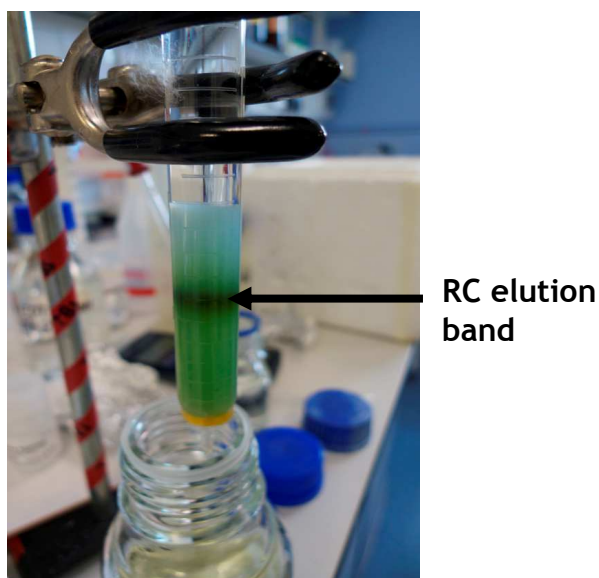


**Figure 3.6 observation of the RC band during nickel purification.**

A dark green band can clearly be seen being eluted off, after the wash. Indicating the His-tagged RC had successfully been bound and eluted at appropriate imidazole concentrations.

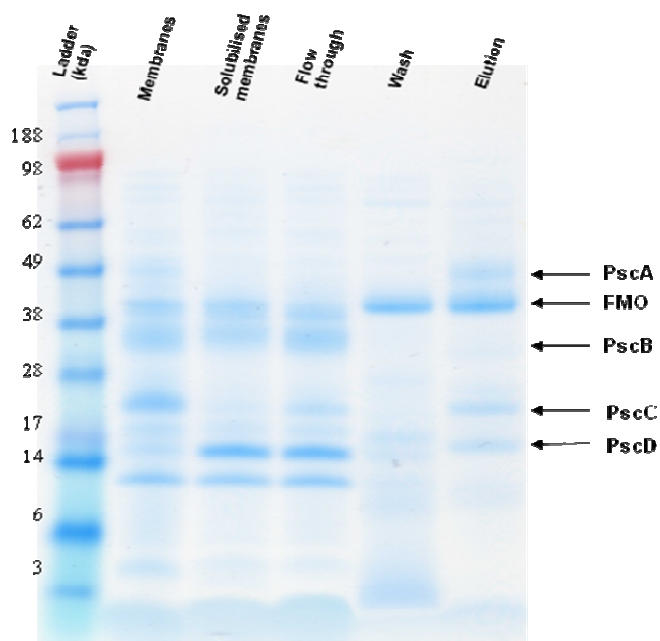


**Figure 3.7 Protein gel of *C. tepidum* RC at each stage of the solubilisation and Nickel purification**

4-12% SDS-page gel of *C. tepidum*. Solubilised membranes in  $\beta$ -OG and detergent exchanged into DDM during Nickel purification (**Wash** step). **Wash** lane shows the free FMO that is eluted of the nickel column. **Elution** lane shows the major polypeptides of the green sulphur RC, PscA (55 kDa), PscB (23 kDa), PscC (23 kDa), PscD (17 kDa), and FMO (43 kDa). PscB, is readily oxidised when prepared and is very hard to see when stained with commasie. PscB also runs as a diffuse band depending on the prep it can run anywhere between 25-40 kDa.

At each stage of the purification the absorption spectra were measured to confirm the presence of the RC (Figure 3.8). The solubilisation spectra in figure 3.8 (red line) shows the peak at 808 nm, which is indicative of the FMO and the RC. The Nickel wash (Figure 3.8, blue line) shows the 808 nm peak belonging to the free FMO not bound to the nickel column. The elution (Figure 3.8 brown line) showed three major peaks at 816, 671, and 601nm in the absorption spectrum, which were attributed to characteristic Q bands of BChl *a* and Chl *a* in green sulphur bacterial RC complex. The shoulder around 835 nm, which was ascribable to a specific absorption for a special dimer of BChl *a* molecules (P840) in the RC core protein, was also observed (Figure 3.8, brown line). The wash step allowed for the RC to be detergent exchanged in to DDM from  $\beta$ -OG, this kept the protein monodisperse long enough for the rest of the purification process as well as retaining its stability to allow for structural and biophysical characterisation.

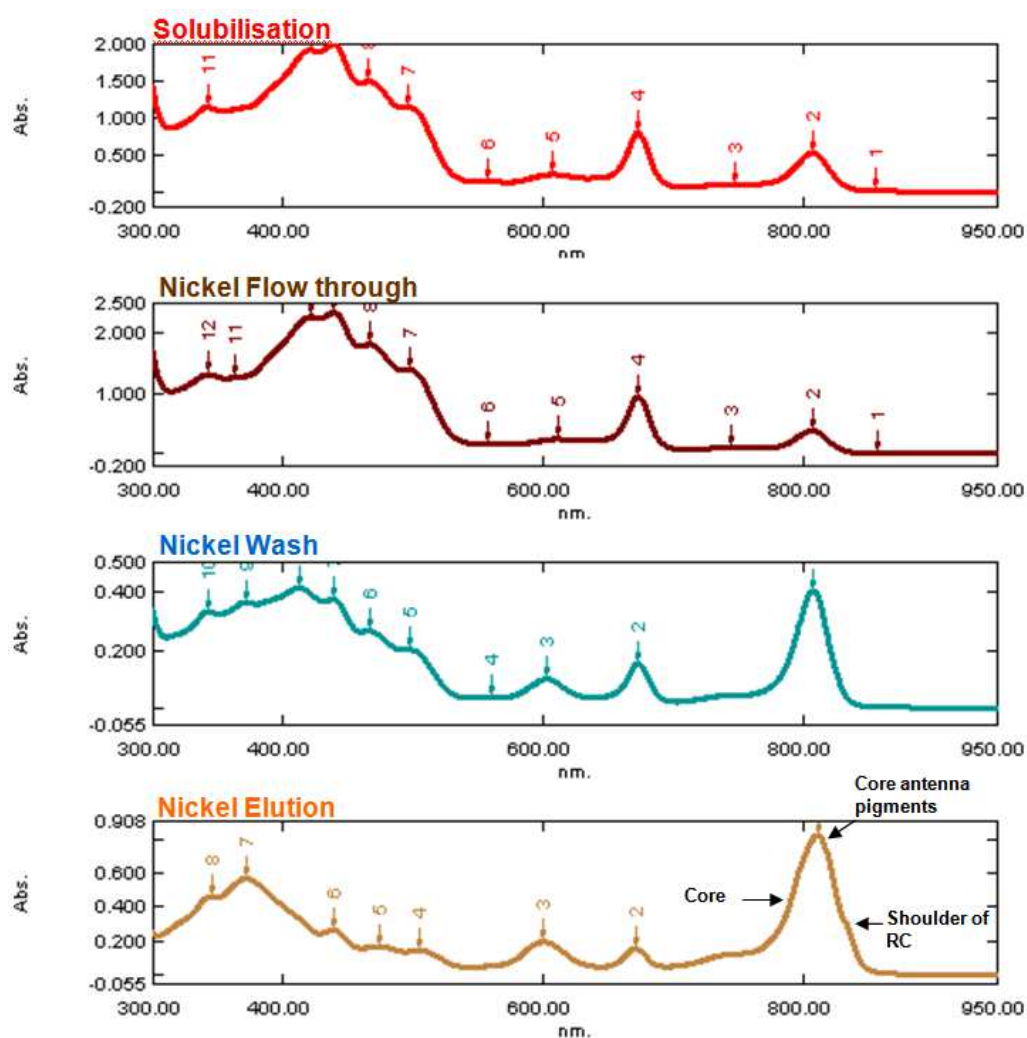


**Figure 3.8 Absorption spectrum of RC after nickel purification.**

RC and at each stage of the nickel purification. Spectrum of the nickel elution peak at around 816 nm is characteristic of the RC. Major peaks can be observed at 815, 671 and 601nm.

### 3.5 SEC purification and detection of the RC by silver staining

After the elution of the RC from the nickel column, the RC was concentrated and passed over the size exclusion column (as stated in section 2.4.4.4). By passing the RC over the Sepharose S-200 column it allowed pure RC to be obtained and to have any free pigments removed. Figure 3.9 revealed a sharp monodisperse peak that comes off at around 60mls corresponding to the RC.

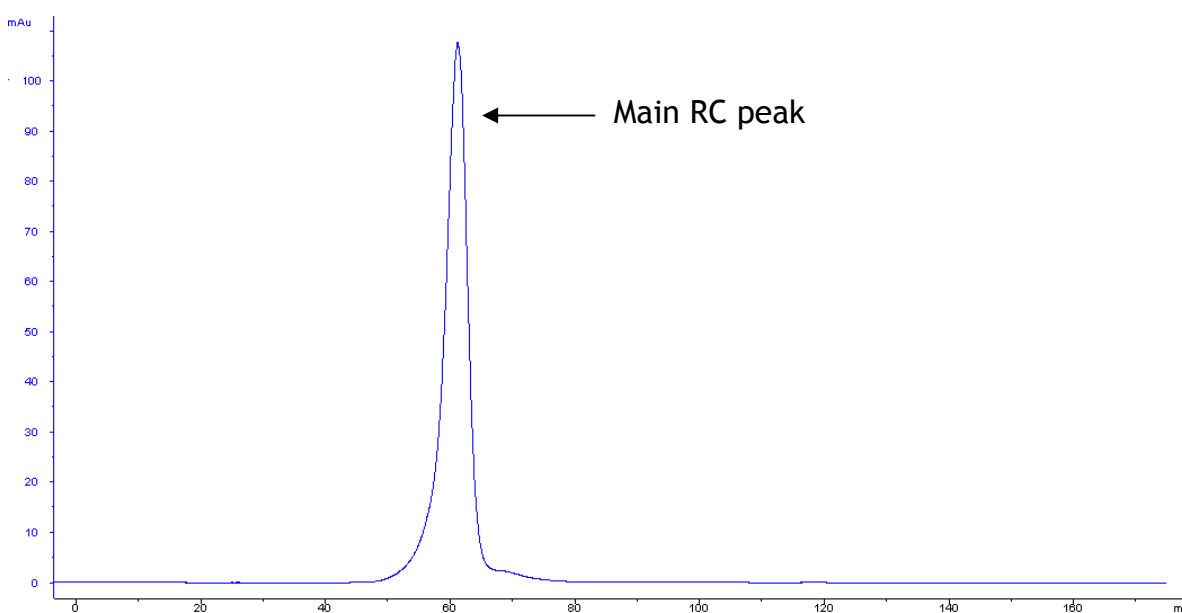


**Figure 3.9 SEC profile of *C. tepidum* RC on a Sepharose S-200 column**

Main RC peaks comes off at around 60mls, any peaks that come off after are either small protein contaminants or free pigments

Fractions were taken over this peak and analysed, both by absorption spectrophotometry and by SDS-page gel. The fractions which contained the unique absorption spectra of the RC were pooled and concentrated. A clear difference was observed in the RC peaks for the before and after purification (Figure 3.10). Figure 3.10 shows the *C. tepidum* RC before the Nickel purification (red line) with peaks at around 808 nm containing both the FMO and the RC. After the Nickel and SEC purification (Figure 3.10, purple line) the RC absorption spectrum showed the Characteristic absorption bands of RC BChl a are the Q<sub>y</sub> transition band at ca. 816 nm, the Q<sub>x</sub> transition band ca 610 nm and the Soret band at ca. 370 nm. The presence of the 816 nm peak was also present (Figure 3.10, purple line), with a shoulder on the left hand side at 808 nm and a

shoulder on the right hand side of the 816 nm peak measured at 837 nm, belonging to the special pair of the RC.

At each stage of the solubilisation and purification samples were kept and put aside to test that pure RC was obtained after the purification steps. This was confirmed by running the pure RC was run on a 4-12% silver stained SDS-page gel (Figure 3.11), showing the four major polypeptides of the RC PscA-D and the water soluble protein FMO. The PscB protein, as stated earlier, runs as a diffuse band on the SDS-page gel (between 25-40 kDa depending on prep).

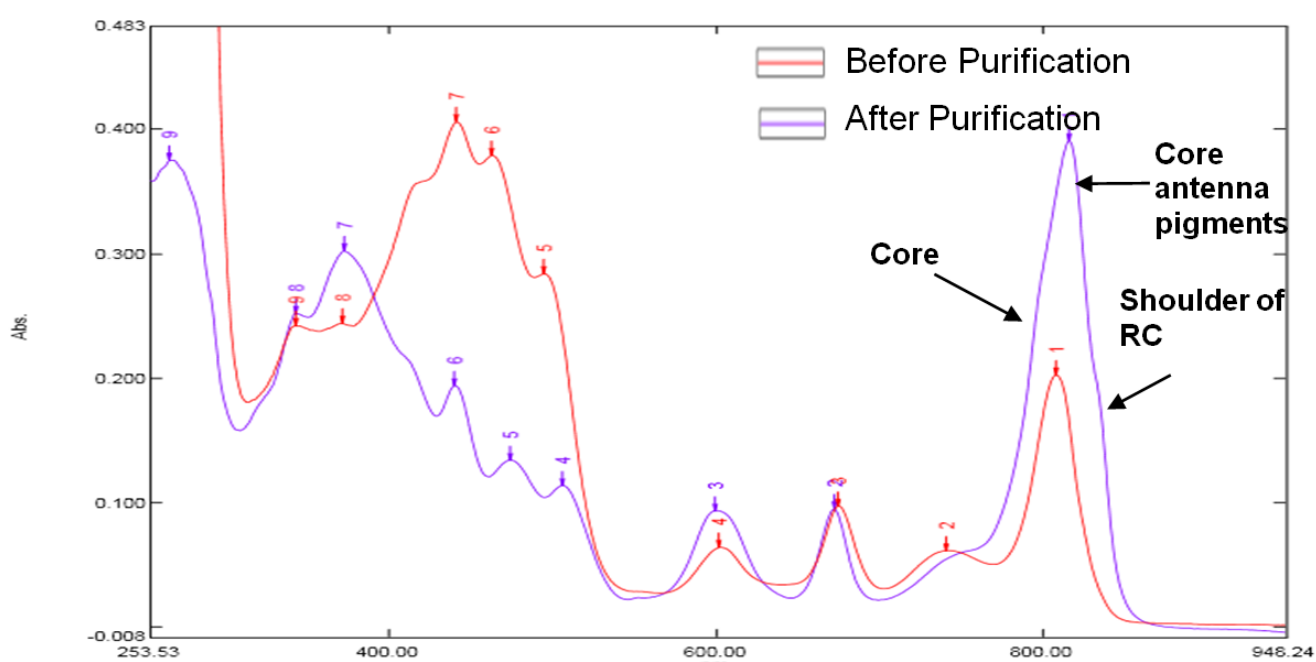


**Figure 3.10 Absorbance spectrum of before and after purification of the RC. Were the distinct features of the RC are observed.**

The after purification spectra (blue line) shows the 340, 370, 603 and 816 nm, the characteristic absorption bands of BChl *a*, and additionally, the shoulder at 837 nm indicating the primary donor, are seen

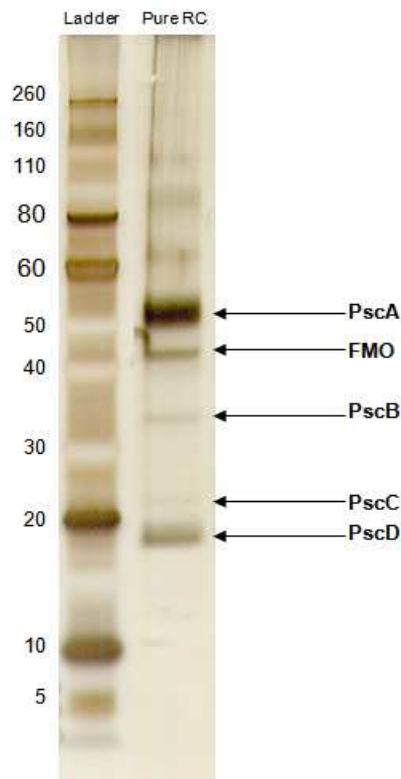


**Figure 3.11 Silver stained gel of pure RC.**

Pure RC lane shows the four major polypeptides, and the water soluble FMO protein, which is associated with the *C. tepidum* RC. PscA (55 kDa), PscB (23 kDa), PscC (23 kDa), PscD (17 kDa), and FMO (43 kDa). PscB runs as a diffuse band anywhere between 25-40 kDa depending on the prep. The bands above the PscA are SDS induced oligomerizations of PscA.

### 3.6 Discovery of RC heterogeneity:

The FMO protein has been shown to be attached to the RC by scanning transmission microscopy and lately by the Blankenship group by cross-linking FMO to the RC [161-162]. As discussed in the Introduction the FMO protein helps mediate energy from the chlorosome to the RC, and the FMO protein itself is well characterized. One of the issues when studying the *C. tepidum* RC is working out how many FMO molecules there are attached to one RC molecule. Robert E. Blankenship [162], Georgios Tsiotis [163] and Günter Haüska [164] have reported 1, 2 or 3 FMO trimers attached per RC, and this proves to be an issue, as will be discussed in this section. The group of Günter Haüska has also reported an active RC core free of FMO [164].

### 3.6.1 Determining RC protein concentration by Amido black assay

For any structural characterisations a known protein concentration of the RC would be required. One of the issues in measuring the concentration of the RC is that since the RC is from a photosynthetic organism a lot of the assays are not compatible as the pigments associated with the RC tend to absorb at the wavelength that most assays measure at. Choosing a protein assay is usually based on convenience, availability of protein for assay, presence or absence of interfering agents, and need for accuracy. The Lowry assay is very sensitive but requires a minimum of 40 minutes of incubation time, but has major interfering agents with the assay such as acids or ammonium sulphate [165-166]. The Bradford assay is more sensitive and can be read within 5 minutes, however proteins with low Arg content will be underestimated, and unlike the Lowry assay has no agents that interfere with the assay [167]. The sensitivity of colorimetric assays to individual proteins tends to differ drastically as different proteins have different amino acid compositions. To allow for a working concentration to be obtained for the RC the amido black assay was utilised as it proved to work best on the RC. Due to the RC being thermophilic the Lowry, Bradford and BCA assays all kept the RC pigments intact, therefore interfering with the absorbance when the concentrations were measured. The Amido Black assay is based on precipitating proteins as insoluble dye complexes with acidic, methanolic amido black solution [168]. The use of trichloroacetic acid (TCA) to precipitate proteins permits removal by filtration of interfering substances in the various sample preparations; these include detergents, dyes, reducing agents, and pigments [169]. By plotting a standard curve of BSA a working concentration of the RC was worked out and correlated back to the 816 nm absorption peak (Figure 3.12). It was worked out that at around an OD of 9 at 816 nm equated to 1 mg of protein in a final volume of 1 ml (Table 4), and to obtain this anywhere between 35-40 litres would have to be grown. Therefore, on average anywhere between 75-120 litres of cells were continuously grown, prepped and purified all at the same time to carry out any structural or biophysical techniques.

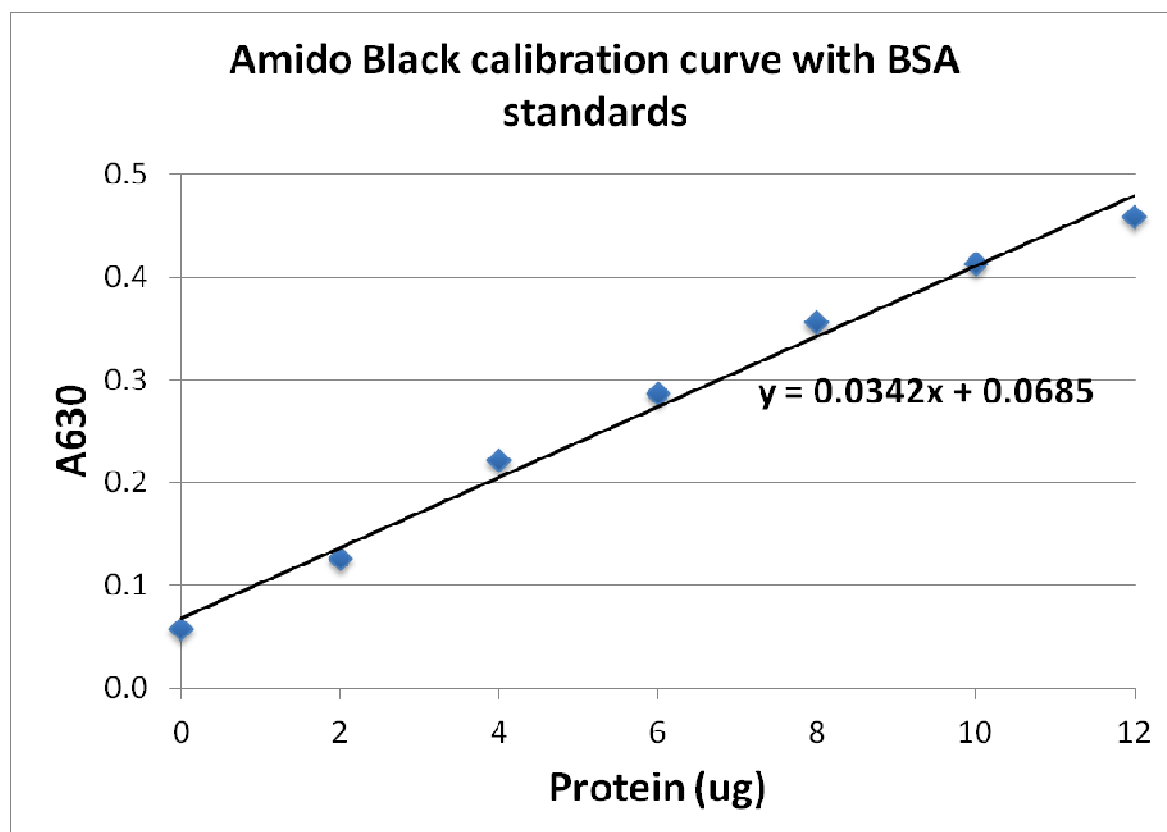


**Figure 3.12 Amido Black calibration curve using BSA standards.**

BSA standards were prepared (0, 2, 6, 8, 10, 12  $\mu\text{g}$ ) using the amido black assay protocol and plotted to obtain a calibration curve to allow for us to obtain concentrations of proteins by using this method.

#### ***C. tepidum* RC – A816 = 9**

Sample added in each well ( $\mu\text{l}$ )	RC sample 1	RC sample 2	Average	Protein ( $\mu\text{g}$ )	[protein] (mg/ml)	Volume (ml)	Total Protein (mg)
40	0.335	0.341	0.338	7.9	0.99	1	1.0

**Table 4 Concentration of purified *C. tepidum* RC obtained by the amido black assay and worked out based on the calibration curve obtained in figure 3.12.**

### **3.6.2 Discovery and separation of the two different populations of FMO-RC by SEC and Sucrose Gradients**

By growing and purifying the RC from 75-120 litres of cells allowed enough RC to be obtained for any biophysical and structural characterisation. The first prep, from 75-120 litres of cells, when passed over the SEC showed a peak at around 60 mls (Figure 3.13,  $V_e$  (elution volume)), with a shoulder on the left hand side of the peak (Figure 3.13). The peak at 60 mls and the shoulder were both pigmented green and had the unique absorption spectrum of the *C. tepidum* RC. Any aggregated protein came off at around 45 mls (Figure 3.13,  $V_o$  (void)). And any free pigments or smaller protein contaminants came off at around 80-90mls (Figure 3.13)

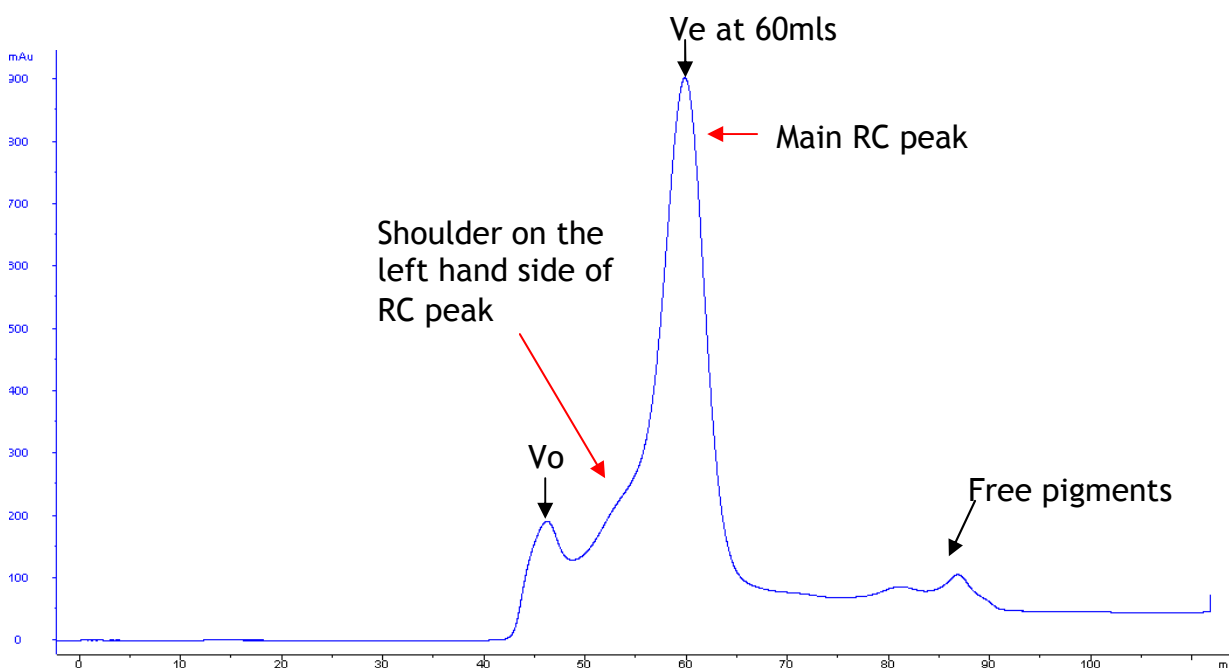


**Figure 3.13 UV absorbance of the *C. tepidum* RC grown from 75-120 litres of cells.**

SEC profile showing the elution volume ( $V_e$ ) of the main RC peak at around 60mls, and the shoulder on the left hand side of the peak, which is at around 55mls.  $V_o$  (void volume) shows any aggregated proteins.

It was originally thought that since the RC concentration was increased so drastically by prepping such large volumes of cells that when the RC, after nickel purification was concentrated to micro litre volumes the protein was being driven towards aggregation, hence why the shoulder was so close to the void. By measuring each of the fractions absorption from 50-65mls it was observed, in figure 3.14, that all the peak fractions had the unique absorption spectra belonging to the RC, but there was a slight shift in the 816 nm (absorption maxima of the *C. tepidum* RC) region of the RC, going from 50-60mls (Figure 3.14). Figure 3.14 shows the absorption spectra of selected fractions covering the main peak observed in figure 3.13 and the shoulder (Fraction 15-24). Fraction 15 in figure 3.14 shows the absorption maxima of the RC to be at around 812 nm (as marked by the red line in Figure 3.14). As each of the fractions are measured, going from fraction 15-24, there is a gradual shift in this peak until the main peak observed in the SEC profile (figure 3.13) is reached where the absorption maxima is measured at around 816 nm (marked by the black line in figure 3.14). Therefore, it was hypothesised that the RC was not aggregating but instead there were two different populations of the RC with different amounts of FMO attached to each. By comparing the 800:816 nm ratio (800 nm region being the shoulder of the FMO) it was establish which fractions

either had more or less FMO. It was concluded that the shoulder on the left hand side of the main RC peak, observed in figure 3.13, contained more FMO trimers attached to the RC as the absorption was closer to the absorption maxima of FMO. And the main RC peak, observed in figure 3.13 (peak at 60mls), contained less FMO as it was closer to the 816 nm absorption. As the peaks in the SEC profiles (Figure 3.13) were overlapped both peaks contained a mixed population of FMO-RC.

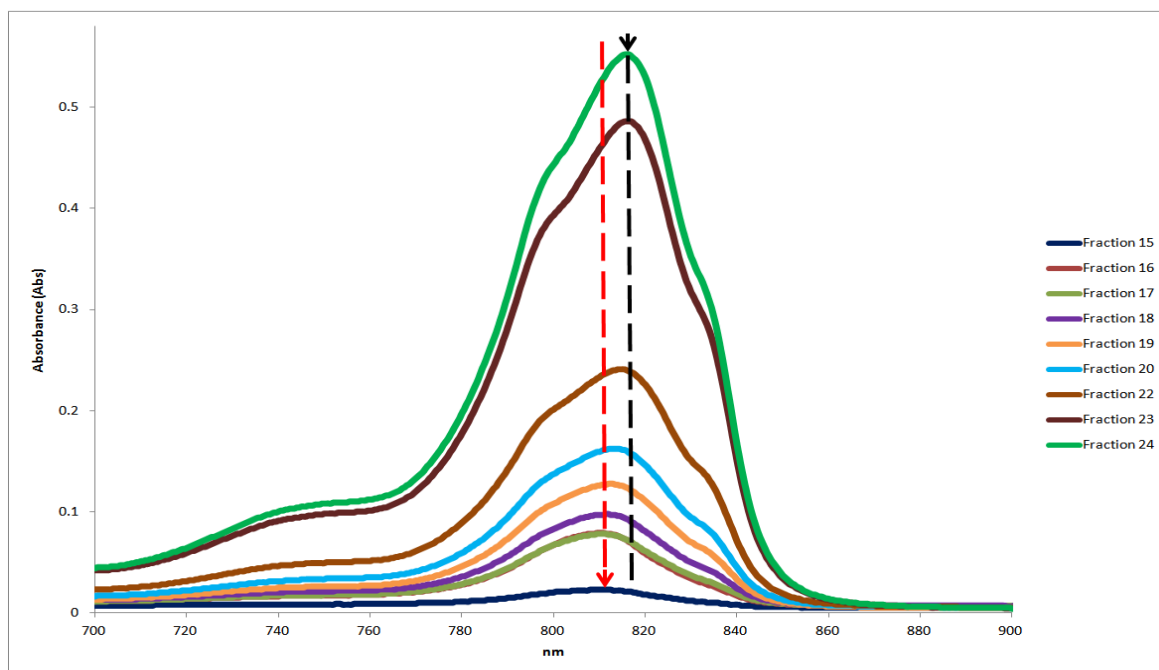


**Figure 3.14 Absorption spectra of fractions taken from SEC profile.**

Absorption spectra of the fractions (Figure 3.10), fractions taken from 55-65mls (Fractions 15-24), which covered both the main RC peak and the shoulder. Red arrow shows were the spectra of where the shoulder of the RC starts from (closer to 808 nm, which is the absorption maxima of the FMO), and the black arrow shows as we go along the fractions (the SEC profile) there is a shift from 808 to 816 nm.

In the hope to obtain a better, more homogeneous RC sample, sucrose gradients were run (as stated in methods and materials). The above SEC sample (Figure 3.13, 55-65mls) of the RC was pooled and concentrated to run on sucrose gradients. Initially a 15-50 % continuous sucrose gradient was prepared with 20 mM Tris pH 8 and 0.01% DDM (Figure 3.15, i) this showed two bands. The first band was the free pigments (**A**) and the second band was of the two different populations of FMO-RC (**B + C**), which could not be separated due to the difference in the gradient being so high. Figure 3.15 ii shows the RC run on the sucrose gradient from 20-45 %. As well as the free pigments (**A**) the two different populations of FMO-RC are observed, represented by (**B**) and (**C**) in figure 3.15 ii. In an attempt to get better separation of the two different

populations of FMO-RC, the RC was run on a 30-45 % sucrose gradient (Figure 3.15 iii). This showed three bands, the free pigments (A), which were much tightly packed than compared to the 15-50 % and the 20-25 % gradients that were run. The two populations of FMO-RC were still present in the 30-35 % gradients, shown in figure 3.15 iii (bands (B) and (C)), but still had to be optimised due to the separation not being sufficient enough.

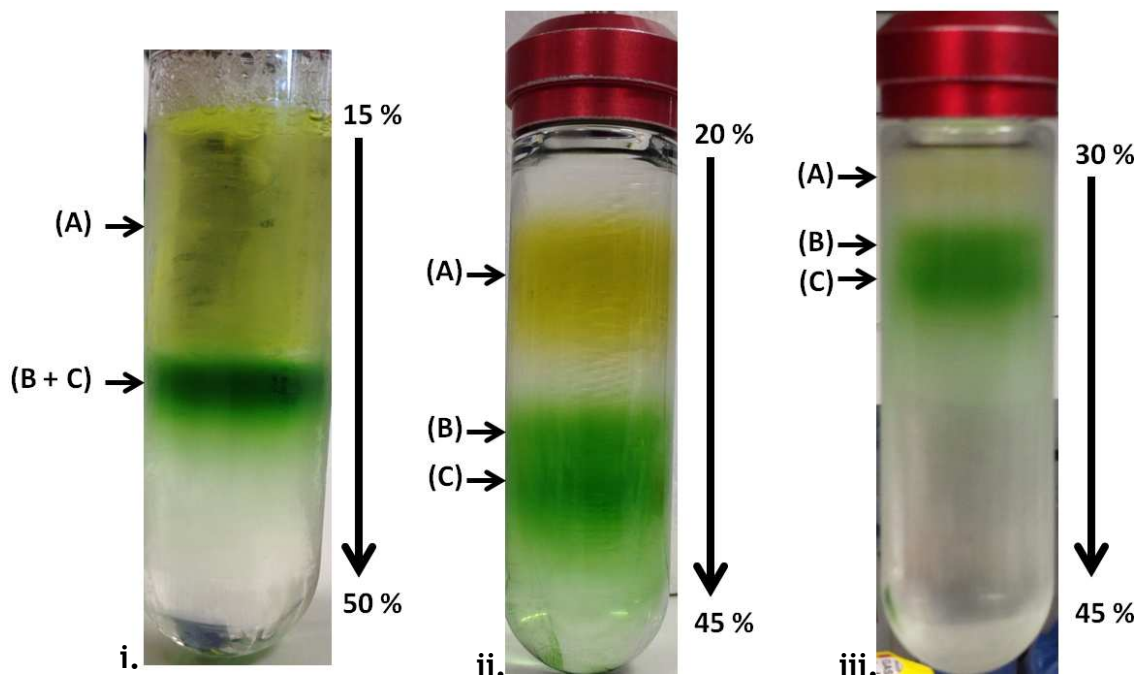


**Figure 3.15 Test sucrose gradients for the identification of the different populations of FMO-RC.**

Three continuous sucrose gradients centrifuged O/N at 110,000 x g for 12 hours (A) represents the free pigments, (B) and (C) are the two different populations of FMO-RC in all three sucrose gradients. i. Shows the RC sucrose gradient run O/N on a 15-20 % gradient, the two different populations of FMO-RC are merged together. ii. Shows the RC run on a 20-45 % continuous gradient were the two different populations of the FMO-RC have become visible. iii. Shows the RC run on a 30-45 % sucrose gradient, in the attempt to get better separation of the two different populations of FMO-RC.

After identifying the percentage of sucrose gradient (30-35 %) to separate these two populations, the FMO-RC was successfully separated. The sample was run O/N yielding three bands (Figure 3.16), one yellow band which contains the free pigments, and two green bands, which are both quite close together, but both containing the *C. tepidum* RC.

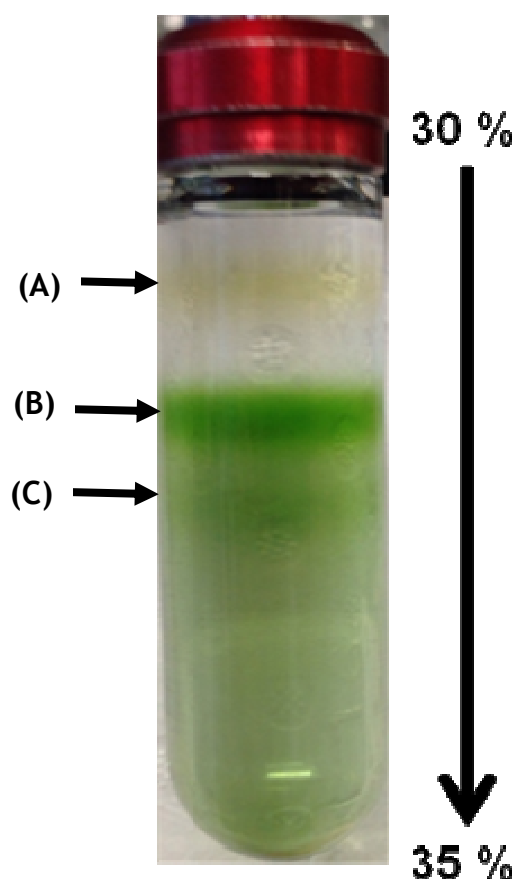


**Figure 3.16 Continuous (30-35%) Sucrose Density Gradients of the *C. tepidum* RC ran O/N.** The yellow band (A) shows the free pigments. The first, intense, green band (B) is the *C. tepidum* RC, as observed by its absorption. The less intense green band (C) is also the *C. tepidum* RC, as observed by its absorption. Both bands B and C have a different 808:816 nm difference.

All three bands from the sucrose gradients (Figure 3.16) had their absorption measured (Figure 3.17 A). The absorption of both green bands (B and C in figure 3.16) had the unique absorption characteristics of the *C. tepidum* RC but had different Ratios (800:816 nm) (Figure 3.17). It was clear on closer inspection of bands B and C that there was also a shift in the 816 nm region (Figure 3.17 B). The upper band (B in figure 3.12) had its absorption maxima at 818 nm (marked by the green line in figure 3.17 B) and had a much higher 800:816 ratio, which was 1:1.25. Whereas the lower band (C in figure 3.12), which was believed to have more FMO attached to the RC its absorption maxima was at around 814 nm (marked by the brown line in figure 3.17 B) the ratio of 800:816, 1:1.11. Due to both bands B and C being so close together on the gradients it proved to be difficult to obtain band C without any contamination from the upper RC band B. Whereas band B was obtained without any contamination from either the free

pigments (band A figure 3.12) or the lower RC band (Band C figure 3.12).

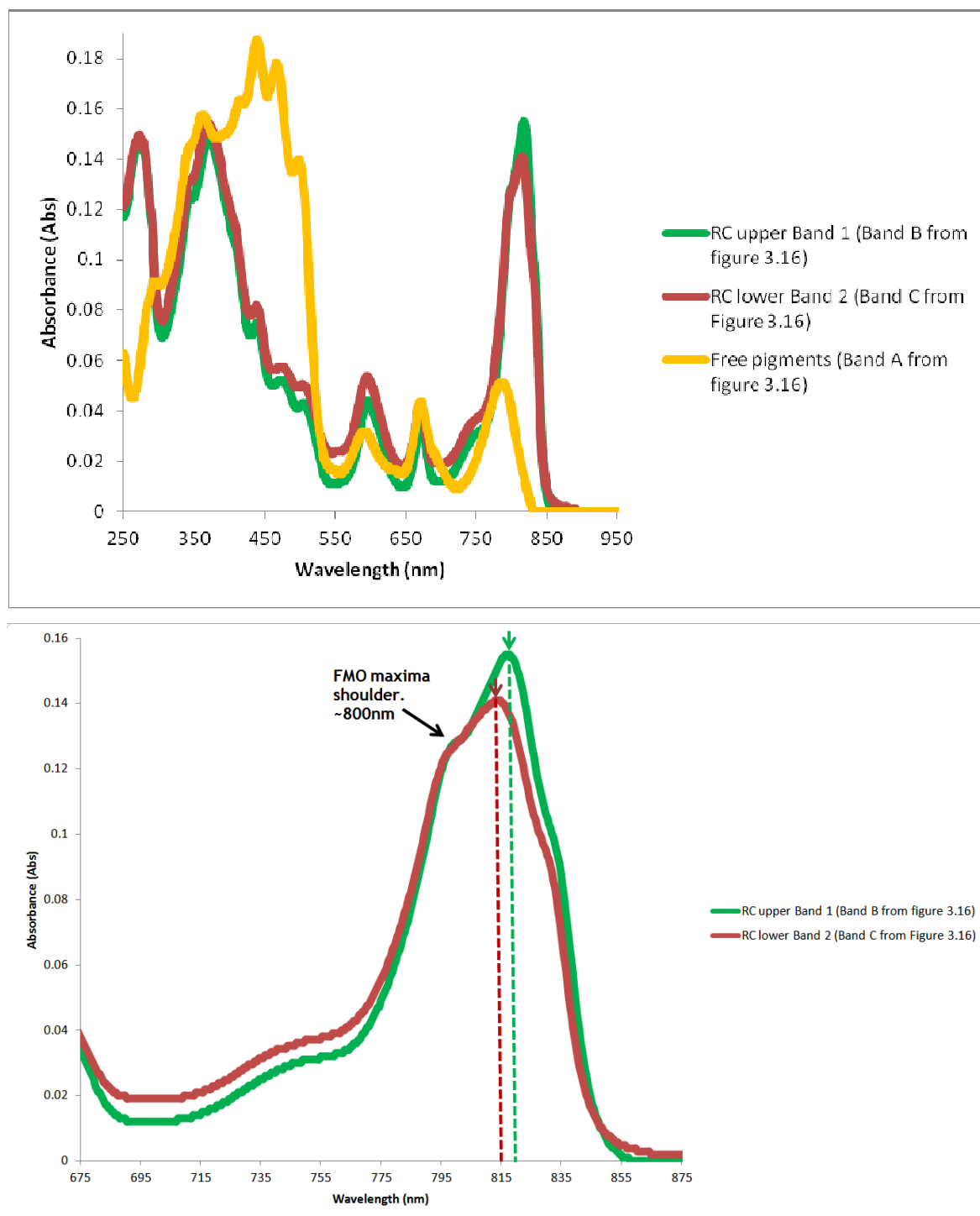


**Figure 3.17 Absorption spectra of the three bands obtained after sucrose density gradients were run.**

A. Shows the absorption spectra of the 3 bands obtained from the sucrose density gradient (Figure 3.12). The yellow shows the free pigments and the green and maroon shows the RC bands, both the upper and lower obtained from the sucrose gradients having the characteristic RC peak. B. Shows a closer look at both the upper and lower RC peak, it is clearly observed that there not only is a shift in the 816nm peak but also the 800:816 ratio in both peaks is different. The green arrow is showing the maxima of the upper RC band at around 818 nm, the maroon arrow is showing the maxima of the lower band at around 800 nm.

The top RC band (band B in figure 3.16) was gently taken off from the sucrose gradients and concentrated again to pass back over the SEC. This yielded a sharp monodispersed peak at around 60mls, with no shoulder (Figure 3.18 A). The absorbance of each of the SEC fractions was measured and it showed no difference in the 800:816 nm, the ratios were all 1:1.25. The bottom RC band was also taken off the sucrose gradients (B and B in figure 3.16) but with some contamination from the upper band and was passed down the SEC column (Figure 3.18 B). This yielded two peaks, a peak at around 60mls which was cross contamination from the upper RC band (band B) and a peak at around 55mls coming mainly from the lower RC band.

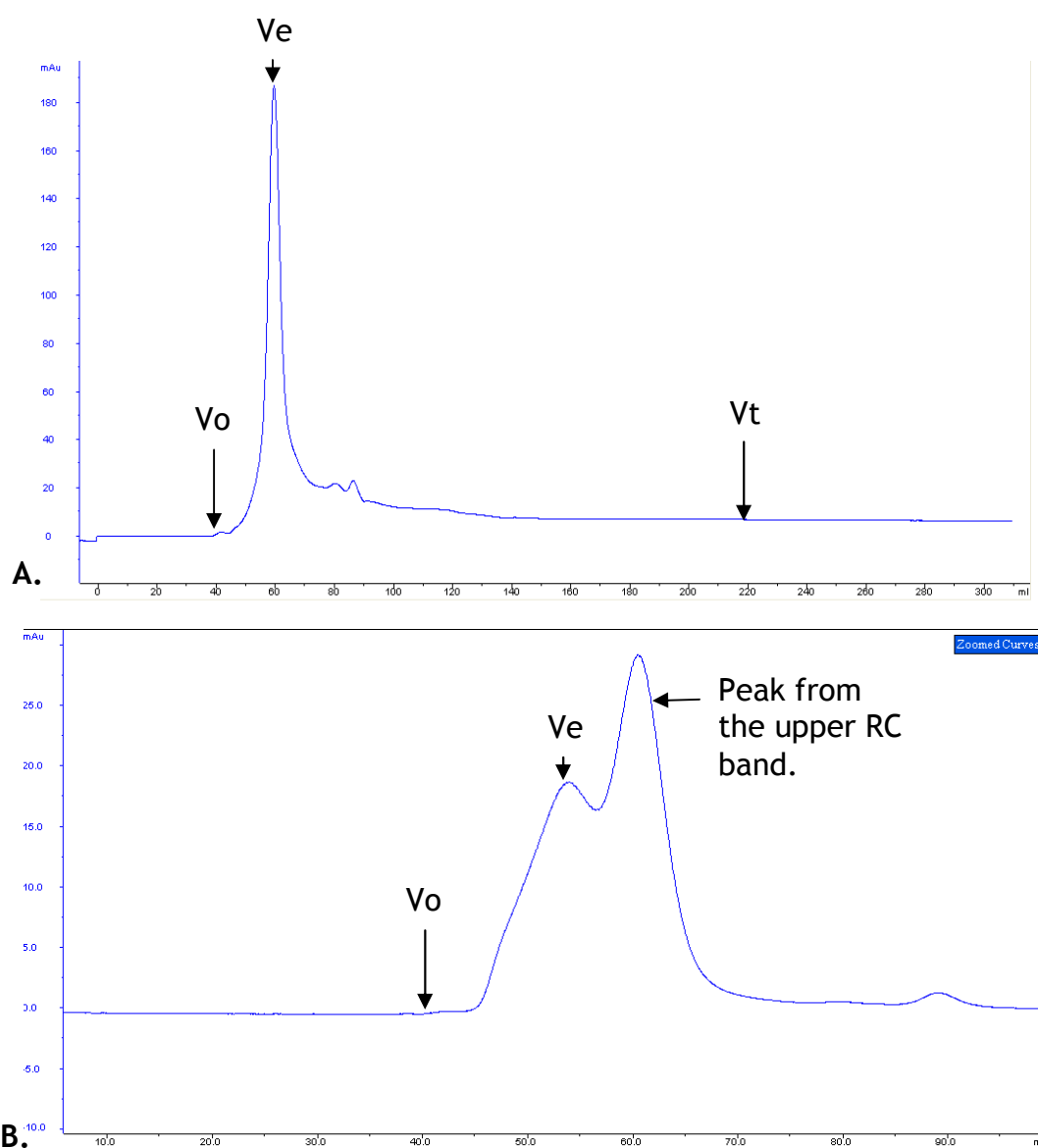


**Figure 3.18 SEC profiles of the upper and lower RC bands taken from sucrose gradients.** **A.** Shows the profile for the upper RC band taken from the sucrose gradient, the elution volume is at around 60mls with no shoulder on the left hand side. **B.** Shows the profile of the lower RC band, with some contamination from the upper band (60mls). The lower RC band comes off at around 55mls and is more distinct.

These experiments clearly showed that two different populations of FMO-RC were present within the sample, but could be separated. The conclusions were that the lower RC band from the sucrose gradients (B and C figure 3.16) had more FMO attached and therefore would be closer to the absorption maxima of FMO (at around 800 nm), this being true meant that this band, when passed over the SEC, should also come off sooner than the upper green band (Figure 3.16 B). The upper band (band B in figure 3.16) had less FMO attached to the RC and therefore would have an absorption maxima further away from the maxima of FMO, which was shown in figure 3.17 B), this being the case would also mean when passed over the SEC column the RC should come off later than the lower band, which was clearly seen in figure 3.18 A.

### **3.7 The effect of light on *C. tepidum* RC**

The whole purification process of the *C. tepidum* RC was carried out over a week and was done under dark conditions or under a green light. As important as light is for photosynthetic organisms to photosynthesis, light can have detrimental effects on photosynthetic proteins directly. The last parameter that was checked was the effect of light on *C. tepidum* RCs. Two samples of RC were left on a lab bench over the course of 8 weeks, one sample was left in darkness and the other under normal light conditions (Figure 3.19) at room temperature. As these are thermophilic reaction centres they can survive under high temperature conditions, room temperature did not have any detrimental effect on these RCs. Figure 3.18 A, shows the *C. tepidum* RC kept under darkness, after each week the absorption was measured. From the absorption there were no significant changes in the RC absorption over the 8 weeks, except for a slight decrease in absorbance, as would be expected of any protein which was left out at room temperature for over 8 weeks. Figure 3.19 shows the absorption of the RC left under normal light conditions. After the first week we can start to see significant changes to the absorption of the RC. Within 4 weeks the absorbance of the RC has nearly disappeared as the pigments are being destroyed due to the light. Figure 3.19 C clearly shows the loss of pigmentation of the RC under normal light conditions in comparison to the RC in darkness after 4 weeks.

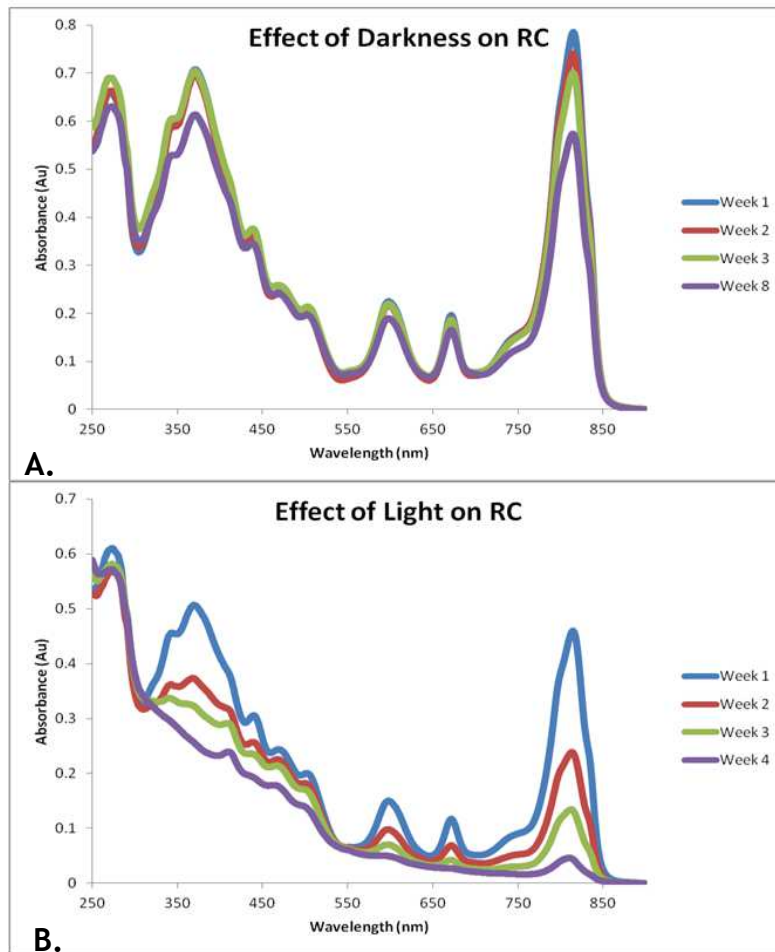


**Figure 3.19 Effect of Light on the *C. tepidum* RC.**

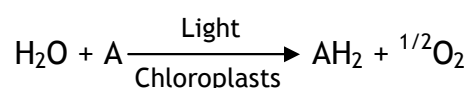
**A.** Shows the absorption spectrum of the *C. tepidum* RC under darkness over an 8 week period. It can be seen that there is not such a huge difference over the 8 weeks. **B.** Shows the RC under normal light conditions and it can clearly be seen that the RC completely falls apart within 4 weeks. **C.** The loss of pigmentation of the RC under normal light conditions in comparison to the RC in darkness after 4 weeks. The top picture shows RC in the light (eppendorf on the left hand side), and the RC kept in the dark (eppendorf on the right hand side covered in foil), the bottom panel shows the exposed RC that is no longer covered in foil, and a clear difference is observed when compared. The eppendorf on the left hand side has lost most of its pigmentation over 4 weeks whereas the right hand side still retains most of its pigments.

RC is clearly more stable under darkness, so it was concluded that the purification would be done under darkness and any other experiments involving the *C. tepidum* RC.

### 3.8 Assaying RC functionality and activity: Light induced oxygen consumption using a Clark-type electrode

Before doing experiments with a protein its integrity and full functionality have to be assayed. In the case of the photosynthetic RC from *C. tepidum*, functionality can be assayed as light-induced electron transport. This can be done by oxygen consumption using a Clarke-type electrode (as described in section 2.4.4.6).

In 1937, Robert Hill discovered that the illumination of isolated chloroplasts can generate oxygen as in the presence a suitable electron acceptor, even in the absence of carbon dioxide [170]. The Hill reaction can be formally defined as the reduction of an electron acceptor (A) by electrons and protons abstracted from water, under evolution of oxygen, when chloroplasts are exposed to light:



The final electron acceptor *in vivo* is NADP, while several artificial electrons acceptors can be used to study the Hill reaction *in vitro*.

To measure the activity of the *C. tepidum* RC Methyl Viologen ( $\text{MV}^{2+}$ ) was used to mediate reduction of dissolved oxygen. Here, oxygen is consumed at exactly the same overall rate as light-induced electron transfer through the RC. And since the activity of the isolated RC is being tested is also necessary to add an artificial electron donor to re-reduce its primary electron donor. Here we use reduced DCPIP as E-donor. Figure 3.18 A depicts that once the RC is added to the reaction medium as described in 2.4.4.6, no reaction will take place until a suitable donor (DCPIP reduced by the addition of ascorbate) and acceptor ( $\text{MV}^{2+}$ ) is also added, and on illumination the MV reduces the oxygen in turn recording the reduction of dissolved oxygen as seen in Figure 3.18 B. Dependant on how much RC is added to the reaction we can calculate the rate of reduced oxygen, in this case it is around  $-10 \mu\text{mol}/\text{ml}/\text{s}$  (red line in figure 3.20 B), calculated the rate from the devolution of oxygen. This can then be calculated as  $60 \text{ mmol O}_2/\text{h.mg BChl } a$ .

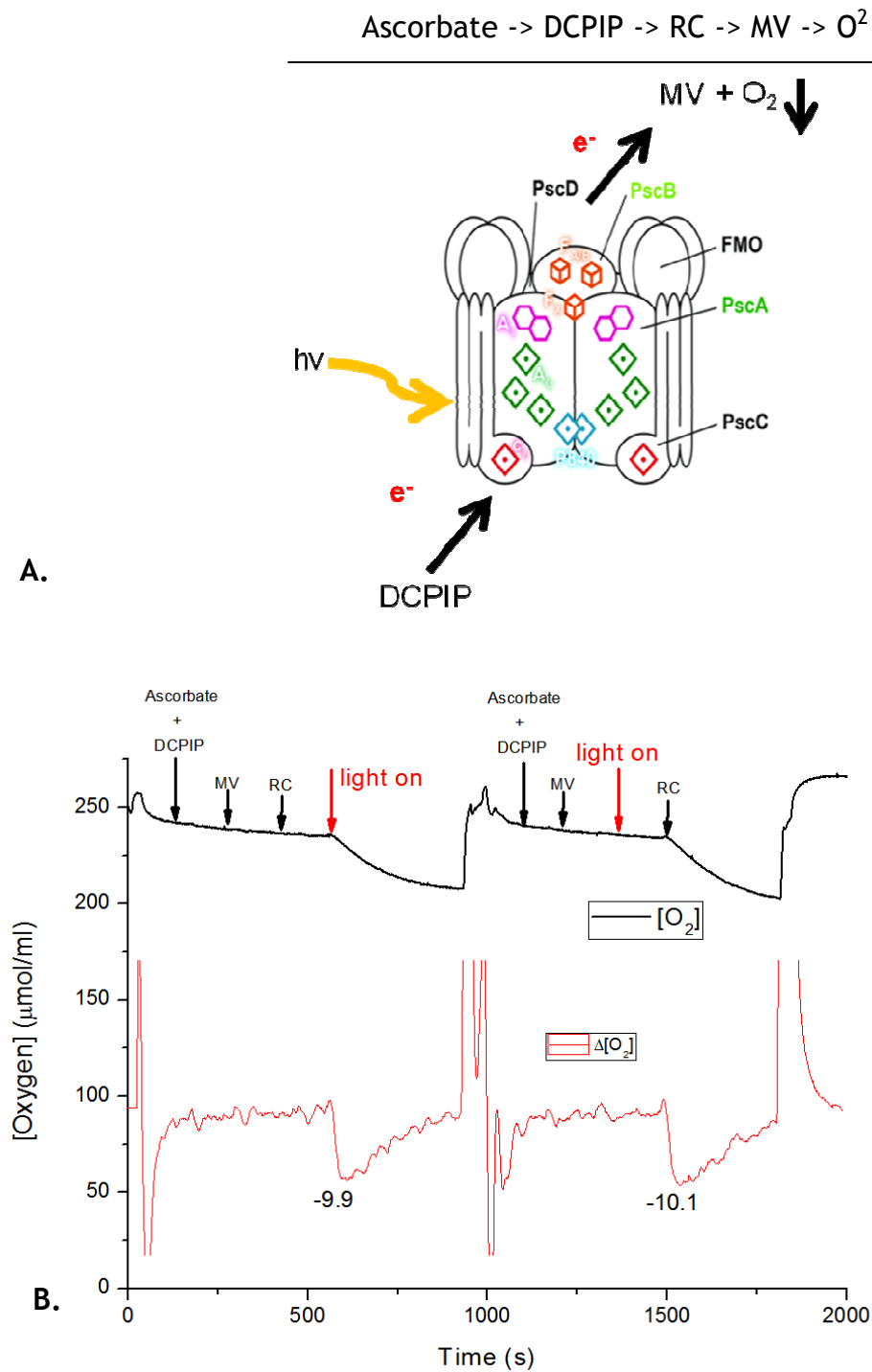


**Figure 3.20 Clarke-type electrode trace of MV reduction of dissolved oxygen**

**A.** Shows the diagrammatic representation of the reduction of oxygen when an electron donor (DCPIP) and an electron acceptor (MV) is added to the RC in the presence of light. **B.** Shows the trace of the dissolved oxygen (black line) and the rate of oxygen consumed (red line). This was carried out twice first when all the components were added together and light was turned on and the second time it was repeated to show that oxygen was reduced only in the presence of the RC.

It was observed that in the presence of no RC the reaction would not take place, this reaction also showed that the electron transfer with the RC was active.

### 3.9 FMO purification

FMO (Fenna-Matthews-Olson) is a water soluble complex attached to the *C. tepidum* RC. It mediates energy transfer from outside to the inside of the reaction centre [1, 6, 53, 171]. It has been put forward that the FMO is attached to the RC via the PscD polypeptide, no experimental evidence has ever been shown to back this, and only Scanning Transmission Electron Microscopy results have indicated that this could be the case [161]. To be able to test this hypothesis, along with others (as will be described in Chapter 4 and 5) it is important to be able to purify the FMO protein for these characterisation experiments.

During the nickel purification of the *C. tepidum* RC (as described in 2.4.4.2), when the RC is still bound to the nickel resin, the FMO can be washed off by using the wash buffer (50 mM Tris-HCl pH 8.0, 300 mM NaCl, 20 mM imidazole, and 0.1% DDM). The wash step, as described in the methods and materials section 2.4.4.2, as well as removing any other impurities does not dissociate all the FMO bound to the RC. To completely remove the FMO from the RC high concentrations of NaCl are required, usually over 500 mM NaCl this however, in turn also dissociates PscD and PscB from the RC leaving the core RC intact, as reported by Hauska (2001) [57].

The wash sample was taken after the nickel purification of the RC and was subjected to an O/N buffer exchange in 20 mM Tris pH 8, no salt buffer. The O/N wash sample was then passed and bound on to the DE52 resin (as described in section 2.5). The FMO was eluted of the DE52 resin with increasing concentrations of salt (150 - 200 mM) until a nice blue colour came off (Figure 3.19 A) and yielding pure protein, which was confirmed by a silver stained SDS-page (Figure 3.19 B), showing a protein band at 43 kDa. The presence of FMO was also confirmed by the absorbance spectrum of the FMO (Figure 3.19 C) as reported by Robert E. Blankenship [135], where the  $Q_y$  transition band at ca. 808 nm, the  $Q_x$  transition band ca 598 nm and the Soret band at ca. 370 nm are observed.

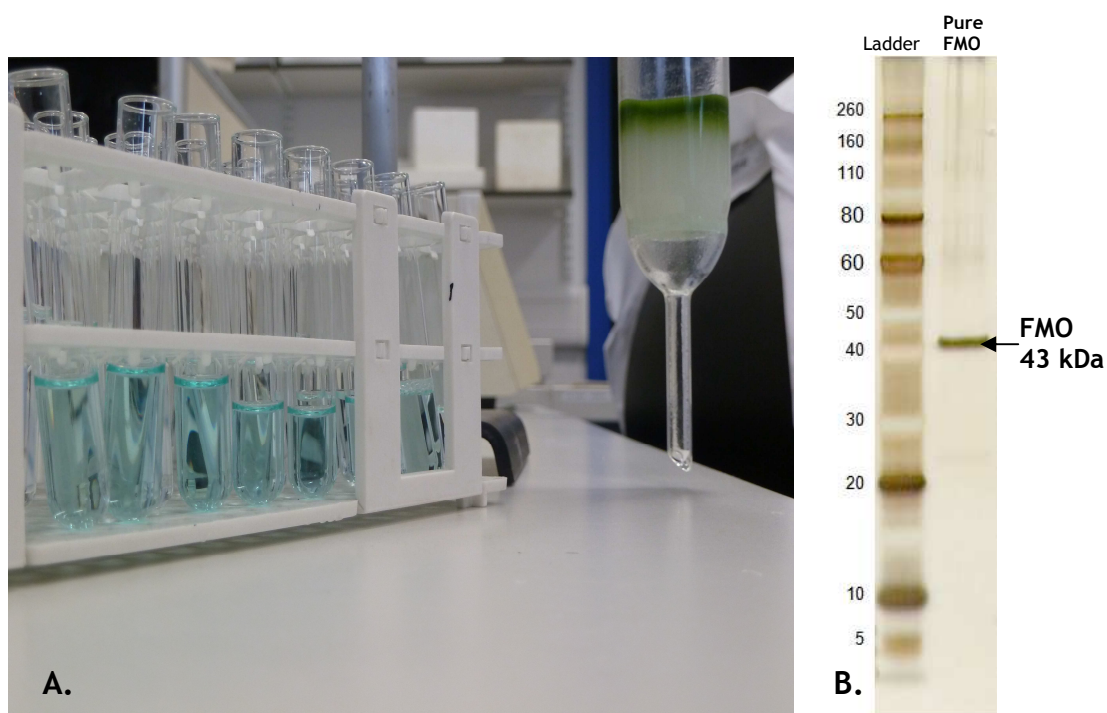


**Figure 3.21 Purification, identification and absorbance spectrum of FMO.**

**A.** Shows the wash bound on to the DE52 (as seen on the right hand side of the picture) and the blue FMO eluted with high concentrations of salt. **B.** depicts pure FMO protein (43 kDa) as seen on SDS page analysis after silver staining. **C.** FMO measured in solution at room temperature. At 340, 370, 598 and 808 nm, the characteristic absorption bands of BChl *a* from FMO. The  $Q_y$  transition band is at 808 nm, the  $Q_x$  transition band 598 nm.

## Chapter 4 – Plasmonic fluorescence enhancement with photosynthetic pigment-protein complexes

---

### 4.1 Introduction

To utilise energy harvested from sunlight sufficiently to promote photochemical reactions or to produce solar fuels, we must understand and improve both the effective capture of photons at a reactive site and the transfer of excitation energy. This would allow the design of molecular devices that can directly sort, and respond to sophisticated ways to excitation energy.

In order to organise photosynthetic complexes as a monomolecular layer on surfaces you will always have a limited amount of absorbance from solar-energy. Nature has found a way around this by stacking these complexes on top of each other to get that high absorbance, but another way which can be used is Plasmons.

As mentioned in the introduction (Section 1.4.1) one strategy to achieve fluorescence enhancement (or, ultimately enhancement of the ensuing photochemical reactions) is to utilise plasmonic metallic nanoparticles. These may drastically alter the emission of vicinal fluorophores. Metallic nanoparticles can influence the fluorescence emission of nearby molecules by enhancing the absorbance of the molecule, and by modifying the radiative decay rate of that molecule.

The aim of the investigation was to find out if and under which conditions silver nanoparticles can enhance fluorescence of photosynthetic pigment-protein complexes. To be able to understand how to enhance the absorption/fluorescence on surfaces by coupling surface plasmons to metallic nanoparticles.

## 4.2 Coupling *C. tepidum* RCs to silver nanoparticles

Purified RCs were attached to silver nanoparticles, or Silver Island Films (SIF) by spin coating, as described in section 2.25. The RC preparation was diluted with a 5% water solution of PVA that gave a final concentration of 0.5 mg/ml of RC. The RCs were tested to see if it was possible to enhance the fluorescence emission of the RCs when coupled to a silver nanoparticle. These hybrid assemblies were excited at specific wavelengths (405 nm, 485 nm, 532 nm, 589 nm, and 640 nm) once the RCs were coupled to the SIFs. The absorption spectra of RCs (red line) and the SIFs (black line) were measured and are shown in figure 4.1 together with the lasers used to excite the RC-SIFs at specific excitation wavelengths (green lines). By using a 780 nm long-pass filter it was ensured that the only observed emission was derived from the RCs (with a maximum at 840 nm).

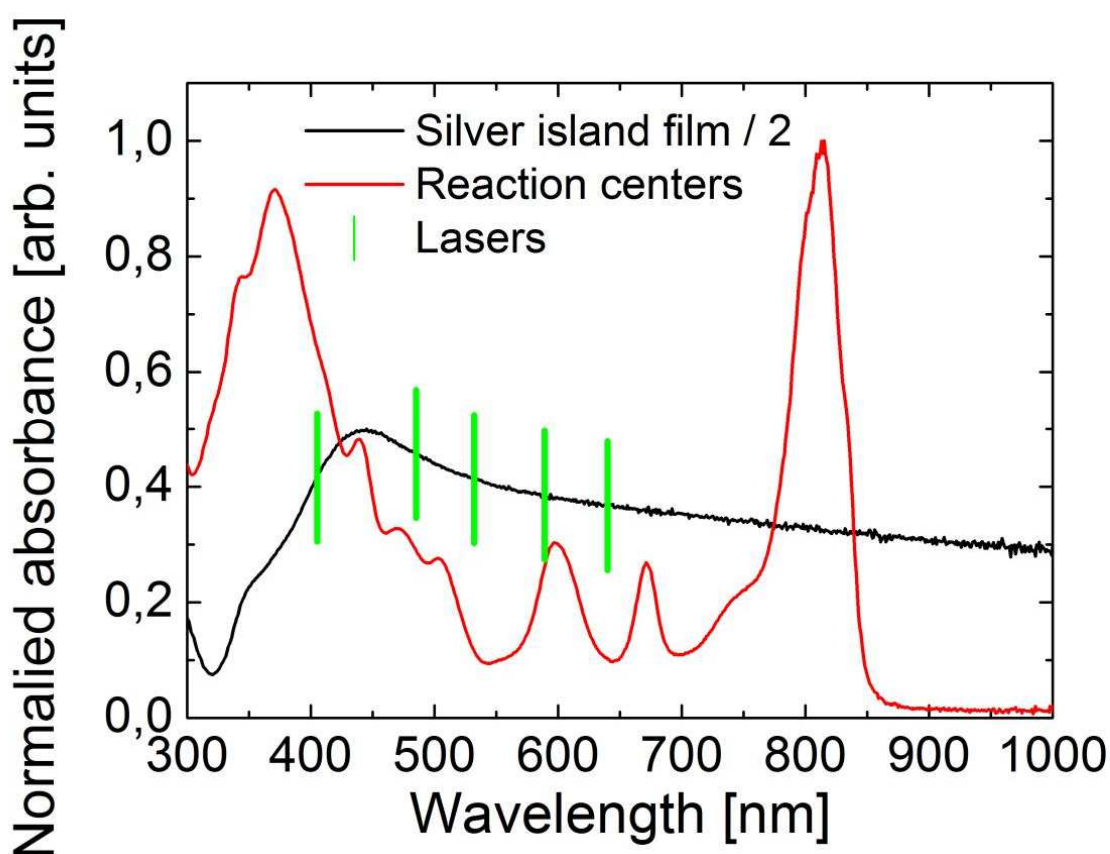


**Figure 4.1 Absorption spectra of Silver Island Film (SIF) (black line) and RCs (red).** Absorption spectra of the RC solution (red line). Bright green lines show the excitation wavelengths used.

### 4.3 Fluorescence Enhancements of *C. tepidum* RC

The intensity of the emission signal for the excitation wavelengths was measured. The excitation laser wavelength varied from 405 to 640 nm. 750 nm and 780 nm long-pass filters were used to block any emission not emanating from the RCs and any scattered excitation light. A 50-fold increase of RC fluorescence is observed upon 589 nm excitation when spin-coated SIFs as compared to a glass support (Figure 4.4 and Table 5).

Excitation spectra, at 405 nm, were obtained of RCs on SIFs and on glass, which are shown in figure 4.2. The spectra was measured using a 550 nm long pass filter for emission on SIF and a 550, and 665 nm long pass filter on glass. In order to exhibit the fact that the enhancement of the fluorescence does not change the shape of the reaction centres emission. The spectra were normalised due to intensity differences at around 838 nm, as observed in figure 4.2. The same concentrations, 0.5 mg/ml, of RCs were deposited on each of the SIFs and on glass, after spin coating, the glass and SIFs were excited and there fluorescence measured. It was clearly observed that even though there was a slight shift in the peak at 838 nm (as seen in figure 4.2) when comparing the RCs on SIFs with RCs on glass that the overall shape was the same. The peak at around 650 nm was from back ground noise. Since the ratios of the 838:650 nm were different for the RCs on SIFs compared to the RCs on glass this could be explained due to the enhancement of fluorescence of the RCs on SIFs.

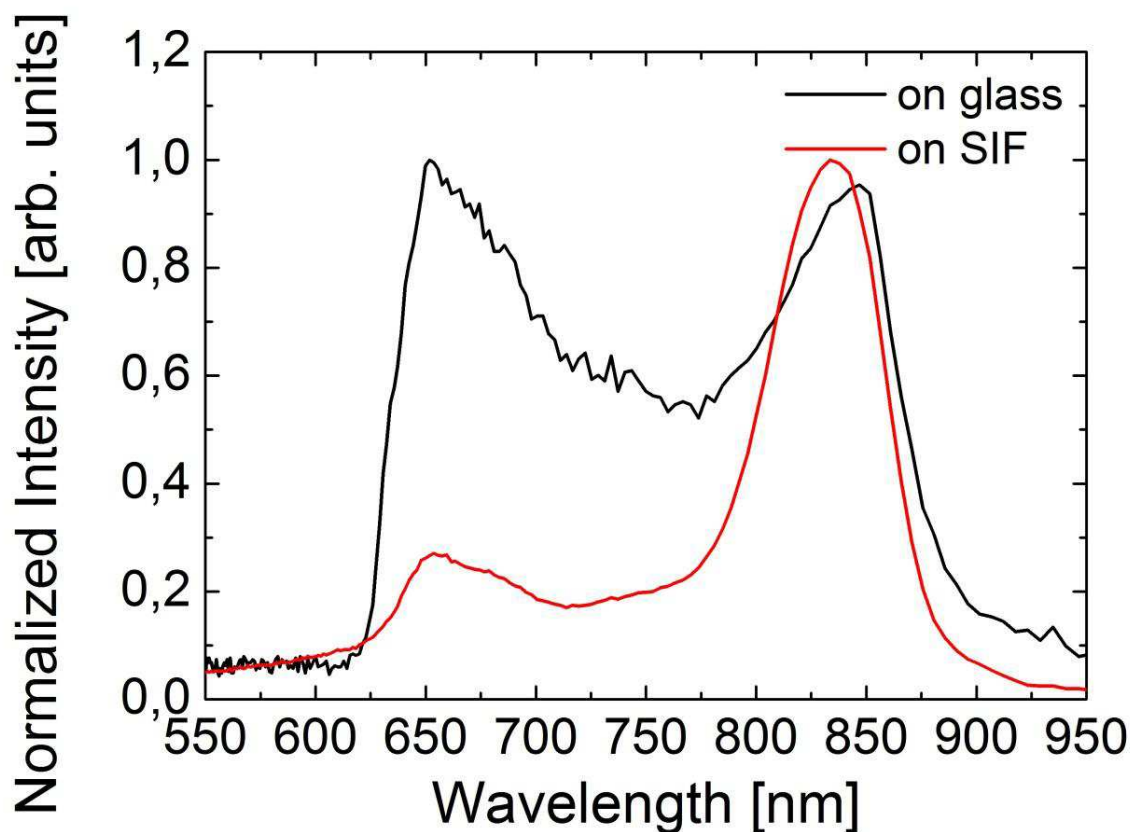


**Figure 4.2 Emission spectra of reaction centre.**

RC in PVA matrix spin-coated on glass (black line) and silver island film (red line)

To show that there was an enhancement when the RCs were coupled to the SIFs, emission spectra were measured by recording the maxima at 838 nm, when exciting at specific wavelengths. From these points we calculated the histograms shown below in figure 4.3. Fluorescence intensities of RCs on glass (black) and SIF (red) for various excitation wavelengths (405, 485, 532, 589 and 640 nm) were obtained at the peak of emission of the RCs (838 nm), and a clear enhancement was observed when the RCs were on SIFs than on glass, when excited with all the specific wavelengths.

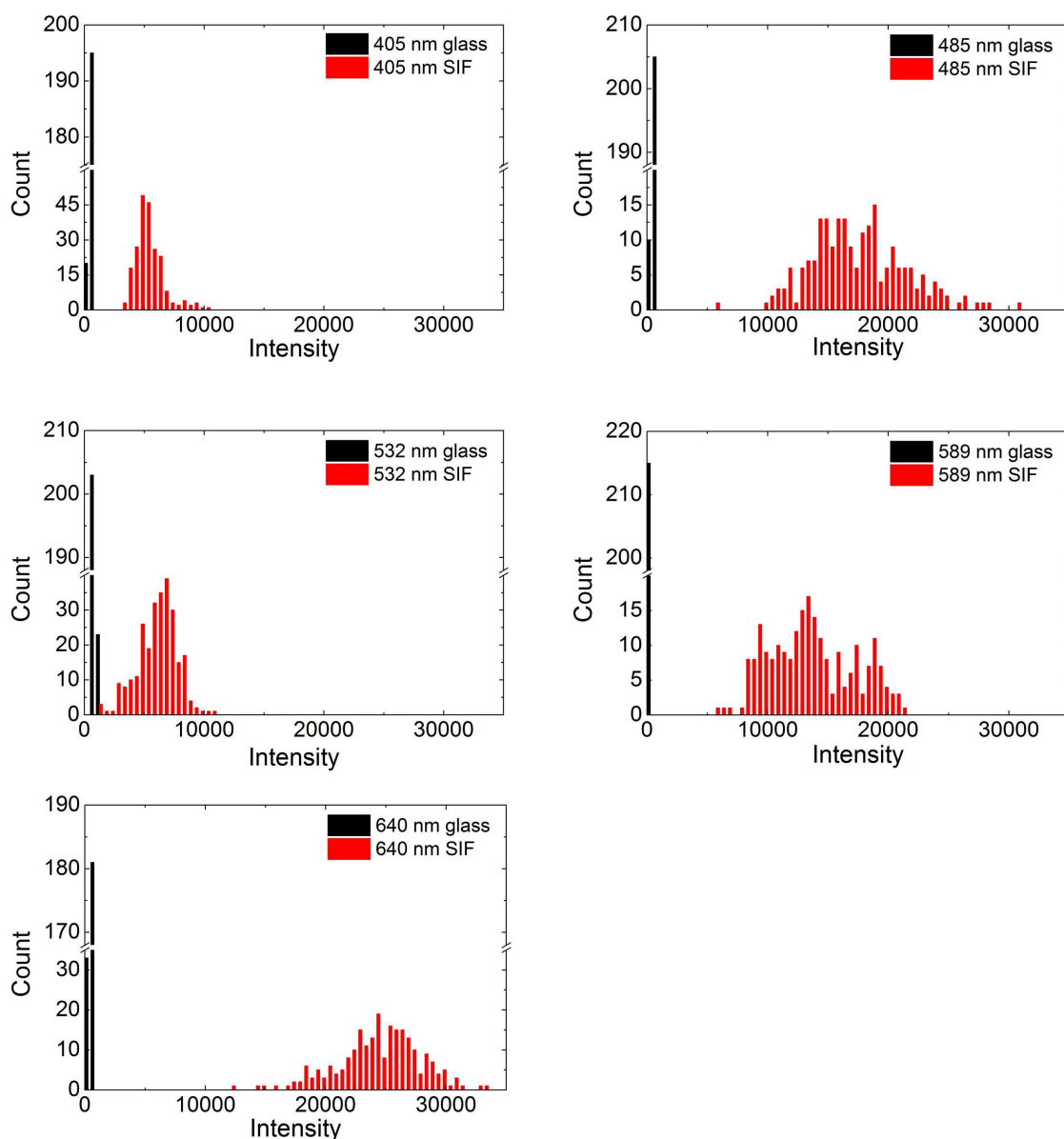


**Figure 4.3 Histograms of emission intensities of RCs on glass and SIFs.**

Fluorescence intensities of RCs on glass (black) and SIF (red) for various excitation wavelengths (405, 485, 532, 589 and 640 nm) obtained at the peak of emission of the RCs (838 nm). Note the increase in RC emission on SIFs as compared to RCs on glass. The RCs are better disturbed, and are more homogeneous, hence it is more of a gaussian peak (red), whereas the fluorescence intensities on glass (black) is narrowly disturbed, and tend to reside in the same environment.

By dividing the mean intensity of emission of the RC on SIF by the mean intensity of RC emission on glass, it was possible to calculate the enhancement factors shown in figure 4.4 and table 4. A clear increase can be seen compared to that of glass, and a near 50 fold increase can be seen when exciting at 589 nm. To allow a suitable system to be designed as well as an enhancement we would hope to see a longer life time. For this fluorescence life times were measured at specific wavelengths.

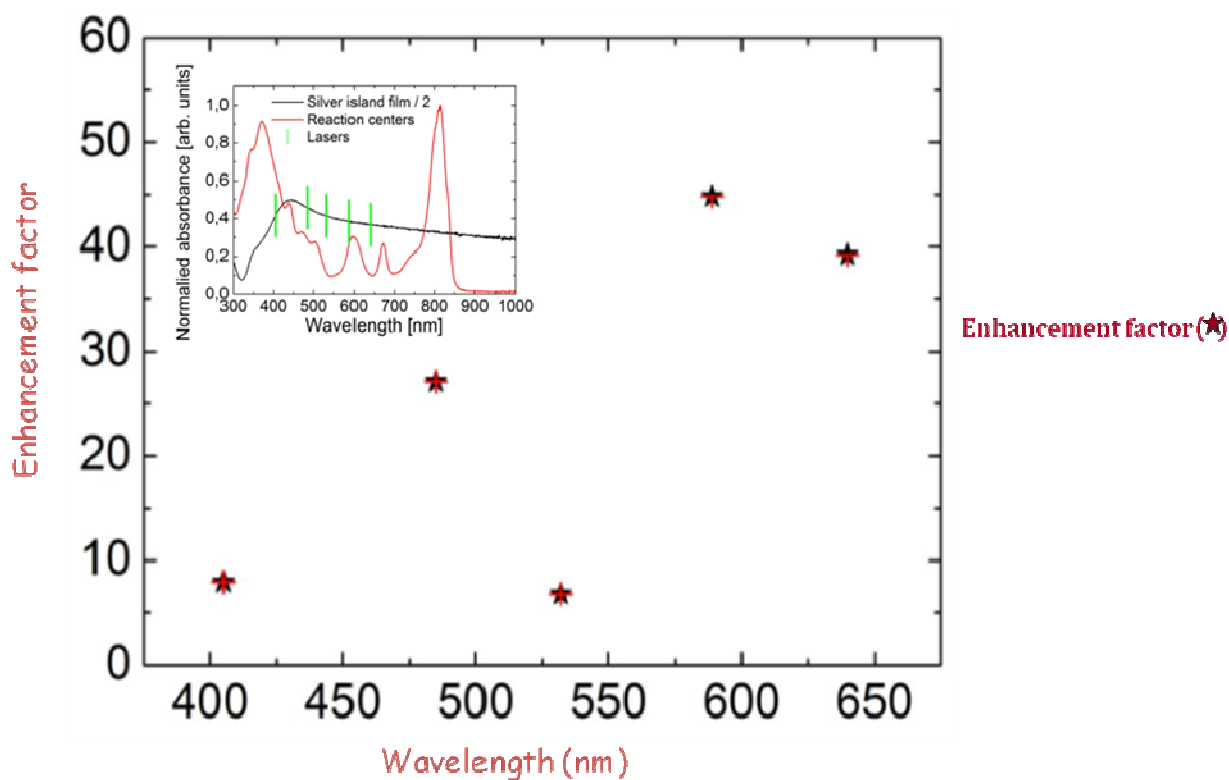


**Figure 4.4 Enhancement factors for the different excitation wavelengths**

Shows enhancement factors when excited at specific wavelengths, these are the mean intensities calculated after each excitation. A near 50 fold increase is observed when excited at 590 nm.

Calculated enhancement factors.		
Wavelength (nm)	Enhancement Factor	Enhancement Factor error
405	7,96	0,06
485	27,09	0,02
532	6,80	0,06
589	44,82	0,02
640	39,22	0,01

**Table 5** Calculated enhancement factors of RCs on SIFs compared to that of RCs on glass

## 4.4 Fluorescence Decays of *C. tepidum* RCs on SIFs and glass substrates

Fluorescence may occur when a molecule, atom or nanostructure relaxes to its ground state by emitting a photon after being excited to a higher state. A Jablonski Diagram explaining metal enhanced fluorescence is shown in (Figure 1.25).

The ground state of the fluorophore (fluorescent molecule) is designated  $S_0$  and  $S_1$  is its first (electronically) excited state. A molecule in  $S_1$  can relax by various competing pathways. It can undergo non-radiative relaxation in which the excitation energy is dissipated as heat (vibrations). Excited molecules can also relax via conversion to a triplet state, which may subsequently relax via phosphorescence or by another non-radiative relaxation step. Relaxation of the  $S_1$  state can also occur through excitation energy transfer to a second molecule (fluorescence quenching). Molecular oxygen ( $O_2$ ) can be an extremely efficient quencher of phosphorescence because of its unusual triplet ground state. Molecules that are excited through light absorption or via a different process (e.g. as the product of a chemical reaction) can transfer energy to a second sensitised molecule, which is converted to its excited state and can then fluoresce.

Fluorescence decays for both the RCs on glass and on SIF were measured in order to elucidate a possible mechanism of the observed fluorescence enhancement. The decays were measured by exciting the RC samples (both on glass and SIF) at 405 (Figure 4.5 A) and 640 nm (Figure 4.5 B). The emission was monitored using a 780 nm long pass filter. As observed in section 4.3, a clear enhancement is detected when exciting at all the wavelengths when RC is coupled to SIF as compared to glass. However, the life times observed in figure 4.5 show that the decay is much faster for RCs when coupled to SIFs (red line) than on glass (black line), when excited at 405 and 640 nm. The fluorescence quantum yield ( $\Phi$ ) is defined as the ratio of the number of photons emitted to the number of photons absorbed. The maximum possible fluorescence quantum yield would be 1.0 (100%); every photon absorbed would result in a photon emitted. Compounds

with quantum yields of 0.10 are still considered quite fluorescent. RCs on SIF have a faster decay as compared to RCs on glass.

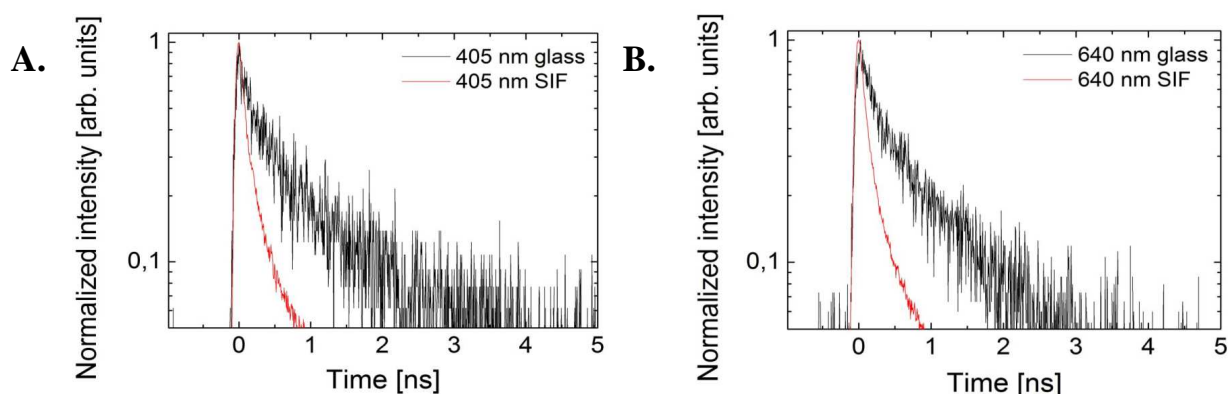


**Figure 4.5 Fluorescence decays of *C. tepidum* RCs on SIFs and glass substrates.**

Fluorescence decays were measured by exciting the RC samples at 405 (A) and 640 nm (B). Both, (A) & (B) show the emission monitored using a 780 nm filter.

One possible cause for seeing such a fast decay could be due to quenching (back transfer). This often occurs in photosynthetic plants and bacteria when they have to protect themselves from the adverse effects of high light intensity. This involves a competing pathway, the quenching of singlet excited state chlorophylls (Chl) via enhanced internal conversion to the ground state (non-radiative decay), thus harmlessly dissipating excess excitation energy as heat through molecular vibrations. This often happens in photosynthesis when light energy absorption exceeds its capacity for light utilisation. By coupling the RCs to SIFs and increasing the fluorescence intensities this might in turn exceed the capacity for light utilisation, hence the shorter lifetimes.

An overall fluorescence enhancement coupled with a shortened lifetime can be explained by quenching. This increase in absorption due to plasmon enhancement provides a way to maximise the light harvesting capability of any artificial module based on an ordered monolayer, but further work has to be done in order to increase the lifetimes before a suitable system can be built.

## 4.5 Effect of Silicon dioxide (SiO<sub>2</sub>) spacers

As there was a greater enhancement in fluorescence but a shorter life time when RCs were coupled to SIFs, we wanted to address the question why this could possibly be the case. Fluorescence of a fluorophore directly adsorbed onto

a surface of a metallic nanoparticle can be strongly quenched. This issue can be modified by placing spacers with varying thickness to modify this quenching. As fluorescence can be quenched when too close to the nanoparticle the opposite may just be as true, if the complex is too far apart from the metallic nanoparticle there will be no enhancement, or a much weaker signal. But at the optimal distance from the nanoparticle its fluorescence can be strongly enhanced (Figure 4.6 A). By SiO<sub>2</sub> spacers with varying thickness we tested if there was a greater enhancement in absorbance (Figure 4.6 B & C) for RCs coupled to nanowires as compared to RCs coupled to glass. Increase of fluorescence intensity can be observed when SiO<sub>2</sub> spacers were placed between the RCs and the nanowire. As well as the increase of RCs on SIFs compared to that of glass a clear 2 fold increase could be observed here when a 5 nm SiO<sub>2</sub> spacer was placed between the RC and the nanowire. This was calculated from figure 4.6 B, by dividing the mean intensities of RCs coupled to nanowires with varying levels of SiO<sub>2</sub> thickness with that of RCs coupled to glass with the same level of thickness. This allowed for enhancement factors to be calculated and observed in figure 4.6 C.

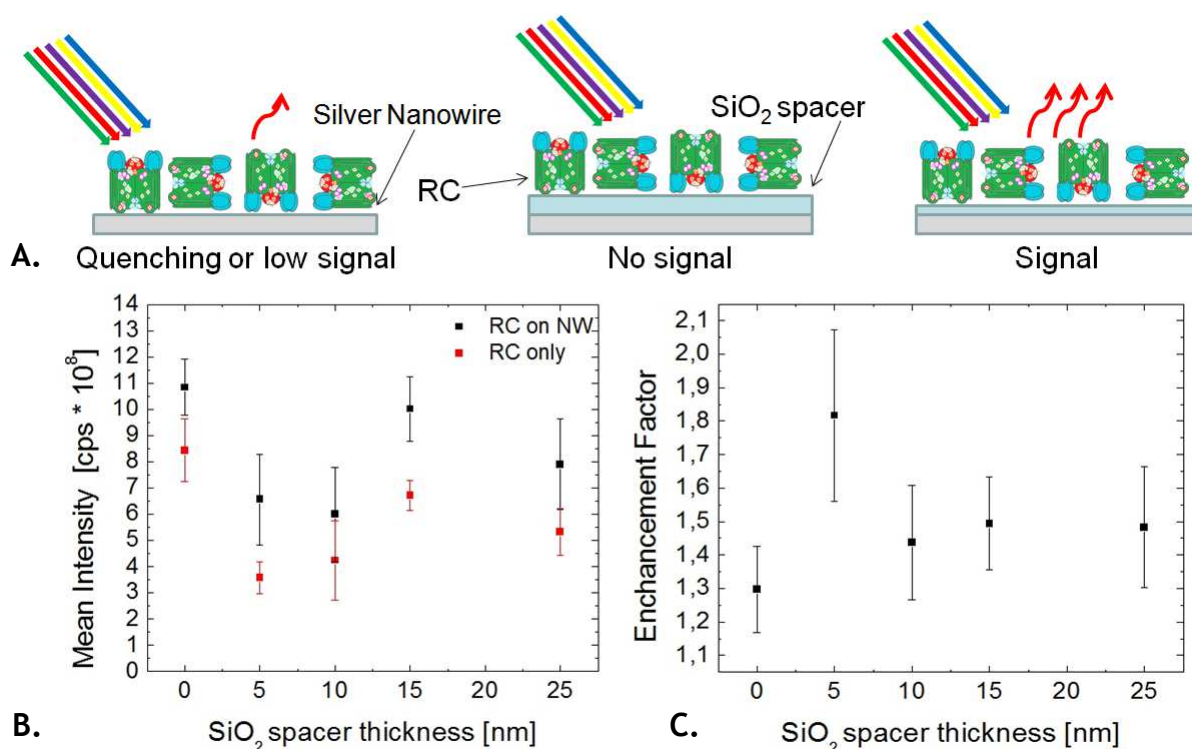


**Figure 4.6 Effects of a SiO<sub>2</sub> spacer thickness on fluorescence of RCs coupled to nanowires**  
**A.** Schematic representation of the possible effects of introducing spacers of variable thickness between a fluorophore and plasmonic nanoparticles. coupling the RC with a nanowire. Quenching if directly coupled. If the SiO<sub>2</sub> is too far there will be low or no signal (depicted by red arrows), but at the optimal distance a large increase could be seen. **B.** Mean intensities calculated for RCs on and off the nanowires with varying spacer thickness. **C.** Enhancement factor of the RCs coated on the silver nanowires.

This could also possibly account for why there was a shorter life time (fluorescence decay) when RC's were measured. Further investigation in to the fluorescence decay experiments in the presence of SiO<sub>2</sub> would have to be carried out.

## 4.6 RCs on Silver Nanowires

Information obtained from enhancement and decay experiments allowed for us to spin coat the RC on silver nanowires, to observe if enhancement using different Plasmon properties from different types of substances such as nanowires or nanorods which had more fine edges could be viewed on the wide field microscope (Figure 3.20). Metallic nanoparticles can influence the fluorescent emission of nearby molecules in several ways. All these processes can be controlled by molecule nanoparticle separation, nanoparticle size, and geometry. RCs on Silver nanowires can be seen ( figure4.7 A) to be illuminated by white light, this is light transmitted through sample, so the nanowires are dark due to the light being reflected. Figure 4.7 B shows the RCs spin coated on NW, and excited by a 485 illuminator, here the fluorescence of the RCs is only observed.

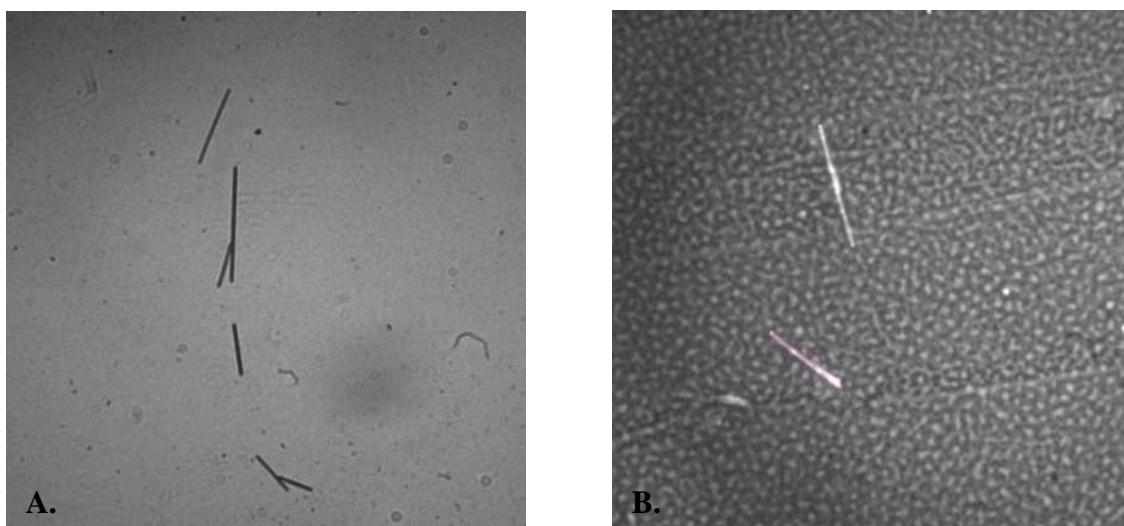


**Figure 4.7 Wide field microscope view of RC on nanowires.**

**A.** is picture of nanowires which are illuminated by white light, observing light transmitted through sample, so on nanowires we have dark image because they reflects light. **B.** Shows the RC spin coated on nanowires, and excited by 485 nm illuminator, we are observing fluorescence only from RC. The nanowires are 100 nm by 100  $\mu$ m.

Fluorescence of RC spin coated on silver nanowires was very intense; this confirmed and matched the rest of the data obtained from the SIF fluorescence

enhancement and fluorescence decay experiments, as this was visualised through the wide field microscope. Understanding the structure, of the *C. tepidum* RC, will give us insight into understanding this huge enhancement.

## 4.7 Plasmonic enhancement of FMO fluorescence

The Fenna-Matthews-Olson protein (FMO) is a water soluble pigment-protein protein complex. FMO is associated with the *C. tepidum* RC (section 1.2.5.2). FMO mediates excitation energy transfer from the baseplate of the chlorosomes to the RC. The structure of the FMO was solved in 1986 [172]. FMO is a trimeric complex. The structure to date shows 8 BChl *a* molecules that allow the transfer of energy in to the RC (Figure 3.21) [123, 137].

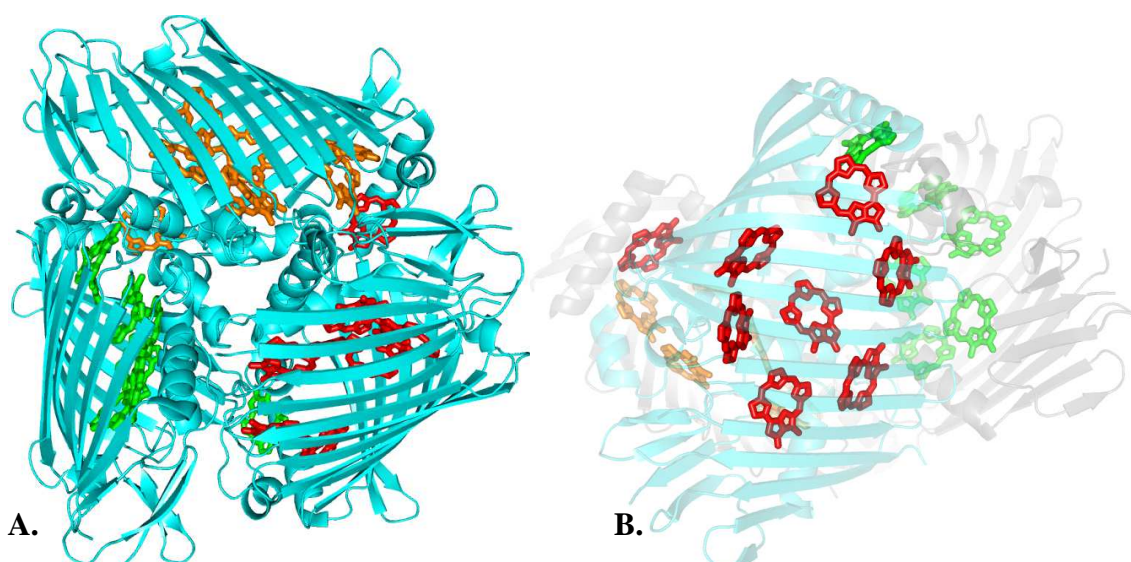


**Figure 4.8 X-ray structure of the FMO trimer.**

**A.** Structure of a FMO trimer. Each FMO monomer is composed of 20  $\beta$ -sheets and 9  $\alpha$ -helical turns that all face towards each other. **B.** Shows the bacteriochlorophylls of one FMO monomer that are involved in the energy transfer. The most recent school of thought is that there are 8 Bacteriochlorophyll *a* molecules in one monomer of FMO.

FMO can be readily purified and be easily separated from the RC as reported by Robert E. Blankenship and Oh-Oka [135, 173]. However, obtaining RCs devoid of FMO can be challenging. A high salt wash can easily dissociate most of the FMOs from the RCs. However, by doing this two of the peripheral soluble RC proteins (PscB and PscD) then easily dissociate as well, as demonstrated by Hauska and Oh-Oka [57, 122, 173]. Hence, all the plasmonic experimental results were obtained by with RC-FMO complexes. To be able to show that the fluorescence

enhancement of the *C. tepidum* RCs (section 3.4) was mainly from the RC and not the FMO, similar experiments were carried out with pure FMO (Figure 4.8). The absorption spectrum of the FMO protein features three main bands, corresponding to the Soret (370 nm), Q<sub>x</sub> (600 nm), and Q<sub>y</sub> (810 nm) absorption bands of BChl *a* (Figure 4.9 A). The emission maximum of the FMO is around 830 nm (Figure 4.9 B).

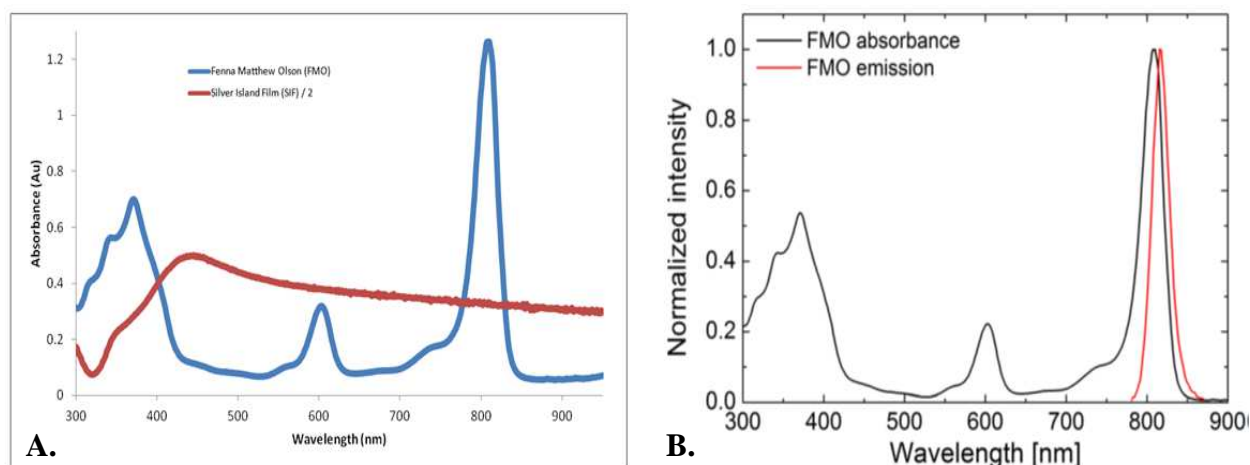


**Figure 4.9 Spectral properties of FMO and SIFs.**

**A.** Absorption spectra of FMO (blue) and the SIFs (red). **B.** Absorption (black) and fluorescence (red) spectrum upon excitation at 590 nm of FMO in solution. The main peak at 808 nm has slightly shifted when excited at 590 nm, as observed by the FMO emission.

To measure the fluorescence intensities of FMO on the SIFs, FMO was coupled in a similar fashion to that of RC-FMO. The SIF were prepared in two different ways, either by wet chemistry or e-beam evaporation (Figure 4.10). Wet chemistry deposition was mainly used for most of the FMO and all of the RC-FMO plasmonic experiments. The main difference in sample preparation is that with using wet chemistry the sample is prepared by spin coating of the RC on the SIF to provide an equal distribution, where for the e-beam evaporation substrates the RC is being dropped onto the SIF and let dry. It was observed that the wet-chemistry way of preparing the sample gave the best results, as it provided a more even, homogeneous sample. The FMO on SIF prepared by wet chemistry had clearly higher emission counts than compared to FMO on glass and that of FMO on SIF prepared by e-beam evaporation (Figure 4.10)

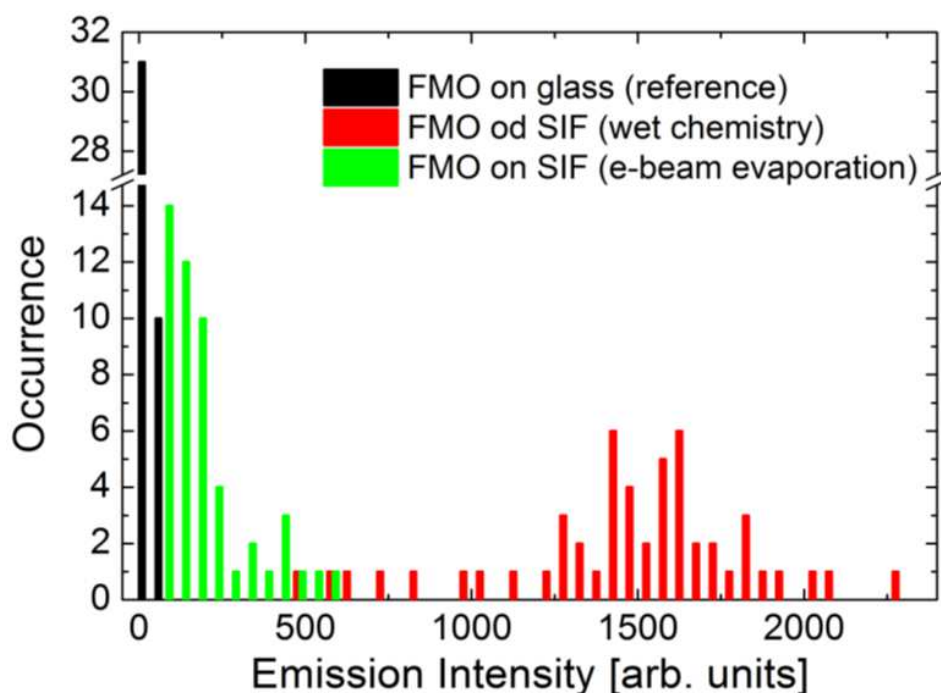


**Figure 4.10 Histograms of emission intensities of FMO on differently prepared substrates.** Histogram of emission intensity of FMO on glass and on SIF for spin-coated samples. There is a clear enhancement compared to that of glass. A sample of FMO prepared on SIFs obtained by e-beam evaporation is shown for comparison.

The fluorescence intensity of FMO on SIFs is clearly enhanced as compared to FMO on the glass substrates. There is a significant difference between the RC-FMO and FMO alone. Obviously, the fluorescence enhancement factor for FMO depends on the sample geometry as well as on the SIF fabrication method. The above described /obtained results have several important implications. First, SIF substrates can be used for the emission detection of photosynthetic complexes or other fluorophores with low emission quantum yields. The interactions between the photosynthetic complexes and plasmons induced in SIF results in an increased absorption rate of the FMO to and the radiative rate apparently being unaffected (Figure 3.24). This can be deduced from increased fluorescent intensities but unaffected fluorescence kinetics.

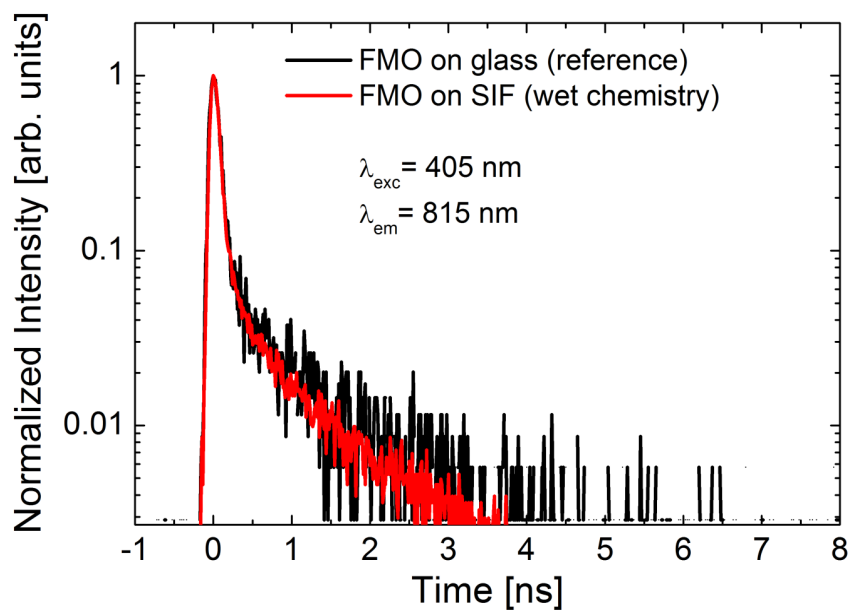


**Figure 4.11 Fluorescence decay curves of FMO on glass and on SIF**

Presented results confirm that metallic nanostructures can be used to modify optical properties of fluorophores, e.g. in sensing or energy-harvesting applications. Here it has been shown that the enhancement is due to the RC and not the FMO. Further optimisation is required before allowing for a more stable mimic to be designed of the RC on metallic structures.

## Chapter 5 - Expression, purification and characterisation of PscD and PscB

---

### 5.1 Introduction

There are no known examples of crystal structures of green sulphur bacterial Type I RCs. Obtaining the structure of the RC from *C. tepidum* would therefore give us a structure of the “missing link” as the *C. tepidum* RC is homodimeric and all other RC structures, solved to date, are heterodimeric. As the *C. tepidum* RC is a membrane protein, obtaining crystals for structural determination prove to be challenging. Since the RC protein is made up of 4 peripheral proteins (PscA-D) gaining insight into any of these peripheral proteins would be of great advantage and would give an increased insight on how the RC functions.

This chapter will focus on the construct design (including the modification of the already existing CLBH construct), expression and purification of two of the polypeptides associated with the RC, PscD (protein of unknown function) and PscB (an iron sulphur protein, which contains two 4Fe-4S clusters, FA and FB, as terminal electron acceptors), for purposes of structural and biophysical characterisation.

### 5.2 The CLBH tag

It has been shown by Tsiotis et al. 2001 that by removing FMO to obtain pure RC causes the dissociation of two of the soluble subunits of the RC (PscD and PscB), leaving the core of the RC intact and stable. To learn more about these components PscD and PscB were each expressed in *E. coli*, and purified using our in-house purification tag containing a fluorescent iLOV domain (a gift from Prof. John Christie) (Figure 5.1). An understanding of how PscD is associated with FMO will be investigated to help elucidate electron transfer from chlorosomes to the FMO protein and on to the RC.

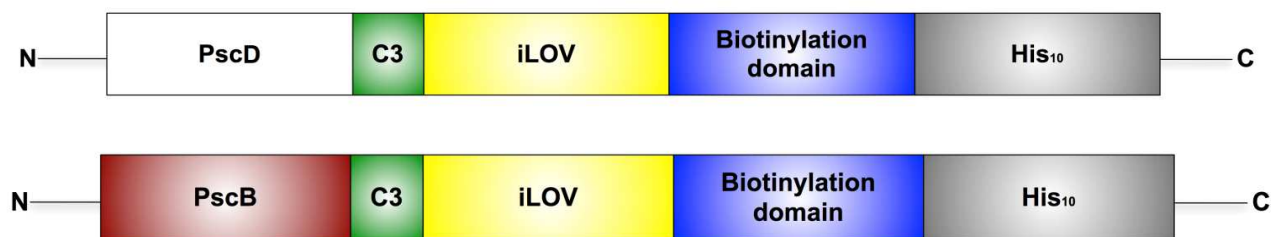


**Figure 5.1 Incorporation of PscD and PscB into the CLBH tag.**

Tags show the target protein attached to the CLBH – The C3, for cleavage, the iLOV for fluorescence, the biotinylation domain as a purification tag (if required) and the His<sub>10</sub> tag used during the nickel purification stage.

To allow the recombinant expression and purification of PscD and PscB in *E. coli*, both the DNA encoding target proteins were ligated into a modified pET21a (Novagen)-CLBH construct. The already existing construct was modified to allow both target proteins to be ligated in to the construct. The CLBH tag was a gift from Dr Niall Fraser (Table 6).

<b>3C</b>	Human rhinovirus 3C protease. To allow the removal of the purification tag.
<b>iLOV</b>	The improved Light Oxygen Voltage domain allows proteins to be seen under UV light.
<b>Biotinylation Domain</b>	Allows for the binding of Biotin to streptavidin. Can also be used to help aid purification.
<b>His10</b>	Helps in the purification protocol by binding to a nickel column.

**Table 6 Information on the CLBH tag**

### 5.3 pET21a expression vector modification and insertion of CLBH

To be able to incorporate the DNA encoding the target protein (PscD and PscB) with flanking EcorI and NotI sites, along with the C terminus CLBH tag in to an expression vector (as shown in figure 5.1), a construct had to be made to allow the DNA encoding CLBH to be inserted into a pET21a (Novagen) expression vector. The CLBH insert contained N and C terminus NotI and BamHI flanking sites, as well as this, an NdeI site was in the middle of the CLBH insert. To insert the CLBH encoding DNA into the expression vector, firstly the pET21a (Novagen) recombinant plasmid was modified by the removal of the NdeI and BamHI sites

(as described in methods and materials section 2.8) (Fig. 5.2). After the removal of the NdeI and BamHI sites the plasmid was blunt ended and re-ligated back together (Fig. 5.2 B).

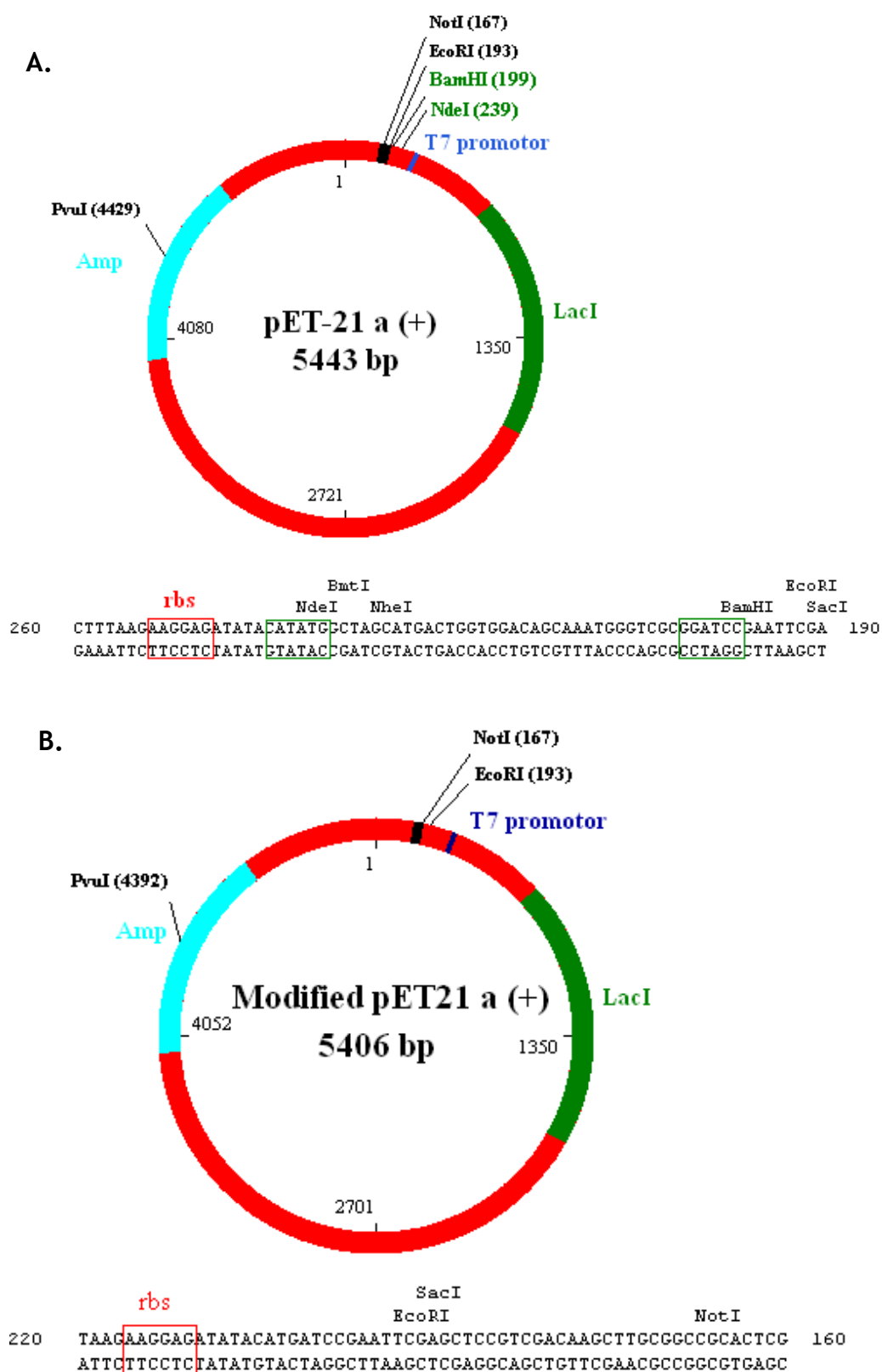


**Figure 5.2 Restriction maps of the WT pET21a and the modified pET21a.**

**A.** Restriction map of the recombinant pET21a (Novagen) plasmid, showing the restriction sites NdeI and BamHI (highlighted in green). **B.** Restriction map of modified pET21a plasmid showing no NdeI or BamHI sites present.

Successful modification of the pET21a vector allowed the insertion of the CLBH tag into the vector (Fig. 5.3). The CLBH tag, in an already existing pET21a vector, was digested at its NotI site and also further upstream at the PvuI site, the modified pET21a vector was also digested at these sites allowing the ligation of the CLBH to the modified vector (Fig. 5.3 A). This also introduced, along with the CLBH insert, a BamHI site upstream of the multiple cloning site flanking the C terminus of the CLBH tag. Having obtained the modified pET21a vector with the CLBH tag inserted (Fig. 5.3 B and C) allowed us to obtain a construct for the insertion of any protein of interest to be inserted with EcoRI and NotI flanking sites on either end of the protein of interest. Successful ligation of the CLBH tag to the modified pET21a plasmid was confirmed by digestion of the CLBH tag with NotI and BamHI (Fig. 5.3 C), with bands observed corresponding to the modified vector (~6 Kbp) and a band corresponding the CLBH tag (~0.6 Kbp), on a 1% agarose gel. Confirmation of modified pET21a vector and the insertion of the CLBH tag were also established by DNA sequencing (MWG neurofins).

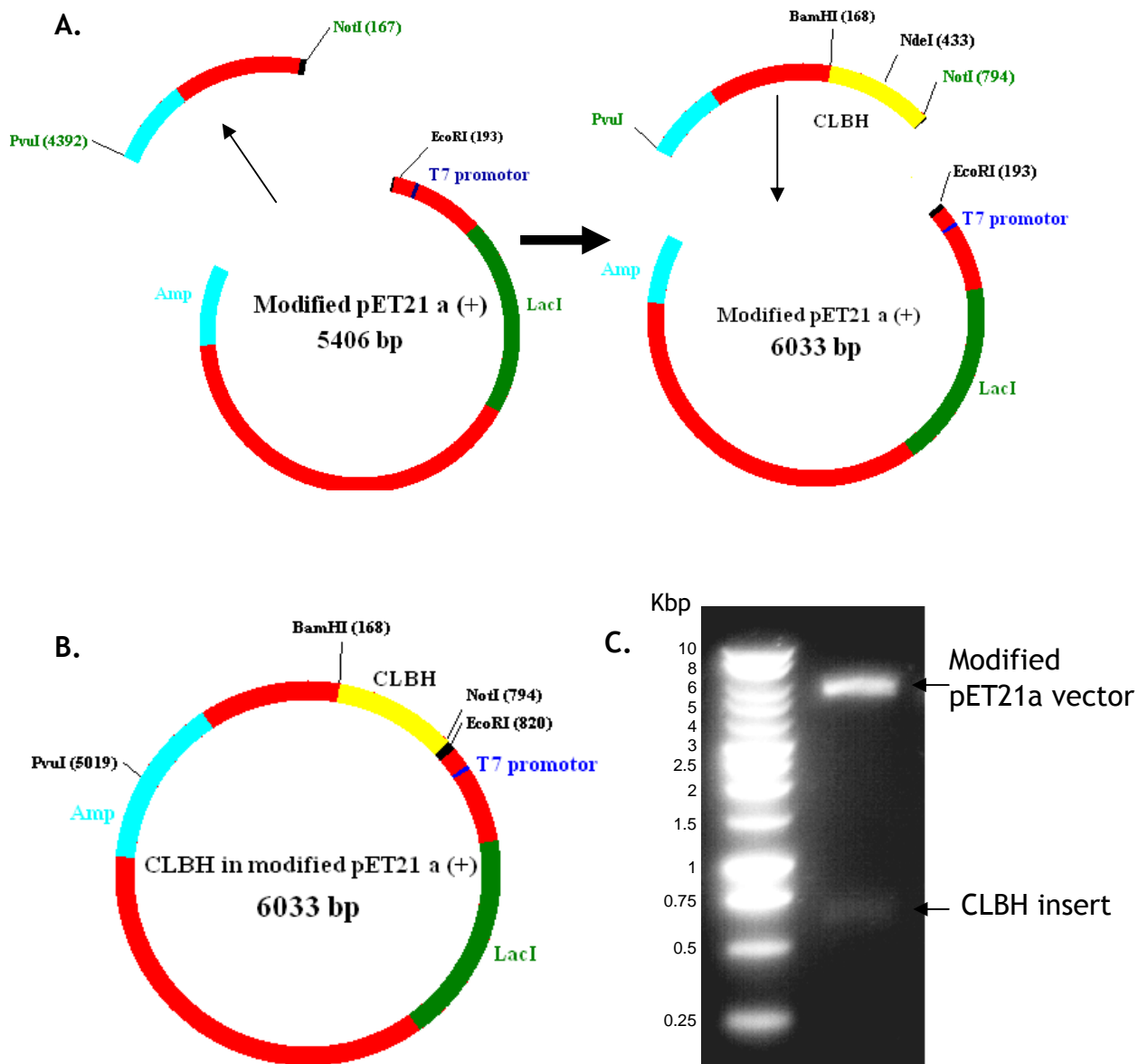


**Figure 5.3 Restriction maps and DNA gel for successful construction of the CLBH encoding gene incorporated into the modified pET21a vector.**

**A.** Restriction map depicting the digestion of the modified pET21a at the PvuI and NotI site and the ligation of the CLBH insert, digested from an already existing pET21a vector at the same restriction sites, being ligated together. **B.** Restriction map of the newly modified pET21a plasmid with the CLBH insert in the NotI BamHI flanking regions. Restriction analysis of pET21a plasmid containing CLBH. Digestion of the vector with NdeI and BamHI resulted in release of the pET21a vector (~6 kb) and the CLBH (~0.6 kb).

## 5.4 PscD and PscB amplification and insertion in to pET21a vector containing CLBH

Successful construction of the modified pET21a vector, with the CLBH insertion, allowed for the insertion of any known target DNA encoding the protein of interest with EcoRI and NotI sites flanking on either end. This was carried out by extracting the genomic DNA from *C. tepidum* (as described in section 2.6). The genomic extraction of the *C. tepidum* allowed for PscD and PscB to be amplified with forward and reverse primers that encoded flanking EcoRI and NotI sites on either end of the PscD and PscB sequence (as described in the methods and materials section 2.7 & 2.10). Successful amplification was confirmed by running the amplified DNA on a 1% agarose gel, were bands corresponding to PscD (0.4 Kbp) and PscB (0.6 Kbp) were observed (Fig. 5.4). Both these bands were cut out, gel purified and sub-cloned into a pJET1.2 vector (as described in section 2.7). The successful amplification of PscD and PscB was confirmed by DNA sequencing in the pJET1.2 vector, this also confirmed that no frame shift mutations were seen within the sequence.

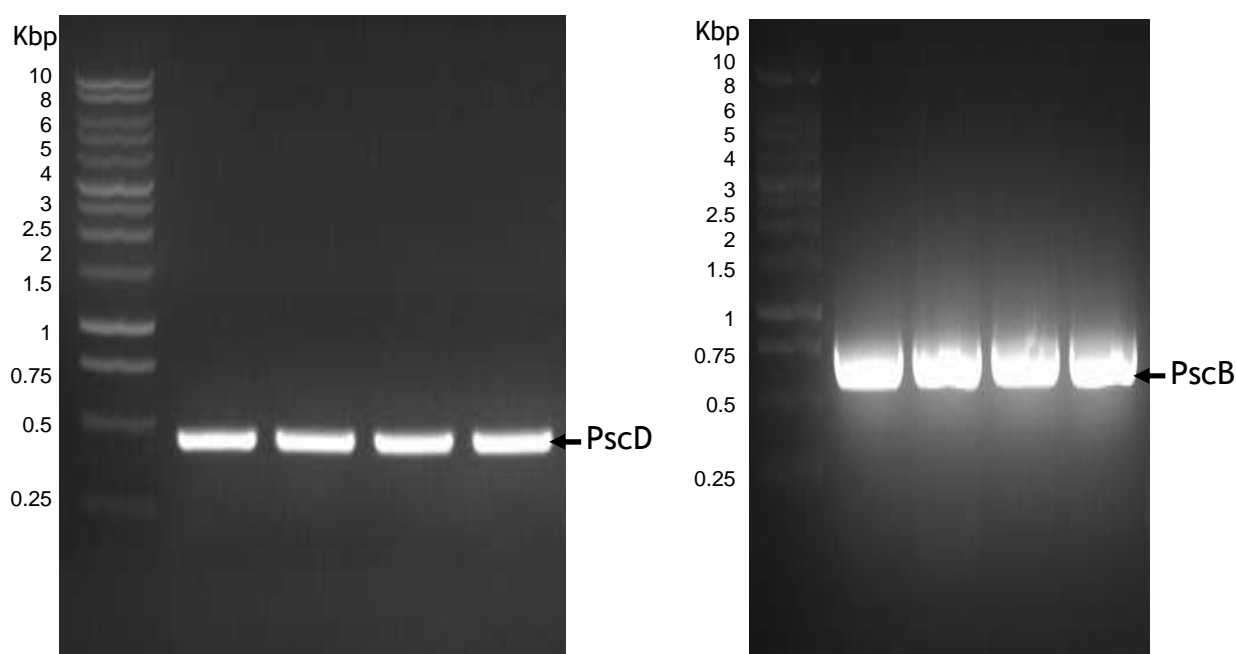


**Figure 5.4 1% DNA agarose gels showing amplification of PscD and PscB.**

PCR amplification of PscD (0.4 kbp) and PscB (0.6 kbp) from extracted genomic *C. tepidum* DNA, run on 1% agarose gel.

Obtaining the modified Pet21a with the CLBH inserted allowed easy ligation of both PscD and PscB (as described in section 2.11). As well as the modified pET21a-CLBH vector, both PscD and PscB inserts in the pJET1.2 sub-cloning vector were digested with EcoRI and NotI enzymes and ligated together. The ligation was transformed into DH5 $\alpha$  cells and recombinant PscD/PscB-CLBH in the modified pET21a plasmid was grown overnight and isolated using the Qiagen miniprep kit. Successful ligation was confirmed by digesting the modified pET21a-CLBH vector encoding the genes of interest with EcoRI and NotI enzymes. These digestions were run on a 1% agarose gel confirming the presence of two bands corresponding to the size of PscD (0.4 Kbp) and PscB (0.6Kbp). The undigested DNA was then sent off for sequencing to confirm the successful ligation of PscD and PscB into modified pET21a-CLBH vector. The successful construction of these vectors allowed for transformations to be carried out in DH5 $\alpha$  cells to be stored as glycerol stocks at -80°C (as described in section 2.7) until further use.

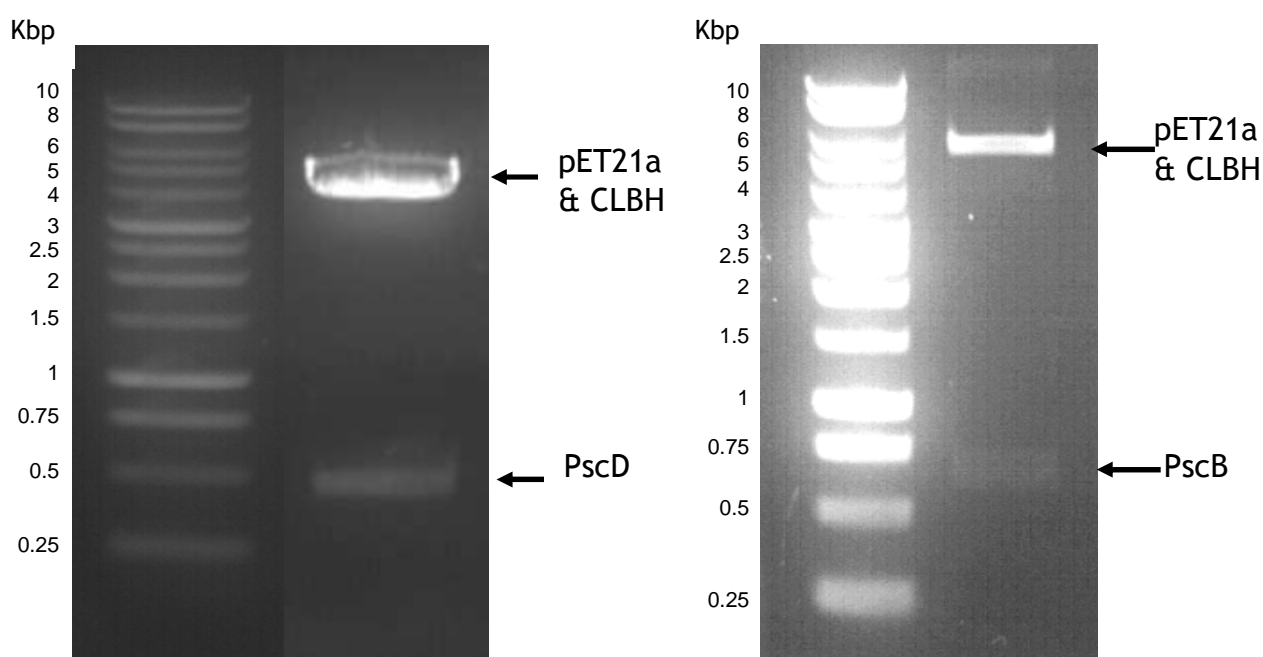


**Figure 5.5 Restriction analysis of modified pET21a plasmid containing CLBH with the DNA encoding for PscD and PscB.**

Digestion of the vector with EcoRI and NotI resulted in release of the pET21a-CLBH (~6 kb) vector, and the PscD (~0.4 kbp) and PscB (0.6 kbp) inserts.

## 5.5 Test expression of PscD-CLBH and PscB-CLBH

Successful construction of PscD and PscB-CLBH, in the modified pET21a, lead on to carrying out small-scale test expressions, in LB (Luria broth) and TB (Terrific broth), to be able to test at what temperature and for how long the induction time would give the most abundant amounts of protein (as described in section 2.13.1).

Both PscD-CLBH and PscB-CLBH were grown O/N in 5 ml of LB and TB from glycerol stocks for each construct with appropriate antibiotics. 50  $\mu$ l of the O/N was then sub-cultured in 4 x 50 ml conical flasks, two flask containing LB and two flasks containing TB (with potassium salts) with appropriate antibiotics for both PscD-CLBH and PscB-CLBH (as described in section 2.13.1). All the flasks were grown at 37°C until an OD (optical density) of 0.6 was reached, and then all the *E. coli* containing the plasmid were induced with IPTG. After induction half the flasks, one flask of LB and one flask of TB was moved to a 22°C shaker incubator, while the rest stayed shaking at 37°C. All the flasks were left shaking (inducing) for 16 hrs, which during a 1 ml sample was taken from each, 1 ml before induction and 1 ml after 1, 2, 3, 4, 8, 16 hrs of induction both at 22°C and 37°C. All the samples were spun on a table top centrifuge at 13,000 rpm and pelleted. The pellets were then resuspended in water and 20  $\mu$ l of the samples were then prepared as described in section 2.13.2 of the methods and materials to run on a 4-12% SDS-page gel (Fig 5.6 & 5.7).

As observed in figure 5.6 and 5.7 there was an increase in intensity over time, after induction in all the conditions between 38-49 kDa. Gel analysis showed that pre induction there was a thick band seen at about the estimated molecular weight of both PscD-CLBH (39.5 kDa) and PscB-CLBH (45 kDa). This was indicative of endogenous *E. coli* expression, were cells grown showed expression at around 38-49 kDa, which happened to be at around the same molecular weight of PscD-CLBH and PscB-CLBH making it harder to confirm that both these proteins were being induced.

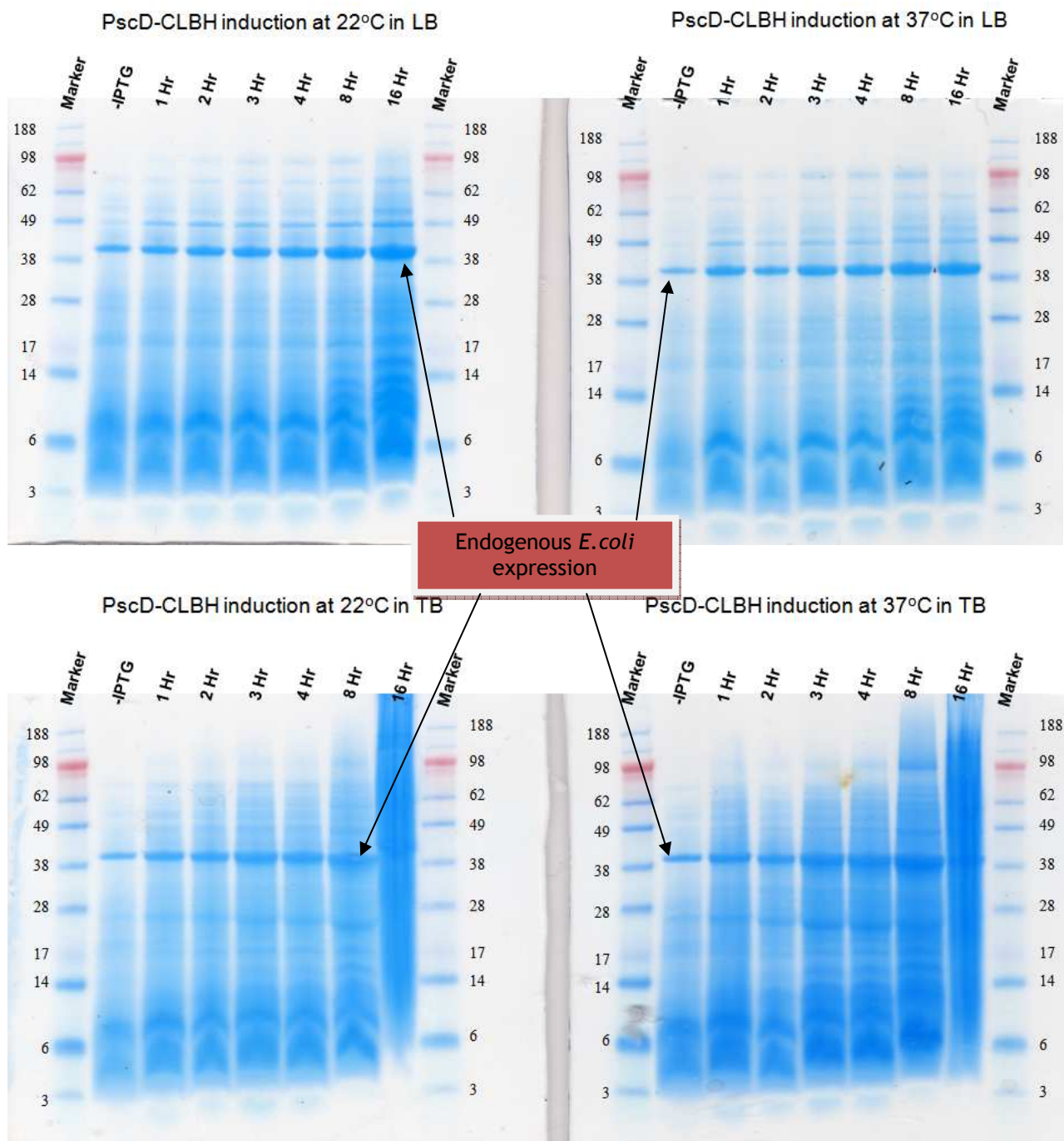


**Figure 5.6 4-12% SDS-page gel of PscD-CLBH time course test expression on LB and TB at 22°C and 37°C induction times.**

PscD-CLBH (39.5 kDa) expression at different temperatures and different time points after induction run on a 4-12% SDS-page gel. PscD-CLBH 39.5 kDa. **(marker)** Marker (SeeBlue Plus2 Pre-Stained Standard). A band observed between 38-49 kDa is of endogenous *E. coli* expression

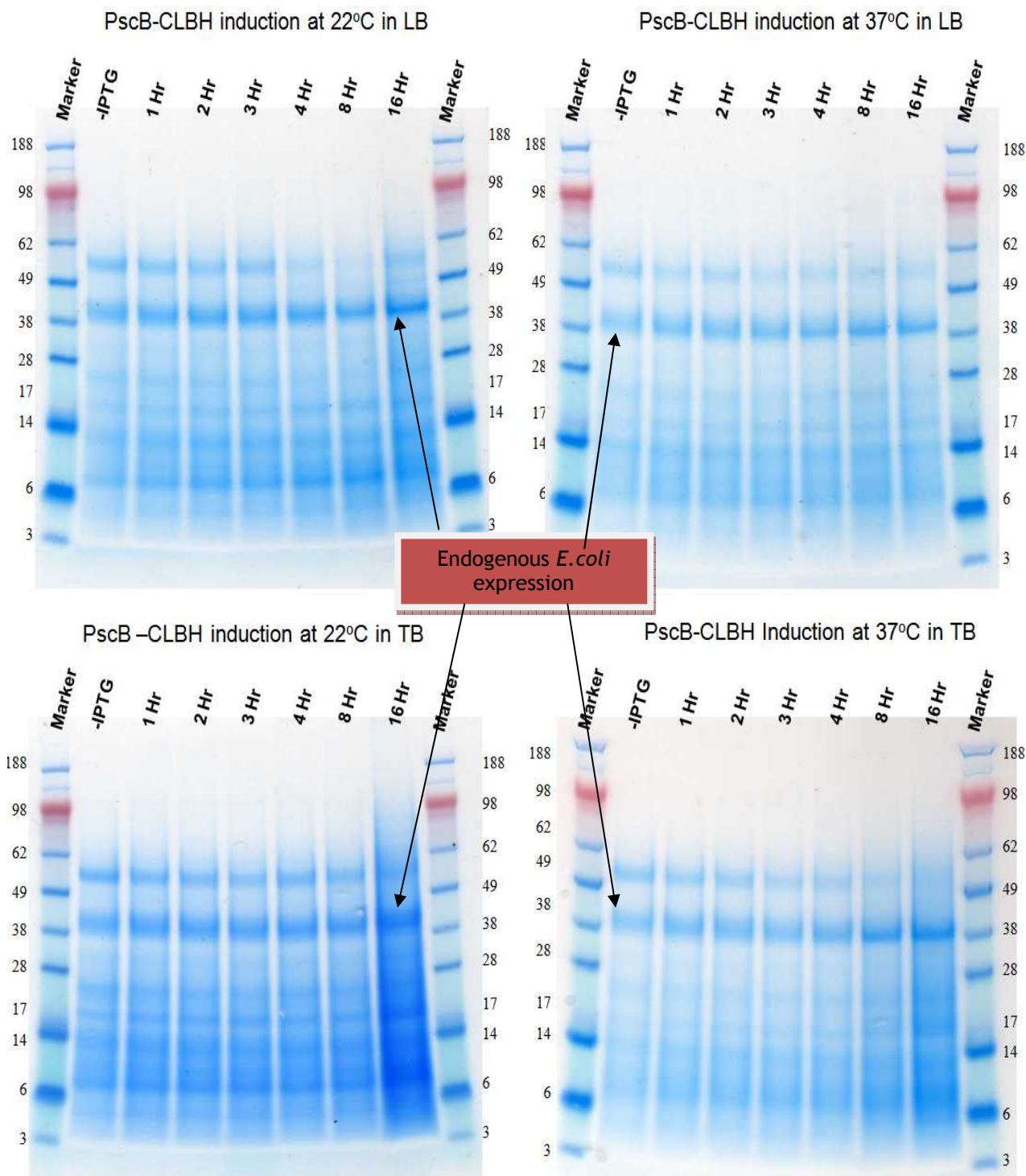


**Figure 5.7 4-12% SDS-page gel of PscB-CLBH time course test expression on LB and TB at 22°C and 37°C induction times.**

PscB-CLBH (45 kDa) expression at different temperatures and different time points after induction run on a 4-12% SDS-page gel. PscB-CLBH 45 kDa. **(marker)** Marker (SeeBlue Plus2 Pre-Stained Standard). A band observed between 38-49 kDa is of endogenous *E. coli* expression.

Due to the endogenous *E. coli* expression there was no noticeable expression of the proteins of interest being observe. So by using the CLBH tag attached to PscD and PscB to measure the increase in fluorescence of iLOV we were able to quantitatively quantify if the protein of interest was being expressed.

## 5.6 Using iLOV to measure expression of PscD and PscB

iLOV is a flavin-based fluorescent protein derived from the LOV2 (light, oxygen or voltage sensing) domain of phototropin 2 from *Arabidopsis thaliana* [174]. Following excitation of the wild-type LOV2, the LOV domains form a covalent bond between a bound flavin mononucleotide (FMN) and a conserved cysteine residue (Cys426 of phototropin 2) in a central cavity through hydrogen bonds and van der Waals interactions [175-178] (Figure 5.8). This allows for a structural change within the LOV domain initiating a response in an effector domain. This structural change is inhibited on mutating the cysteine, this however still allows for the formation of the initial photoproduct allowing for the excitation to go back to its ground state resulting in increased fluorescence emission compared to the wild-type. Three additional mutations in close vicinity to the FMN co-factor were identified giving a further 2-fold increase in fluorescence emission. This mutant was named iLOV. The iLOV protein, which gives off a green fluorescence when excited with UV light, was engineered as an alternative to GFP (green fluorescent protein). The iLOV protein allows for several advantages over its counterpart. iLOV is naturally monomeric and is therefore not prone to aggregation, whereas GFP is dimeric. GFP is a 25 kDa protein as compared to iLOV, which is only 10 kDa, this drastically reduces the steric impedance caused by the marker, and also the genetic strain upon the expression system as its fluorescence is not oxygen dependant. Finally iLOV, also has the ability to recover spontaneously from photobleaching, unlike its counterpart GFP.

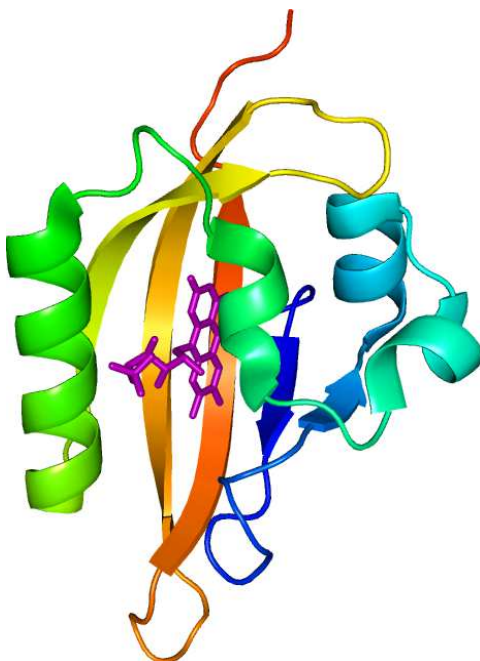


**Figure 5.8 Structure of the light oxygen volage 2 (LOV2 or iLOV) domain from *Arabidopsis thaliana*.** iLOV is 10 kDa. The structure is colored in chainbows, with the FMN chromophore colored in purple (PDB 1G28) [175].

### 5.6.1 Absorption spectra of iLOV

iLOV has a strong absorption region between 350-500 nm (Figure 5.9), with the major UV-A absorption maximum occurring at 378 nm. The absorption maximum in the blue region of the spectrum is at 447 nm for iLOV [179]. FMN also has regions which absorb at around these wavelengths, but Prof John Christie (University of Glasgow) has shown the presence of the excitation peak at around 450 nm for the iLOV, which is not present for FMN allowing for iLOV to be excited at 450 nm without exciting FMN [179-180].

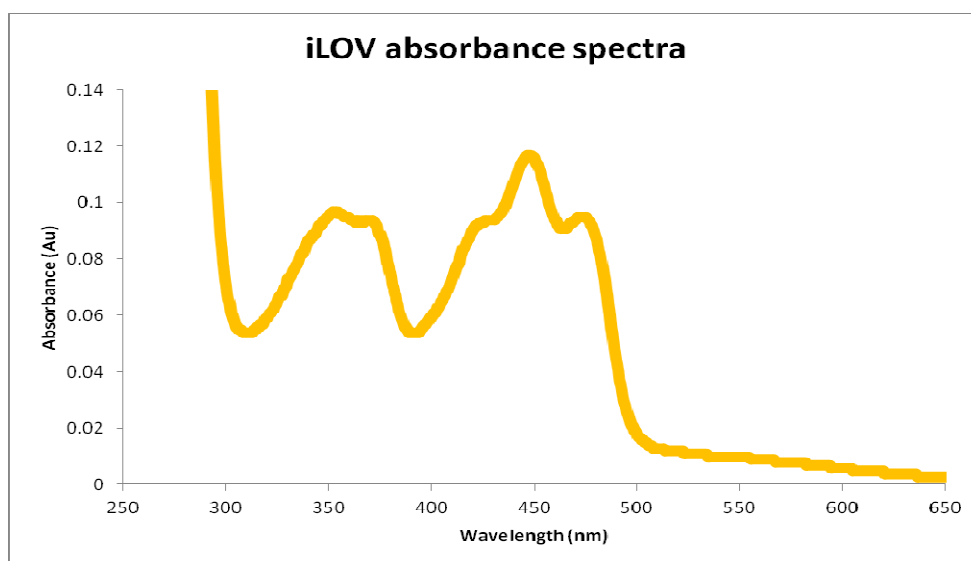


**Figure 5.9 Absorption spectra of iLOV**

iLOV absorbs in the visible region a peak at 355 nm with a shoulder at 375 nm, and a second peak at 447 nm with shoulders at 430 and 475 nm..

### 5.6.2 Expression of PscD and PscB using iLOV

Samples prepared, in section 5.4, which were not used to run on a SDS-page gel were used to have its fluorescence measured (as described in section 2.13.1 and 2.131.3). 1 ml samples were spun down at regular intervals after induction. At each time point the cell pellets were weighed and washed in water to remove any free flavin. For each of the re-suspended pellets 200  $\mu$ l of each of the sample were dispensed in a black 96 well plate (Corning) and excited at 450 nm. It was possible to calculate the expression of both PscD-CLBH and PscB-CLBH as at each time point the level of iLOV fluorescence for the intact cells and the cell weight were determined (Fig 5.10 & 5.11). PscD-CLBH showed highest fluorescence at 22°C for 16 hrs with the highest fluorescence counts at around  $3 \times 10^6$  (FU) in TB (Fig 5.10 A) as compared to when induced at 37°C, where the highest fluorescence counts were  $1.6 \times 10^6$  (FU) when induced O/N for 16 hrs in

TB (Fig 5.10 B). Whereas, PscB-CLBH showed highest fluorescence in TB at 37°C for 16 hrs with  $2 \times 10^6$  (FU) (Fig 5.11 B) as compared to when induced at 22°C, where the highest fluorescence counts were  $1.2 \times 10^6$  (FU) when induced O/N for 16 hrs in TB (Fig 5.10 B).

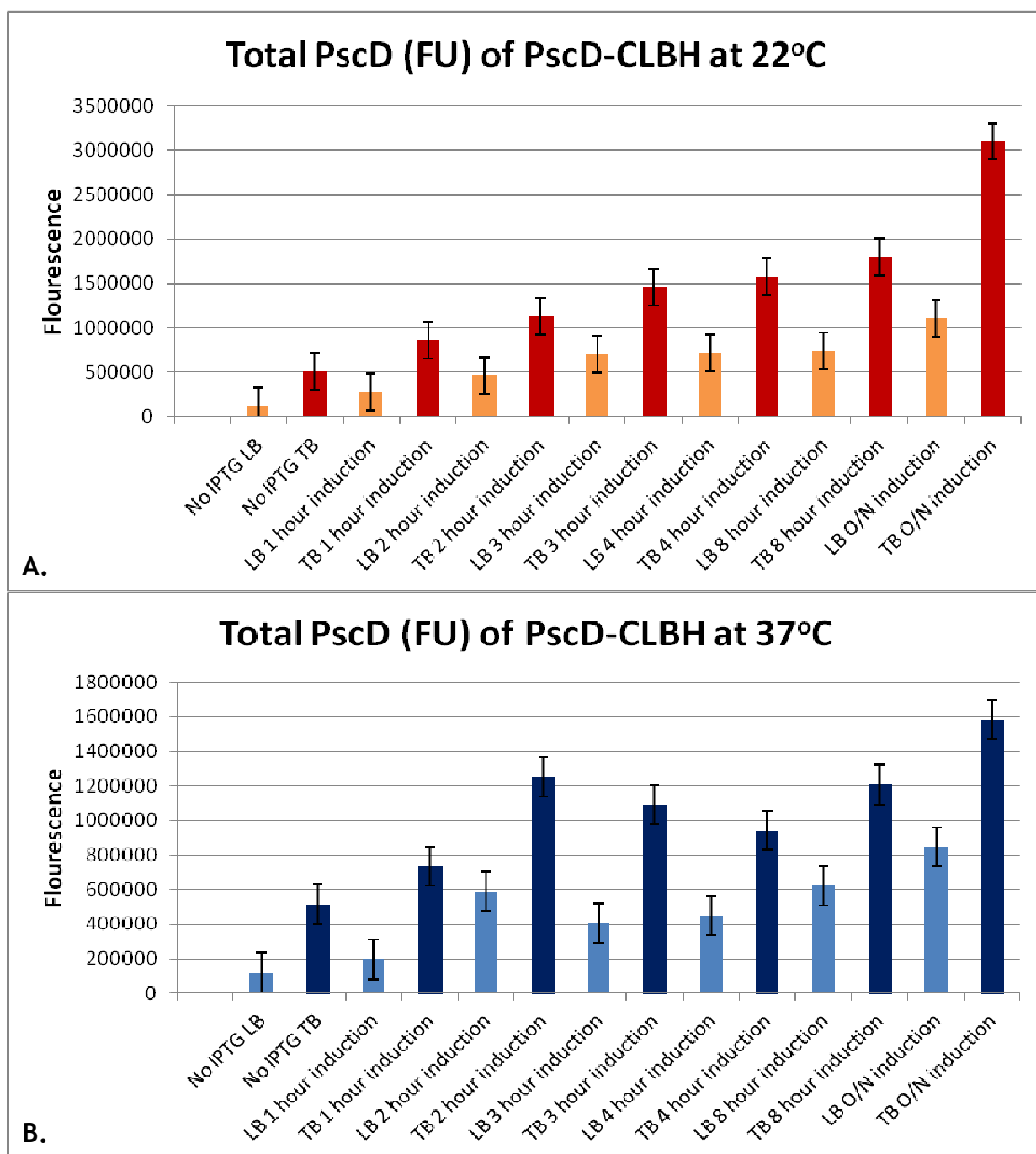


**Figure 5.10 Absorbance measurement of iLOV of PscD-CLBH taken at different time intervals, in TB and LB, at 22°C and 37°C.**

Samples were taken at regular intervals. The production level of PscD-CLBH was expressed as iLOV fluorescence per amount of wet weight of cells. **A.** Shows expression of PscD-CLBH in LB and TB when induced at 22°C. The highest fluorescence counts were seen in the TB O/N induction. **B.** Shows expression of PscD-CLBH in LB and TB when induced at 37°C. The highest fluorescence counts were seen in the TB O/N induction. Overall 22°C induction O/N in TB gave the highest fluorescence counts.

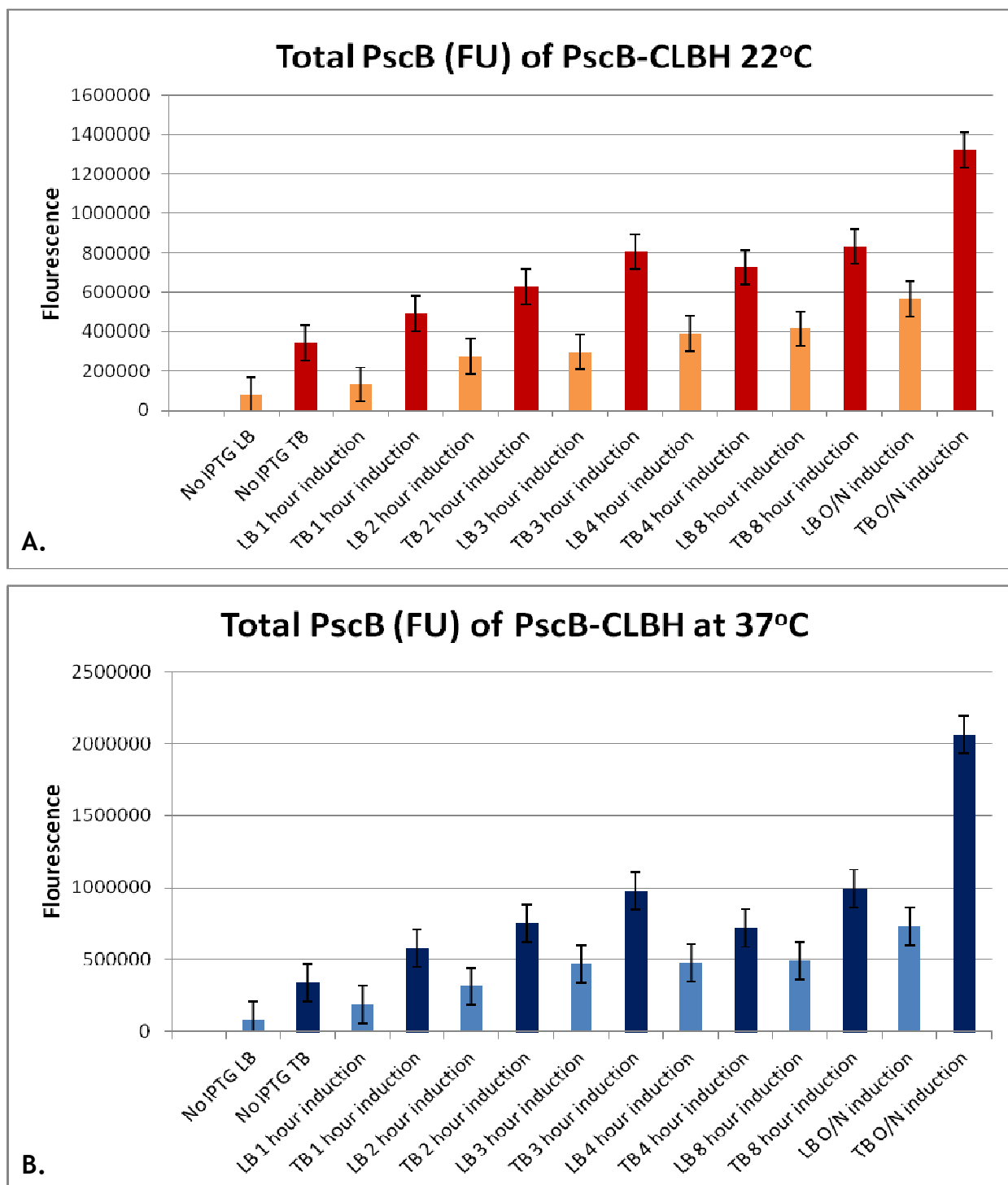


**Figure 5.11 Absorbance measurement of iLOV of PscB-CLBH taken at different time intervals, in TB and LB, at 22°C and 37°C.**

Samples were taken at regular intervals. The production level of PscB-CLBH was expressed as iLOV fluorescence per amount of wet weight of cells. **A.** Shows expression of PscB-CLBH in LB and TB when induced at 22°C. The highest fluorescence counts were seen in the TB O/N induction. **B.** Shows expression of PscB-CLBH in LB and TB when induced at 37°C. The highest fluorescence counts were seen in the TB O/N induction. Overall 37°C induction O/N in TB gave the highest fluorescence counts.

## 5.7 Expression and Purification of His tagged 3C protease for the removal of the CLBH tag

Proteases or enzymes that act on specific sites, such as the Tobacco Etch Virus (TEV) protease are commonly used to remove any purification tags once the protein of interest has been purified. This is so the tag itself will not interfere in any way with the biophysical or structural characterisation of the target protein.

As both the recombinant proteins PscD and PscB have a CLBH tag attached to the C- terminus of the proteins it is important for the removal of this large 23 kDa tag. The Fraser group had designed the removal of the CLBH tag with the use of the human rhinovirus 3C protease (HRV 3C Protease), which is a cysteine protease that recognizes the cleavage site of Leu-Glu-Val-Leu-Phe-Gln-Gly-Pro, commonly referred to as the Pre-Scission Site. It cleaves between Gln and Gly.

The His-tagged HRV 3C was a gift from the Fraser group (University of Dundee). The his tagged 3C was, readily expressed in *E. coli* and purified by immobilised metal affinity chromatography (IMAC) and size-exclusion chromatography (SEC) (as described in section 2.15). 3C protease was prepped from a -80°C glycerol sample. A 5 ml O/N culture, with appropriate antibiotic, was inoculated in to 8 x 500 ml flasks until and OD of 0.6 was reached before induction with 1 mM IPTG O/N at 22°C. Following induction, the next day, the cells were pelleted by a high speed centrifugation (12,000 x g for 30 minutes) and re-suspended in appropriate buffer to allow cell breakage by using the cell disrupter (as described in section 2.15). Broken cells were centrifuged using a sorvall (4,000 x g for 30 mins) and the supernatant was subjected to IMAC. The nickel column was washed (50mM Tris pH 8, 150mM NaCl, 50mM imidazole), and bound protein was eluted with a high imidazole buffer (50mM Tris pH 8, 150mM NaCl, 500mM imidazole). The eluted protein was concentrated and applied to a superdex 75 gel filtration column (Fig 5.12), which revealed a large peak at around 55 ml, with a shoulder on the left hand side of the main peak. The main 3C peak and the shoulder were run on a 4-12 % SDS-page gel, revealing the shoulder was from contaminants, and the main 3C peak showed a single band at around 23 kDa, which was off 3C (Fig 5.13).

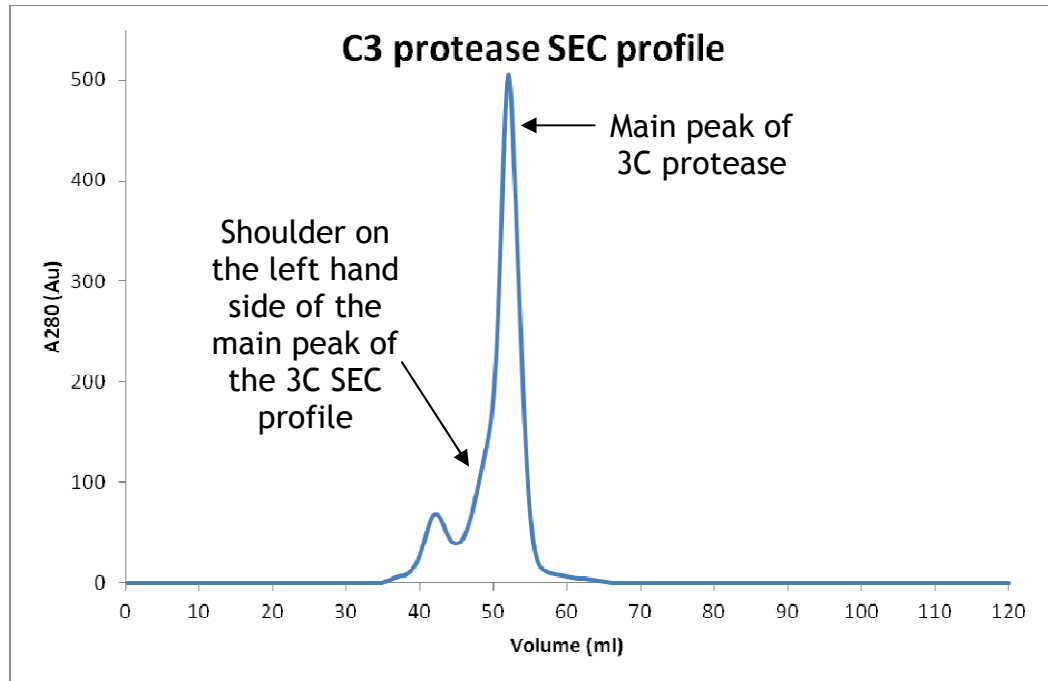


**Figure 5.12 Purification of human rhinovirus 3C protease by size exclusion chromatography**

3C protease purified by Ni<sup>2+</sup>-affinity chromatography was concentrated using a 10 kDa MWCO centricon (Sartorius), and applied to a superdex 75 gel filtration column (GE Healthcare) equilibrated with 50 mM Tris pH 8.0, 150 mM NaCl, 1 mM EDTA and 1 mM DTT. The major elution peak can be seen at around 55 ml, with a small contaminant shoulder on the left hand side of the peak.

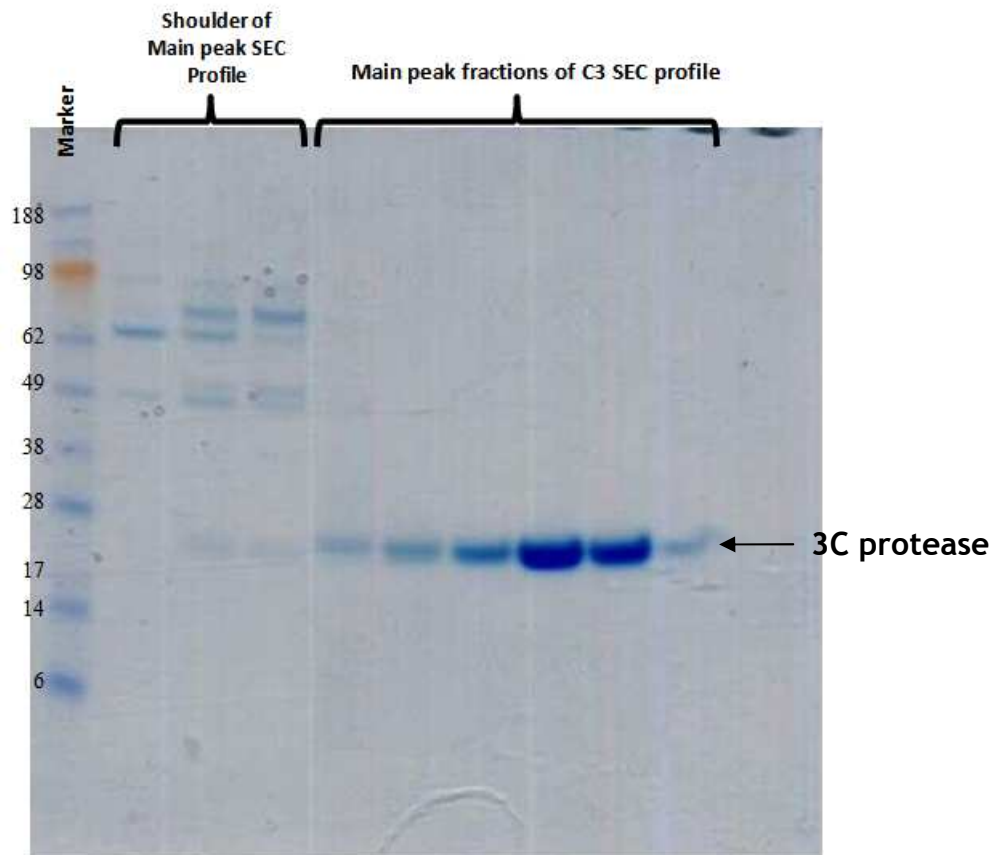


**Figure 5.13 4-12% SDS-page gel of the 3C SEC profile.**

The SDS-page gel shows the main peak fractions of the SEC profile (Fig 5.12) to contain a single band at around 23 kDa belonging to 3C. Whereas the shoulder in the left of the main peak was off contaminants.

## 5.8 Identifying the disordered segments of the PscD and PscB

Proteins that contain natively-disordered regions tend to hinder the formation of lattice contacts necessary for crystallisation and can also be difficult purifying as the protein might be unstable. By using the online disorder prediction program RONN [181] it is possible to predict the flexible regions for a protein. Just as the online program BLAST, designed by the National Centre for Biotechnology Information (NCBI), uses a query sequence to compare and then align it to that of a protein sequence, of known function, if the alignment score is high enough. RONN works on the same premise, by predicting disorder of a protein by comparing the sequence of the protein of interest to sequences of an ensemble of proteins which have had their structures resolved. The disordered regions that were identified for PscB was the N-terminus of the sequence 1-128 (Fig 5.14). For PscD the disordered regions were 1 - 26, 42 - 43, and 45 - 61 (Fig 5.15).

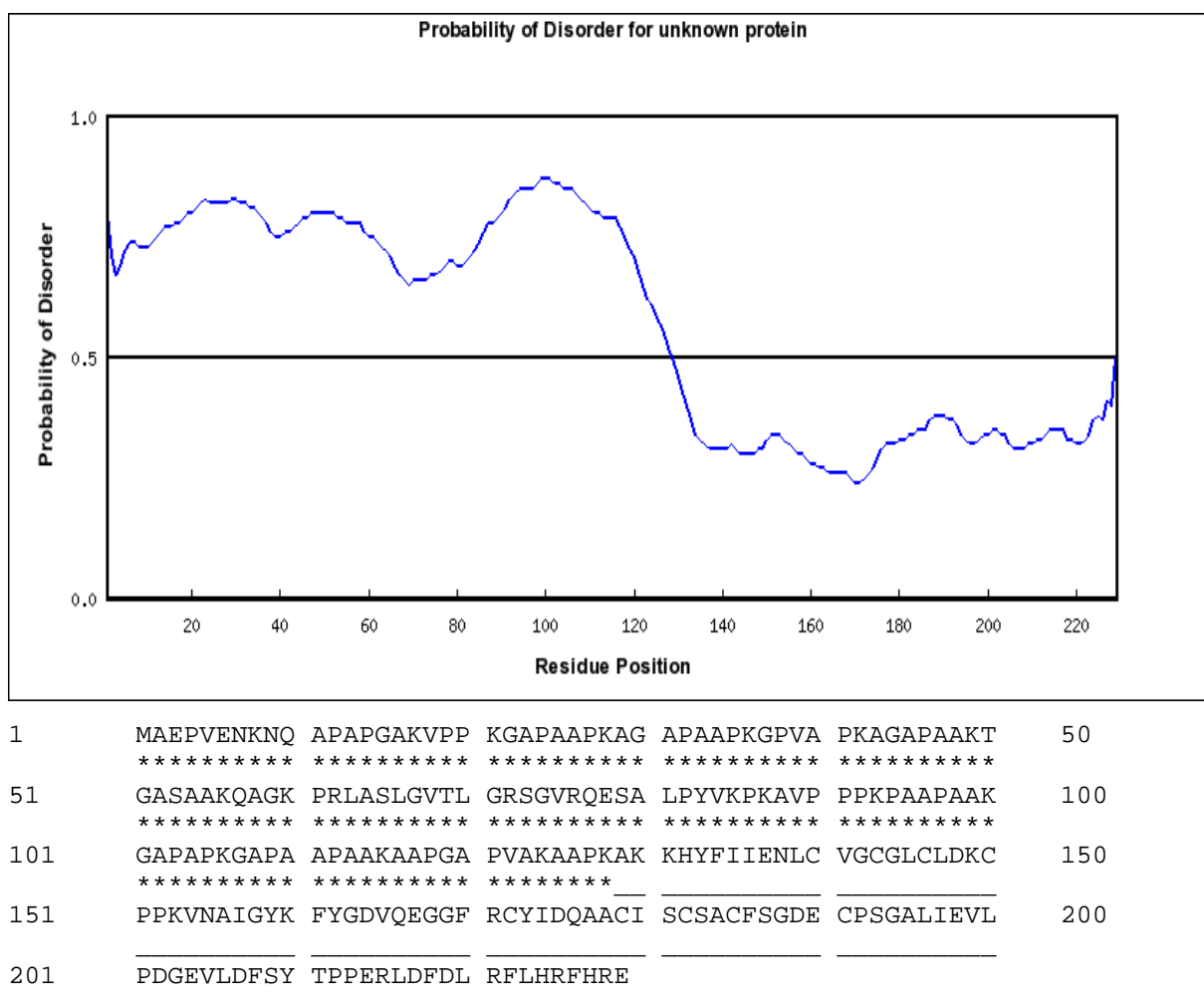


**Figure 5.14 Disorder prediction order of PscB.**

Residues 1 – 128, of PscB, are predicted to be disordered (unstructured), as observed in the sequence marked underneath by the star.

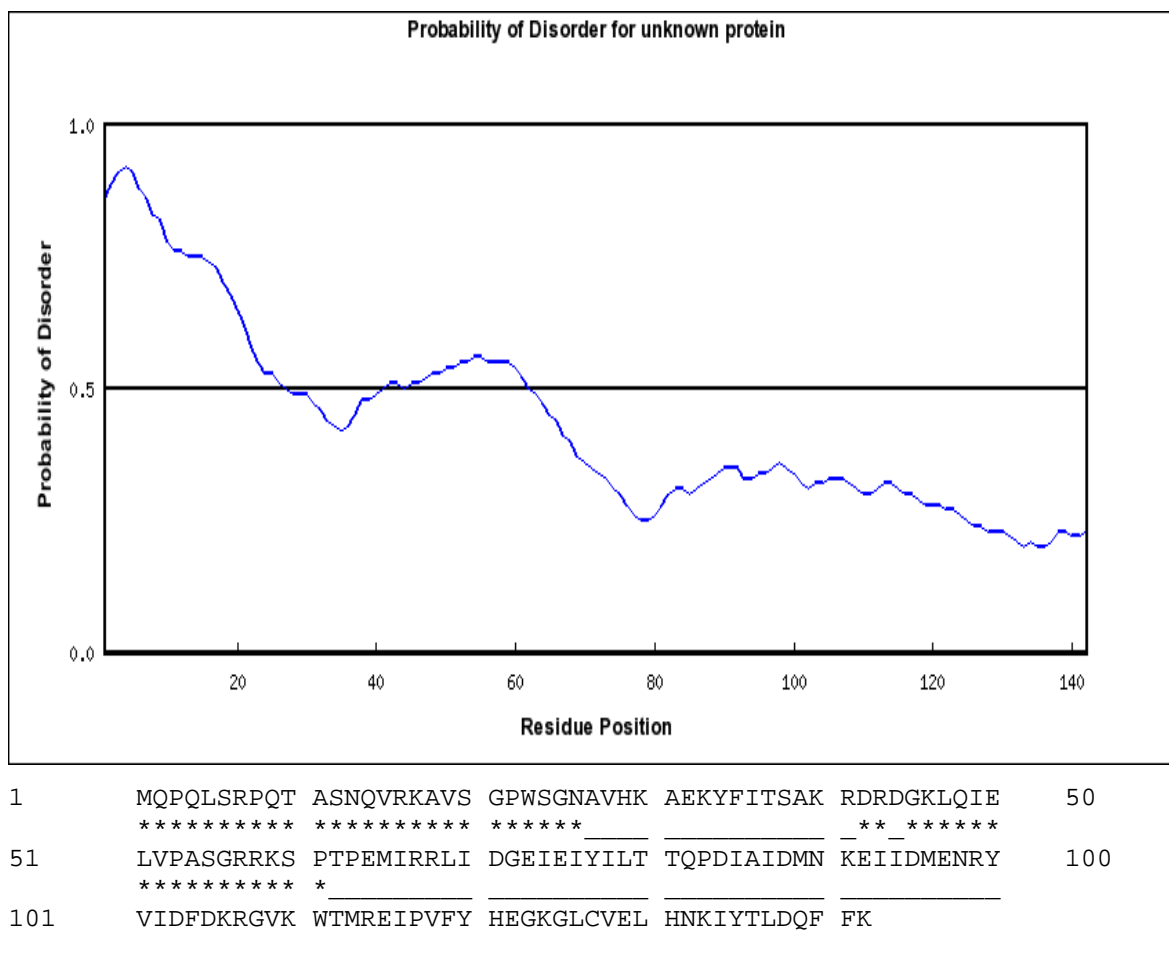


**Figure 5.15 Disorder prediction order of PscD.**

Residues 1 - 26, 42 - 43, and 45 – 61 of PscD, are predicted to be the disordered parts of the protein, as observed by the star underneath the amino acid codes of the protein sequence.

## 5.9 Purification of PscD and Cleavage of CLBH tag

After the optimal expression conditions were obtained for PscD-CLBH a large scale expression was carried out (as described in section 2.14). Results from section 5.5.2 had shown the highest fluorescence came from growing the cells in TB for 16 hrs after induction with IPTG at 22°C. This allowed for 16 x 500 ml flasks to be grown under these conditions. After 16 hr induction the cells were spun down (12, 000 x g for 30 min) and re-suspended in a buffer (50 mM NaPi pH 7.5, 150 mM NaCl, 10% Glycerol 0.1 mM EDTA) before subjecting it to 3 passes over the cell disrupter (at 20 kpsi). The broken cells were spun down (4,000 x g for 30 min) before retaining the supernatant to pass it over a nickel column (as described in section 2.14.1 & 2.14.2). Nickel purification of the PscD-CLBH protein could easily be followed by observing the fluorescence of the iLOV which was present in the CLBH tag (Fig 5.16). As the CLBH tag contains the iLOV as well as His10 tag, it was possible to observe the yellow color with the naked eye

as observed in Fig 5.16 A, were a clear difference can be seen when the supernatant is passed over the nickel column and washed with buffer containing low imidazole (50 mM NaPi pH 7.5, 300 mM NaCl, 0.1 mM EDTA, 10% Glycerol and 75 mM imidazole). Subsequently the fluorescence could be followed when the PscD-CLBH was eluted with a high imidazole buffer (50 mM NaPi pH 7.5, 150 mM NaCl, 0.1 mM EDTA, 10% Glycerol and 500 mM imidazole) and was held under a UV light (Fig 5.16 B).

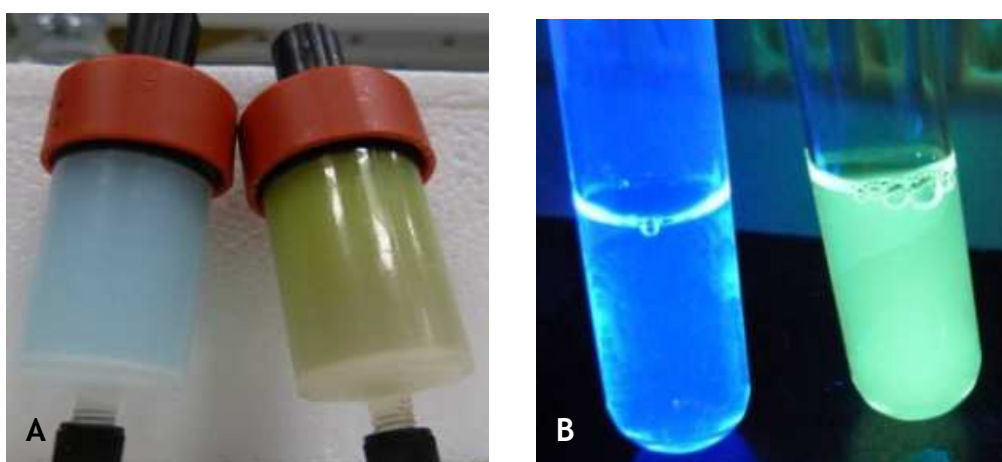


**Figure 5.16 Fluorescence of iLOV from the CLBH tag during IMAC.**

A. Nickel column before (left hand side) and after (Right hand side) binding of PscD-CLBH. B. Elution of PscD-CLBH, fluorescence detected by UV exposure (on right hand side).

After elution of PscD-CLBH, PscD-CLBH was buffer exchanged in to a buffer containing no imidazole (50 mM NaPi pH 7.5, 150 mM NaCl, and 10% Glycerol), for the cleavage of the CLBH tag using the 3C protease purified in section 5.6 (as described in the methods and materials in section 2.14.3). The PscD-CLBH was left incubating O/N at 4°C with the 3C protease with the addition of 1 mM DTT and 1 mM EDTA. The O/N cleaved sample was then buffer exchanged in to a buffer containing no DTT or EDTA (50 mM NaPi pH 7.5, 150 mM NaCl, and 10% Glycerol) as the DTT would have reduced the nickel resin and the EDTA would have chelated it. The sample was then retained to pass back over the nickel column to separate the CLBH and 3C protease from the PscD protein.

Nickel purification and the 3C cleavage were analysed on a 4-12% SDS-page gel (Fig 5.17). The Nickel purification was analysed from lanes 2-5 in fig 5.15, were bands corresponding to the 40 kDa PscD-CLBH (lane 5) could be observed. After cleavage of PscD-CLBH (Fig. 5.17, lanes 6) a band corresponding to the MW of PscD was observed (17 kDa) with no longer any 40 kDa band observed in lane 6 of fig 5.17. When the cleaved CLBH tag was passed over the nickel column the hope

was the cleaved CLBH tag and the 3C would stay bound to the nickel column and the PscD would elute off, which was not the case as observed in Fig 5.17 lane 7. The amount of PscD protein recovered from the column was less than expected relative to the amount of fluorescence. The hypothesis was that cleaved PscD weakly bound to the nickel column as PscD contains two Histidines on the -C terminus and one on the -N terminus. This was investigated when the cleaved PscD-CLBH and the 3C was eluted of the nickel column (Fig 5.17 lane 8) and buffer exchanged back in to a no imidazole buffer, and then passing it back over the nickel column. By washing the nickel column with buffer containing a low imidazole concentration (50 mM NaPi pH 7.5, 150 mM NaCl, 0.1 mM EDTA, 20 mM imidazole) a band corresponding to the MW of PscD at around 17 kDa was observed (Fig 5.17 lane 9). And once the CLBH tag and the 3C protease was eluted of the column there was no longer any band that corresponded to the 17 kDa band was observed. Once PscD had been eluted, the band was excised and analysed by Mass spec (University of Dundee) to confirm the presence of PscD.

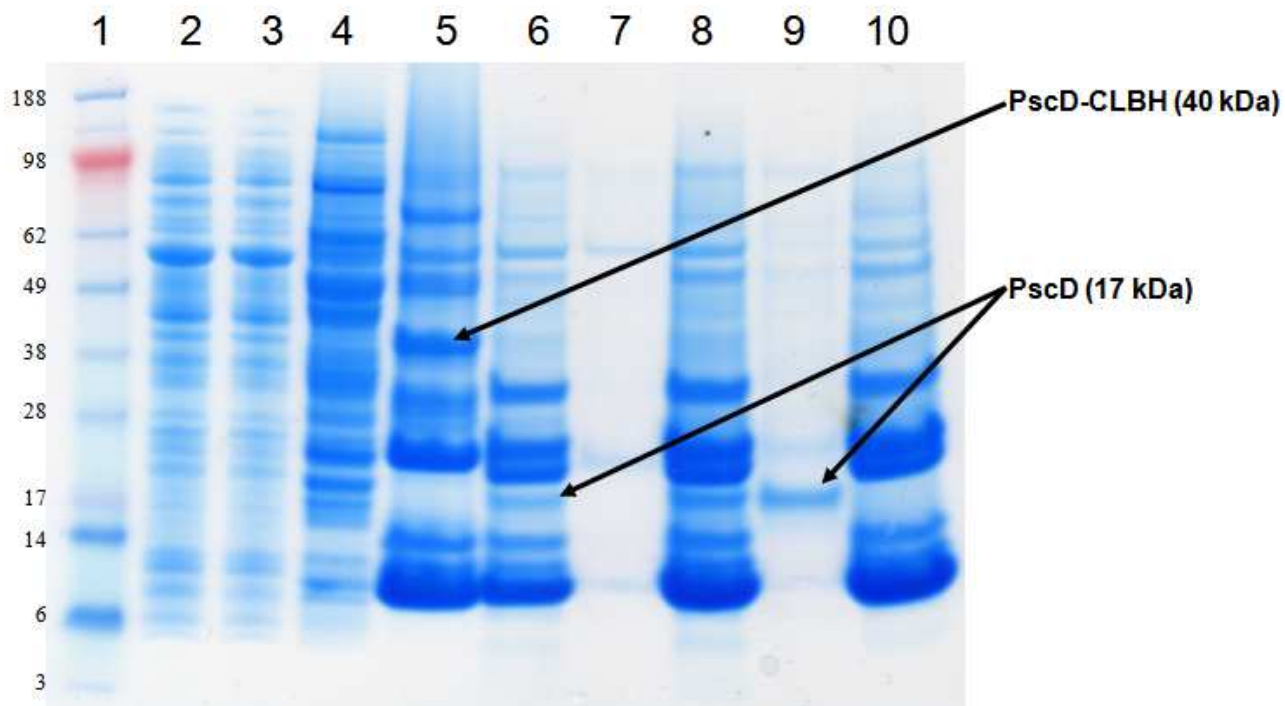


**Figure 5.17 4-12% SDS-page analysis of PscD Nickel purification and 3C cleavage**

**Lane 1.** M/W (SeeBlue Plus2 Pre-Stained Standard). **Lane 2.** Loading sample (supernatant) loaded on nickel column. **Lane 3.** Flow through from nickel column. **Lane 4.** Nickel Wash (50mM NaP pH 7.5, 300mM NaCl, 0.1mM EDTA, 75mM imidazole) to remove unspecific bound proteins. **Lane 5.** Elution (50mM NaP pH 7.5, 150mM NaCl, 0.1mM EDTA, 500mM imidazole) Showing a band 40 kDa belonging to PscD-CLBH. **Lane 6.** PscD-CLBH elution from Nickel column plus the addition of the 3C protease before passing back over the nickel column, a band corresponding to the MW of PscD is observed at around 17 kDa. **Lane 7.** Cleaved CLBH tag from PscD passed back over Nickel Column (Unbound). **Lane 8.** Elution of Bound CLBH + PscD. **Lane 9.** Eluted CLBH, Buffer exchanged into no imidazole and passed back over Column (Nickel) and then washed with 50 mM imidazole in NaP buffer. Pure PscD 17 kDa band observed. **Lane 10.** Elution of bound CLBH tag, no longer band observed at around 17 kDa.

Further analysis to prove 3C protease had cleaved the CLBH tag was confirmed by western blot using an iLOV antibody, a gift from Prof John Christie (as described in section 2.14.6). The IMAC purification fractions of PscD-CLBH were run on a 4-12% SDS-page gel as well as the 3C cleavage of the CLBH tag (Fig 5.18). Initially a distinct band at 40 kDa representing PscD-CLBH was observed in lanes 2 and 5 of fig 5.18. Lane 2 represents the loading sample of the supernatant on to the nickel column which contains the PscD-CLBH. Lane 5 represents the elution sample of the nickel column. Post-cleavage a band representing CLBH at 23 kDa was observed in lane 6 (Fig 5.18), showing that the cleavage of CLBH was taking place.

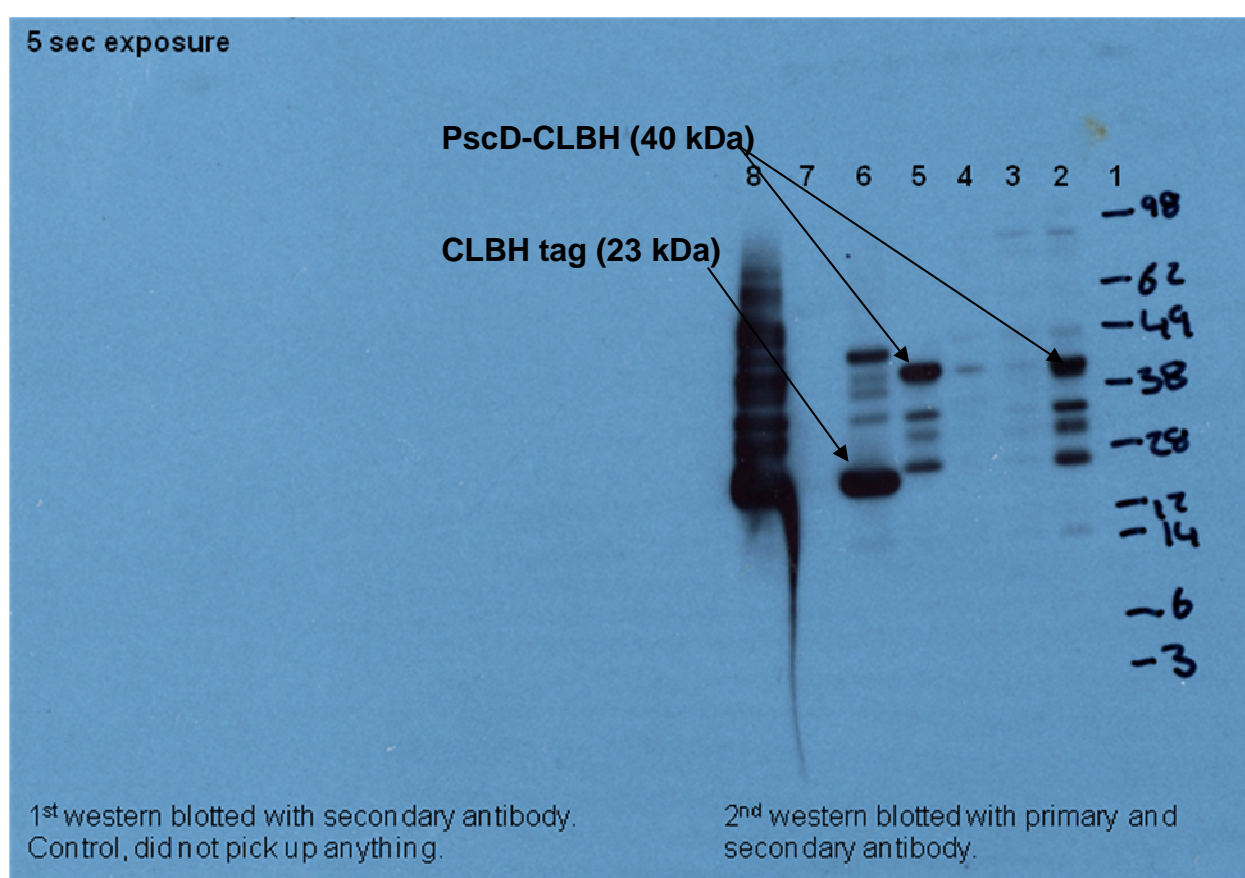


**Figure 5.18 Western blot analysis using the polyclonal iLOV antibody CLBH**

**Lane 1.** M/W (SeeBlue Plus2 Pre-Stained Standard). **Lane 2.** Loading sample (supernatant) loaded on nickel column. **Lane 3.** Flow through from nickel column. **Lane 4.** Nickel Wash (50mM NaP pH 7.5, 300mM NaCl, 0.1mM EDTA, 75mM imidazole) to remove unspecific bound proteins. **Lane 5.** Elution (50mM NaP pH 7.5, 150mM NaCl, 0.1mM EDTA, 500mM imidazole) Showing a band at 40 kDa belonging to PscD-CLBH. **Lane 6.** PscD-CLBH elution from Nickel column plus the addition of the 3C protease before passing back over the nickel column, a band corresponding to the MW of the CLBH tag is observed at around 23 kDa. **Lane 7.** Cleaved CLBH tag from PscD passed back over Nickel Column (Unbound). **Lane 8.** Elution of Bound CLBH + PscD. Overloaded well, unspecific binding of antibody to proteins.

## 5.10 Purification of PscB & challenges with the CLBH-tag

Unlike PscD, which contains no pigments, PscB does. PscB of *C. tepidum* is an iron sulphur protein. Mössbauer and colleagues had shown through spectroscopical analysis that recombinant PscB contains a heterogeneous mixture of  $[4\text{Fe-4S}]^{2+,1+}$  and other types of Fe/S clusters tentatively identified as  $[2\text{Fe-2S}]^{2+,1+}$  clusters and rubredoxin-like  $\text{Fe}^{3+,2+}$  centers [97].

As the optimal expression conditions were obtained for PscB-CLBH a large scale expression was carried out (as described in section 2.14). Results from section 5.5.2 had shown the highest fluorescence came from growing the cells in TB for 16 hrs after induction with IPTG at 37°C. The fluorescence here however also was considerably less than that of PscD-CLBH when induced at 22°C for 16 hrs. This is due to expressing Iron-sulphur proteins in *E. coli*, which are naturally not ideal hosts for such proteins to be expressed as they don't fully have the correct posttranslational modification machinery. 24 x 500 ml flasks were grown of PscB-CLBH. After 16 hr induction the cells were spun down (12, 000 x g for 30 min) and re-suspended in a buffer (50 mM NaPi pH 7.5, 150 mM NaCl, 10% Glycerol 0.1 mM EDTA) before subjecting it to 3 passes over the cell disrupter (at 20 kpsi).

The broken cells were spun down (4,000 x g for 30 min) before retaining the supernatant to pass it over a nickel column (as described in section 2.14.1 & 2.14.2). Like PscD-CLBH, PscB-CLBH could be seen due to the iLOV (Fig 5.16). The sample, after elution, could also have its absorption measured, which would reveal the presence of the iLOV absorption as seen in figure 5.9 and figure 5.19 (yellow line), with the iLOV absorption maximum occurring at 378 nm, with a shoulder on the right hand side and the absorption maximum in the blue region of the spectrum at 447 nm with shoulders on the left and right hand side for iLOV. This was true for PscD-CLBH, but as PscB contains an iron sulphur protein, it will have additional absorption bands (Fig 5.19, purple line). Iron sulphur proteins tend to have absorption bands at 315 nm and at 415 nm, the iron (Fe) itself absorbs at 315 nm [182]. Figure 5.19 depicts the difference of the iLOV from the CLBH tag (yellow line) and the absorption of PscB-CLBH (purple line). The left hand shoulder of the 447 nm peak of iLOV, which absorbs at around 430 nm has shifted to 415 nm, and the 378 nm peak cannot be observed as it is

masked along with the absorption of the 315 nm peak from the PscB protein. This concluded that expression of the PscB-CLBH was successful and that PscB-CLBH could be Nickel purified.

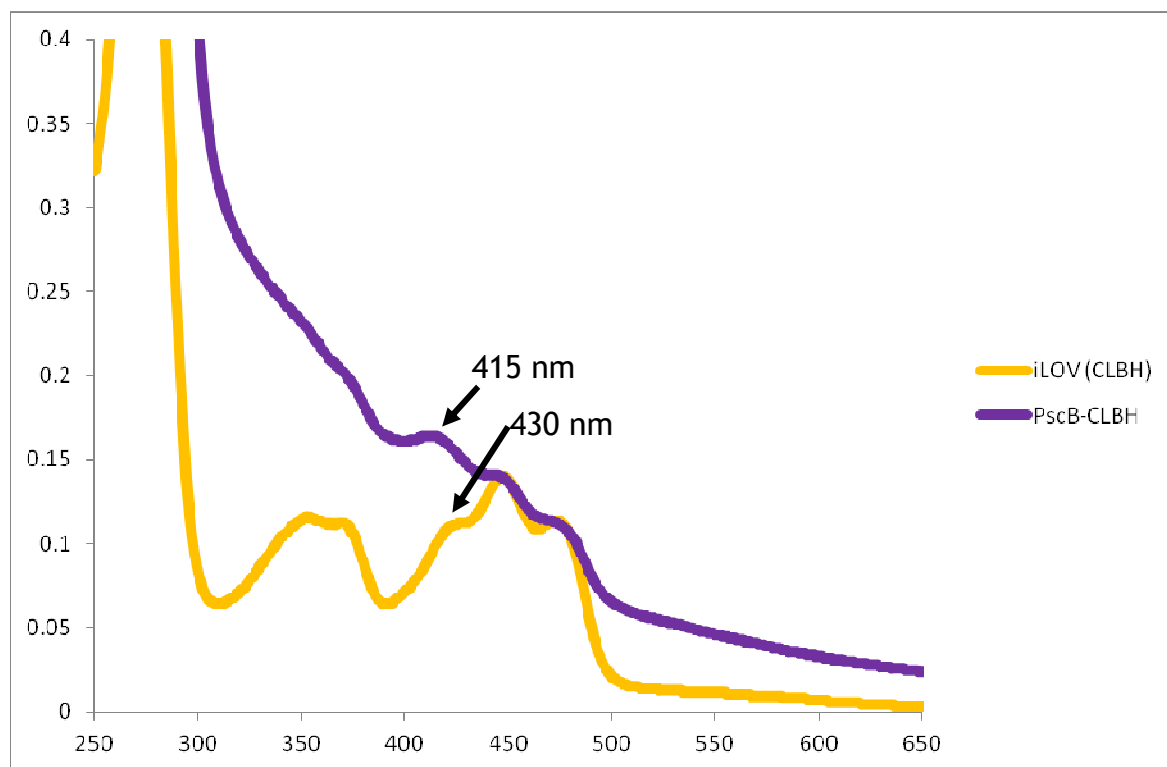


**Figure 5.19 Absorption Spectra comparison of iLOV from the CLBH tag and PscB-CLBH.** iLOV (yellow line) absorbs in the visible region a peak at 355 nm with a shoulder at 375 nm, and a second peak at 447 nm with shoulders at 430 and 475 nm. PscB-CLBH (purple line) shows the an absorption peak from the PscB at 415 nm, the 447 nm with shoulder on the right at 475 nm is still observed.

As PscB-CLBH could be Nickel purified, the next step was to cleave of the CLBH tag, which proved to be more challenging. The PscB-CLBH was incubated with the 3C protease in the same way as PscD-CLBH tag (as described in section 5.8). This however did successfully cleave the CLBH tag from PscB but had left no presence of the target protein. After cleavage there was no sign of the PscB on a SDS-page gel stained with commasie and silver stain, and also there was no indication through measuring the spectral absorption of the elute after cleavage that PscB was present as there was no indication of the 315 nm and the 415 nm peak. It was concluded, that the presence of the 3C, DTT and the EDTA necessary for the cleavage of the CLBH tag was in some way having an adverse effect on the PscB protein. Since optimal expression conditions had been found for PscB-CLBH, it was decided that the PscB would be put in to a pET28a (novagen) vector, without the presence of the CLBH tag. And since the PscB

protein was pigmented and had a unique absorption spectra it would be easier to assess if the protein was pure and present.

Optimal expression conditions for the PscB-CLBH was in TB induced O/N at 37°C. The new construct with just PscB was expressed exactly the same way. After the optimal expression conditions were obtained for PscB, a large scale expression was carried out. Nickel purification of the PscB protein could easily be followed by observing the brown colour, yielding high amount of PscB (Figure 13). After 16 hr induction the cells were spun down (12, 000 x g for 30 min) and re-suspended in a buffer (50 mM NaPi pH 7.5, 150 mM NaCl, 10% Glycerol 0.1 mM EDTA) before subjecting it to 3 passes over the cell disrupter (at 20 kpsi). The broken cells were spun down (4,000 x g for 30 min) before retaining the supernatant to pass it over a nickel column (as described in section 2.14.1 & 2.14.2). The supernatant was passed over the nickel column and washed with buffer containing low imidazole (50 mM NaPi pH 7.5, 300 mM NaCl, 0.1 mM EDTA, 10% Glycerol and 50 mM imidazole). After the wash any proteins was eluted with a high imidazole wash (50 mM NaPi pH 7.5, 150 mM NaCl, 0.1 mM EDTA, 10% Glycerol and 500 mM imidazole). The Nickel samples were run on a 4-12% SDS-page gel (Fig 5.20 A), were a band (in the elution lane) is observed at the MW of PscB (23 kDa) this was confirmed by mass spec. When the elution sample was concentrated a brown color was observed (Fig 5.20 B), indicative of Iron-sulphur proteins.

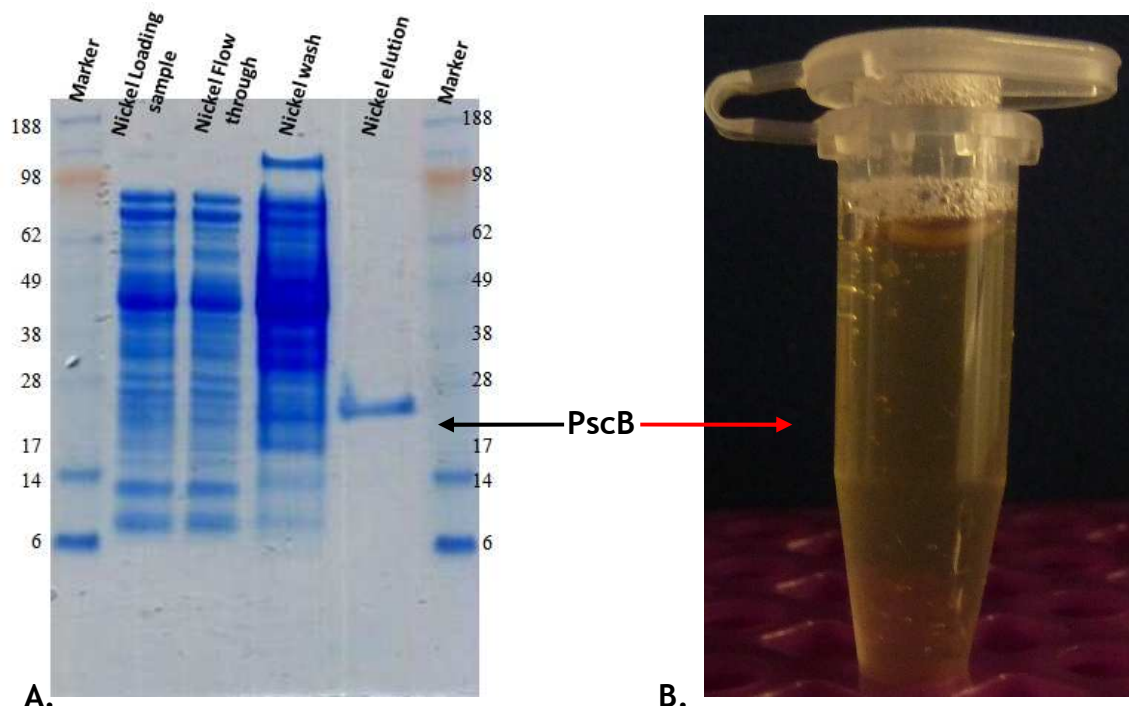


**Figure 5.20** 4-12% SDS-page analysis of PscB nickel purification and the PscB pigmented sample.

**A.** Shows an SDS-page gel, where the Nickel elution lane shows a band at around 23 kDa, which is the MW of PscB. **B.** Shows the eluted sample of the Nickel column after concentrating, a brown color can be seen indicative of iron-sulphur proteins.

The presence of PscB was also confirmed by measuring the absorption after elution (Fig 5.21) were peaks at around 315 nm and 415 nm for PscB were observed (Fig 5.21 A), indicative of PscB. This was compared with the absorption of PscB-CLBH and the CLBH tag by itself (Fig 5.21 B). This showed the 430 nm peak in the iLOV spectra (yellow line) which had shifted to 415 nm in the PscB-CLBH spectra (purple line), was still present when expressed and purified in the PscB absorption spectra by itself (red line).

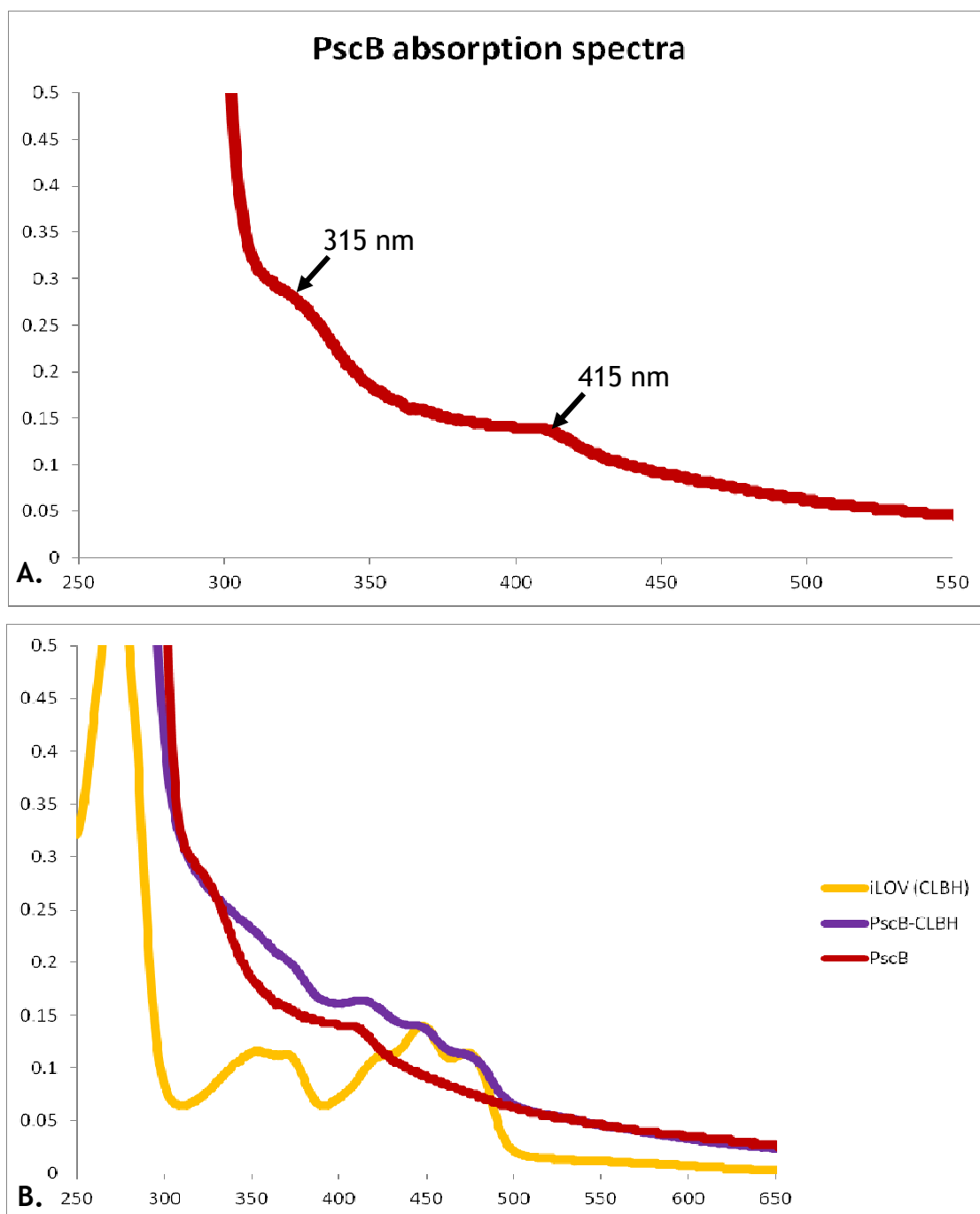


**Figure 5.21 Absorption spectra of PscB, PscB-CLBH and the iLOV from the CLBH tag.** **A.** Shows the absorption spectra of purified PscB with peaks at 315 and 415 nm. **B.** Shows the comparison of PscB (Red line, purified without the CLBH tag), PscB-CLBH (Purple line) and iLOV (yellow line). The 415 nm peak can be observed in both the PscB and the PscB-CLBH.

## 5.11 PscD CD (circular dichroism)

Circular dichroism (CD) spectropolarimetry measurements were used to confirm that PscD was folded in solution and to assess its conformation at low resolution. Near UV CD spectra was used to provide information on the tertiary structure of proteins when they contain aromatic amino acids held rigidly in an asymmetric environment (Fig 5.23). Far UV CD spectra provided important information on

overall secondary structure composition (%  $\alpha$ -helix,  $\beta$ -sheet, turns, etc) arising from the geometry of the peptide backbone. The far UV CD spectrum (Fig 5.22) was analysed using DICHROWEB (an online server with access to algorithms for the estimation of protein secondary structure content from CD spectra). The CONTIN LL algorithm was used to analyse data between 260-190nm. The secondary structure estimates obtained suggested that PscD contains around 30.4%  $\alpha$ -helix, 25.3%  $\beta$ -sheet, 21.6% turns, and 28.7% unordered. These estimates are dependent upon accuracy of protein concentration determination, purity and signal to noise ratios.

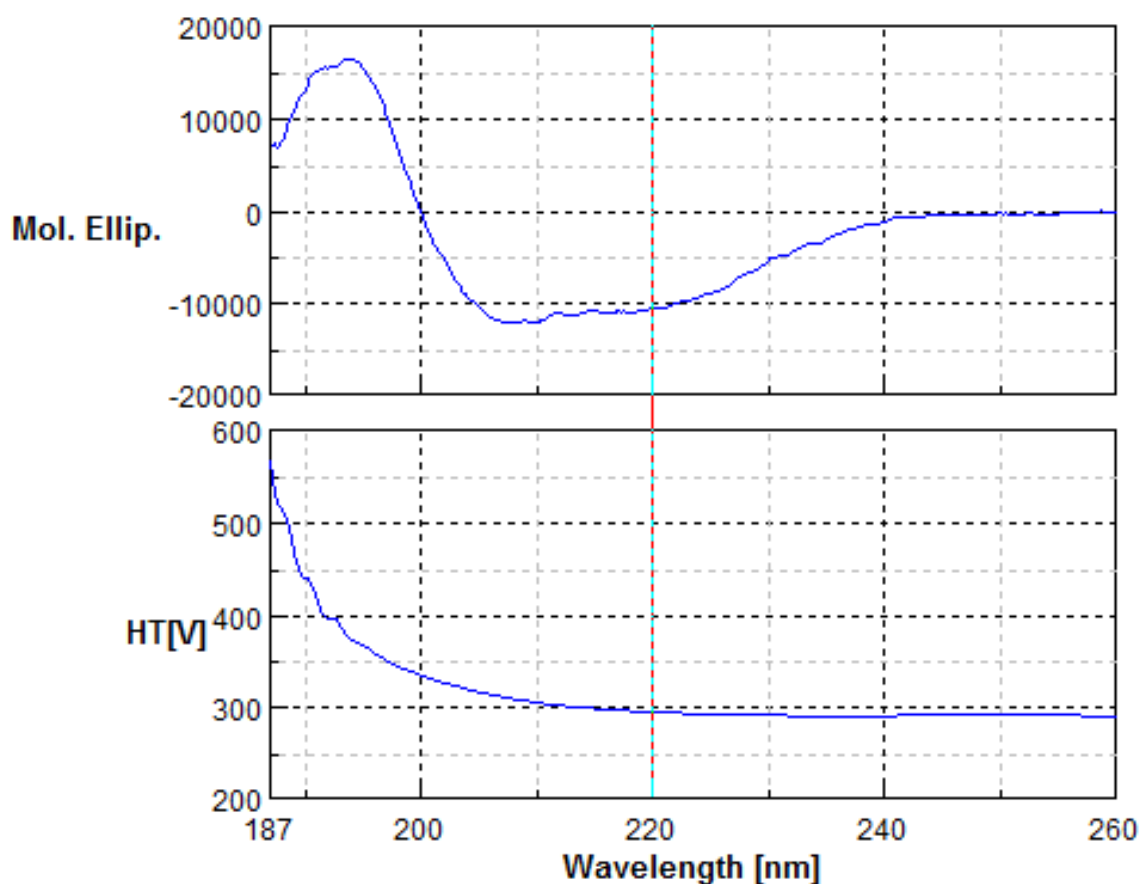


**Figure 5.22 Far UV CD spectrum of PscD**

This spectrum was measured using a protein concentration of 0.24mg/ml and a cell pathlength of 0.02cm.

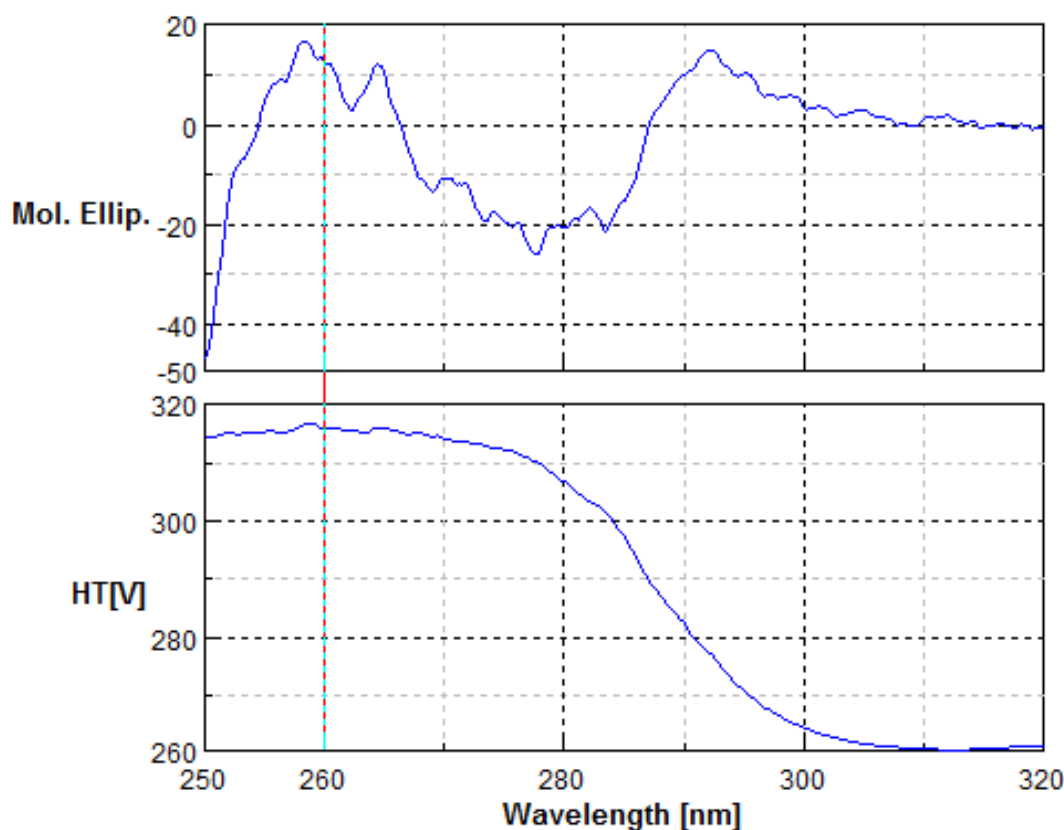


**Figure 5.23** Near UV CD spectrum of PscD

This spectrum was measured using a protein concentration of 0.8mg/ml and a cell pathlength of 0.5cm.

## 5.12 PscD and PscB homology modelling

As well as the structures for both PscB and PscD, the function of PscD is still unknown. To look in to the functionality both PscD and PscB were compared to that of their homologues in different organisms to give more of an idea of how these proteins function.

### 5.12.1 PscD

Due to the absence of co-factors the function of PscD has been difficult to elucidate. The 3D imaging analysis with the electron microscopic technique (STEM) suggested that PscD was in contact with the FMO protein on the cytoplasmic side [161]. Although PscD has been assumed to function in the same way as PsaD in photosystem I, as judged from their sequence similarities [183], there has never been any scientific evidence to back this. Since the amino acid sequences of PscD has been shown to have similarities to those of that of PsaD of photosystem I, PscD had been thought to stabilise the iron sulphur protein for the docking of ferredoxin (electron acceptor). Oh-Oka and colleagues had shown

that PscD resides in the vicinity of PscB, on the cytoplasmic side of RC, and that this topology appears to be similar to the case of PsaD in photosystem I [121].

The amino acid sequences of the PscD in *C. tepidum* show significant similarities to those of the PsaD subunit in photosystem I (Fig 5.24). Even though these similarities are low, their polypeptides have about the same numbers of amino acid residues (around 140 amino acid residues) containing charged basic residues distributed evenly throughout the sequences.

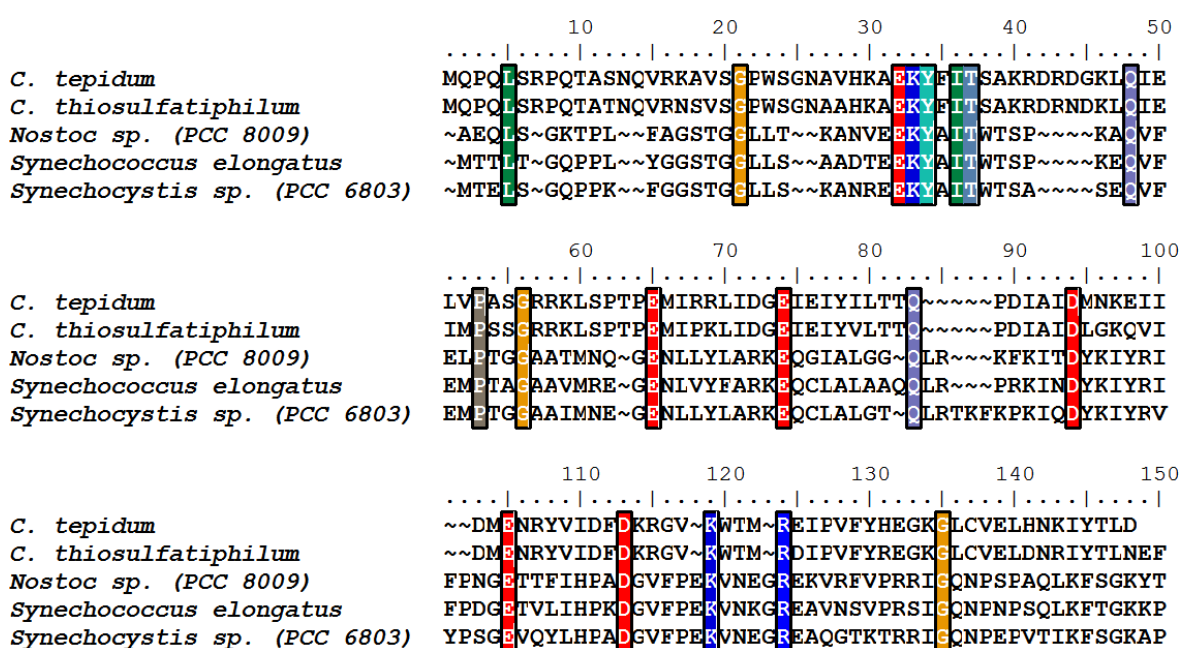


**Figure 5.24** Sequence alignment of the *C. tepidum* PscD amino acid sequences with PsaD from photosystem I from different organisms.

Amino acid residues, which show similarities, are in colored boxes. Most of the residues are charged basic residues.

Homology modelling using the Phyre2 fold recognition server [184], showed the protein to have two  $\alpha$ -helices with eight  $\beta$ -sheets (Fig 5.25 A). This structure was produced using the trap dicarboxylate transporter, dctp subunit, which is a transport protein. The PscD structure produced had a 67.1% confidence value, even though this confidence value is not very high the secondary structure prediction of PscD showed the  $\beta$ -strands and the  $\alpha$ -helices to be of high confidence (Fig 5.25 B)



With the use of the the three-dimensional structure of the PsaD from the photosystem I RC complex, the structure of the PscD complex, from figure 5.25 A. could be roughly depicted/aligned to the PsaD (Fig 5.26). The structural homology modeling of PscD, which is shown in figure 5.26, was conducted on the basis of sequence alignment and the structure comparison of PsaD of *Synechococcus elongatus* and the PscD structure produced with Phyre2. This was carried out using the software Deepview-SWISS-modeller [185]. Once a predicted structure was made using Deepview, the structure was imported in to Pymol to show the alignment of PscD to PsaD of photosystem I (Figure 5.26 B). The predicted structure of PscD in indicates that its C-terminal portion containing a conserved lysine residue (corresponding to lysine 106 in PsaD), which was considered to be involved in the direct interaction with Fd in photosystem I, surrounds the surface of the  $F_A/F_B$  protein and that its exposed surface to solvent could be easily accessible by ferredoxin. Since the C-terminal portion of PscD is also rich in charged amino acid residues, it seems nevertheless to regulate and/or enhance the reactivity with ferredoxin. The N-terminal portion of PscD, on the other hand, may bind a trimer of FMO protein, although the structural information of  $F_A/F_B$ -containing PscB is still lacking.

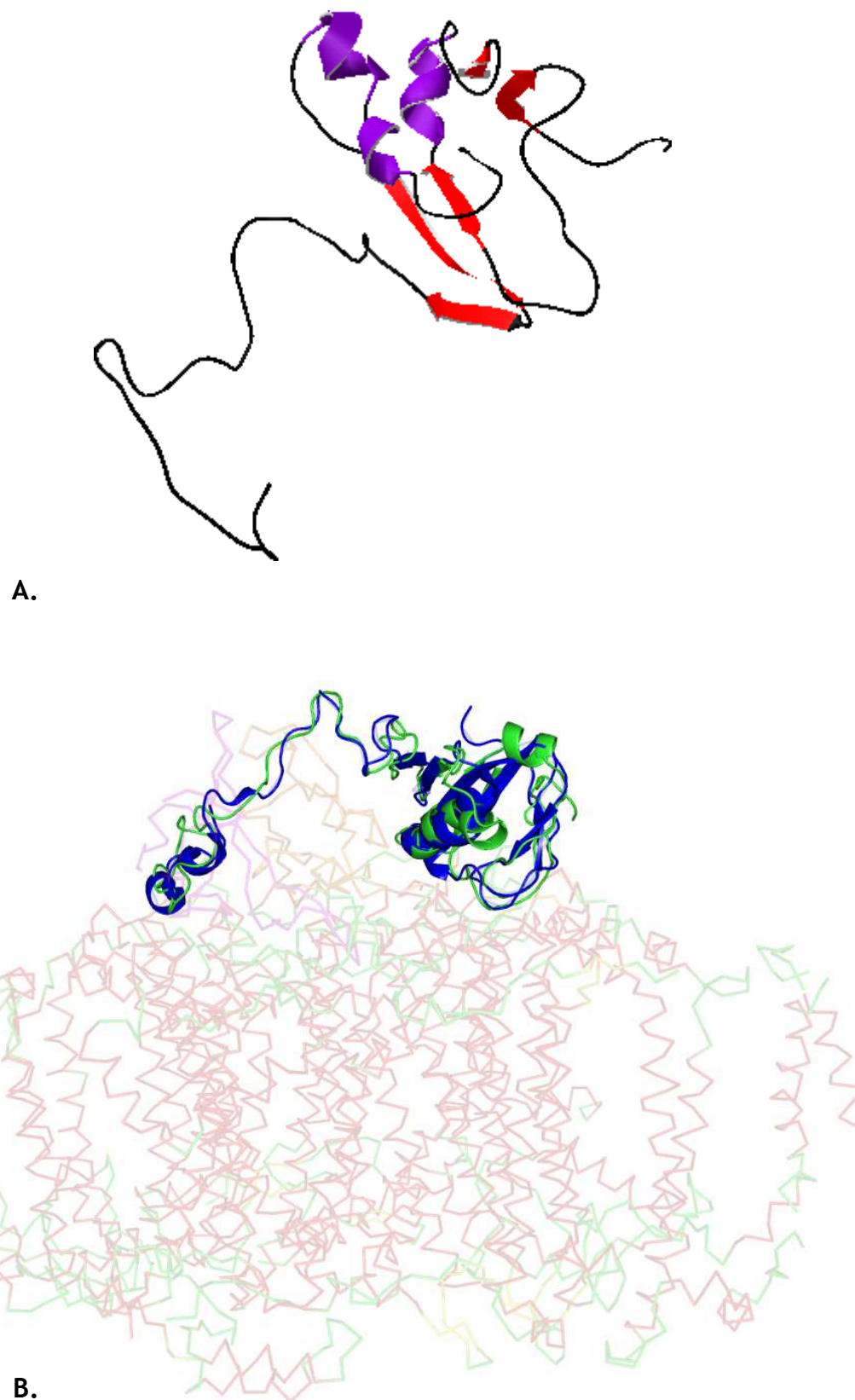


**Figure 5.26 structural homology modeling of PscD in comparison to PsaD.**

**A.** The modeling of PscD was conducted using Deepview with the structure of PsaD in photosystem I RC of *S. elongatus*. **B.** The predicted structure of PscD was represented by a *green ribbon*. PsaA and PsaB were *colored* in red ribbon, respectively. PsaD was represented in blue.



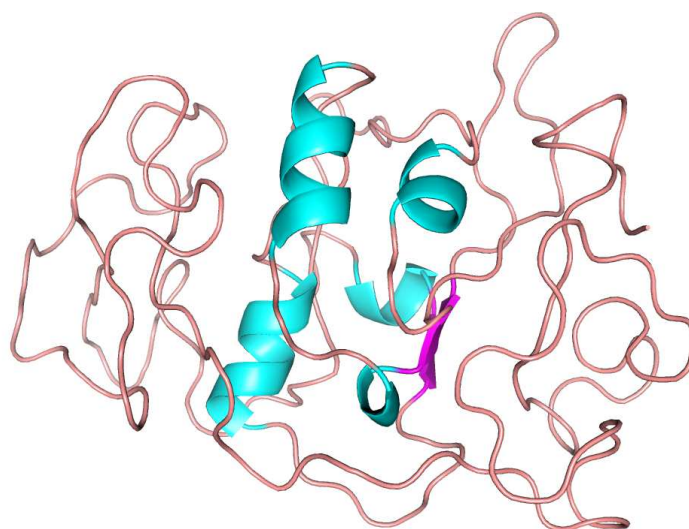


**Figure 5.28 Phyre2 homology model of PscB with secondary structure prediction**

**A.** Shows homology model produced with 99.6% confidence. **B.** Secondary structure prediction produced by Phyre2. All the beta strands and alpha helices have high confidence values.

### 5.13 Expression and purification of Ferredoxin from *Arabidopsis thaliana* for binding experiments

To show that ferredoxin and PscD may interact with each other, for binding experiments it is important that high quantities of ferredoxin is firstly obtained.

The ferredoxin construct (pET21a NOVAGEN) was a gift from Rhys Grinter (Walker group, University of Glasgow). The ferredoxin, isolated from *Arabidopsis thaliana* was expressed and purified as described in section 2.17. Ferredoxin was grown in 8 x 500 ml flasks at 37°C until an OD of 0.6 was reached and then was induced with IPTG (1 mM) and was left to induce O/N at 28°C. Following induction, the next day, the cells were spun down and resuspended in cell breakage buffer (50 mM NaPi pH 7.5, 150 mM NaCl, 10% Glycerol 0.1 mM EDTA) before subjecting it to 3 passes through the cell disrupter (at 20 kpsi). The broken cells were spun down (4,000 x g for 30 min) before retaining the supernatant to pass it over a nickel column (as described in section 2.14.1 & 2.14.2). Nickel purification of the ferredoxin protein could easily be followed by observing the brown colour bound to the nickel column (Fig 5.29 A). The ferredoxin was eluted with a high imidazole buffer (50 mM NaPi pH 7.5, 150 mM NaCl, and 500 mM imidazole) and was concentrated before passing over the size exclusion column (Superdex S-75) (Fig 5.29 B).

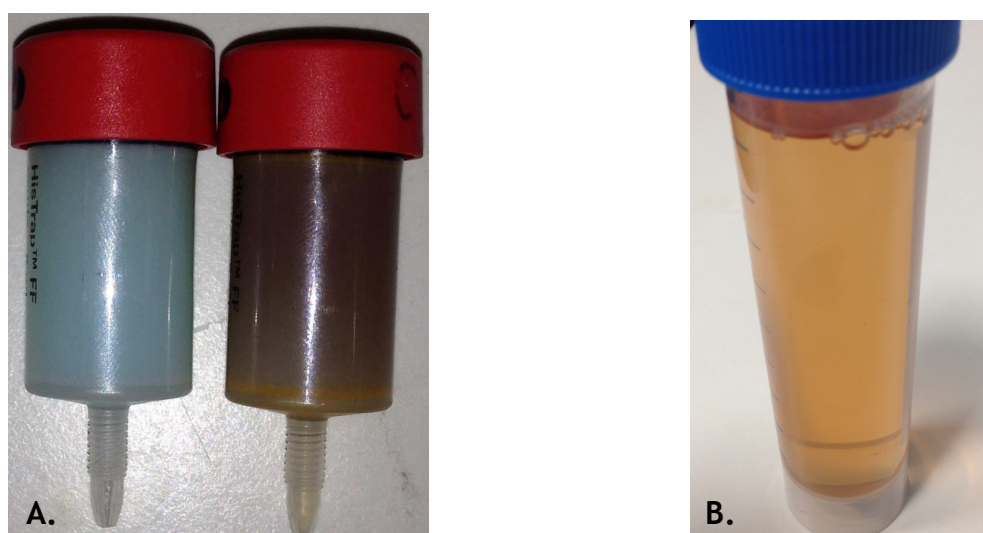


**Figure 5.29 A. Ferredoxin bound to nickel and B. After elution of the Nickel column**

Fractions from the SEC were monitored based on the brown colour, as the ferredoxin does not contain any Tryptophans it would be difficult using the detector attached to the Akta prime machine. Fractions containing brown colour

were taken to run on a 4-12% SDS-page gel (Figure 5.30). Bands were observed at around 14 kDa, the ferredoxin is a 10 kDa protein that runs as a diffuse band on a SDS-page gel. The selected samples were also confirmed by the unique absorption spectra of ferredoxin (Fig 5.31), with absorption bands at 330 nm and the maxima at 415 nm with a shoulder at 460 nm.

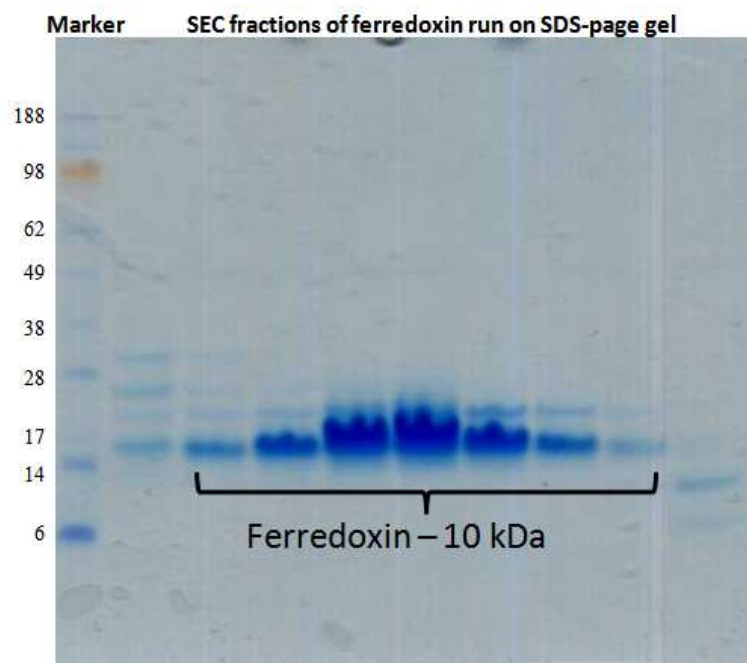


**Figure 5.30** SDS-page gel of ferredoxin after passing it over the Superdex S75 SEC column. Fractions containing a brown color were taken and run on a 4-12% SDS-page gel. Bands at around 14 kDa were observed. These bands were off Ferredoxin which runs as a diffuse band on a SDS-page gel.

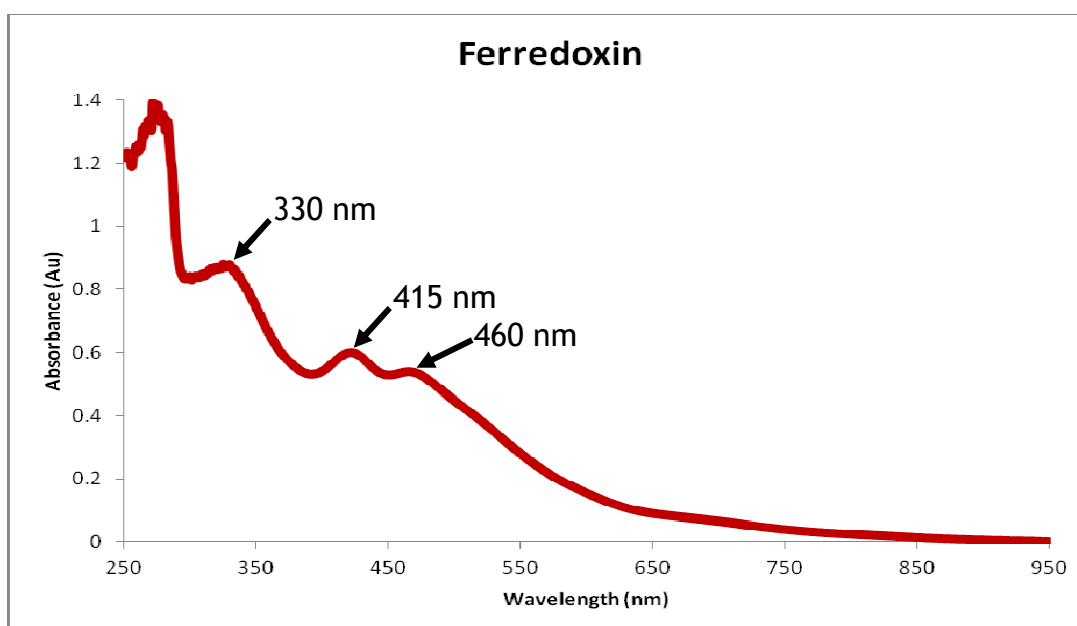


**Figure 5.31** Absorption spectra of ferredoxin

Absorption of ferredoxin from *Arabidopsis thaliana* after SEC purification in 50 mM NaPi pH 7.5, and 150 mM NaCl with absorption bands at 330, 415 and 460 nm, indicative of the ferredoxin.

## 5.14 ITC of PscD with FMO and ferredoxin

Any interaction between molecules can usually be detected and measured by isothermal titration calorimetry (ITC). ITC allows for any changes to be measured by heat which may occur between a target protein and its ligand. A normal ITC set up consists of 2 cells, the first cell is known as a reference cell. This cell is kept constant, as opposed to the other cell, which is a sample cell. Both of these cells temperature are monitored and kept constant. To the sample cell, an injection syringe, containing the ligand, also in buffer solution, is connected. Pre-selected volumes of the ligand are then injected into the target solution. Any binding interactions between the ligand and target will result in a temperature change in the sample cell. This can be an endothermic or an exothermic reaction.

Three reactions were initially looked at, and were carried out as described in section 2.20. The first reaction involved titrating buffer in to buffer (20mM NaP buffer pH7, 75 mM NaCl), to make sure that there was no interactions (Figure 5.32 A). This was also repeated with PscD into buffer, FMO into Buffer and Ferredoxin into buffer all gave the same data as observed in figure 5.32 A. The second reaction involved having the PscD (0.01 mM) in the cell and titrating FMO (0.06 mM) into PscD through the syringe. No heat was given off or no endothermic reaction observed (Fig 5.32 B), indicating that initial experimental data had shown no interactions of FMO with PscD. The third reaction involved having PscD in the cell and titrating the purified ferredoxin (0.1 mM) into PscD (Fig 5.32 C). Initial data showed that there was a possibility of an interaction taking place, but if there was it was observed at the end of the reaction, hence the slight incline as observed in Figure 5.32 C just before levelling off. Another possibility could be that the on and off rates are so fast for these reactions that ITC might not be a sensitive technique. This data may also suggest that more than two proteins might be needed for interactions to take place, for example PscD might require the presence of PscB for the interaction of ferredoxin. These preliminary data would have to be repeated to obtain conclusive answers of what is happening.

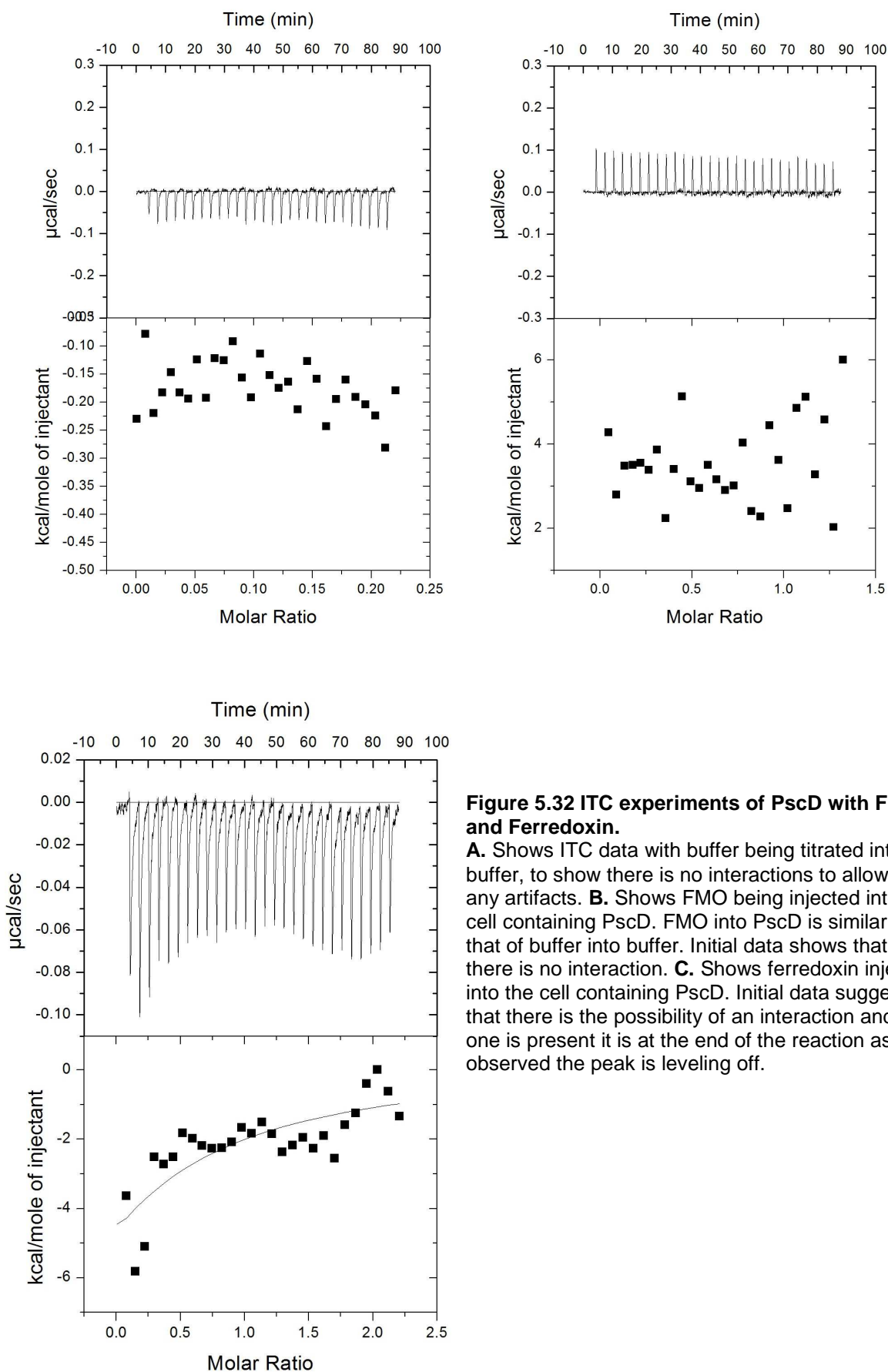


**Figure 5.32 ITC experiments of PscD with FMO and Ferredoxin.**

**A.** Shows ITC data with buffer being titrated into buffer, to show there is no interactions to allow for any artifacts. **B.** Shows FMO being injected into the cell containing PscD. FMO into PscD is similar to that of buffer into buffer. Initial data shows that there is no interaction. **C.** Shows ferredoxin injected into the cell containing PscD. Initial data suggests that there is the possibility of an interaction and if one is present it is at the end of the reaction as observed the peak is leveling off.

# Chapter 6 – Structural studies on the *C. tepidum* RC and the two peripheral proteins PscB and PscD

---

## 6.1 Introduction

This chapter describes the work towards structural determination by means of NMR and X-ray crystallography for the two peripheral proteins associated with the *C. tepidum* RC; PscB and PscD, as well as the *C. tepidum* RC complex itself.

To date there is no known structure of a green sulphur type I RC, this is the only RC that is homodimeric as compared to the other RC structures which have been solved to date (Table 1.1) [112]. Work towards the structure over the past 20 years, by many different research groups, has yielded no positive results in elucidating its structure. None the less it has given insightful information, through homology modelling, to help elucidate how it functions [73, 111-112, 129]. However, there is still a lot to be understood about the RC and for this, amongst other reasons i.e. designing a type I green sulphur RC mimic, a crystal structure is required.

## 6.2 NMR of PscD and PscB

Two of the peripheral RC proteins PscB and PscD are water soluble proteins that have not been characterised. PscD and PscB were both grown for NMR studies and purified as described in section 2.14 and 2.16 with the difference being that the cells were grown in M9 minimal media (section 2.2.3) for NMR studies. The NMR media was supplemented with  $^{15}\text{N}$ -labelled media, which replaced the  $\text{NH}_4\text{Cl}$  to  $^{15}\text{NH}_4\text{Cl}$  (98%  $^{15}\text{N}$ ), when carrying out the HSQC (Heteronuclear Single Quantum Coherence) experiments. And to allow for backbone assignments of PscB the  $^{15}\text{N}$ ,  $^{13}\text{C}$ -labelled media, replaced the  $\text{NH}_4\text{Cl}$  with  $^{15}\text{NH}_4\text{Cl}$  (98%  $^{15}\text{N}$ ) and D-glucose with D-Glucose (99%  $^{13}\text{C}$ ). Uniformly ( $^{15}\text{N}$ ) and double ( $^{15}\text{N}$  &  $^{13}\text{C}$ ) labelled samples of PscD and PscB for NMR were expressed in M9 minimal media

enriched with the relevant isotope(s) and purified as described in Chapter 5 section 5.8 and 5.9. Pure, labelled protein samples were exchanged into 50 mM NaPi pH 7.7, 75 mM NaCl, using a PD-10 column and concentrated to 570  $\mu$ L, before the addition of 30  $\mu$ l of D<sub>2</sub>O (5% deuterated water) for field frequency locking, and then transferred into a 5 mm diameter NMR tube to be placed into the NMR magnet.

### 6.2.1 1D NMR spectra of PscD and PscB

A 1D proton experiment (Fig 6.1 & 6.2) and a 2D <sup>15</sup>N-HSQC experiments (Fig 6.3 & 6.4) was carried out on both PscD and PscB. A 1D NMR spectrum is indicative of the structure of the sampled protein. The 1D shows peaks for hydrogen (<sup>1</sup>H) nuclei, except for the ones that exchange rapidly with water. The secondary, tertiary and quaternary structure of the sample protein has a great effect of the resonant frequencies of the NMR active nuclei within the protein. If a protein is not folded the protein shows a low dispersion of chemical shifts in nuclei such as protons in backbone amide or aliphatic groups. A broad peak at a chemical shift at around 8.3 ppm indicates disorder of the protein as this is indicative of a chemical shift of the backbone amides in random-coil. Alternatively, well dispersed signals at 8.5 ppm or higher show varying chemical environments experienced by amide protons in a folded protein. Similarly a range of signals within the -1.0 to 1.0 ppm region, as opposed to a broad peak at 1.0 ppm, is indicative of aliphatic protons in a folded protein. Figure 6.1 and 6.2 shows a 1D NMR spectra of both PscD and PscB. PscB (Fig 6.2) shows dispersed resonance frequencies in both the aliphatic (-1.0 to 1.0 ppm) and the amide (7-10 ppm) regions indicating that PscB is well folded. PscD, in comparison, also shows dispersed resonance in both the aliphatic and amide regions, but not as well dispersed with broadened regions in comparison to PscB, which could indicate unstructured elements of the protein.

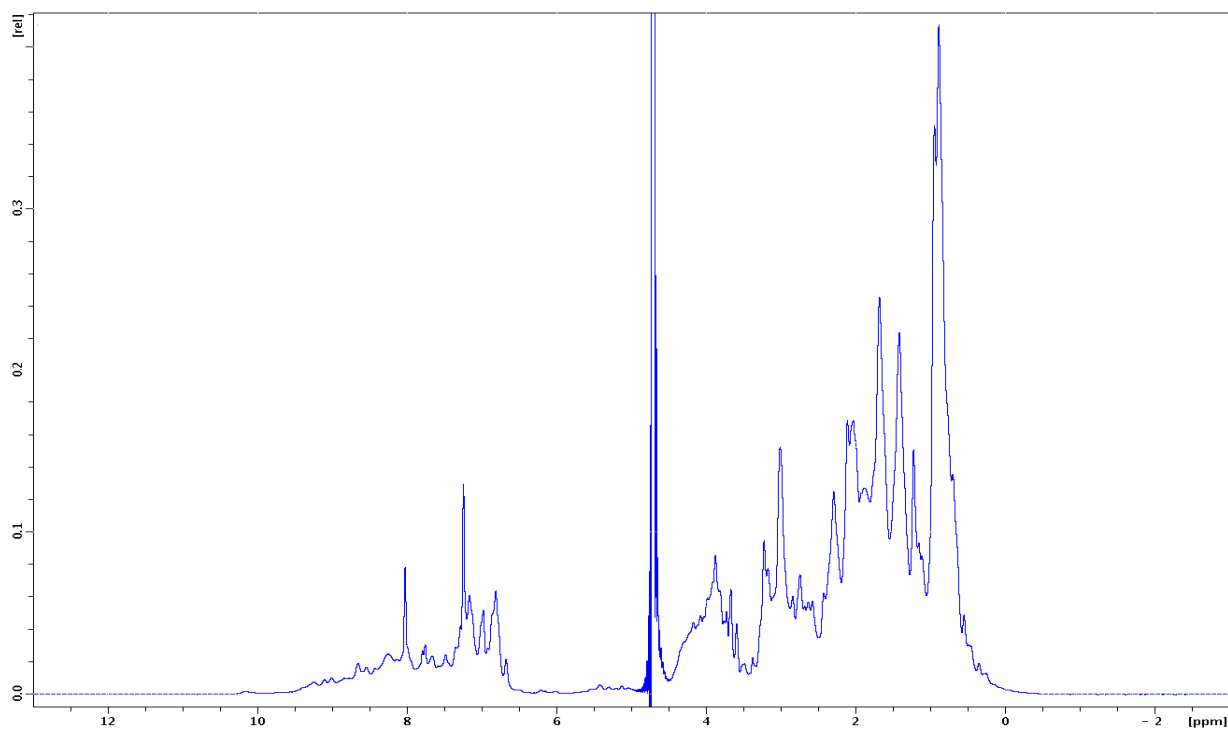


**Figure 6.1 1D <sup>1</sup>H-NMR spectrum of recombinant PscD.**

The horizontal axis is chemical shift in parts per million, p.p.m and the vertical axis is signal strength (in arbitrary units). Each peak originates from an H atom within the protein, i.e. to the right, some of the peaks are from aliphatic and methyl groups, and to the left the NH<sub>2</sub><sup>+</sup> and back bone amides.

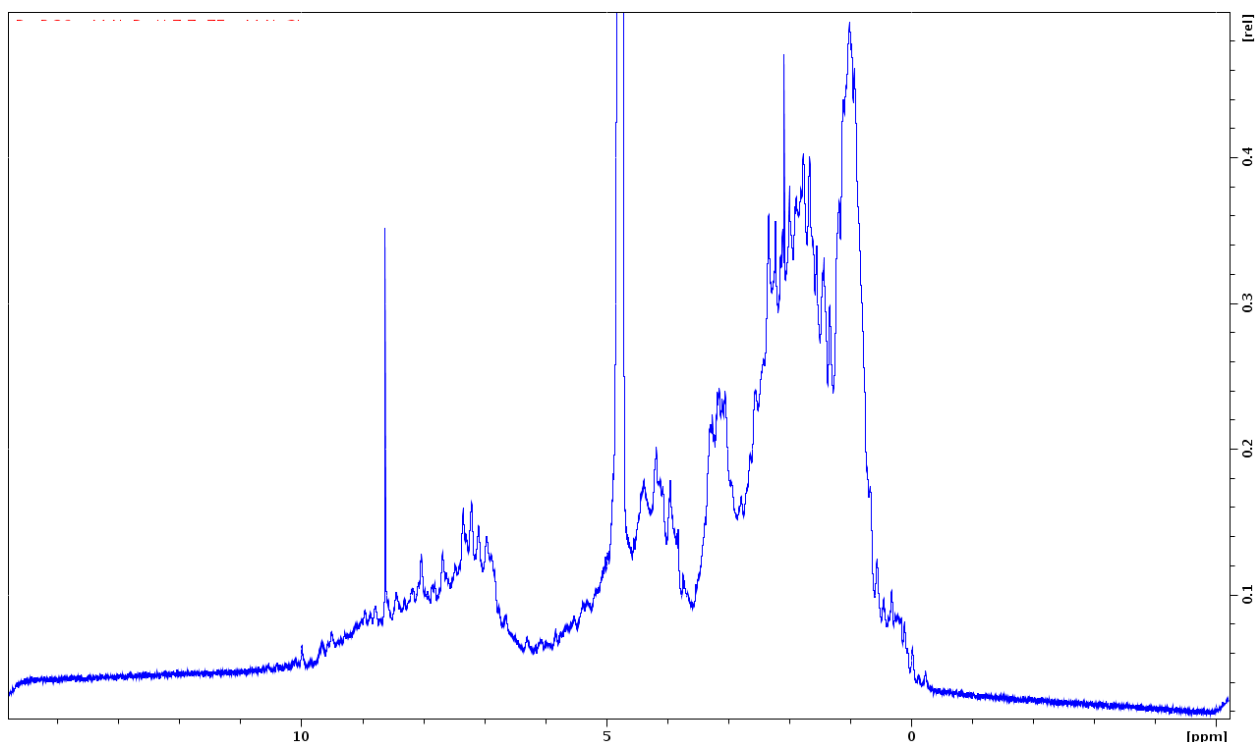


**Figure 6.2 1D <sup>1</sup>H-NMR spectrum of recombinant PscB.**

The horizontal axis is chemical shift in parts per million, p.p.m and the vertical axis is signal strength (in arbitrary units). Each peak originates from an H atom within the protein, i.e. to the right, some of the peaks are from aliphatic and methyl groups, and to the left the NH<sub>2</sub><sup>+</sup> and back bone amides.

## 6.2.2 2D HSQC NMR spectra of PscD and PscB

The 2D  $^{15}\text{N}$ -HSQC correlates resonances of covalently bonded  $^1\text{H}$  and  $^{15}\text{N}$  nuclei. Thus, each cross peak originates from a backbone amide  $-\text{NH}$  or the side chains of Asn (asparagine), Glu (glutamine), Trp (tryptophan) or Arg (arginine). If the protein is folded, the peaks are usually well-dispersed, and most of the individual peaks can be distinguished. The  $\text{NH}_2$  peaks belonging to the side chains of Asn and Glu usually appear as doublets on the top right corner of the spectra, and a smaller peak may appear on top of each peak due to the exchange with  $\text{D}_2\text{O}$ . The side chain amine peaks from Trp are usually shifted downfield and appear near the bottom left corner, normally around 10 ppm. The backbone amide peaks of Gly (glycine) normally appear near the top of the spectrum.

If there is a large cluster of severely overlapped peaks around the middle of the spectrum, that would indicate the presence of significant unstructured elements in the protein, as observed in figure 6.3, which shows the  $^{15}\text{N}$ -HSQC of PscD. This spectra is indicative of the protein having unstructured elements, as a large cluster of overlapped peaks are observed in the middle as well as single peaks around the cluster, which are quite broad indicating a part of the protein as well as being unstructured is also structured. This information, along with the information obtained from chapter 5 section 5.11 and 5.13 may indicate that the structure of PscD cannot be resolved until the unstructured elements take up a structured conformation; this might require the addition of Ferredoxin and/or PscB. Based on the  $^{15}\text{N}$ -HSQC of PscD, the structure on its own cannot be resolved until conditions are found allowing for a much better  $^{15}\text{N}$ -HSQC spectra. In comparison to PscD the  $^{15}\text{N}$ -HSQC of PscB (Fig 6.4) shows sharp, well dispersed individual peaks, which is indicative of a well structured protein.

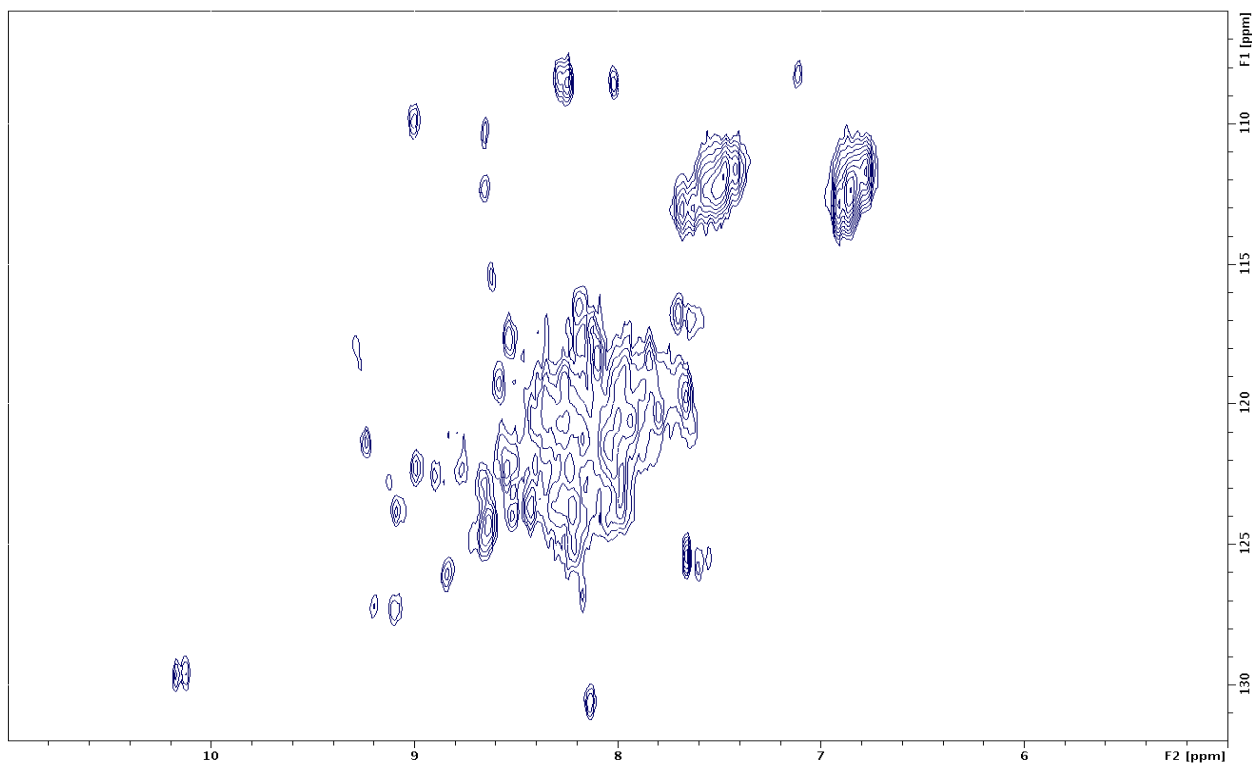


**Figure 6.3 2D,  $^{15}\text{N}$ -HSQC, spectrum of recombinant PscD**

The horizontal axis is the proton chemical shift and the vertical axis is the  $^{15}\text{N}$  chemical shift. Each signal, in a  $^{15}\text{N}$  HSQC spectrum, represents a proton that is bonded to a nitrogen atom. Temperature 308K, in 50mM sodium phosphate buffer pH 7.7, and 75 mM NaCl. Large cluster of severely overlapped peaks around the middle of the spectrum indicate unstructured elements of PscD.

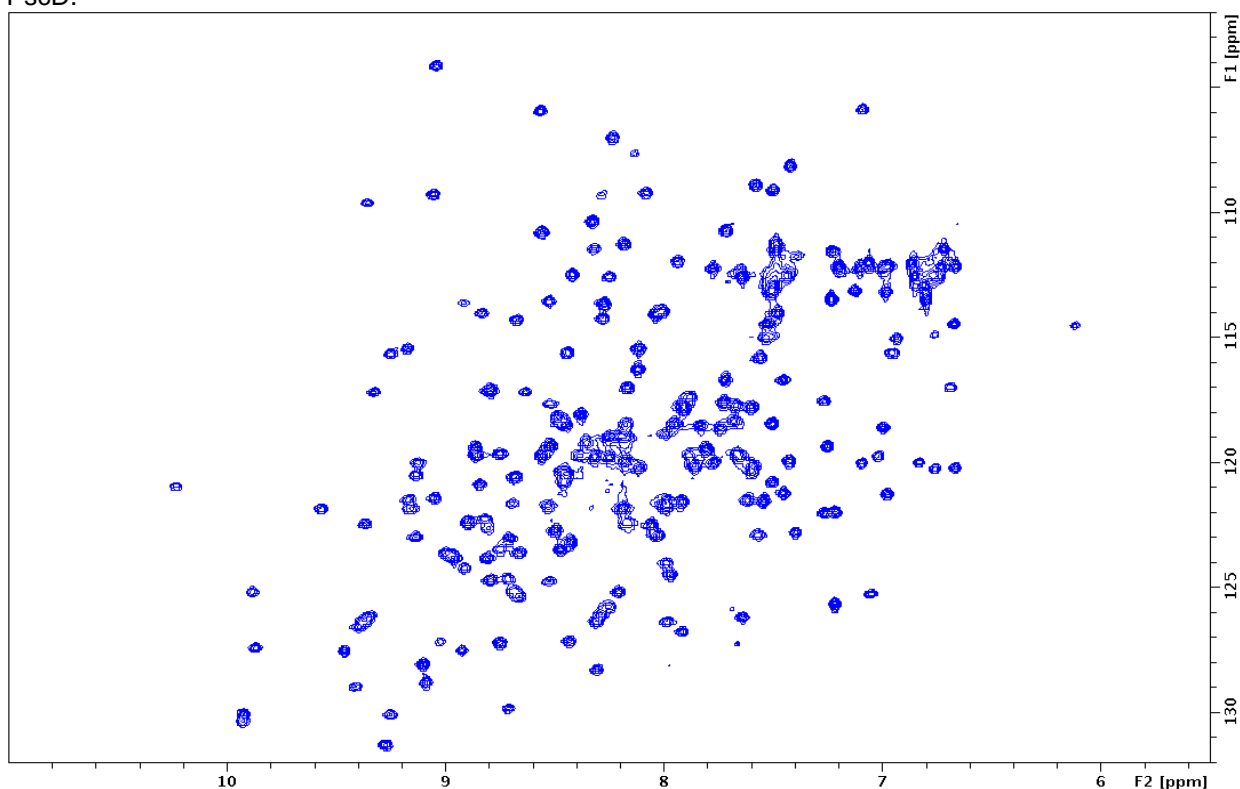


**Figure 6.4 2D,  $^{15}\text{N}$ -HSQC, spectrum of recombinant PscB**

The horizontal axis is the proton chemical shift and the vertical axis is the  $^{15}\text{N}$  chemical shift. Each signal, in a  $^{15}\text{N}$  HSQC spectrum, represents a proton that is bonded to a nitrogen atom. Temperature 314K, in 50mM NaP pH 7.7, and 75 mM NaCl. Sharp, well dispersed peaks, indicative of structured protein

### 6.2.3 PscB – NMR temperature studies to increase tumbling

As the M9 minimal media is not as rich media as TB or LB, the amount of protein expressed is automatically reduced to less than half in M9, especially when you change the nitrogen and carbon source to their labelled counterparts ( $^{15}\text{N}$  and  $^{13}\text{C}$ ). Therefore, growing and purifying PscB from 16 litres of M9 media gave less than 0.2 mM of protein, which is not ideal for NMR studies. This required further optimisation on the NMR magnet to allow for better signals to be detected in the NMR spectra. There are two ways to allow for better spectra to be obtained if there are limited concentrations of the target protein. The first way is by using a NMR machine with a higher magnetic field allowing for higher resolution in the direct-detection dimension (free induction decay or FID). Another way to obtain a better signal is to speed up the tumbling of the protein in the NMR machine, which requires heating the protein. The higher the temperature the faster the tumbling of the protein this in turn allows for better signals. The lower the temperature the slower the protein will tumble, which gives broader NMR peaks. The temperature has both advantages and disadvantages, since increasing the temperature allows for a better signal it also means that the protein has a propensity to precipitate faster, which is not advantageous for the triple resonance experiments as some can take weeks. Another disadvantage would be that some of the NMR signals might be lost due to the fast tumbling. So an optimal temperature would be required. As the NMR machine available within the University of Glasgow was a Bruker AVANCE 600 MHz NMR spectrometer it was opted to go down the temperature route to allow for better NMR spectra. PscB labelled with  $^{15}\text{N}$  was placed in the NMR machine to allow for a 2D-HSQC spectrum to be obtained at 298 K (Kelvin), which is observed in figure 3.6 A & B, on the far right hand side as blue peaks. An additional 5 HSQC spectra were obtained by increasing the temperature by 5°C after each NMR HSQC experiment, up until 323 K. On close observation, figure 6.5 B, it was observed that the optimal signal was around 313 K- 323 K. Comparing the last three peaks (far left hand side, pink to red) observed in figure 6.5 B to the first three peaks (far right hand peaks, blue to purple), as the contour levels had increased due to the increase in temperature, indicative of better signal. The peaks at higher temperatures, between 318 K to 323 K, also meant that peaks in other parts of the spectra had disappeared due to the fast tumbling. Even though the protein was stable at 323 K all the NMR experiments were carried out at 314 K, as this

was the optimal temperature to give the best signal without the loss of any peaks.

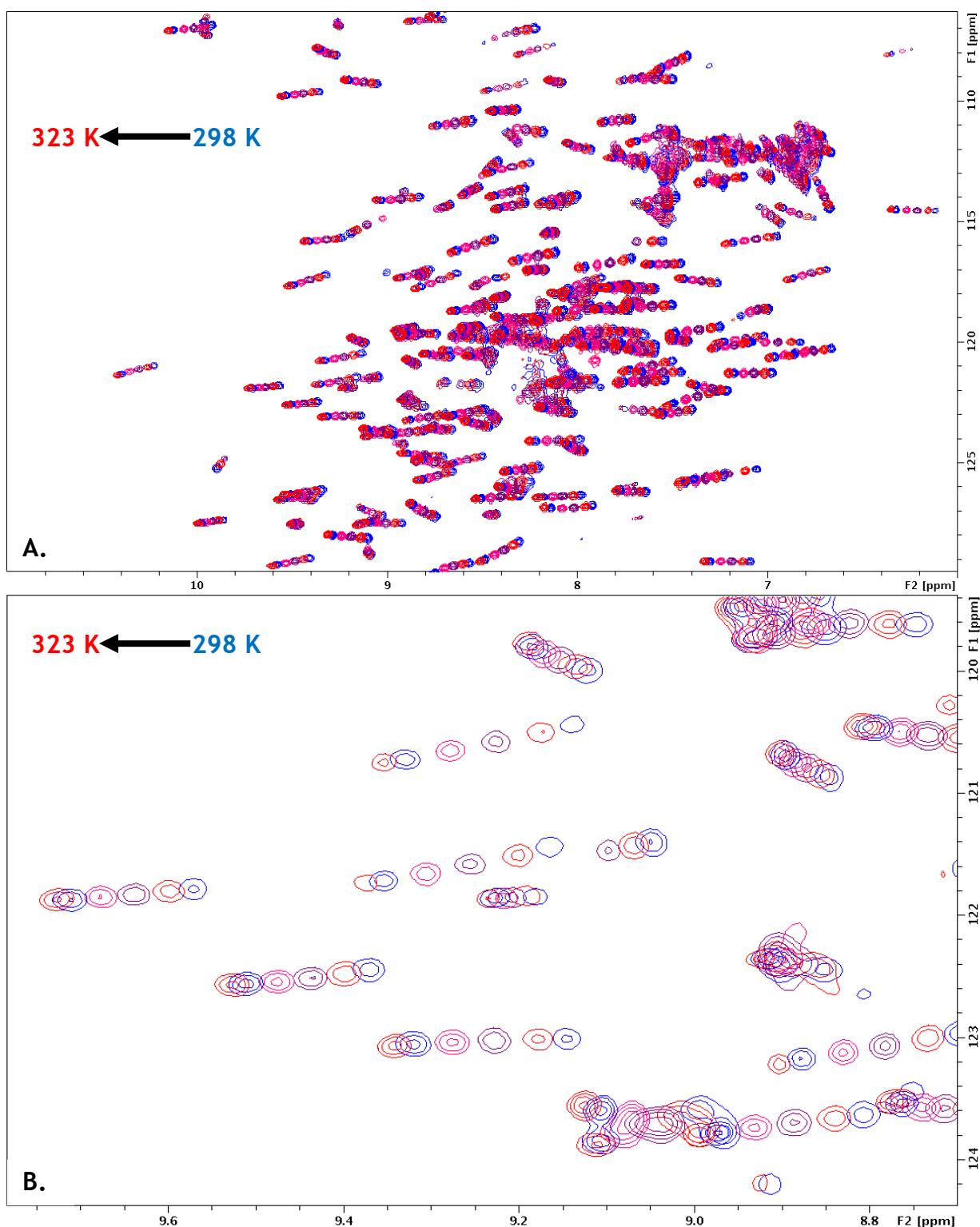


**Figure 6.5** 2D-HSQC spectra of PscB. Temperature effects of PscB ranging from 298 K to 323 K.

Effect of temperature on PscB going from peaks on the right hand side to the left. 298 K (Blue), 303 K (maroon), 308 K (purple), 313 K (pink), 318 K (blue), 323 K (red). **A.** Shows the whole 2d-HSQC spectra with the temperature series. **B.** Shows the spectra focused on specific peaks to show the effect of temperature on PscB. Peaks going from right to left as the temperature increases have much sharper peaks with more contours, indicative of better signal.

## 6.2.4 PscB - T<sub>2</sub> (Spin-spin relaxation) experiments

Another parameter, which is commonly looked at in NMR, is the relaxation of the protein. Information obtained from the relaxation of protons and other spins in the protein are essential for the optimal setup for the NMR experiments. Spin-spin (or transverse) relaxation time  $T_2$  is used to quantify the rate of the decay of the magnetization within the xy plane. After a  $90^\circ$  pulse the nuclear spins are aligned in one direction (are said to be phase coherent), but this arrangement is gradually lost due to field inhomogeneities and/or direct interactions between the spins without energy transfer to the lattice.  $T_2$  relaxation does not affect the total amount of z-magnetization, but the degree of synchronization of the transverse magnetization components.  $T_2$  is related to the linewidth at half-height of the NMR signal.

The  $T_2$  value was measured utilising a pseudo 3D <sup>15</sup>N HSQC format experiment with selected time points as the third dimension. In order to measure  $T_2$  the contribution from sample inhomogeneity and chemical shift evolution must be removed. This is achieved through a series of CPMG (Carr-Purcell-Meiboom-Gill) pulses resulting in signal decay proportional to the pure rate of  $T_2$  relaxation. Delay times used were 16.96 ms, 33.92 ms, 50.88 ms, 67.84 ms, 101.76 ms, 135.68 ms, and 169.6 ms with experiment delay of 16.96 ms within each loop of the delay experiment. Figure 6.6 A shows the  $T_2$  experiments over the delay times mentioned, and figure 6.6 B shows the peaks that are normalised on over the first signal (Marked by an red arrow), this shows the scale at which the peaks have been normalised over. For the  $T_2$  experiment a relaxation time and associated error were calculated for each peak by applying an exponential fitting function ( $I = A \cdot e^{-Bt}$ ) to peak intensity by height (I) plotted against delay time (t) (figure 6.7). The  $T_2$  was calculated to be at  $65 \pm 4$  ms

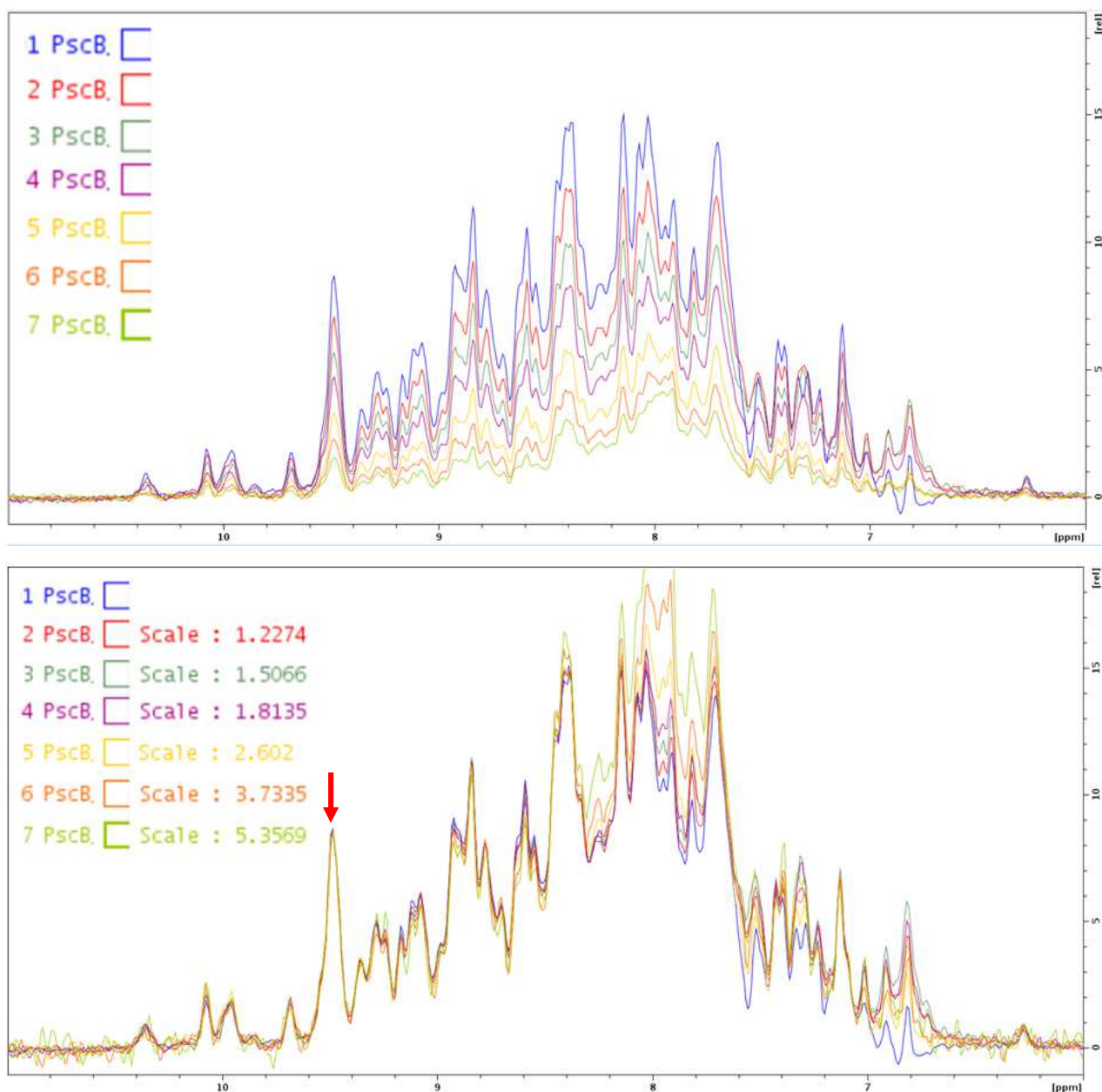


**Figure 6.6  $T_2$  (Spin-Spin) relaxation delay of PscB**

A. Shows the relaxation delay over the delay times used (1) 16.96 ms, (2) 33.92 ms, (3) 50.88 ms, (4) 67.84 ms, (5) 101.76 ms, (6) 135.68 ms, and (7) 169.6 ms. B. shows the scale when normalised on the peak marked by the red arrow.

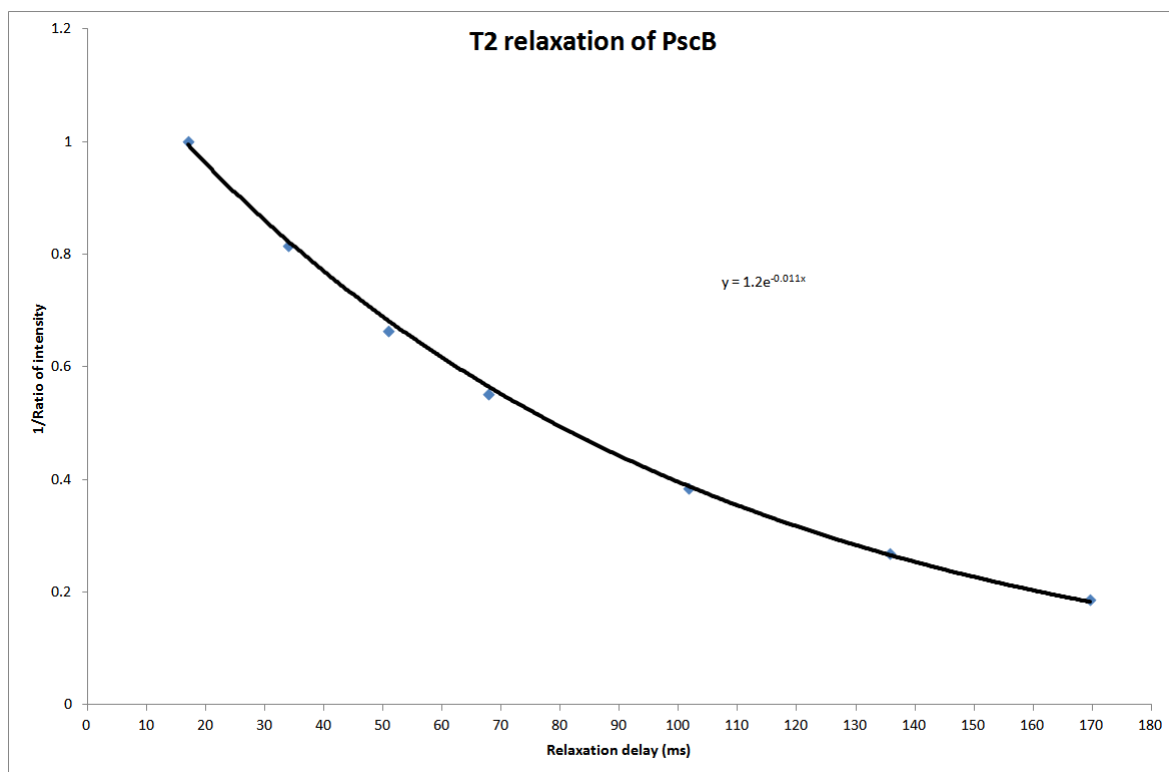


**Figure 6.7 T2 relaxation of PscB**

The T2 experiment a relaxation time and associated error was calculated for each peak by applying an exponential fitting function ( $I = A \cdot e^{-Bt}$ ) to peak intensity by height (I) plotted against delay time (t). The T2 was calculated to be at  $65 \pm 4$  ms

## 6.2.5 Triple resonance experiments

Triple resonance experiments were used to identify specific resonances correlated to the NH (2D HSQC) resonances. Complementary pairs of experiments allowed for identification of both resonances for the same, and the preceding residue as the NH group (intra and inter-residue  $i$  and  $i-1$ ) resonances. For example, HNCA, HNCB and CBCA(CO)NH experiments were used to correlate intra residue and inter-residue  $C\alpha$  and  $C\beta$  resonances to the amide cross peaks.

Here, in the CBCA(CO)NH, the magnetisation is transferred from  $^1H\alpha$  and  $^1H\beta$  to  $^{13}C\alpha$  and  $^{13}C\beta$ , respectively, and then from  $^{13}C\beta$  to  $^{13}C\alpha$ . From here it is transferred first to  $^{13}CO$ , then to  $^{15}N^H$  and then to  $^1H^N$  for detection. The chemical shift is evolved simultaneously on  $^{13}C\alpha$  and  $^{13}C\beta$ , so these appear in one dimension (Figure 6.8, blue peaks). In the case of HNCA the magnetisation is passed from  $^1H$  to  $^{15}N$  and then via the N- $C\alpha$  J-coupling to the  $^{13}C\alpha$  and then back again to  $^{15}N$  and  $^1H$  hydrogen for detection. Since the amide nitrogen is coupled both to the  $C\alpha$  of its own residue and that of the preceding residue, both these transfers occur and peaks for both  $C\alpha$ 's are visible in the spectrum. In each NH

strip two  $\text{Ca}$ 's should be visible. The stronger one belongs to the same residue  $\text{Ca}_i$  and the weaker one belongs to the preceding residue  $\text{Ca}_{i-1}$  (Fig 6.8, red peaks). For the HNC0 the magnetisation passes from  $^1\text{H}$  to  $^{15}\text{N}$  and then to the carbonyl  $^{13}\text{C}$  via the  $^{15}\text{N}^{\text{H}}\text{-}^{13}\text{CO}$  J-coupling. Magnetisation is then passed back via  $^{15}\text{N}$  to  $^1\text{H}$  for detection, in each HNC0 strip there is one CO visible belonging to the preceding residue (Fig 6.8, green peaks).

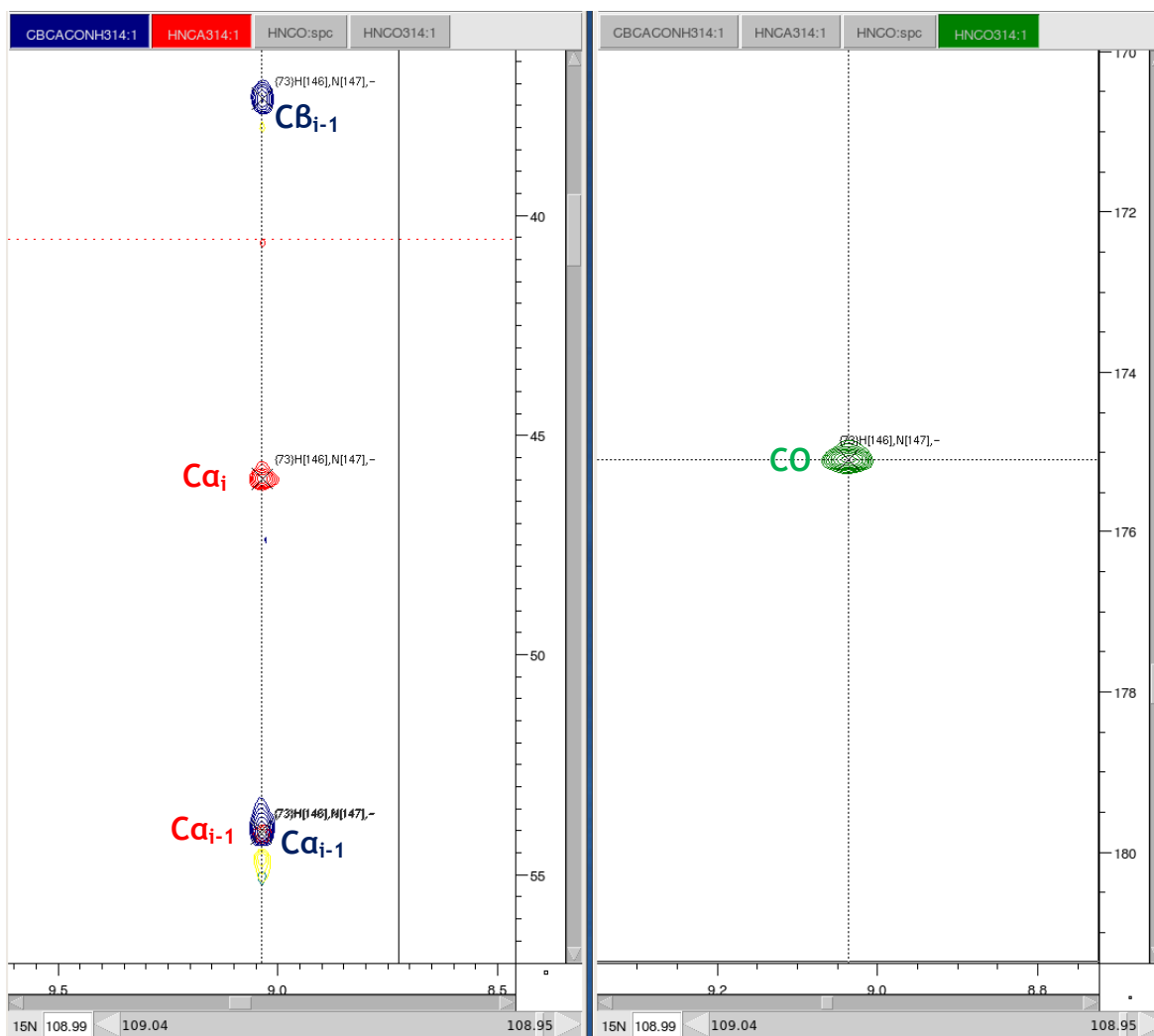


**Figure 6.8 Triple resonance experiments HNC0, HNCA and CBCA(CO)NH**

HNC0 triple resonance experiments in red showing the peak  $\text{Ca}_i$  and the weaker peak which belongs to the preceding residue  $\text{Ca}_{i-1}$  (in red). HNC0 shows the CO belonging to the preceding residue (green). And the CBCA(CO)NH shows the  $\text{Ca}$  and the  $\text{C}\beta$  (in blue) of the residue preceding the NH group.

The HBHA(CO)NH experiment is similar to that of CBCA(CO)NH in that the magnetisation is transferred from  $^1\text{H}_\alpha$  and  $^1\text{H}_\beta$  to  $^{13}\text{C}_\alpha$  and  $^{13}\text{C}_\beta$ , and then from  $^{13}\text{C}_\beta$  to  $^{13}\text{C}_\alpha$ . From here it is transferred first to  $^{13}\text{CO}$ , then to  $^{15}\text{N}^{\text{H}}$  and then to  $^1\text{H}^{\text{N}}$  for detection. Each strip in this experiment contains a  $\text{H}_\alpha$  and an  $\text{H}_\beta$  peak of the

preceding residue, sometimes there are two H $\beta$  peaks for the preceding residue as observed in figure 6.9.

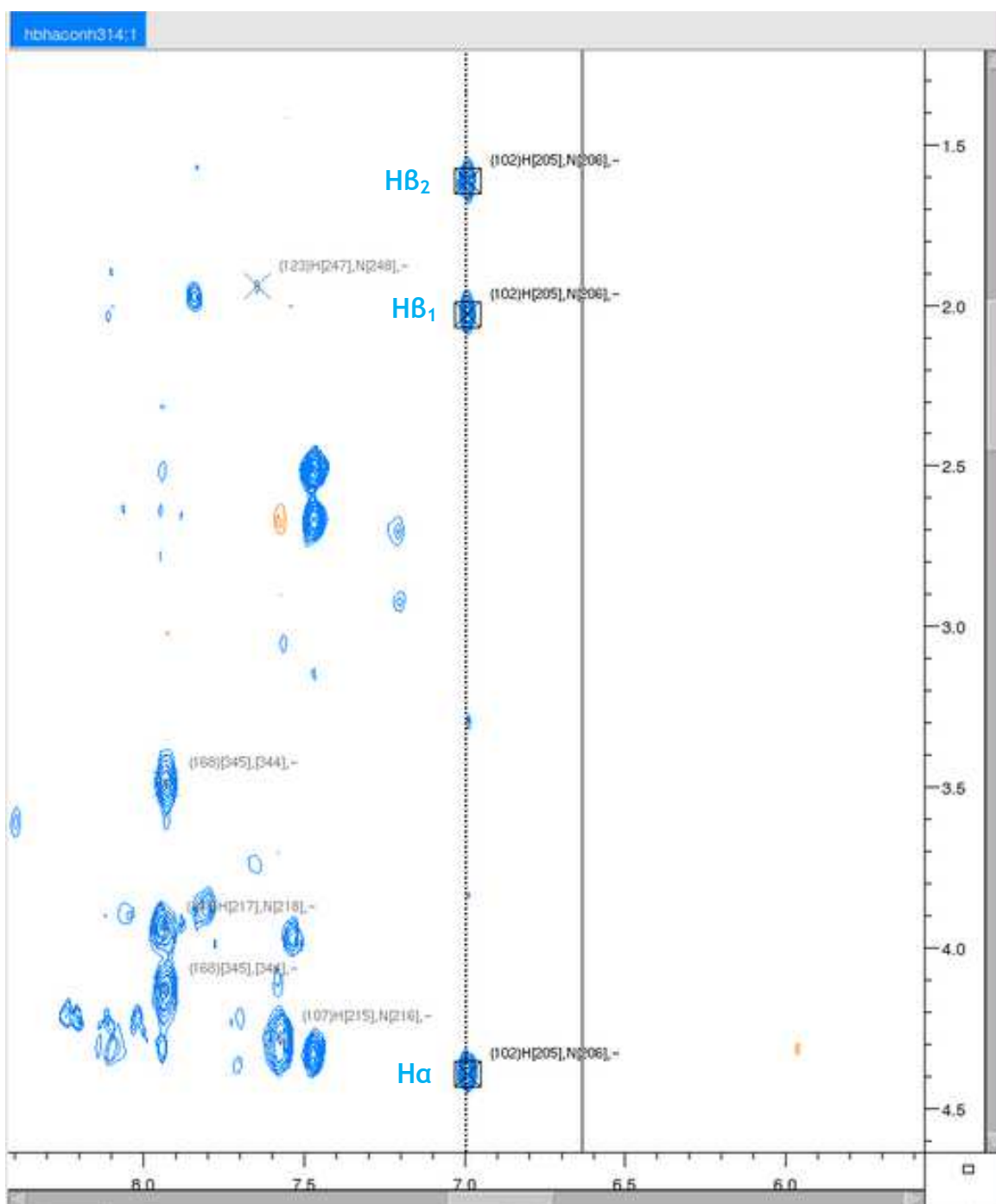


**Figure 6.9 HBHA(CO)NH triple resonance experiment of PscB**

Strip shows H $\alpha$  and an H $\beta$  peak of the preceding residue, sometimes there are two H $\beta$  peaks as observed.

As the triple resonance experiments are well on its way more data is required to resolve the structure, for this more protein is needed at a much higher concentration as some experiments are more sensitive than others. This part of the project is still ongoing.

## 6.3 Crystallisation of the *C. tepidum* RC

The ultimate goal of this project was to obtain crystals of the RC to elucidate the structure. Obtaining a structure would not only be intellectually satisfying, as this would be the first 3D crystal structure of a homodimeric RC, but it would also aid in being able to design an artificial mimic that could be coupled to plasmons.

To allow for the structure of RC to be solved the protein has to be surrounded (micelle formation) with the shortest chained detergent while having the characteristics mentioned earlier in section 1.3.1 for the protein to be able to crystallise. By being able to put the protein in the shortest chained detergent, greatly aids in protein-protein contact when setting up crystal trays. As the RC is stable and monodisperse only in DDM, as shown in chapter 3, this meant that this detergent would also be extremely challenging to crystallise in. All vapour diffusion crystal trays set up at the University of Glasgow on the Cartesian robot yielded no RC crystals. This had led on to other crystallisation methods that had to be adopted. The first of which was the In-meso method, as described in section 1.3.2.2.

The In-meso method has major advantages as compared to the vapour diffusion method for the *C. tepidum* RC. The first one being that a lot more conditions could be measured with the In-meso method as compared to the vapour diffusion. For one 96-well commercial screen, for the vapour diffusion method, would require 60  $\mu\text{l}$  of pure RC. In comparison the In-meso method would only need 2  $\mu\text{l}$  of pure RC protein to test in a 96-well commercial screen. Since only a small concentration of protein is purified from such large quantities of cells that are grown, as discussed in section 3.1.5.1, means that the purified RC can be tested in many different conditions. This also allows for a higher concentration to be obtained since such little volumes are needed for crystallisation.

### 6.3.1 In meso Crystallisation

Pure RC was prepared as previously mentioned in chapter 3 as described in section 2.4 of the methods and materials. A final concentration of 50 mg/ml in a final volume of 100  $\mu\text{l}$  was obtained, before sending it off to Trinity college

Dublin to Prof Martin Caffrey's lab. Before setting up in meso trays the absorption spectrum of the *C. tepidum* RC was measured, in solution, for allowing the detection of any changes to reassure that the RC was not damaged by seeing if there were any spectral changes to the RC over the two weeks it had been sent. The spectrum showed no changes, and was the same as observed in figure 6.10, the RC had the characteristic peaks with the 816 nm peak, and the Qx transition band 610 nm and the Soret band at 370 nm.

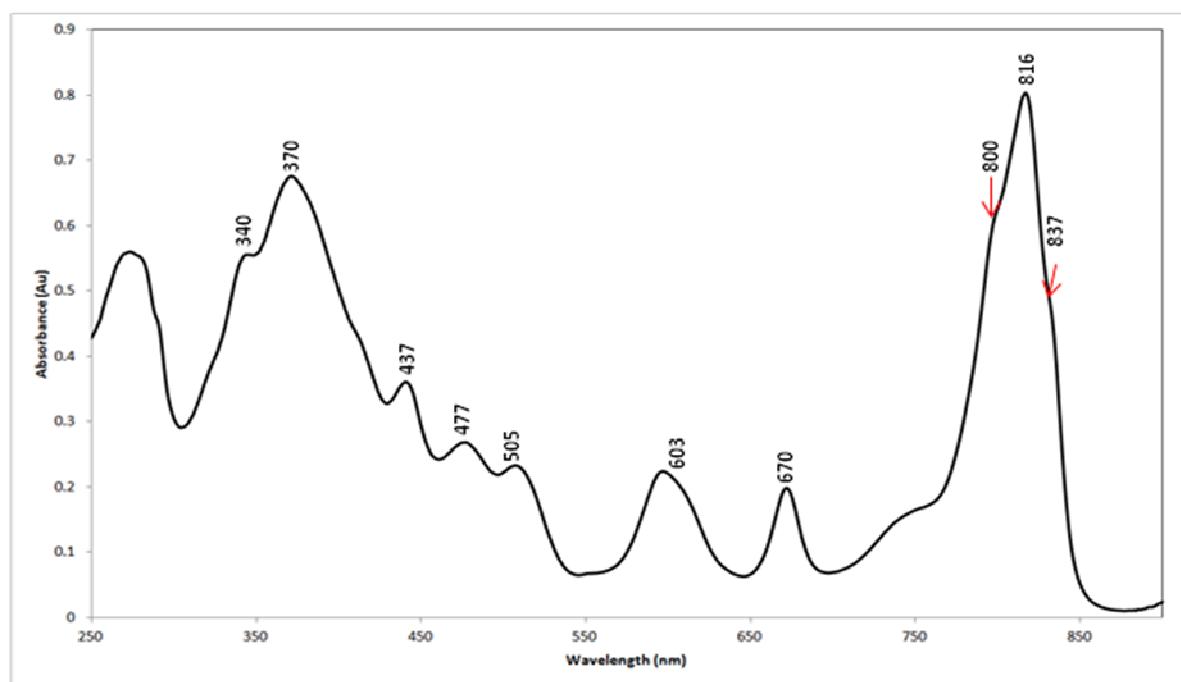


**Figure 6.10 Absorption spectrum of the *C. tepidum* RC**

*C. tepidum* RC measured in solution at room temperature. At 340, 370, 603 and 816 nm, the characteristic absorption bands of BChl *a*, and additionally, the shoulder at 837 nm indicating the primary donor, are seen. The peak at 670 nm contributes to the primary electron acceptor, which is the Chl *a*. Absorption bands in the wavelength range from 437 to 505 nm arise from the carotenoids, rhodopin and/or hydroxychlorobactene.

This allowed for us to proceed and mix the sample with the lipid monoolein (9.9 MAG) (as stated in the section 2.23). Monoolein (NuChek Prep., Inc. a gift from the Caffrey lab) and 53 mg/ml of RC protein solution (in 20 mM Tris pH 8, 75 mM NaCl, and 0.01% DDM) were mixed 3:2 (Lipid:Protein, in a final volume of 85  $\mu$ l) The sample and lipid were mixed until the sample was no longer birefringent and could be seen transparently (Fig 6.11).

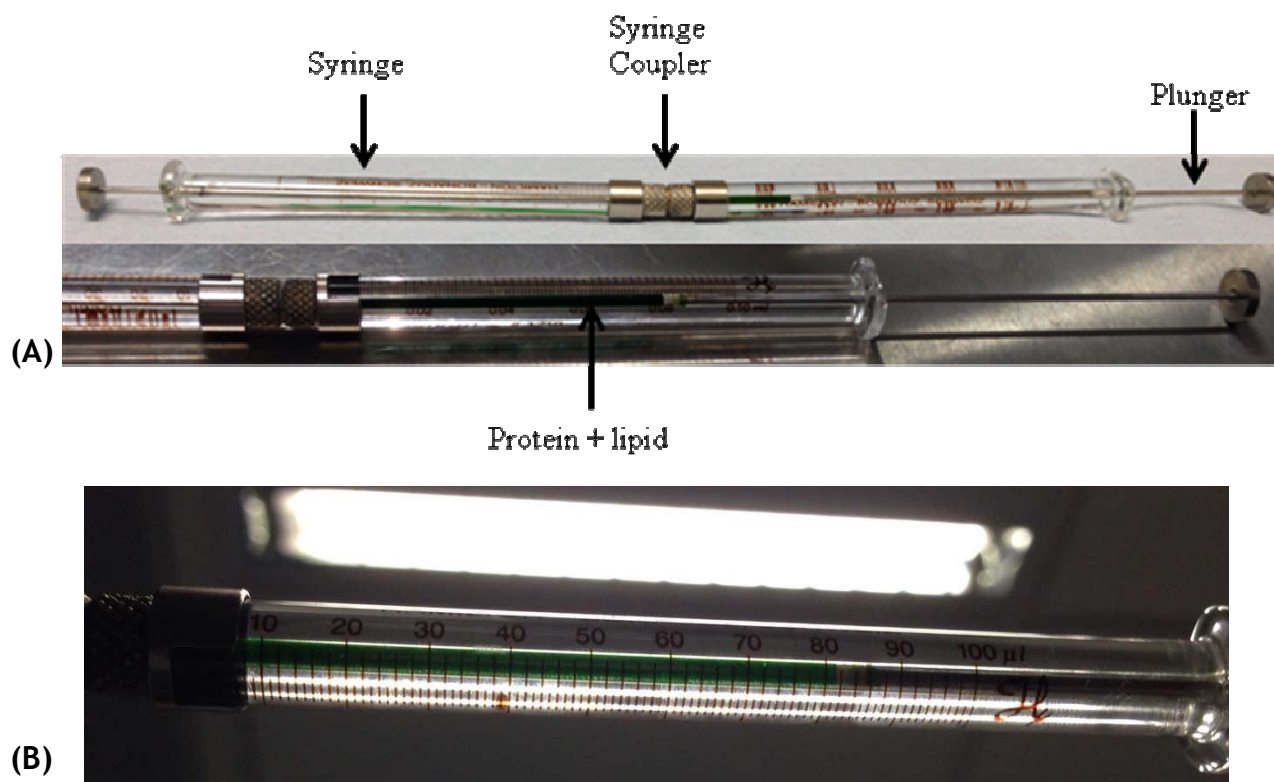


**Figure 6.11 In-meso set up using the lipid syringe to mix the monoolein and the RC (A).** Protein sample and lipid (monoolein) mixed in the syringe until the sample becomes transparent (B), allowing the formation of a solid cubic phase.

### 6.3.2 In meso absorption spectrum

The RC, after putting it in to cubic phase, was then put in a 96 well plate reader, as described in section 2.23 to measure the absorption of the sample in meso. This yielded an interesting absorption spectrum of the RC. As the *C. tepidum* RC has a unique absorption spectrum, with the absorption maxima at around 816 nm, the stability of the protein can be measured by the decrease in the RC spectrum at 816 (Fig 6.12 A) nm and the increase/release of bacteriochlorophyll a at 786 nm (Fig 6.12 B).

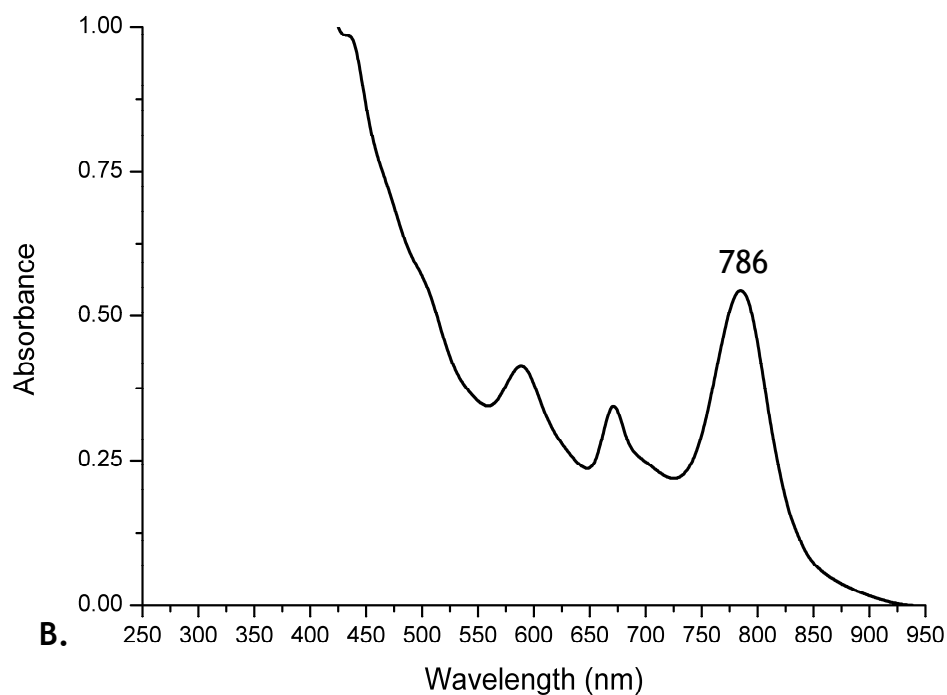
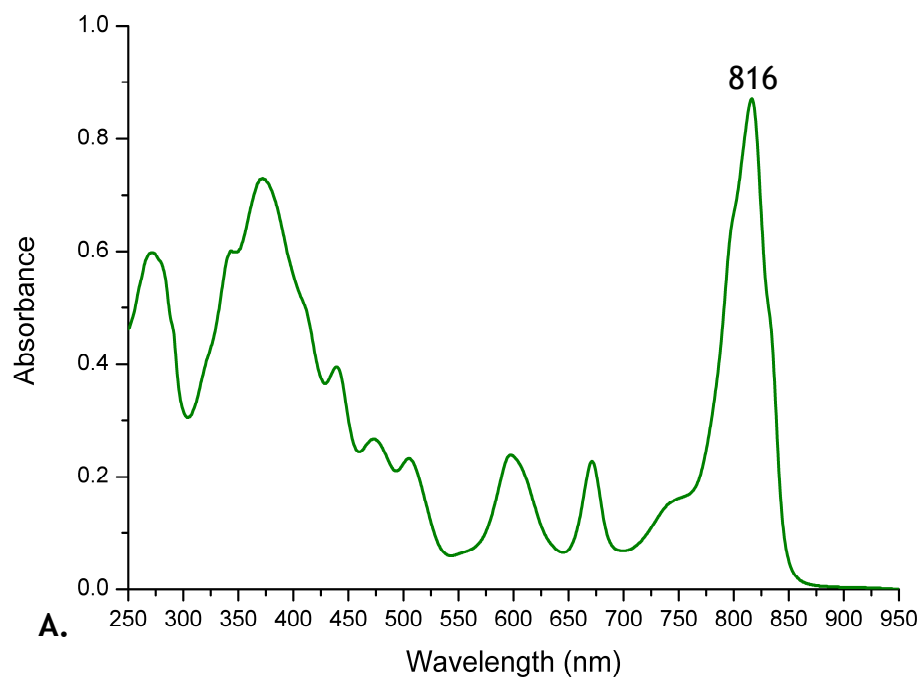


**Figure 6.12 Spectral changes on the breakdown of the *C. tepidum* RC**

**A.** Shows the absorption spectra of the purified *C. tepidum* RC with the absorption maxima at 816 nm. **B.** Absorption spectrum of *C. tepidum* RC broken down by the addition of 0.5% SDS. The main Peak observed at around 786 nm is of the bacteriochlorophyll a released after the RC is broken down.

When the RC in meso absorption spectra was measured, the absorption spectrum of the RC looked similar to that when it was measured in solution, it had the same overall shape but there was a shift at the 816 nm peak (Fig 6.13). At first glance it looked similar to that of the release of Bchl *a*, as the peak shifted from 816 nm to 786 nm, which for the *C. tepidum* RC is the characteristic breakdown product. But on further analysis it was observed that even though there was a decrease in absorbance and the shift from 816 to 786, the characteristic shape of the RC peak was still there, more so the shoulder of the RC (at 837 nm) seemed to be more defined in this spectrum (Fig 6.13) as this is where the absorption maxima is of the PscA dimer, at 837 nm (as mentioned in the introduction section 1.2.5.1).

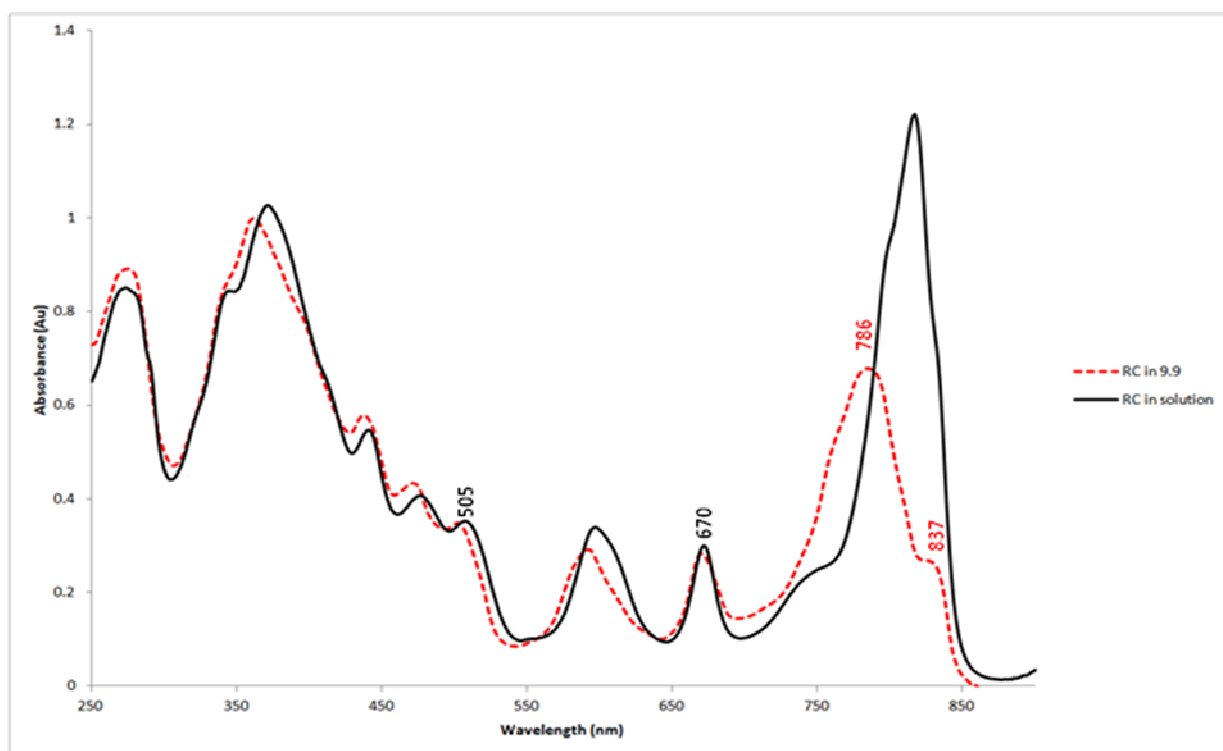


**Figure 6.13 Spectral difference of RC in solution with RC in monolein**

Absorption spectrum of *C. tepidum* RC In solution (black line) and RC in 9.9 (red line). The RC in solution has been normalised to the 505 nm carotenoid band of the RC in 9.9 MAG. All the pigments and carotenoids are still present, there is a slight shift. No change in the 670 nm region.

As the 837 nm peak does not shift, it was hypothesised that FMO was being disassociated from the complex. This could be further analysed by normalising the absorption spectra at 837 nm and taking away the RC in 9.9 from the RC in solution. By superimposing the difference spectra (Fig 6.14, red line) on top of the RC in solution (Figure 15 black line) and normalising at 837 nm we are able

to observe the difference spectrum containing no shoulder at ca. 800 nm, which potentially could be from the FMO, which absorbs at around 800-808 nm.

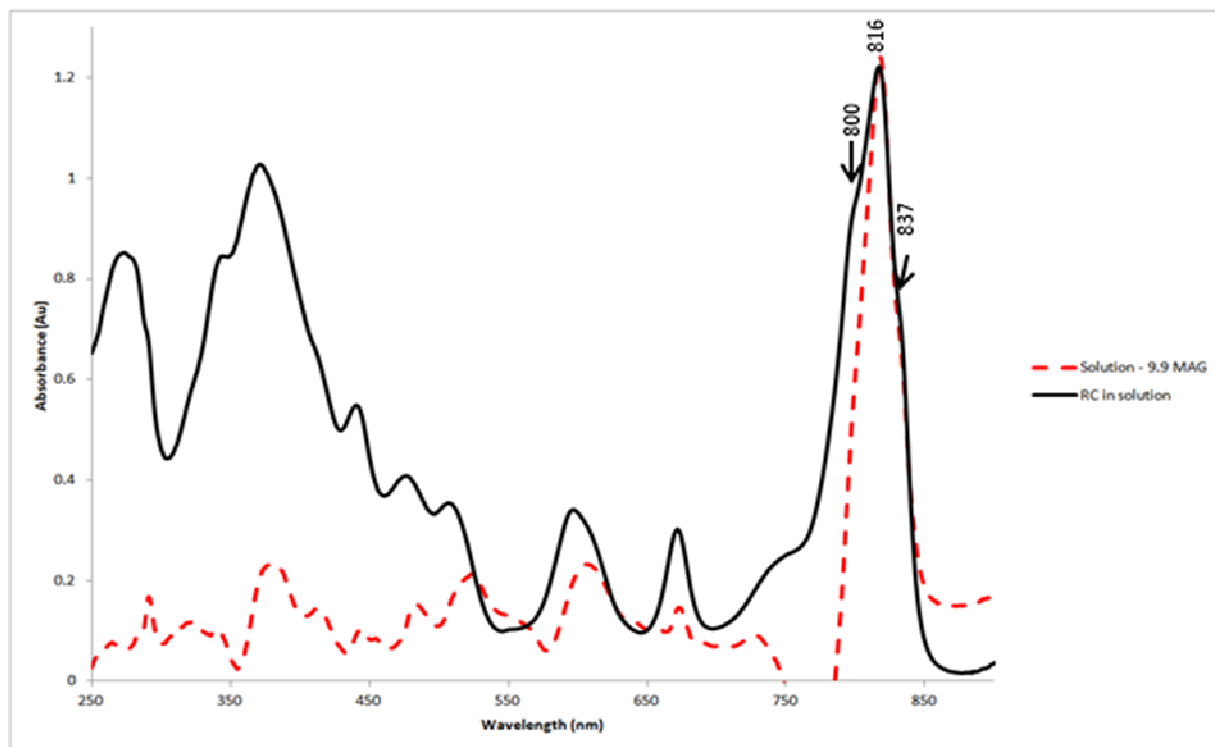


**Figure 6.14 Absorption spectrum of the difference of *C. tepidum* RC in 9.9 MAG taken away from the RC in solution.**

The RC in solution (black line) and RC in 9.9 MAG taken away from the RC in solution (red line). The RC 816 nm and 837 nm is still present in the difference spectrum, but the shoulder at ca. 800 nm is no longer present.

### 6.3.3 *C. tepidum* RC in 7.7 MAG

The absorbance of the RC was also measured in 7.7 MAG (Fig 6.15, green line), this was a much harder to measure as it would phase separate at higher temperatures compared to 9.9 (Fig 6.15, red line), regardless of this data was still collected. Unlike the RC in 9.9 MAG, the RC in 7.7 MAG seemed to have completely broken down, the pigments and carotenoids, again, a slight shift in comparison to the RC in 9.9 MAG, but the main RC peak had completely disappeared and the appearance of the 770 nm peak (Fig 6.15, green line) indicated that the BChl *a* had been released due to the breakdown of the FMO and the RC.

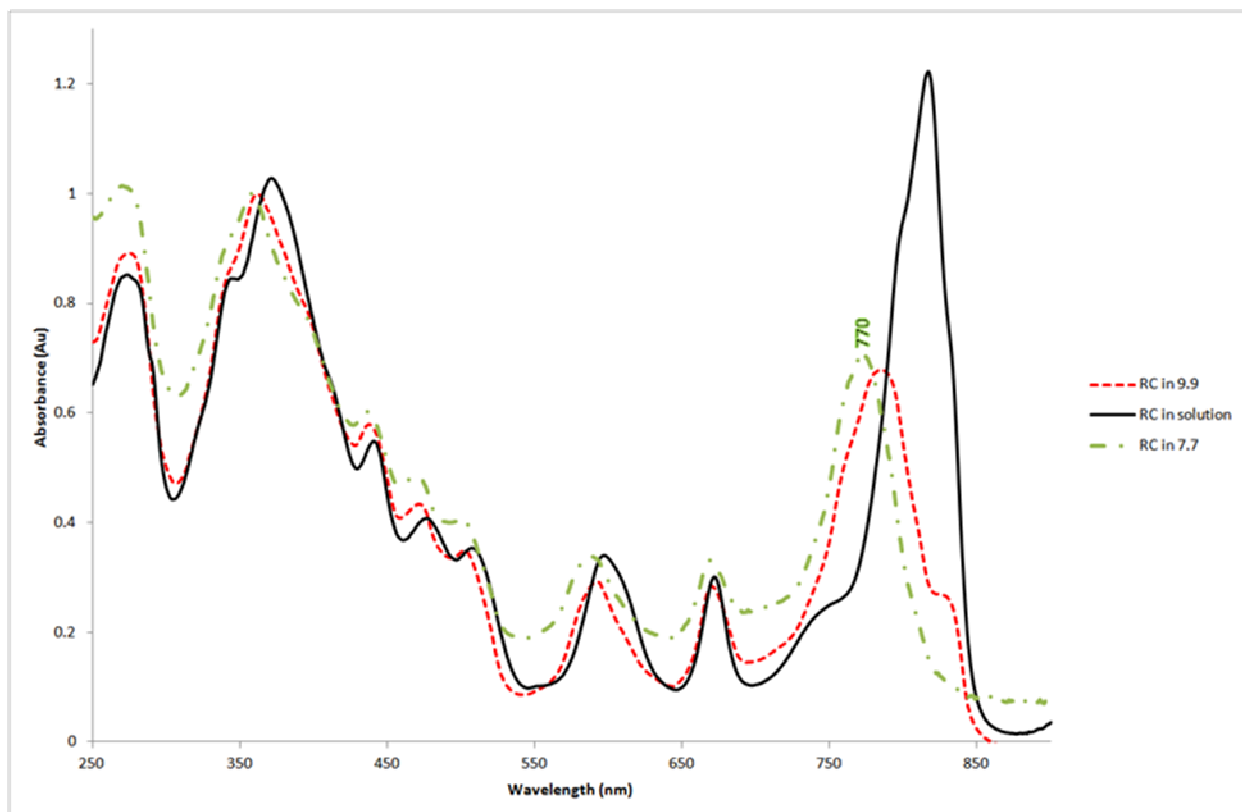


**Figure 6.15** Absorption spectrum of *C. tepidum* RC In solution (black line) and RC in 9.9 (red line) and the RC in 7.7 MAG (Green line).

As 9.9 seemed to be more stable, in comparison to 7.7, it was concluded that setting up the LCP trays would be done in monoolein. As it is more desirable to have crystals of FMO+RC, the RC by itself is just as interesting. The structure of FMO has been solved, but the RC structure has yet to be determined. Leading further from this, we might be able to hypothesize that not all FMO has been dissociated from the RC. Figure 6.16 depicts diagram of three possible outcomes of what potentially might crystallise, if any crystals are obtained (Fig 6.16).

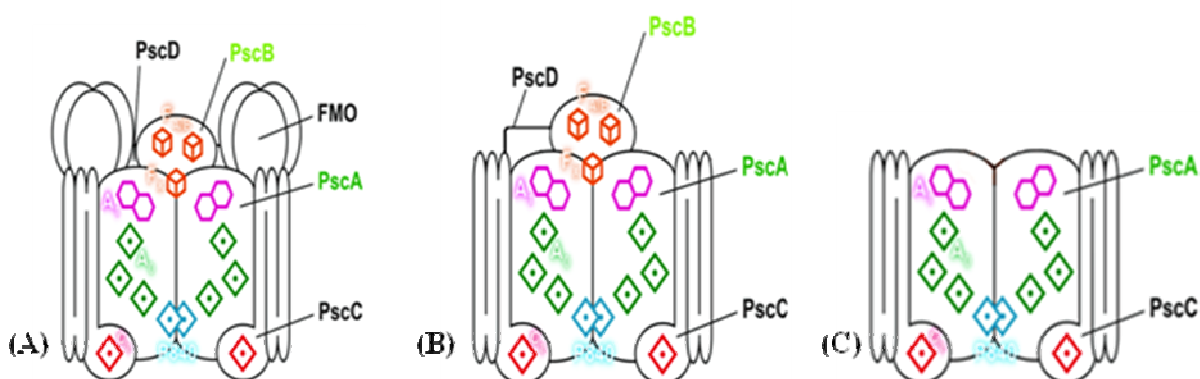


**Figure 6.16** Three possible outcomes of the in meso crystallisation of the *C. tepidum* RC. (A) The FMO, which is unaffected by the lipid might co-crystallise with the RC. (B) The core RC crystallises by itself. (C) The water soluble parts of the RC may also have been affected by the lipid (PscB and PscD), leaving the core intact and possibly allowing the core to crystallise.

### 6.3.4 Lipid Bicelles for the crystallisation of *C. tepidum* RC

As there was a spectral change with the *C. tepidum* RC when incorporated with the monoolein (9:9 MAG) and the 7:7 MAG lipid, there was no way of knowing if the FMO was dissociating from the RC, or if the RC was breaking down. If this was the case the chances of crystal formation would be highly unlikely (as observed to date). This would mean an alternative method would have to be adopted. A happy medium where by the RC was taken out of its detergent micelle (DDM) and incorporated in to an environment that would have least change to the RC spectrally. One such method utilised was by incorporating the RC in to artificial bicelles. Bicelles have been used extensively for both solid and solution state NMR, and are believed to be a lipidic medium for the crystallisation of membrane proteins in a native like bilayer environment [186]. Bicelles are a aqueous lipid-detergent assemblies in which discrete bilayer fragments are edge-stabilised by certain detergents.

Pure RC was prepared as previously mentioned in chapter 3 according to the methods described in section 2.4 in 20 mM Tris pH 8, 75 mM NaCl, and 0.01% DDM. The bicelles were prepared as described in section 2.24, with lipid:amphiphile combinations of DMPC:CHAPSO. The molar ratio of DMPC:CHAPSO was chosen to be 2.8:1 and the final bicelle concentration was 40%. To obtain homogeneous lipid in water it was subjected to repeated cycles of heating (40-50°C), cooling (on ice) and vortexing for the lipid to go in to solution. After completion the bicelles were stored at -20°C to stop hydrolysis of the phospholipd head group. The bicelle was added to the purified RC (~20mg/ml) in a 1:4 (v/v) ratio, giving a final bicelle concentration of 8%. As the bicelle is temperature sensitive going from a viscous liquid at low temperatures to turning in to a gel at higher temperatures, the RC-bicelle mixture was done on ice at 4°C. The mixture of RC-bicelle was gently pipetted until the solution was clear and homogenous. The sample was incubated on ice for 30 min to allow for complete reconstitution of protein in to bicelle. To detect for any changes off the RC an absorption spectra was measured of the RC in solution and when incorporated into the bicelles (Fig 6.17). Figure 6.17 shows the absorption spectra of the RC in solution (Fig 6.17, blue line) with the characteristic 816 nm peak with a shoulder at 837 nm and 800 nm. The spectra of the RC in solution was normalised at 816 nm with the absorption spectra of the RC incorporated in

to the bicelles (Fig 6.17, red line). As it can be seen from figure 6.17 all the characteristic peaks are present when the RC is incorporated in to the bicelles, and most importantly there is no shift within the absorption spectra. The only noticeable difference is the increase in absorbance near the 250 nm region when the RC is in the bicelles, and this is expected as the RC when incorporated in to the bicelles have a different phase to that of RC when in solution making the sample more turbid and allowing for light passing through to the sample to be scattered.

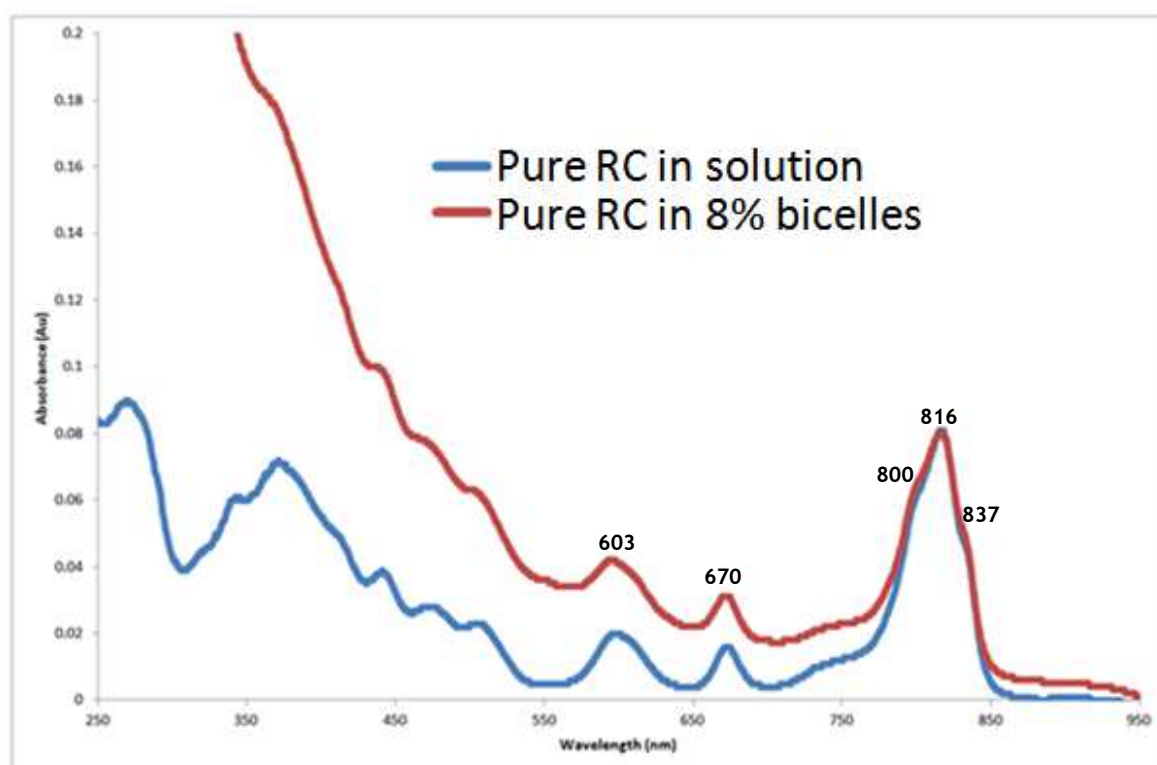


**Figure 6.17 RC absorption comparison of RC in solution and RC in bicelles**

RC in solution (in blue) contains the characteristic absorption spectra peaks at 816, 800, 837, 670 and 603 nm. When RC is in Bicelles (in red) there is no shift. Increase in absorbance near the 250 nm region when the RC is in the bicelles is due to scattering of the light.

Crystal trays were set up using the in house Cartesian robot. The trays used for the bicelles were made by the Cartesian by dispensing the percipetants in there allocated wells (500 nl) but the RC-bicelle solution was added to each well by hand with a pipette (500 nl) as the robot could not dispense the RC-bicelle due to the room temperature being too high causing the change in phase for the RC-Bicelle.

### 6.3.5 Interaction of RC with Ferredoxin using light induced oxygen consumption assay and SPR

The RC had been taken out of its detergent micelle and put in to an environment where there was an increased chance of protein to be able to crystallise. As incorporating the RC in to the bicelle seemed to be a success, in that when its absorption spectra were measured there were no visible changes. But one more final method can be used and that is to co-crystallise with a protein that associates with your target protein, in this case it was ferredoxin. This provides a soluble anchor to allow for protein-protein contacts to form. In 2002 Petra Fromme lab managed to successfully co-crystallise the homologue of the *C. tepidum* RC, PS I with its electron acceptor ferredoxin [187]. Using similar methods as described in this paper the hope was to attempt test if co-crystallisation experiments could be set up with the RC and then use this in conjunction with the artificial bicelles.

As ferredoxin, from *Arabidopsis thaliana*, could already be expressed and purified in large quantities in *E. coli* (as described in section 5.12) this was to be tested to observe if any interactions were taking place with the RC. An obvious experiment to carry out to see if any interactions were taking place was by using the assay activity of the RC, the light induced oxygen consumption using a Clark-type electrode. Instead of using the electron acceptor MV, ferredoxin would be used. An electron donor, which had been used successfully used in the Cogdell lab with this assay was Cyt (Cytochrome) c from horse heart (a gift from Dr Heiko Lokeinstein), who had also utilised the light induced oxygen consumption using a Clark-type electrode to obtain rates for PSI using Cyt c and ferredoxin (results not shown).

The light induced oxygen consumption was carried out as previously described in section 3.1.7. Around 0.6 mg/ml of RC was prepared for this assay, at first to insure that the RC had activity both DCPIP and MV were added to measure if there was any light induced oxygen consumption. This was observed in figure 6.18 were in the first reaction the amount of reduced oxygen was at around -7.4 nmol/ml/min. The second reaction had the addition of Cyt c as the electron donor and no DCPIP (Fig 6.18), when the light was turned on (indicated by the red arrow in figure 6.18) there was no oxygen reduced, on addition of DCPIP a

rate was measured of reduced oxygen at  $-8.8$  nmol/ml/min. The final reaction was replacing MV with ferredoxin, as observed in figure 6.18 experiment 3. The third reaction showed a similar rate to that of the first reaction of RC with DCPIP and MV as its electron acceptor, and this gave a rate of  $-7.3$  nmol/ml/min.

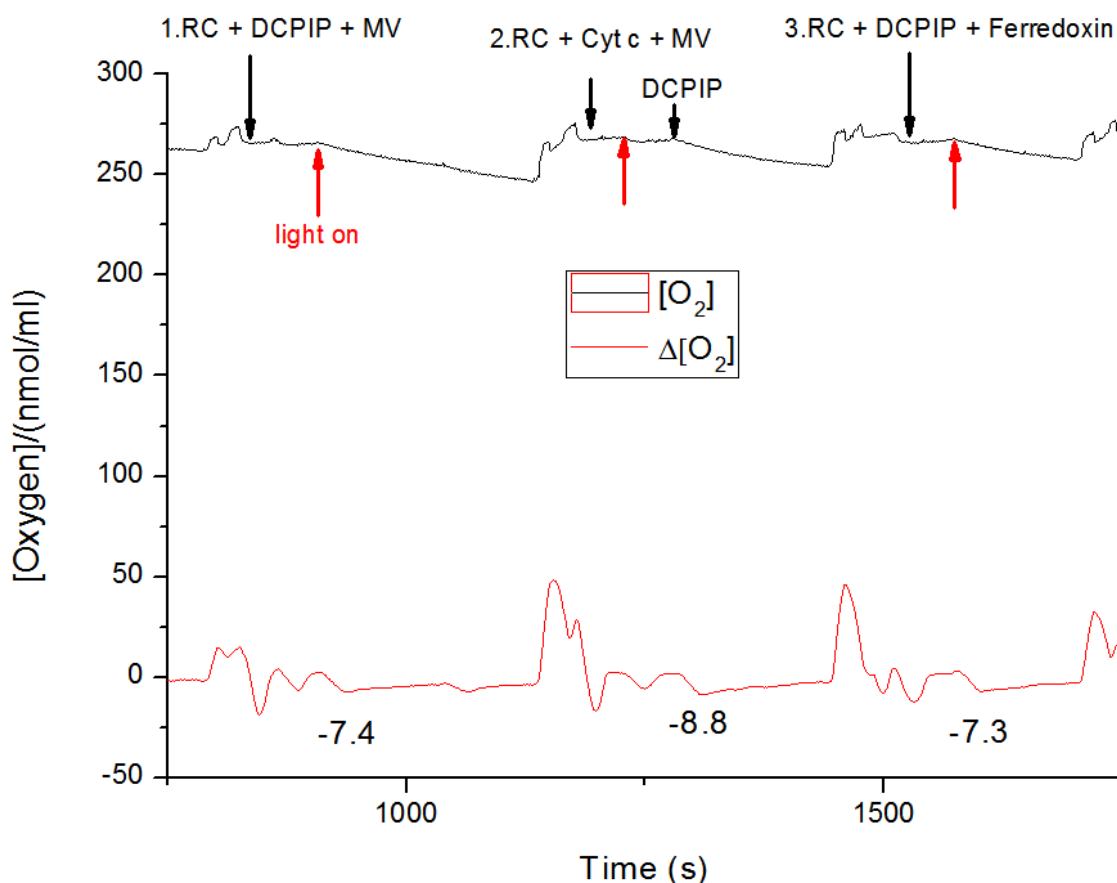


**Figure 6.18 Clarke-type electrode trace of ferredoxin reduction of dissolved oxygen**

Shows the trace of the dissolved oxygen (black line) and the amount of oxygen consumed (red line). First reaction shows DCPIP and MV as electron donor and acceptor, reduced oxygen calculated as  $-7.4$  nmol/ml/min. Second reaction in with Cyt c and MV as electron donor and acceptor, no reaction is observed until the addition of reduced DCPIP as electron donor. The last reaction was of DCPIP and ferredoxin as an electron acceptor were the reduced oxygen was calculated as  $-7.3$  nmol/ml/min. Red arrows indicate the light being turned on.

These results indicated that the RCs had successfully accepted electrons from the donor and passed them on to the acceptor (ferredoxin). This however does not conclusively prove that there is an interaction. One might argue that the RC and ferredoxin came in to close enough proximity to allow for electrons to pass from donor to acceptor. Another method that can be utilised is SPR to show that an interaction is taking place.

Initially ITC experiments had shown no interaction between the RC and ferredoxin, this could have been due to either the on and off rates being too fast or potentially due to the difference in sizes of the RC compared to ferredoxin where no change could be measured. So a more sensitive method was employed and this was SPR. SPR detects refractive index changes at the surface of a sensor chip. The protein of interest, ferredoxin, at a concentration of 0.5 mg/ml was prepared as described in section 5.12. The ferredoxin was covalently coupled to the chip by amine coupling (as described in section 2.21) until all of the chip had been saturated. To the chip the RC, at a concentration of 0.5 mg/ml, was passed over to observe if any interactions were taking place. Figure 6.19 shows the results of the interactions, were in the first step the ferredoxin in 20 mM NaPi pH 7.5, and 75 mM NaCl was passed over the chip. The decline in figure 6.19 at around 600 s indicates that the chip has been saturated. At around 1100 s the RC at a flow rate of 40  $\mu\text{l}/\text{min}$  in 20 mM NaP pH 7.4, 150 mM NaCl, and 0.01% DDM was passed over the chip to observe an interaction, as indicated by the increase in response units observed in Figure 6.19.

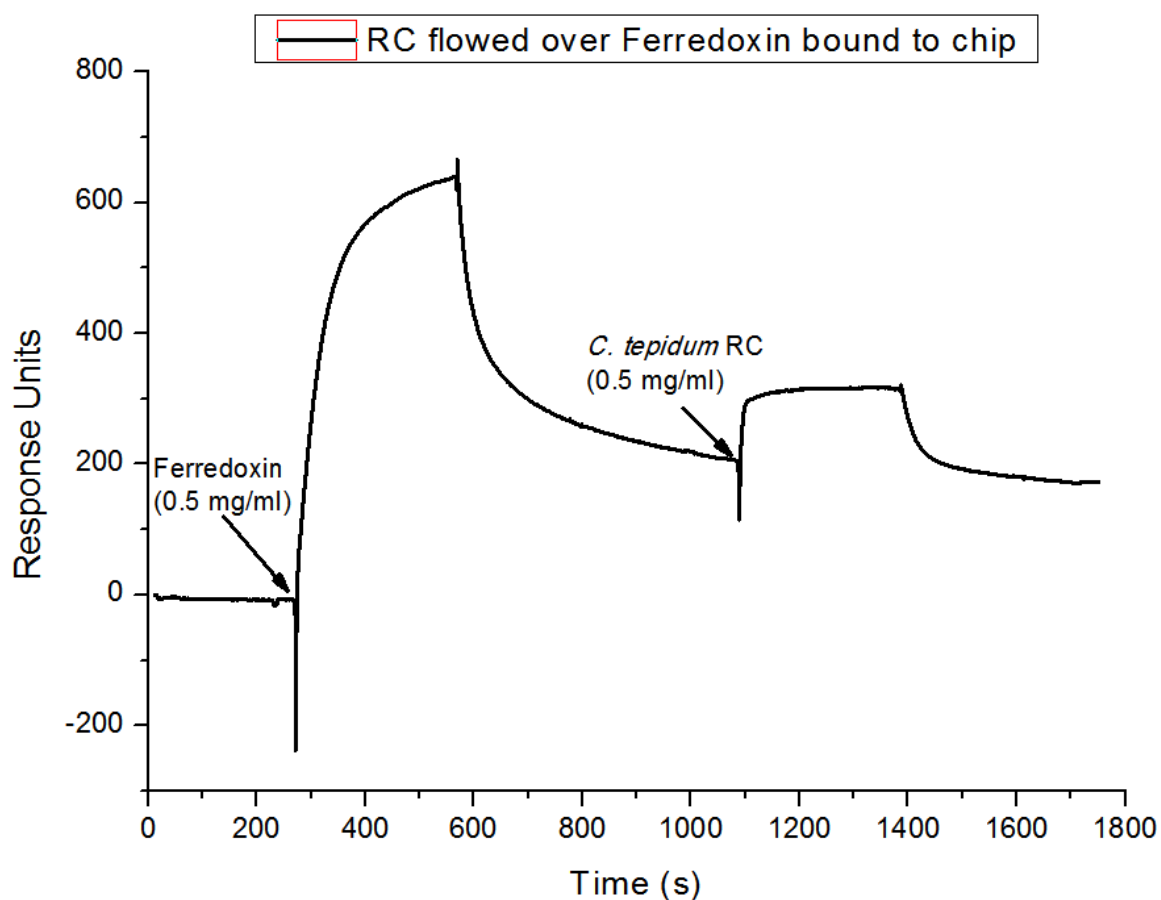


**Figure 6.19 SPR of RC and ferredoxin**

Ferredoxin at a concentration of 0.5 mg/ml was bound to the chip. Once the chip was saturated any unbound ferredoxin flow offas observed at around 600 s. once level the RC was passed over the chip at around 1100 s showing an increase in response unit indicative of binding of RC to ferredoxin

These initial experiments would have to be repeated to obtain rates of binding and dissociation, but as an initial experiment they had shown that there is an interaction of the RC with ferredoxin, and had provided enough data to attempt a co-crystallisation experiment with these two proteins.

### 6.3.6 Co-crystallisation with Ferredoxin

Co-crystallisation experiments were set up of RC + ferredoxin in 7 different commercial screens (Table 7) using our in house robot. The ferredoxin was prepared as described in section 5.12 at a concentration of 85 mg/ml in a final volume of 1 ml. The ferredoxin was added to the RC at a 2:1 (ferredoxin:RC) ratio, where the final concentration of the ferredoxin was 40 mg/ml and the RC had a final concentration of 20 mg/ml in a buffer containing 20 mM Tris pH 8, 75 mM NaCl, and 0.01% DDM. This was then left incubating on ice for 30 mins before setting up the crystal screen using the Cartesian robot.

Screen	Manufacturer
Cryo 1 + 2	Emerald Biosystems
JCSG	Emerald Biosystems
MemGold	Molecular Dimensions
MemGold 2	Molecular Dimensions
MemSys/Start	Molecular Dimensions
Morpheus	Molecular Dimensions
Peglon	Emerald Biosystems

**Table 7 Sparse matrix crystal screens used to set up crystal trays of RC + ferredoxin**

The trays were left incubating at 20°C, and checked weekly at regular intervals. It was noticed that the only screens to produce crystals were cryo 1 & 2 and JCSG as observed in figure 6.20 and 6.21.



35% (v/v) 2-ethoxyethanol  
100 mM CaCodylate



35% (v/v) 2-ethoxyethanol  
100 mM Na/K phosphate  
200 mM Sodium Chloride

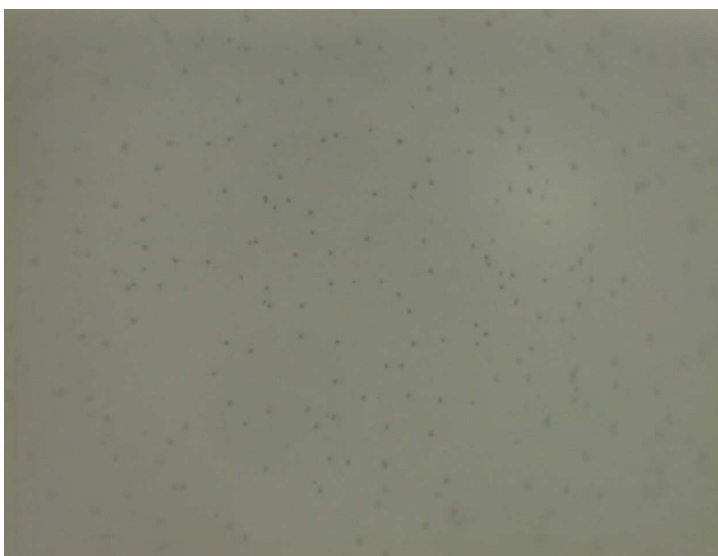
**Figure 6.20** Examples of crystals of RC + ferredoxin in the Cryo 1 & 2 screens



0.1 M Phosphate/citrate pH 4.2  
40% v/v Ethanol  
5% PEG 1000



0.2 M Sodium Chloride  
0.1 M Bis Tris pH 5.5  
25% w/v PEG 3350



0.1 M Bicine pH 9.0  
20% w/v PEG 6000

**Figure 6.21** Examples of crystals of RC + ferredoxin in the JCSG screens

Most of the crystals obtained were star shaped, some had 2 or more crystals that overlapped one and other. All the crystals obtained were too small to shoot in house and had to be tested at the Diamond Light Source (DLS), Oxford UK. These crystals did not diffract well, as was expected with such small crystals. The main purpose for attempting to shoot these crystals was to allow for confirmation that what was being seen was in fact protein crystals and not aggregates of some sort of spheroplasts that had formed. Due to the crystals being so small a grid scan of the loop containing a bunch of crystals was shot, as observed in figure 6.22 A. Out of 14 crystals collected only one had given clear indication that the crystals obtained were in fact protein crystals. These crystals showed high anisotropy with a high level of mosaic spread and only a few spots visible at 60 Å from a crystal grown in 35% (v/v) 2-ethoxyethanol and 100 mM cacodylate. Figure 6.22 B shows an example of the defraction of the RC + Ferredoxin crystal when exposed to the synchrotron radiation.

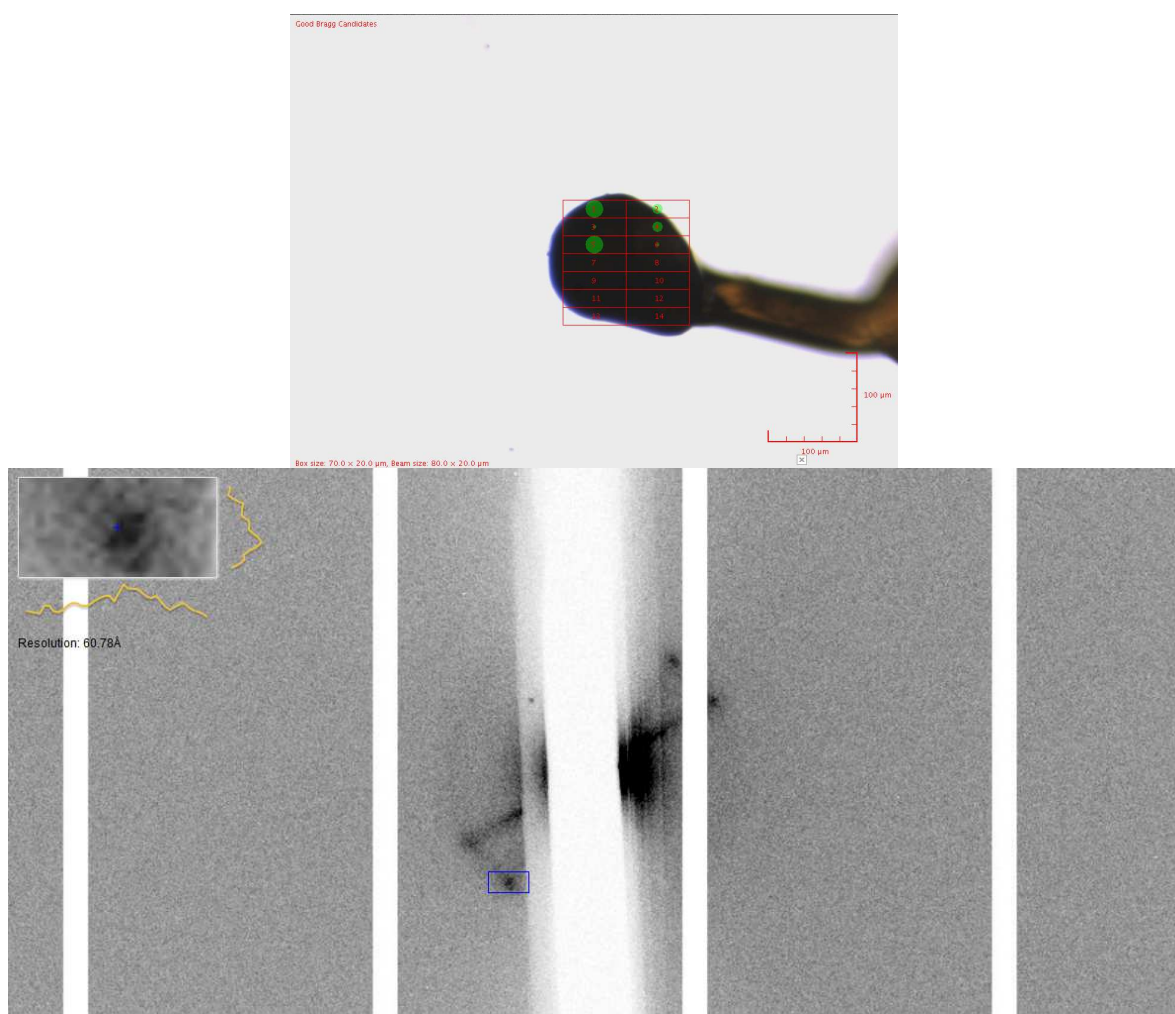


**Figure 6.22 Grid loop and diffraction pattern of the *C. tep* RC + ferredoxin crystal**

A. Shows the mesh loop that was used to collect a few of the RC + ferredoxin crystals, since they were so small and hard to observe they were shot as grids and each individual grid was exposed to the synchrotron beam. B Shows the diffraction pattern of the crystal a 60 Å resolution was obtained indicating that the crystals were in fact protein crystals.

## Chapter 7 – Conclusions and Future Outlook

---

Photosynthesis is one of the most important biological processes on earth, converting light into chemical energy. More energy, in the form of light, falls on the surface of the earth per hour ( $\sim 4.3 \times 10^{20}$  Joules) than the whole world consumes per year ( $\sim 4.1 \times 10^{20}$  Joules) [188]. Research into future alternatives has been and is still being conducted aiming to solve the complex problems of rising energy requirements of a constantly growing world population and environmental pollution [189]. Globally the energy consumption, to date, is estimated to be 22 billion kWh yr<sup>-1</sup> (kilowatts-hour per year), and 53 billion kWh yr<sup>-1</sup> by the year 2020. As the average population increases, by higher than 2% per year, the need for more energy is also exacerbated. The energy provided from sunlight is less than 0.1% of the world's electricity [190]. Major challenges in the area of renewable energy are being able to devise sustainable ways of making fuels, as using photosynthesis directly to make fuels (biofuels), is the rather low efficiency conversion of solar energy into fuel. By studying photosynthesis at the level of primary reactions then, in principle, higher energy conversions are possible allowing us to design devices and photosynthetic mimics capable of producing solar fuels [188, 191]. Here, the green sulphur RC *C. tepidum* was used as a model organism to study in conjunction with plasmons to allow for a possible device to be constructed allowing for higher energy conversions.

Green sulphur bacteria are obligatory anaerobic photoautotrophic bacteria *C. tepidum* is a green sulphur, anaerobic, thermophilic bacteria, that contains a homodimeric Type I RC. The Cofactors involved in electron transfer are similar to those of photosystem (PS) I (bacterial analogue) in plants and cyanobacteria [114]. The *C. tepidum* RC is a type 1 RC, the only type of RC that is homodimeric and does not have its structure solved to date. The only information on this RC is STEM data. By obtaining a 3D-structure of the RC it will reveal the details of the electron transfer pathway and enable us to understand its unique thermophilic properties.

As there was limited information on the *C. tepidum* RC expression and stabilisation experiments had to be carried out from the offset. As the *C.*

*tepidum* RC was thermophilic the initial growth temperatures had to be between 43-50°C to allow for optimal growth, and as these organisms utilised elemental sulphur it was evident that they were oxygen sensitive and therefore had to be grown under limited oxygen environments. As the RC is a membrane protein it had to be solubilised and purified using detergents. It was important, from a structural aspect that the detergent used would not only aide in keeping the RC monodisperse and stable, but it would also allow for the RC to form protein-protein contacts for crystallisation purposes. Here, it was discovered that the best detergent to solubilise with was  $\beta$ -OG, but was later on buffer exchanged in to DDM as this detergent proved to be more stable. This detergent, however, would prove to be challenging to crystallise in.

One of the major issues faced with crystallising the RC in DDM was that initial attempts had shown crystals forming but of FMO by itself. The hope was that the RC would co-crystallise with FMO. This proved not to be the case, and reinforced the belief that other structural means would have to be studied to elucidate the structure of the RC. One of the major challenges faced when studying the RC and the FMO protein is the question of how many FMO proteins are there per RC. Robert E. Blankenship [162], Georgios Tsiotis [163] and Günter Haüska [164] have reported 1, 2 or 3 FMO trimers attached per RC, and this proves to be an issue. In this research when studying the *C. tepidum* RC, it became evident that there were two different populations of the RC. It was hypothesised and shown spectrally that these two populations had different ratios of 808:816 nm. After looking at different ways to separate these two populations the best method proved to be by sucrose density gradients, between 30-35%. These could also be observed on the SEC. Successful separation of these two different populations proved to be beneficial, as with any type of crystallisation, to obtain crystals of a protein it is essential if there is any heterogeneity that it is removed. By being able to express and purify the protein in a stabilising detergent it also became apparent that the concentration of pure protein that had to be expressed was important. For structural studies the standard minimum concentration required is around 10 mg/ml, and for any repetition of experiments required needs to be assured that the concentration of a target protein would not be a variable. Since the green sulphur community that worked on the RC would relate their concentration in OD, or mg/ml of membranes rather than pure protein a simple

assay was carried out to deduce the amount of pure RC obtained from 10 l of cells. This proved to be greatly informative as initial expression and purification experiments that were carried out revealed that the concentration of protein that was being purified would never have had a chance of crystallising as the concentration was too low.

Being able to successfully purify these RCs allowed for the Plasmon enhancement techniques to be utilised, by coupling the RCs to silver nanoparticles. There have been many systems reported that use plasmons in conjunction with photosynthetic pigments, but none with the RCs that work at such high efficiency. Here, we reported a 50 fold increase in fluorescence enhancement with an additional 2 fold increase when a 5 nm SiO<sub>2</sub> spacer is used between the RC and nanoparticle. Similar experiments of pure FMO were also carried out to identify if the high fluorescence was due to the RC or the FMO trimer. As these techniques are quite novel and in their infancy stages a lot more work has to be done. One of the issues that was not addressed was due to the difference in size of the FMO compared to the size of the RC, how would one be able to measure the distance between the Plasmon and the protein-pigment complex as this would have an effect on the fluorescence emission. Another issue not addressed was the orientation of these molecules, there is no way that can be said conclusively all the RCs on the SIFs are active, or all are upside down or right side up. One way to however tackle this is, since the RC is His tagged, the tagged can be utilised to orient the protein in a specific way.

Here, it is also reported the construction of a modified CLBH tag (gift from Dr Niall Fraser), for the purification of two of the peripheral proteins PscD and PscB. Both these soluble proteins are associated with the *C. tepidum* RC. PscD contains no pigments and is of unknown function where as PscB is the Fe-S protein that donates electrons to ferredoxin. A modified CLBH tag was constructed and successfully ligated with the target proteins to be expressed in *E.coli*. The iLOV within the CLBH tag proved to be useful in allowing for expression levels to be measured and for also the observation of PscD along every purification method. Once pure protein had been obtained C3 protease was used to cleave the CLBH tag from the target protein. When the CLBH tag was cleaved from PscD the hope was that pure protein would be obtained,

instead the protein was not present anywhere. On further analysis it was made evident that the PscD had 3 histidines on its N- and C- termini. It was hypothesised that PscD was weakly binding to the nickel column after it had been cleaved from the CLBH tag, this issue was resolved when passing very low concentrations of imidazole over the sample allowing for PscD to be observed. The PscB also had similar issues, in that when cleaved with C3 it would most likely precipitate. Since iron sulphur proteins are not well expressed in *E.coli* they is a low concentration to begin with, due to the addition of C3 when cleaving the CLBH tag showed that the protein was in some way precipitating leading onto the design of another construct that contained no CLBH tag. Once both proteins had successfully been purified they were compared to with both there homologues from PSI PsaD and PsaC.

Lagotte reports that the C-terminus of PsaD plays a critical role on the stability of the complex and is part of a docking site for ferredoxin [74]. Structural homology programs were used to look at the similarities of the sequence and of the structure, from this a 3D model was produced of PscD, which showed a flexible C- terminus tail which could play an important role in the docking of ferredoxin. Initial ITC experiments had shown that PscD did not interact with FMO, but there was a high chance that ferredoxin did. As these experiments are in their infancy stages more work has to be carried out on using different combinations of PscD, PscB and ferredoxin to see if there is an interaction.

As there is no structure of PscD and PscB the next steps were to attempts look at these proteins in more structural detail. Both these proteins were expressed and purified for both crystallography and NMR. As no crystals were obtained the investigation led down the NMR path, which revealed that a part of the PscD protein was unfolded, this would also explain why no crystals of this protein had yet been obtained. Due to PscD being partially unfolded measures had to be taken to allow the structure of PscD to be resolved. A solubility and stability screen for soluble proteins was ordered, this contained 96 different conditions that would be tested for PscD, precipitation of the protein within each condition would imply that the protein was not “happy” in those conditions. Secondly, a trypsin cleavage will be undertaken for this protein to allow for the removal of any flexible regions, which might play a role in the disorder of the protein. PscB,

however was the opposite. Under the NMR machine the protein was beautifully folded, and the pursuit of the NMR structure went on its way. It was as the experiments were proceeding that it was realised that due to the lack of protein being expressed it may not be financially viable to pursue the NMR structure.

The overall aim of the project was to successfully establish an expression and purification protocol of the *C. tepidum* RC in an attempt to couple the RCs to plasmons and to also allow for the structure to be obtained. As mentioned no type I RC structures from green sulphur bacteria have ever been obtained, in fact no one has reported a crystals of a type I RC to date. One of the aims of this research was to elucidate the RC structure and many methods were utilised, such as the in-meso method. This however was challenging as there were changes to the RC when putting the RC in-meso. Other methods such a lipidic bicelles were more promising and leading on from this a co-crystallisation experiment with ferredoxin revealed, for the first time, crystals of the *C. tepidum* RC that diffracted to 60 Å. These crystals however, being so small would most likely be better suited for the electron-free laser. As these crystals obtained are in their infancy stages more optimisation will have to be carried out. By using the bicelles in conjunction with the ferredoxin may increase the chances of better protein-protein contact or bigger crystals.

# Appendices

---

## Appendix 1.

### Solutions for the growth of *Chlorobaculum tepidum*

#### Solution I (Basal Salt solution) Microbiol)

EDTA-2Na	1g
MgSO <sub>4</sub> ·7H <sub>2</sub> O	20g
CaCl <sub>2</sub> ·2H <sub>2</sub> O	5g
NaCl	40g
KH <sub>2</sub> PO <sub>4</sub>	50g

D.W.(distilled water) to 1L

#### Solution II (ammonium, acetate, thiosulfate solution)

CH <sub>3</sub> COONH <sub>4</sub>	50g
NH <sub>4</sub> CL	40g
NA <sub>2</sub> S <sub>2</sub> O <sub>3</sub> ·5H <sub>2</sub> O	230g

D.W. to 1l

#### Solution III (1M MOPS)

MOPS [3-{N-morpholino} propanesulfonic acid]	209g
--	------

D.W. 1l

#### CS solution

Na <sub>2</sub> S·9H <sub>2</sub> O	0.6-1.0 g
NaHCO <sub>3</sub>	2 g

D.W. to 50 ml

#### Trace Elements (T.M. Wahlund et al., 1991 Arch.

EDTA-2Na	5.2g
CoCl <sub>2</sub> ·6H <sub>2</sub> O	190mg
MnCl <sub>2</sub> ·4H <sub>2</sub> O	100mg
FeCl <sub>2</sub> ·4H <sub>2</sub> O	1.5g
CuCl <sub>2</sub> ·2H <sub>2</sub> O	17mg (or CuSO <sub>4</sub> ·5H <sub>2</sub> O 24.5mg)
NaMoO <sub>4</sub> ·2H <sub>2</sub> O	188mg
ZnCl <sub>2</sub>	70mg
VO <sub>2</sub> SO <sub>4</sub> ·2H <sub>2</sub> O	30mg
NiCl <sub>2</sub> ·6H <sub>2</sub> O	25mg
H <sub>3</sub> BO <sub>3</sub>	6mg
NA <sub>2</sub> WO <sub>4</sub> ·2H <sub>2</sub> O	2mg
NaHSeO <sub>3</sub>	2mg (or Na <sub>2</sub> SeO <sub>3</sub> 2.3mg)

D.W. to 1l

#### Vitamin Solution

Vitamin B <sub>12</sub>	2mg
	D.W. to 1l

## Appendix 2.

### LB recipe

(Sambrook and Russell, 2001 Gerhardt, et al. 1994).

Tryptone	10 g
Yeast Extract	5 g
NaCl	10 g

Dissolve components in 1 liter of distilled or deionized water.

For LB agar\* add agar to a final concentration of 1.5%.

Heat the mixture to boiling to dissolve agar and sterilize by autoclaving at 15 psi, from 121-124°C for 15 minutes.

\* Strictly speaking, LB agar should be called LA.

### TB recipe

Deionized H<sub>2</sub>O, to 900 mL

Tryptone, 12 g

Yeast extract, 24 g

Glycerol, 4 mL

For solid medium, please see “Media containing agar or agarose.”

Shake until the solutes have dissolved and then sterilize by autoclaving for 20 min at 15 psi (1.05 kg/cm<sup>2</sup>) on liquid cycle. Allow the solution to cool to 60°C or less, and then add 100 mL of a sterile solution of 0.17 M KH<sub>2</sub>PO<sub>4</sub>, 0.72 M K<sub>2</sub>HPO<sub>4</sub>. (This solution is made by dissolving 2.31 g of KH<sub>2</sub>PO<sub>4</sub> and 12.54 g of K<sub>2</sub>HPO<sub>4</sub> in 90 mL of H<sub>2</sub>O. After the salts have dissolved, adjust the volume of the solution to 100 mL with H<sub>2</sub>O and sterilize by autoclaving for 20 min at 15 psi [1.05 kg/cm<sup>2</sup>] on liquid cycle.)

**Appendix 3.****M9 minimal medium**

1 x M9

To make 1L of M9

Na<sub>2</sub>HPO<sub>4</sub>·7H<sub>2</sub>O - 6.78gKH<sub>2</sub>PO<sub>4</sub> - 3g

NaCl - 0.5g

H<sub>2</sub>O up to - 1L(Can be split in to 2 x 500ml  
Flasks)

5 x M9 (Stock solution)

To make 1L of 5 x M9

Na<sub>2</sub>HPO<sub>4</sub>·7H<sub>2</sub>O - 34gKH<sub>2</sub>PO<sub>4</sub> - 15g

NaCl - 2.5g

H<sub>2</sub>O up to - 1L(Has to be first diluted to 1 x M9  
and then can be split)**Autoclave.**

Salt Mix

Added just before use to 1 x M9 medium.

	50 ml of 1 x M9	500 ml of 1 x M9
MgSO <sub>4</sub> (1M)	100ul	1000ul
CaCl <sub>2</sub> (1M)	10ul	100ul
20% Glucose	1ml	10ml
Amp (1M)	50ul	500ul
Cells	1ml	5-10ml
NH <sub>4</sub> Cl 15N (1g in 2mls)	Do not need to add small scale	800ul

NB. When you plan to double label with <sup>15</sup>N and <sup>13</sup>C the 20% Glucose can be replaced when labelling with <sup>13</sup>C.

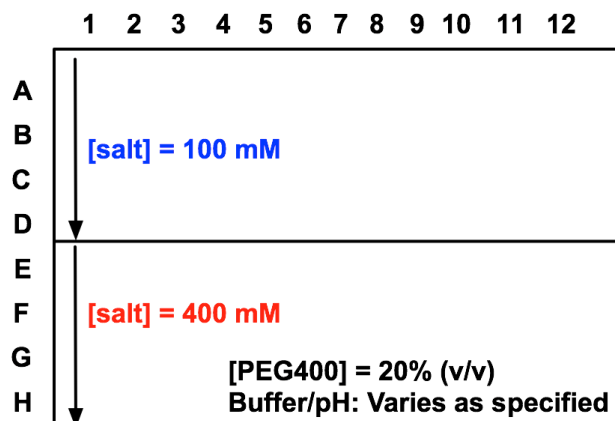
Also add 100uL of the trace elements to every 500ml flask of M9,

Trace element solution (Vishniac and Santer, 1957):

Na<sub>2</sub>-EDTA 50.00 gZnSO<sub>4</sub> x 7 H<sub>2</sub>O 22.00 gCaCl<sub>2</sub> x 2 H<sub>2</sub>O 5.54 gMnCl<sub>2</sub> x 4 H<sub>2</sub>O 5.06 gFeSO<sub>4</sub> x 7 H<sub>2</sub>O 5.00 g(NH<sub>4</sub>)<sub>6</sub>Mo<sub>7</sub>O<sub>24</sub> x 4 H<sub>2</sub>O 1.10 gCuSO<sub>4</sub> x 5 H<sub>2</sub>O 1.57 gCoCl<sub>2</sub> x 6 H<sub>2</sub>O 1.61 g

Distilled water 1000.00 ml

Adjust pH to 6.0 with KOH.

**Appendix 4****Salt stock options screen layout**Homemade screens

<b>Buffer</b>	<b>pH</b>
Sodium acetate	pH 4.5
Sodium citrate	pH 5.5
MES	pH 6.5
ADA	pH 6.5
HEPES	pH 7.5
Tris-HCl	pH 8.5

Commercial Screens

Memsys & Memstart  
 MemGold  
 HT Structure screen  
 MemMeso

<b>Salt Stocks</b>	<b>100 mM</b>	<b>400 mM</b>
ammonium acetate	A1	E1
ammonium chloride	A2	E2
ammonium phosphate monobasic	A3	E3
ammonium fluoride	A4	E4
ammonium formate	A5	E5
ammonium citrate	A6	E6
ammonium phosphate dibasic	A7	E7
ammonium nitrate	A8	E8
ammonium sulfate	A9	E9
ammonium tartrate	A10	E10
calcium acetate	A11	E11
calcium chloride	A12	E12
lithium acetate	B1	F1
lithium chloride	B2	F2
lithium citrate tribasic	B3	F3
lithium nitrate	B4	F4
lithium sulfate	B5	F5
Magnesium acetate	B6	F6
magnesium chloride	B7	F7
magnesium formate	B8	F8
magnesium nitrate	B9	F9
magnesium sulfate	B10	F10
nickel chloride	B11	F11
potassium acetate	B12	F12
potassium chloride	C1	G1
potassium citrate tribasic	C2	G2
potassium phosphate monobasic	C3	G3
potassium fluoride	C4	G4
potassium formate	C5	G5
potassium phosphate dibasic	C6	G6
potassium nitrate	C7	G7
potassium sodium tartrate	C8	G8
potassium thiocyanate	C9	G9
sodium acetate	C10	G10
sodium chloride	C11	G11
sodium citrate tribasic	C12	G12
sodium phosphate	D1	H1
sodium fluoride	D2	H2
sodium formate	D3	H3
sodium phosphate dibasic	D4	H4
sodium malonate	D5	H5
sodium nitrate	D6	H6
sodium sulfate	D7	H7
sodium tartrate dibasic	D8	H8
sodium thiocyanate	D9	H9
succinic acid	D10	H10
zinc acetate	D11	H11
zinc sulfate	D12	H12

## Bibliography

1. Blankenship, R.E., *Early evolution of photosynthesis*. Plant Physiology, 2010. **154**(2): p. 434-438.
2. Hohmann-Marriott, M.F. and R.E. Blankenship, *Evolution of photosynthesis*. Annu Rev Plant Biol, 2011. **62**: p. 515-48.
3. Jagannathan, B., G.Z. Shen, and J.H. Golbeck, *The Evolution of Type I Reaction Centers: The Response to Oxygenic Photosynthesis*, in *Functional Genomics and Evolution of Photosynthetic Systems*, R.L. Burnap and W.F.J. Vermaas, Editors. 2012. p. 285-316.
4. Gest, H. and R. Blankenship, *Time Line of Discoveries: Anoxygenic Bacterial Photosynthesis*. Photosynthesis Research, 2004. **80**(1-3): p. 59-70.
5. Allen, J.P. and J.C. Williams, *The evolutionary pathway from anoxygenic to oxygenic photosynthesis examined by comparison of the properties of photosystem II and bacterial reaction centers*. Photosynthesis Research, 2011. **107**(1): p. 59-69.
6. Olson, J. and R. Blankenship, *Thinking about the evolution of photosynthesis*, in *Discoveries in Photosynthesis*, Govindjee, et al., Editors. 2005, Springer Netherlands. p. 1073-1086.
7. Van Niel, C., *The bacterial photosyntheses and their importance for the general problem of photosynthesis*. Advances in enzymology, 1941. **1**: p. 263-328.
8. Larsen, H., C.S. Yocum, and C.B. van Niel, *ON THE ENERGETICS OF THE PHOTOSYNTHESSES IN GREEN SULFUR BACTERIA*. The Journal of General Physiology, 1952. **36**(2): p. 161-171.
9. Woese, C.R., *Bacterial evolution*. Microbiological reviews, 1987. **51**(2): p. 221.
10. Singhal, G., *Concepts in photobiology: photosynthesis and photomorphogenesis*. 1999: Springer.
11. Yanyushin, M.F., et al., *New Class of Bacterial Membrane Oxidoreductases†*. Biochemistry, 2005. **44**(30): p. 10037-10045.
12. Olson, J., *Photosynthesis in the Archean Era*. Photosynthesis Research, 2006. **88**(2): p. 109-117.
13. Buick, R., *When did oxygenic photosynthesis evolve?* Philosophical Transactions of the Royal Society B: Biological Sciences, 2008. **363**(1504): p. 2731-2743.
14. Shevela, D., L.O. Björn, and Govindjee, *Oxygenic Photosynthesis*, in *Natural and Artificial Photosynthesis*. 2013, John Wiley & Sons Inc. p. 13-63.
15. Pompa, P.P., et al., *Metal-enhanced fluorescence of colloidal nanocrystals with nanoscale control*. Nat Nano, 2006. **1**(2): p. 126-130.
16. Loll, B., et al., *Towards complete cofactor arrangement in the 3.0[thinsp]Å resolution structure of photosystem II*. Nature, 2005. **438**(7070): p. 1040-1044.
17. Bryant, D.A. and N.-U. Frigaard, *Prokaryotic photosynthesis and phototrophy illuminated*. Trends in Microbiology, 2006. **14**(11): p. 488-496.
18. Nelson, N. and A. Ben-Shem, *The complex architecture of oxygenic photosynthesis*. Nat Rev Mol Cell Biol, 2004. **5**(12): p. 971-982.
19. Xiong, J. and C.E. Bauer, *Complex evolution of photosynthesis*. Annual review of plant biology, 2002. **53**(1): p. 503-521.
20. Nelson, N. and A. Ben-Shem, *The structure of photosystem I and evolution of photosynthesis*. BioEssays, 2005. **27**(9): p. 914-922.
21. Stackebrandt, E., R. Murray, and H. Trüper, *Proteobacteria classis nov., a name for the phylogenetic taxon that includes the "purple bacteria and their relatives"*. International Journal of Systematic Bacteriology, 1988. **38**(3): p. 321-325.
22. Blankenship, R., *Molecular mechanisms of photosynthesis, 2002*. 2002, Blackwell Publishing: Oxford.
23. Madigan, M.T. and D.O. Jung, *An overview of purple bacteria: systematics, physiology, and habitats*, in *The purple phototrophic bacteria*. 2008, Springer. p. 1-15.
24. Madigan, M. and D. Jung, *An Overview of Purple Bacteria: Systematics, Physiology, and Habitats*, in *The Purple Phototrophic Bacteria*, C.N. Hunter, et al., Editors. 2009, Springer Netherlands. p. 1-15.
25. Cogdell, R., et al., *The purple bacterial photosynthetic unit*. Photosynthesis Research, 1996. **48**(1-2): p. 55-63.
26. Yeates, T.O., et al., *Structure of the reaction center from Rhodobacter sphaeroides R-26: membrane-protein interactions*. Proceedings of the National Academy of Sciences, 1987. **84**(18): p. 6438-6442.
27. Codgell, R.J., et al., *How purple photosynthetic bacteria harvest solar energy*. Comptes Rendus Chimie, 2006. **9**(2): p. 201-206.

28. Cogdell, R.J., et al., *How photosynthetic bacteria harvest solar energy*. Journal of bacteriology, 1999. **181**(13): p. 3869-3879.
29. Kaufmann, K., et al., *Picosecond kinetics of events leading to reaction center bacteriochlorophyll oxidation*. Science, 1975. **188**(4195): p. 1301-1304.
30. Deisenhofer, J. and J.R. Norris, *Photosynthetic Reaction Center*. Vol. 1. 1993: Academic Press.
31. Michel, H., O. Epp, and J. Deisenhofer, *Pigment—protein interactions in the photosynthetic reaction centre from Rhodospseudomonas viridis*. The EMBO journal, 1986. **5**(10): p. 2445.
32. Fleming, G.R., J.L. Martin, and J. Breton, *Rates of primary electron transfer in photosynthetic reaction centres and their mechanistic implications*. Nature, 1988. **333**(6169): p. 190-192.
33. Roszak, A.W., et al., *Crystal Structure of the RC-LH1 Core Complex from Rhodospseudomonas palustris*. Science, 2003. **302**(5652): p. 1969-1972.
34. Overmann, J., H. Cypionka, and N. Pfennig, *An extremely low-light-adapted phototrophic sulfur bacterium from the Black Sea*. Limnology and oceanography, 1992(1): p. 150-155.
35. Beatty, J.T., et al., *An obligately photosynthetic bacterial anaerobe from a deep-sea hydrothermal vent*. Proceedings of the National Academy of Sciences of the United States of America, 2005. **102**(26): p. 9306-9310.
36. Ward, D.M., et al., *A natural view of microbial biodiversity within hot spring cyanobacterial mat communities*. Microbiology and Molecular Biology Reviews, 1998. **62**(4): p. 1353-1370.
37. Heising, S., et al., *Chlorobium ferrooxidans sp. nov., a phototrophic green sulfur bacterium that oxidizes ferrous iron in coculture with a "Geospirillum" sp. strain*. Archives of Microbiology, 1999. **172**(2): p. 116-124.
38. Frigaard, N.-U. and D. Bryant, *Genomic Insights into the Sulfur Metabolism of Phototrophic Green Sulfur Bacteria*, in *Sulfur Metabolism in Phototrophic Organisms*, R. Hell, et al., Editors. 2008, Springer Netherlands. p. 337-355.
39. Knaff, D.B. and R. Malkin, *Iron-sulfur proteins of the green photosynthetic bacterium Chlorobium*. Biochimica et Biophysica Acta (BBA) - Bioenergetics, 1976. **430**(2): p. 244-252.
40. Vassiliev, I.R., M.L. Antonkine, and J.H. Golbeck, *Iron—sulfur clusters in type I reaction centers*. Biochimica et Biophysica Acta (BBA) - Bioenergetics, 2001. **1507**(1–3): p. 139-160.
41. Beinert, H. and P.J. Kiley, *Fe-S proteins in sensing and regulatory functions*. Current Opinion in Chemical Biology, 1999. **3**(2): p. 152-157.
42. Chitnis, P.R., *Photosystem I: function and physiology*. Annual review of plant biology, 2001. **52**(1): p. 593-626.
43. Nelson, N. and C.F. Yocum, *Structure and function of photosystems I and II*. Annu. Rev. Plant Biol., 2006. **57**: p. 521-565.
44. Amunts, A. and N. Nelson, *Plant Photosystem I Design in the Light of Evolution*. Structure (London, England : 1993), 2009. **17**(5): p. 637-650.
45. Deisenhofer, J., et al., *Structure of the protein subunits in the photosynthetic reaction centre of Rhodospseudomonas viridis at 3Å resolution*. Nature, 1985. **318**: p. 618-624.
46. Jordan, P., et al., *Three-dimensional structure of cyanobacterial photosystem I at 2.5[thinsp]Å resolution*. Nature, 2001. **411**(6840): p. 909-917.
47. Ben-Shem, A., F. Frolow, and N. Nelson, *Crystal structure of plant photosystem I*. Nature, 2003. **426**(6967): p. 630-635.
48. Amunts, A., O. Drory, and N. Nelson, *The structure of a plant photosystem I supercomplex at 3.4[thinsp]Å resolution*. Nature, 2007. **447**(7140): p. 58-63.
49. Guskov, A., et al., *Cyanobacterial photosystem II at 2.9-Å resolution and the role of quinones, lipids, channels and chloride*. Nat Struct Mol Biol, 2009. **16**(3): p. 334-342.
50. Allen, J.P., et al., *Structure of the reaction center from Rhodobacter sphaeroides R-26: the protein subunits*. Proceedings of the National Academy of Sciences, 1987. **84**(17): p. 6162-6166.
51. Ermler, U., et al., *Structure of the photosynthetic reaction centre from Rhodobacter sphaeroides at 2.65 Å resolution: cofactors and protein-cofactor interactions*. Structure, 1994. **2**(10): p. 925-936.
52. Heathcote, P. and M.R. Jones, *8.7 The Structure-Function Relationships of Photosynthetic Reaction Centers*, in *Comprehensive Biophysics*, E.H. Egelman, Editor. 2012, Elsevier: Amsterdam. p. 115-144.
53. Olson, J.M. and R.E. Blankenship, *Thinking about the evolution of photosynthesis*. Photosynthesis Research, 2004. **80**(1-3): p. 373-386.
54. Blankenship, R., *Protein structure, electron transfer and evolution of prokaryotic photosynthetic reaction centers*. Antonie van Leeuwenhoek, 1994. **65**(4): p. 311-329.

55. Heathcote, P., P.K. Fyfe, and M.R. Jones, *Reaction centres: the structure and evolution of biological solar power*. Trends in Biochemical Sciences, 2002. **27**(2): p. 79-87.
56. Rutherford, A. and P. Faller, *Photosystem II: evolutionary perspectives*. Philosophical Transactions of the Royal Society of London. Series B: Biological Sciences, 2003. **358**(1429): p. 245-253.
57. Hauska, G., et al., *The reaction center of green sulfur bacteria*. Biochimica Et Biophysica Acta-Bioenergetics, 2001. **1507**(1-3): p. 260-277.
58. Allen, J.P. and J.C. Williams, *Photosynthetic reaction centers*. FEBS Letters, 1998. **438**(1-2): p. 5-9.
59. Ferreira, K.N., et al., *Architecture of the Photosynthetic Oxygen-Evolving Center*. Science, 2004. **303**(5665): p. 1831-1838.
60. Rhee, K.-H., et al., *Three-dimensional structure of the plant photosystem II reaction centre at 8Å resolution*. Nature, 1998. **396**(6708): p. 283-286.
61. Leeuwen, P., et al., *Rapid and simple isolation of pure photosystem II core and reaction center particles from spinach*. Photosynthesis Research, 1991. **28**(3): p. 149-153.
62. Barber, J. and W. Kühlbrandt, *Photosystem II*. Current Opinion in Structural Biology, 1999. **9**(4): p. 469-475.
63. Leonova, M.M., et al., *Structure-function investigations of bacterial photosynthetic reaction centers*. Biochemistry (Moscow), 2011. **76**(13): p. 1465-1483.
64. Cardona, T., et al., *Charge separation in Photosystem II: A comparative and evolutionary overview*. Biochimica et Biophysica Acta (BBA) - Bioenergetics, 2012. **1817**(1): p. 26-43.
65. Renger, G. and T. Renger, *Photosystem II: The machinery of photosynthetic water splitting*. Photosynthesis Research, 2008. **98**(1-3): p. 53-80.
66. Wydrzynski, T.J. and K. Satoh, *Photosystem II: the light-driven water: plastoquinone oxidoreductase*. Vol. 22. 2006: Springer.
67. Babcock, G.T., et al., *Water oxidation in photosystem II: from radical chemistry to multielectron chemistry*. Biochemistry, 1989. **28**(25): p. 9557-9565.
68. Zouni, A., et al., *Crystal structure of photosystem II from Synechococcus elongatus at 3.8 Å resolution*. Nature, 2001. **409**(6821): p. 739-743.
69. Kok, B., B. Forbush, and M. McGloin, *Cooperation of charges in photosynthetic O<sub>2</sub> evolution-I. A linear four step mechanism*. Photochemistry and Photobiology, 1970. **11**(6): p. 457-475.
70. Klein, M.P., K. Sauer, and V. Yachandra, *Perspectives on the structure of the photosynthetic oxygen evolving manganese complex and its relation to the Kok cycle*. Photosynthesis Research, 1993. **38**(3): p. 265-277.
71. Vrettos, J.S., J. Limburg, and G.W. Brudvig, *Mechanism of photosynthetic water oxidation: combining biophysical studies of photosystem II with inorganic model chemistry*. Biochimica et Biophysica Acta (BBA) - Bioenergetics, 2001. **1503**(1-2): p. 229-245.
72. Jolley, C., et al., *Structure of plant photosystem I revealed by theoretical modeling*. Journal of Biological Chemistry, 2005. **280**(39): p. 33627-33636.
73. Heathcote, P., M.R. Jones, and P.K. Fyfe, *Type I photosynthetic reaction centres: structure and function*. Philosophical Transactions of the Royal Society of London. Series B: Biological Sciences, 2003. **358**(1429): p. 231-243.
74. Lagoutte, B., J. Hanley, and H. Bottin, *Multiple functions for the C terminus of the PsaD subunit in the cyanobacterial photosystem I complex*. Plant Physiology, 2001. **126**(1): p. 307-316.
75. Nogi, T. and K. Miki, *Structural Basis of Bacterial Photosynthetic Reaction Centers*. Journal of Biochemistry, 2001. **130**(3): p. 319-329.
76. Fromme, P. and P. Mathis, *Unraveling the Photosystem I Reaction Center: A History, or the Sum of Many Efforts*. Photosynthesis Research, 2004. **80**(1-3): p. 109-124.
77. Klukas, O., et al., *Photosystem I, an improved model of the stromal subunits PsaC, PsaD, and PsaE*. Journal of Biological Chemistry, 1999. **274**(11): p. 7351-7360.
78. Sétif, P., et al., *The ferredoxin docking site of photosystem I*. Biochimica et Biophysica Acta (BBA) - Bioenergetics, 2002. **1555**(1-3): p. 204-209.
79. Golbeck, J.H., *Structure, function and organization of the photosystem I reaction center complex*. Biochimica et Biophysica Acta (BBA) - Reviews on Bioenergetics, 1987. **895**(3): p. 167-204.
80. Carrillo, N. and E.A. Ceccarelli, *Open questions in ferredoxin-NADP<sup>+</sup> reductase catalytic mechanism*. European Journal of Biochemistry, 2003. **270**(9): p. 1900-1915.
81. Bottin, H., J. Hanley, and B. Lagoutte, *Role of Acidic Amino Acid Residues of PsaD Subunit on Limiting the Affinity of Photosystem I for Ferredoxin*. Biochemical and Biophysical Research Communications, 2001. **287**(4): p. 833-836.

82. Chitnis, V.P., et al., *Mutational analysis of photosystem I polypeptides. Role of PsaD and the lysyl 106 residue in the reductase activity of the photosystem I*. Journal of Biological Chemistry, 1996. **271**(20): p. 11772-11780.
83. Barth, P., B. Lagoutte, and P. Sétif, *Ferredoxin Reduction by Photosystem I from Synechocystis sp. PCC 6803: Toward an Understanding of the Respective Roles of Subunits PsaD and PsaE in Ferredoxin Binding*. Biochemistry, 1998. **37**(46): p. 16233-16241.
84. Li, N., et al., *Polypeptide composition of the Photosystem I complex and the Photosystem I core protein from Synechococcus sp. PCC 6301*. Biochimica et Biophysica Acta (BBA) - Bioenergetics, 1991. **1059**(2): p. 215-225.
85. Li, N., et al., *PsaD is required for the stable binding of PsaC to the photosystem I core protein of Synechococcus sp. PCC 6301*. Biochemistry, 1991. **30**(31): p. 7863-7872.
86. Lelong, C., et al., *Identification of the amino acids involved in the functional interaction between photosystem I and ferredoxin from Synechocystis sp. PCC 6803 by chemical cross-linking*. Journal of Biological Chemistry, 1994. **269**(13): p. 10034-10039.
87. Sétif, P., *Ferredoxin and flavodoxin reduction by photosystem I*. Biochimica et Biophysica Acta (BBA) - Bioenergetics, 2001. **1507**(1-3): p. 161-179.
88. Falzone, C.J., et al., *Three-Dimensional Solution Structure of PsaE from the Cyanobacterium Synechococcus sp. Strain PCC 7002, a Photosystem I Protein That Shows Structural Homology with SH3 Domains*. Biochemistry, 1994. **33**(20): p. 6052-6062.
89. Lushy, A., L. Verchovsky, and R. Nechushtai, *The Stable Assembly of Newly Synthesized PsaE into the Photosystem I Complex Occurring via the Exchange Mechanism Is Facilitated by Electrostatic Interactions*. Biochemistry, 2002. **41**(37): p. 11192-11199.
90. Sonoike, K., H. Hatanaka, and S. Katoh, *Small subunits of Photosystem I reaction center complexes from Synechococcus elongatus. II. The psaE gene product has a role to promote interaction between the terminal electron acceptor and ferredoxin*. Biochimica et Biophysica Acta (BBA) - Bioenergetics, 1993. **1141**(1): p. 52-57.
91. Xu, Q., et al., *Function and organization of photosystem I in a cyanobacterial mutant strain that lacks PsaF and PsaJ subunits*. Journal of Biological Chemistry, 1994. **269**(5): p. 3205-3211.
92. Rutherford, A.W. and P. Heathcote, *Primary photochemistry in photosystem-I*. Photosynthesis Research, 1985. **6**(4): p. 295-316.
93. Croce, R. and H. Amerongen, *Light-harvesting in photosystem I*. Photosynthesis Research, 2013. **116**(2-3): p. 153-166.
94. Melkozernov, A.N., J. Barber, and R.E. Blankenship, *Light Harvesting in Photosystem I Supercomplexes*. Biochemistry, 2005. **45**(2): p. 331-345.
95. Fan, D.-Y., et al., *Quantification of cyclic electron flow around Photosystem I in spinach leaves during photosynthetic induction*. Photosynthesis Research, 2007. **94**(2-3): p. 347-357.
96. Amunts, A. and N. Nelson, *Functional organization of a plant Photosystem I: Evolution of a highly efficient photochemical machine*. Plant Physiology and Biochemistry, 2008. **46**(3): p. 228-237.
97. Jagannathan, B. and J.H. Golbeck, *Unifying principles in homodimeric type I photosynthetic reaction centers: Properties of PscB and the FA, FB and FX iron-sulfur clusters in green sulfur bacteria*. Biochimica et Biophysica Acta (BBA) - Bioenergetics, 2008. **1777**(12): p. 1535-1544.
98. Yordanov, I. and V. Velikova, *Photoinhibition of photosystem 1 Bulg.* J Plant Physiol, 2000. **26**: p. 70-92.
99. Frank, H.A., M.B. McLean, and K. Sauer, *Triplet states in photosystem I of spinach chloroplasts and subchloroplast particles*. Proceedings of the National Academy of Sciences, 1979. **76**(10): p. 5124-5128.
100. DEISENHOFER, J. and H. MICHEL, *The Photosynthetic Reaction Center from the Purple Bacterium Rhodospseudomonas viridis*. Science, 1989. **245**(4925): p. 1463-1473.
101. Nagashima, K.P., K. Shimada, and K. Matsuura, *Phylogenetic analysis of photosynthetic genes of Rhodocyclus gelatinosus: Possibility of horizontal gene transfer in purple bacteria*. Photosynthesis Research, 1993. **36**(3): p. 185-191.
102. Holten, D., et al., *Primary photochemical processes in isolated reaction centers of Rhodospseudomonas viridis*. Biochimica et Biophysica Acta (BBA) - Bioenergetics, 1978. **501**(1): p. 112-126.
103. Mulvaney, R.M., *Studies of light harvesting complexes from purple photosynthetic bacteria*. 2013, University of Glasgow.
104. Holzapfel, W., et al., *Initial electron-transfer in the reaction center from Rhodobacter sphaeroides*. Proceedings of the National Academy of Sciences, 1990. **87**(13): p. 5168-5172.

105. Stowell, M.H.B., et al., *Light-Induced Structural Changes in Photosynthetic Reaction Center: Implications for Mechanism of Electron-Proton Transfer*. Science, 1997. **276**(5313): p. 812-816.
106. Rockley, M.G., et al., *Picosecond detection of an intermediate in the photochemical reaction of bacterial photosynthesis*. Proceedings of the National Academy of Sciences, 1975. **72**(6): p. 2251-2255.
107. Kirmaier, C. and D. Holten, *Primary photochemistry of reaction centers from the photosynthetic purple bacteria*. Photosynthesis Research, 1987. **13**(3): p. 225-260.
108. Eisen, J.A., et al., *The complete genome sequence of Chlorobium tepidum TLS, a photosynthetic, anaerobic, green-sulfur bacterium*. Proceedings of the National Academy of Sciences, 2002. **99**(14): p. 9509-9514.
109. Olson, J.M., T.H. Giddings Jr, and E.K. Shaw, *An enriched reaction center preparation from green photosynthetic bacteria*. Biochimica et Biophysica Acta (BBA) - Bioenergetics, 1976. **449**(2): p. 197-208.
110. Feick, R., M. Fitzpatrick, and R. Fuller, *Isolation and characterization of cytoplasmic membranes and chlorosomes from the green bacterium Chloroflexus aurantiacus*. Journal of bacteriology, 1982. **150**(2): p. 905-915.
111. Wahlund, T., et al., *A thermophilic green sulfur bacterium from New Zealand hot springs, Chlorobium tepidum sp. nov.* Archives of Microbiology, 1991. **156**(2): p. 81-90.
112. Büttner, M., et al., *The Photosystem I-like P840-reaction center of Green S-bacteria is a homodimer*. Biochimica et Biophysica Acta (BBA) - Bioenergetics, 1992. **1101**(2): p. 154-156.
113. Feiler, U., W. Nitschke, and H. Michel, *Characterization of an improved reaction center preparation from the photosynthetic green sulfur bacterium Chlorobium containing the iron-sulfur centers FA and FB and a bound cytochrome subunit*. Biochemistry, 1992. **31**(9): p. 2608-2614.
114. Oh-oka, H., et al., *Two molecules of cytochrome c function as the electron donors to P840 in the reaction center complex isolated from a green sulfur bacterium, Chlorobium tepidum*. FEBS Letters, 1995. **365**(1): p. 30-34.
115. Frankenberg, N., et al., *P840-Reaction Centers from Chlorobium tepidum—Quinone Analysis and Functional Reconstitution into Lipid Vesicles*. Photochemistry and Photobiology, 1996. **64**(1): p. 14-19.
116. Arellano, J.B., et al., *Effect of Carotenoid Biosynthesis Inhibition on the Chlorosome Organization in Chlorobium phaeobacteroides Strain CL1401*. Photochemistry and Photobiology, 2000. **71**(6): p. 715-723.
117. Permentier, H., et al., *Composition and optical properties of reaction centre core complexes from the green sulfur bacteria Prosthecochloris aestuarii and Chlorobium tepidum*. Photosynthesis Research, 2000. **64**(1): p. 27-39.
118. Büttner, M., et al., *Photosynthetic reaction center genes in green sulfur bacteria and in photosystem 1 are related*. Proceedings of the National Academy of Sciences, 1992. **89**(17): p. 8135-8139.
119. Rémy, H.-W., et al., *The reaction centre from green sulphur bacteria: progress towards structural elucidation*. Photosynthesis Research, 2002. **71**(1-2): p. 91-98.
120. Frigaard, N.-U., et al., *Chlorobium Tepidum: Insights into the Structure, Physiology, and Metabolism of a Green Sulfur Bacterium Derived from the Complete Genome Sequence*. Photosynthesis Research, 2003. **78**(2): p. 93-117.
121. Tsukatani, Y., et al., *Function of a PscD Subunit in a Homodimeric Reaction Center Complex of the Photosynthetic Green Sulfur Bacterium Chlorobium tepidum Studied by Insertional Gene Inactivation REGULATION OF ENERGY TRANSFER AND FERREDOXIN-MEDIATED NADP+ REDUCTION ON THE CYTOPLASMIC SIDE*. Journal of Biological Chemistry, 2004. **279**(49): p. 51122-51130.
122. Azai, C., et al., *A heterogeneous tag-attachment to the homodimeric type 1 photosynthetic reaction center core protein in the green sulfur bacterium Chlorobaculum tepidum*. Biochimica et Biophysica Acta (BBA) - Bioenergetics, 2011. **1807**(7): p. 803-812.
123. Bryant, D.A. and Z.F. Liu, *Green Bacteria: Insights into Green Bacterial Evolution through Genomic Analyses*, in *Genome Evolution of Photosynthetic Bacteria*, J.T. Beatty, Editor. 2013. p. 99-150.
124. Romberger, S. and J. Golbeck, *The bound iron-sulfur clusters of Type-I homodimeric reaction centers*. Photosynthesis Research, 2010. **104**(2-3): p. 333-346.
125. Oh-oka, H., M. Iwaki, and S. Itoh, *Viscosity Dependence of the Electron Transfer Rate from Bound Cytochrome c to P840 in the Photosynthetic Reaction Center of the Green Sulfur Bacterium Chlorobium tepidum*. Biochemistry, 1997. **36**(30): p. 9267-9272.
126. Oh-oka, H., M. Iwaki, and S. Itoh, *Membrane-Bound Cytochrome cz Couples Quinol Oxidoreductase to the P840 Reaction Center Complex in Isolated Membranes of the*

- Green Sulfur Bacterium Chlorobium tepidum*†. *Biochemistry*, 1998. **37**(35): p. 12293-12300.
127. Itoh, M., et al., *Kinetics of electron transfer between soluble cytochrome c-554 and purified reaction center complex from the green sulfur bacterium Chlorobium tepidum*. *Photosynthesis Research*, 2002. **71**(1-2): p. 125-135.
  128. Hirano, Y., et al., *Crystal Structure of the Electron Carrier Domain of the Reaction Center Cytochrome cz Subunit from Green Photosynthetic Bacterium Chlorobium tepidum*. *Journal of Molecular Biology*, 2010. **397**(5): p. 1175-1187.
  129. Li, Y.-F., et al., *Crystal structure of the bacteriochlorophyll a protein from Chlorobium tepidum*. *Journal of Molecular Biology*, 1997. **271**(3): p. 456-471.
  130. Borrego, C., et al., *Light intensity effects on pigment composition and organisation in the green sulfur bacterium Chlorobium tepidum*. *Photosynthesis Research*, 1999. **59**(2-3): p. 159-166.
  131. Schmidt, K.A., et al., *Electron Transfer in Reaction Center Core Complexes from the Green Sulfur Bacteria Prosthecochloris aestuarii and Chlorobium tepidum*†. *Biochemistry*, 2000. **39**(24): p. 7212-7220.
  132. Frigaard, N.-U. and D. Bryant, *Seeing green bacteria in a new light: genomics-enabled studies of the photosynthetic apparatus in green sulfur bacteria and filamentous anoxygenic phototrophic bacteria*. *Archives of Microbiology*, 2004. **182**(4): p. 265-276.
  133. Camara-Artigas, A., R. Blankenship, and J. Allen, *The structure of the FMO protein from Chlorobium tepidum at 2.2 Å resolution*. *Photosynthesis Research*, 2003. **75**(1): p. 49-55.
  134. Tronrud, D., et al., *The structural basis for the difference in absorbance spectra for the FMO antenna protein from various green sulfur bacteria*. *Photosynthesis Research*, 2009. **100**(2): p. 79-87.
  135. Wen, J., et al., *Membrane orientation of the FMO antenna protein from Chlorobaculum tepidum as determined by mass spectrometry-based footprinting*. *Proceedings of the National Academy of Sciences*, 2009. **106**(15): p. 6134-6139.
  136. Maresca, J.A., et al., *The bchU gene of Chlorobium tepidum encodes the C-20 methyltransferase in bacteriochlorophyll c biosynthesis*. *Journal of bacteriology*, 2004. **186**(9): p. 2558-2566.
  137. Wen, J., et al., *Structural model and spectroscopic characteristics of the FMO antenna protein from the aerobic chlorophototroph, Candidatus Chloracidobacterium thermophilum*. *Biochimica et Biophysica Acta (BBA) - Bioenergetics*, 2011. **1807**(1): p. 157-164.
  138. White, S. *Membrane proteins of known 3D structure*. 2014 [cited 2014; Available from: <http://blanco.biomol.uci.edu/mpstruc/>].
  139. Bill, R.M., et al., *Overcoming barriers to membrane protein structure determination*. *Nature biotechnology*, 2011. **29**(4): p. 335-340.
  140. Park, S.H., et al., *Structure of the chemokine receptor CXCR1 in phospholipid bilayers*. *Nature*, 2012. **491**(7426): p. 779-783.
  141. Chayen, N.E., *Turning protein crystallisation from an art into a science*. *Current Opinion in Structural Biology*, 2004. **14**(5): p. 577-583.
  142. Arora, A. and L.K. Tamm, *Biophysical approaches to membrane protein structure determination*. *Current Opinion in Structural Biology*, 2001. **11**(5): p. 540-547.
  143. Garavito, R.M. and J.P. Rosenbusch, *Three-dimensional crystals of an integral membrane protein: an initial x-ray analysis*. *The Journal of cell biology*, 1980. **86**(1): p. 327-329.
  144. Michel, H. and D. Oesterhelt, *Three-dimensional crystals of membrane proteins: bacteriorhodopsin*. *Proceedings of the National Academy of Sciences*, 1980. **77**(3): p. 1283-1285.
  145. Mohanty, A.K., C.R. Simmons, and M.C. Wiener, *Inhibition of tobacco etch virus protease activity by detergents*. *Protein Expression and Purification*, 2003. **27**(1): p. 109-114.
  146. Caffrey, M., *Membrane protein crystallization*. *Journal of Structural Biology*, 2003. **142**(1): p. 108-132.
  147. Cherezov, V., et al., *Room to Move: Crystallizing Membrane Proteins in Swollen Lipidic Mesophases*. *Journal of Molecular Biology*, 2006. **357**(5): p. 1605-1618.
  148. Caffrey, M. and V. Cherezov, *Crystallizing membrane proteins using lipidic mesophases*. *Nat. Protocols*, 2009. **4**(5): p. 706-731.
  149. Juan, M.L., M. Righini, and R. Quidant, *Plasmon nano-optical tweezers*. *Nature Photonics*, 2011. **5**(6): p. 349-356.
  150. Aslan, K., J. Lakowicz, and C. Geddes, *Metal-enhanced fluorescence using anisotropic silver nanostructures: critical progress to date*. *Analytical and Bioanalytical Chemistry*, 2005. **382**(4): p. 926-933.
  151. Aslan, K., et al., *Annealed Silver-Island Films for Applications in Metal-Enhanced Fluorescence: Interpretation in Terms of Radiating Plasmons*. *Journal of Fluorescence*, 2005. **15**(5): p. 643-654.

152. Twardowska, M., et al., *Fluorescence enhancement of photosynthetic complexes separated from nanoparticles by a reduced graphene oxide layer*. Applied Physics Letters, 2014. **104**(9): p. -.
153. Oulton, R.F., *Surface plasmon lasers: sources of nanoscopic light*. Materials Today, 2012. **15**(1–2): p. 26-34.
154. Sun, G. and J.B. Khurgin, *Plasmon Enhancement of Luminescence by Metal Nanoparticles*. Selected Topics in Quantum Electronics, IEEE Journal of, 2011. **17**(1): p. 110-118.
155. Tam, F., et al., *Plasmonic Enhancement of Molecular Fluorescence*. Nano Letters, 2007. **7**(2): p. 496-501.
156. Frigaard, N.-U. and D.A. Bryant, *Chromosomal gene inactivation in the green sulfur bacterium Chlorobium tepidum by natural transformation*. Applied and environmental microbiology, 2001. **67**(6): p. 2538-2544.
157. Vishniac, W. and M. Santer, *The thiobacilli*. Bacteriological Reviews, 1957. **21**(3): p. 195.
158. Sambrook, J. and D.W. Russell, *Molecular cloning: a laboratory manual (3-volume set)*. Vol. 999. 2001: Cold spring harbor laboratory press Cold Spring Harbor, New York:.
159. Ujwal, R. and J.U. Bowie, *Crystallizing membrane proteins using lipidic bicelles*. Methods, 2011. **55**(4): p. 337-341.
160. Azai, C., J. Harada, and H. Oh-oka, *Gene Expression System in Green Sulfur Bacteria by Conjugal Plasmid Transfer*. PloS one, 2013. **8**(11): p. e82345.
161. Rémy, H.-W., et al., *The reaction center complex from the green sulfur bacterium Chlorobium tepidum: a structural analysis by scanning transmission electron microscopy*. Journal of Molecular Biology, 1999. **290**(4): p. 851-858.
162. He, G., et al., *Structural Analysis of the Homodimeric Reaction Center Complex from the Photosynthetic Green Sulfur Bacterium Chlorobaculum tepidum*. Biochemistry, 2014.
163. Remigy, H., et al., *Evidence for the association of three FMO subunits per reaction center of Chlorobium Tepidum by scanning transmission electron microscopy*, in *Photosynthesis: Mechanisms and Effects*, G. Garab, Editor. 1998, Springer Netherlands. p. 531-534.
164. Griesbeck, C., et al., *Quantitation of P840 reaction center preparations from Chlorobium tepidum: chlorophylls and FMO-protein*. Biochimica et Biophysica Acta (BBA) - Bioenergetics, 1998. **1365**(1–2): p. 285-293.
165. Fryer, H.J.L., et al., *Lowry protein assay using an automatic microtiter plate spectrophotometer*. Analytical Biochemistry, 1986. **153**(2): p. 262-266.
166. ChandraRajan, J. and L. Klein, *Lowry assay of dilute protein solutions containing high concentrations of Triton X-100*. Analytical Biochemistry, 1975. **69**(2): p. 632-636.
167. Kruger, N., *The Bradford Method for Protein Quantitation*, in *Basic Protein and Peptide Protocols*, J. Walker, Editor. 1994, Humana Press. p. 9-15.
168. Popov, N., et al., *[Reliable micromethod for determination of the protein content in tissue homogenates]*. Acta biologica et medica Germanica, 1974. **34**(9): p. 1441-1446.
169. Schaffner, W. and C. Weissmann, *A rapid, sensitive, and specific method for the determination of protein in dilute solution*. Analytical Biochemistry, 1973. **56**(2): p. 502-514.
170. Hill, R., *Oxygen evolved by isolated chloroplasts*. Nature, 1937. **139**(881): p. i939.
171. Olson, J., *The FMO protein*, in *Discoveries in Photosynthesis*, Govindjee, et al., Editors. 2005, Springer Netherlands. p. 421-427.
172. Tronrud, D.E., M.F. Schmid, and B.W. Matthews, *Structure and X-ray amino acid sequence of a bacteriochlorophyll a protein from Prosthecochloris aestuarii refined at 1.9 Å resolution*. Journal of Molecular Biology, 1986. **188**(3): p. 443-454.
173. Oh-oka, H., *Type 1 Reaction Center of Photosynthetic Heliobacteria*. Photochemistry and Photobiology, 2007. **83**(1): p. 177-186.
174. Chapman, S., et al., *The photoreversible fluorescent protein iLOV outperforms GFP as a reporter of plant virus infection*. Proceedings of the National Academy of Sciences, 2008. **105**(50): p. 20038-20043.
175. Christie, J.M., et al., *Arabidopsis NPH1: A flavoprotein with the properties of a photoreceptor for phototropism*. Science, 1998. **282**(5394): p. 1698-1701.
176. Crosson, S. and K. Moffat, *Structure of a flavin-binding plant photoreceptor domain: Insights into light-mediated signal transduction*. Proceedings of the National Academy of Sciences of the United States of America, 2001. **98**(6): p. 2995-3000.
177. Christie, J.M., *Phototropin blue-light receptors*, in *Annual Review of Plant Biology*. 2007. p. 21-45.
178. Crosson, S. and K. Moffat, *Structure of a flavin-binding plant photoreceptor domain: Insights into light-mediated signal transduction*. Proceedings of the National Academy of Sciences, 2001. **98**(6): p. 2995-3000.

179. Schüttrigkeit, T.A., et al., *Primary photophysics of the FMN binding LOV2 domain of the plant blue light receptor phototropin of Avena sativa*. Chemical Physics, 2003. **294**(3): p. 501-508.
180. Christie, J.M., et al., *Steric Interactions Stabilize the Signaling State of the LOV2 Domain of Phototropin 1f*. Biochemistry, 2007. **46**(32): p. 9310-9319.
181. Yang, Z.R., et al., *RONN: the bio-basis function neural network technique applied to the detection of natively disordered regions in proteins*. Bioinformatics, 2005. **21**(16): p. 3369-3376.
182. Qian, L., C. Zheng, and J. Liu, *Characterization of iron-sulfur cluster assembly protein isca from Acidithiobacillus ferrooxidans*. Biochemistry (Moscow), 2013. **78**(3): p. 244-251.
183. Hager-Braun, C., et al., *Stable photobleaching of P840 in Chlorobium reaction center preparations: presence of the 42-kDa bacteriochlorophyll a protein and a 17-kDa polypeptide*. Biochemistry, 1995. **34**(29): p. 9617-9624.
184. Kelley, L.A. and M.J.E. Sternberg, *Protein structure prediction on the Web: a case study using the Phyre server*. Nat. Protocols, 2009. **4**(3): p. 363-371.
185. Guex, N. and M.C. Peitsch, *SWISS - MODEL and the Swiss - Pdb Viewer: an environment for comparative protein modeling*. electrophoresis, 1997. **18**(15): p. 2714-2723.
186. Sanders, C.R. and R.S. Prosser, *Bicelles: a model membrane system for all seasons?* Structure, 1998. **6**(10): p. 1227-1234.
187. Fromme, P., et al., *Crystallization and Electron Paramagnetic Resonance Characterization of the Complex of Photosystem I with its Natural Electron Acceptor Ferredoxin*. Biophysical Journal, 2002. **83**(4): p. 1760-1773.
188. Donohue, T.J. and R.J. Cogdell, *Microorganisms and clean energy*. Nat Rev Micro, 2006. **4**(11): p. 800-800.
189. Dincer, I., *Renewable energy and sustainable development: a crucial review*. Renewable and Sustainable Energy Reviews, 2000. **4**(2): p. 157-175.
190. Omer, A.M., *Energy, environment and sustainable development*. Renewable and Sustainable Energy Reviews, 2008. **12**(9): p. 2265-2300.
191. Scholes, G.D., et al., *Lessons from nature about solar light harvesting*. Nat Chem, 2011. **3**(10): p. 763-774.